The Mechanics of Mussel Byssal Threads: A Study in Protein Unfolding and Graded Structures

by

Brian P. Greviskes

Bachelor of Science
Massachusetts Institute of Technology, 2008

Submitted to the Department of Mechanical Engineering
in partial fulfillment of the requirements for the degree of

MASTER OF SCIENCE IN MECHANICAL ENGINEERING

at the

MASSACHUSETTS INSTITUTE OF TECHNOLOGY

May 2009

Author . . . . . .

Department of Mechanical Engineering
May 22, 2009

Certified by . . . . . .

Mary C. Boyce
Gail E. Kendall Professor of Mechanical Engineering
Thesis Supervisor

Accepted by . . . . . .

David Hardt
Chairman, Department Committee on Graduate Students

The Mechanics of Mussel Byssal Threads:
A Study in Protein Unfolding and Graded Structures

by

Brian P. Greviskes

Submitted to the Department of Mechanical Engineering
on May 22, 2009, in partial fulfillment of the
requirements for the degree of
MASTER OF SCIENCE IN MECHANICAL ENGINEERING

Abstract

Natural materials and structures have evolved over millions of years to perform very complex and specific biomechanical functions, and as a result can provide insight into optimal designs for particular properties. Mussel byssal threads, the attachment appendage of aquatic mussels, are one example of such structures. These threads protrude from the mussel, connecting the mussel to rocks and other hard surfaces, providing a strong and resilient, yet dissipative attachment (so that the mussel can remain attached to the rocks without being dashed against them during violent wave periods). The threads themselves are graded, with both the geometry (cross-section) and the mechanical properties transitioning from the proximal (proximal to the mussel) thread section, which is compliant and highly dissipative, to the distal thread section, which is stiff (relative to the proximal section) and less dissipative at low strains, but more dissipative at high strains. The goal of this thesis is to develop an understanding of the mechanical properties of the individual thread sections during the large stretches seen during its function, as well as to develop a microstructurally-informed constitutive model that captures the microstructural evolution of these materials with loading (an evolution that is dominated by protein unfolding). These material models will then be incorporated into three dimensional finite element model of the thread, in order to gain insight into the design of graded structures. The constitutive model developed and outlined herein provides a method for modeling protein unfolding caused by mechanical loading, and captures the major characteristics of the mechanical behavior of these threads. The 3-D finite element model presented and discussed provides insight into design parameters for building graded structures.

Thesis Supervisor: Mary C. Boyce
Title: Gail E. Kendall Professor of Mechanical Engineering

Acknowledgements

First, I would like to thank my advisor, Prof. Boyce. I hated 2.002, and after the class, when you offered me the UROP position, I only took it because I couldn't get a UROP in any of the fluids or heat transfer labs. Now, I consider that the best decision of my life. I couldn't imagine doing research in any other subject or with any other advisor, nor could I imagine the last two years of my life going any other way. I am constantly amazed with the simple solutions you provide to problems that I think are too complex to handle, and I am exceedingly grateful for your patience in explaining those solutions to me. I am also extremely thankful to you for always pushing me to the limit, and never letting me settle for 90% complete, or 'just good enough' (no matter how sad I looked in our last few meetings prior to finishing this thesis). Very few people get the chance to work with an advisor, who cares so much more about their personal development than about the research, and I feel truly blessed to have had this opportunity.

I would also like to thank everyone in lab, who guided me in this journey through the wonderful world of solid mechanics. I need to thank Meredith for training me on every piece of mechanical testing equipment known to man, for (almost) always being patient when I ask stupid questions, and for all the bonding we did as TA's together. I need to thank Shawn for answering all my ABAQUS and Latex questions. I need to thank Damien for always keeping the mood in lab light (and for music appreciation nights). Most importantly, I need to thank Katia for answering all the questions that I was too embarrassed to ask Prof. Boyce, and for helping me take my first steps with regards to modeling. Not only were your explanations of all the equations helpful and easy to follow, but all your UMATs and codes made learning how to program infinitely easier (even when they were commented in Italian). I'm sure you'll make an amazing professor, and know that all your future students are extremely lucky.

I would also like to thank my fraternity brothers. Throughout the last two years, the best part of every day has always been going back to the house for lunch. For that half hour every day, I didn't think about work at all. I just sat, ate, and enjoyed your company. I'll never forget some of those lunch conversations, nor will I ever be able to have them again (for a wide variety of reasons).

Last, I would like to thank my family for all their love and support. I need to thank my mother, who gave me 20+ years of private education. Mom, I know you always wanted that Jag, but I hope you think this investment is more worthwhile. I need to thank my sister, who always takes my mind off work. Amber, thank you for being the best sister I could ask for. I especially need to thank my father, who will read this entire thesis, in spite of the fact that he has never seen a mussel byssal thread nor has any idea what stress or strain is. Ya Pop, my 'paper' is finally done.

Contents

List of Figures

List of Tables

1 Introduction

Materials from nature have evolved to meet the harsh loading demands encountered by their host organisms resulting in microstructures designed to perform highly specific functions. A natural material with remarkable mechanical properties is the attachment appendage of the aquatic mussel known as the mussel byssal thread. Mussels have long been revered for their remarkable ability to remain adhered to the rocks of their aquatic habitat, even in the face of the large and repetitive forces produced by the pounding surf, for their remarkable strength, and for their unmatched toughness; these golden fibers were even woven into highly valuable 'sea silk' in ancient cultures (Carrington 2008). With gentle waves, these threads provide an elastic response, which allows the mussel to move freely with the waves. In more violent seas, the threads load beyond their initial elastic response and yield, providing a highly dissipative response, which simultaneously retains resiliency. This dissipation keeps the threads from 'snapping' back when the force is removed, allowing the mussels to return to their original position gradually (Carrington, 2004). Without this property, the mussels would be dashed against the rocks with each valley between wave crests.

1.1 Mussel Anatomy

The anatomy of the mussel is quite simple. A foot, which is used for mussel locomotion, connects to the mussel stem (an organic tissue located at the base of the mussel shell). Protruding from the stem are byssal threads - protein-rich fibers, which vary in diameter from approximately $80\mu m$ to $200\mu m$. As can be seen in the schematic of Figure 1 these threads protrude outward from the stem in all directions. The shortest threads (those located at the center of the attachment) are rarely more than half a centimeter in length, while the longest (those located at the outermost diameter of the circle) range upwards of $3cm$. At the end of each thread is an adhesive plaque, which binds each thread to the rock surface.

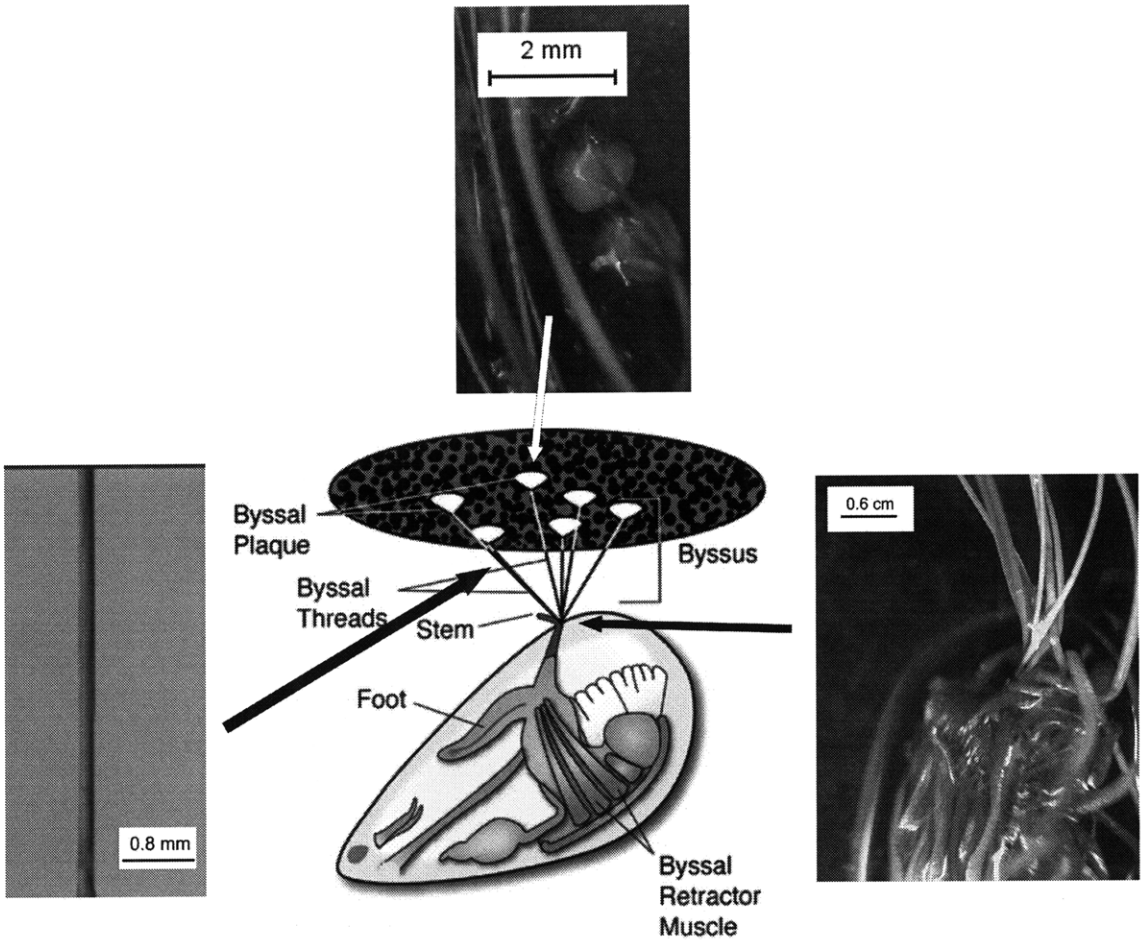

Figure 1: Anatomy of the aquatic mussel. The threads project out from the stem at the base of the shell, and attach to rocks in a pseudo-circle (From Silverman and Roberto [25]

1.1.1 Stem-Thread Attachment

The stem serves as the connection between the foot and threads, and is ambulatory i.e. can move outside of the shell, though the majority of the stem is most often drawn completely into the shell. As can be seen in Figure 1 the stem is essentially a cylinder with one end attached to the mussel foot (located inside the shell) and the other end protruding out of the shell. The diameter of the stem is graded, transitioning gradually from a thick end (approximately $1.50mm$ in diameter) attached to the foot, to a thin end (approximately $1mm$ in diameter). The threads are located all along the stem.

The threads attach to the stem with a hoop of thin tissue, approximately $750\mu m$ wide

and approximately $300\mu m$ thick (Figure 2 shows a thread after it has been detached from the stem with this hoop still intact). Most hoops are much wider than their thread, so that

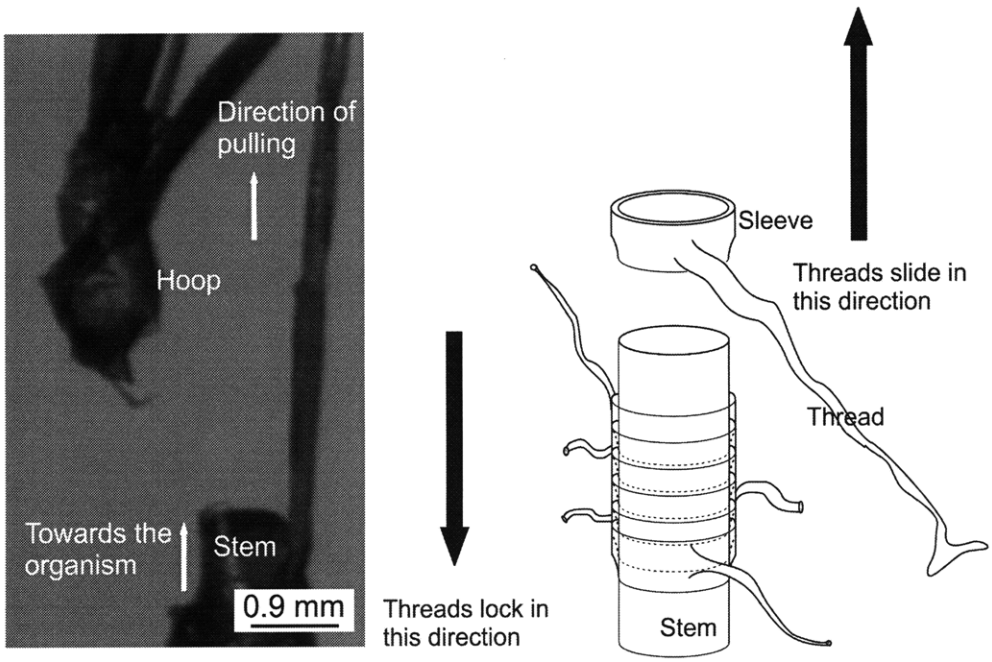

Figure 2: Threads after they have been pulled off of the stem. The tissue hoop that connects the thread to the stem is seen in the upper left corner of this figure. Behind the main hoop are several other threads and hoops, none of which are attached to the main hoop. This serves to demonstrate that each thread attaches with its own hoop of tissue and each hoop slides off the stem individually. On the right, another thread is shown still attached to the stem.

the hoops layer on top of each other, coating the stem with several layers of tissue. The design of this stem-thread attachment allows the threads to 'slide' off the stem smoothly in one direction, but locks the threads in the opposite direction. Thus, if the threads are pulled backwards towards the mussel (a loading condition that is not possible in their natural environment), they slide individually and detach without much force required (see Figures 2 and 3). However, if the threads are pulled in the opposite direction i.e. away from the mussel (as they are loaded in their natural environment) the threads pile up on top of each other, keeping neighboring threads from slipping. This 'piling up' of neighboring threads provides a type of locking mechanism, and the threads remain attached to the stem until they fail outright (see Figure 4).

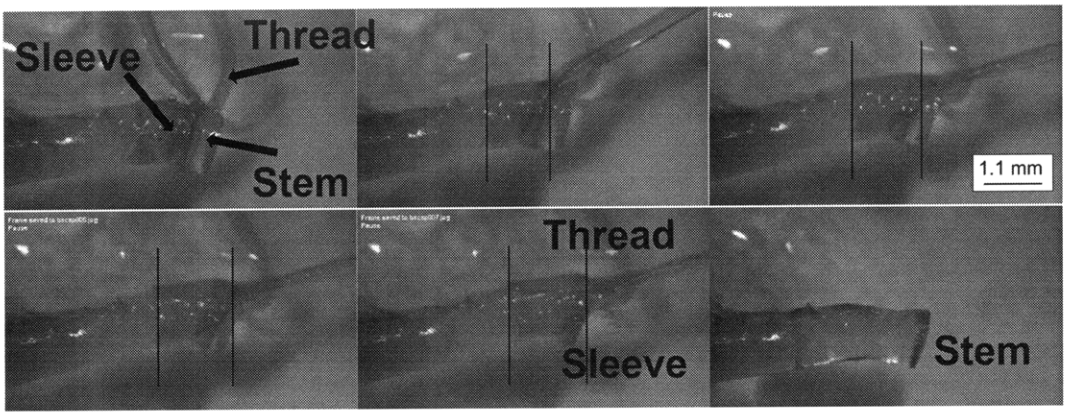

Figure 3: An individual thread slipping off of the stem as the load is increased. Again, the direction of loading is towards the organism.

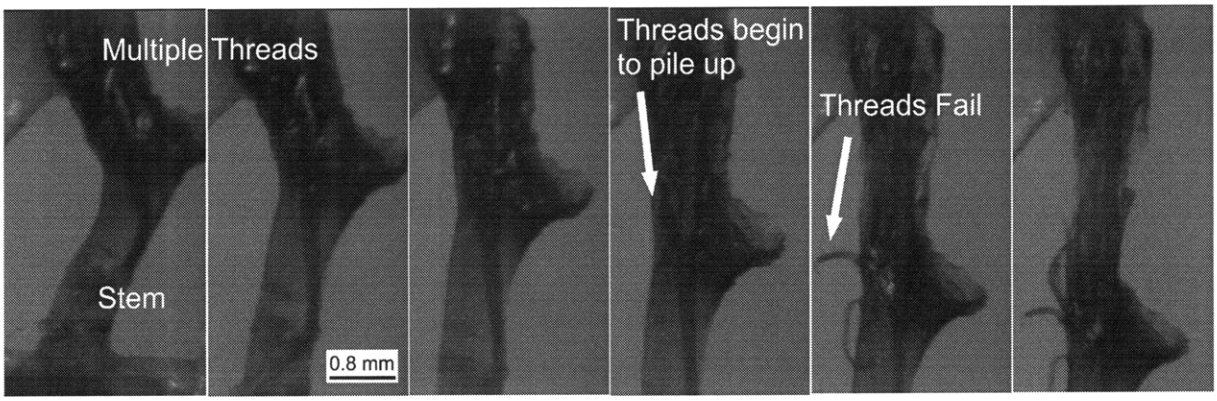

Figure 4: Threads being pulled away from the organism (as is seen in nature). Initially the threads slip along the stem slightly, but as they run into neighboring threads the threads begin to lock into place. As loading continues the weakest threads fail until eventually all threads fail.

The density of threads along the stem, and the overall number of threads per organism varies from mussel to mussel, and increases with water turbulence (Moeser and Carrington 2006). However, nearly all the mussels tested in this study had between 20 and 50 threads. This large number of threads, coupled with the fact that these threads protrude from all sides of the stem and in all directions allows the mussel to attach to several surfaces, providing a more versatile connection. Figure 5 shows mussels attached to the two most common attachment surfaces i.e. rocks and the shells of nearby mussels.

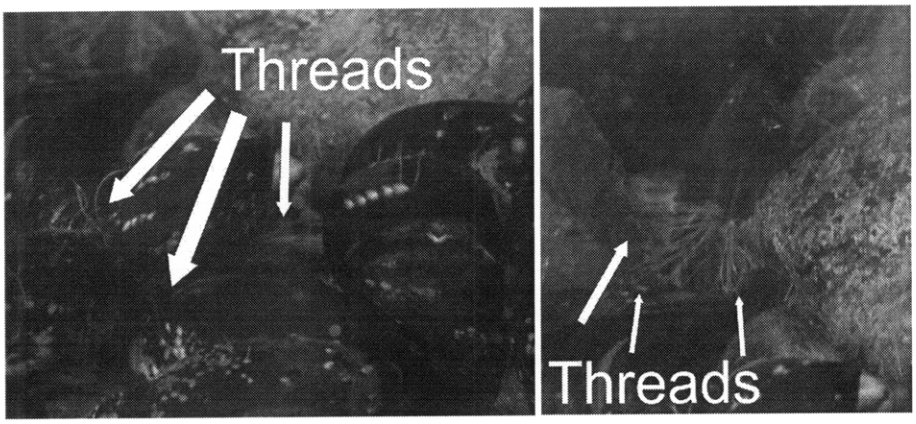

Figure 5: Mussels in the storage tank at MIT. On the left are 'bed' mussels i.e. mussels that group together and attach both to rocks and to nearby mussels. On the right is a solitary mussel attached to two different rocks.

1.1.2 Macro-Structure of the Threads

The threads themselves are highly graded, with both physical structure (diameter and smoothness) and mechanical properties varying from the proximal (closest to the stem) thread section to the distal thread section. Although the threads vary significantly in length, an 'average' thread can be considered to consist of a proximal section approximately $5mm$ in length, a proximal-to-distal transition region approximately $3mm$ in length, a distal section approximately $10mm$ in length, and a distal-to-plaque transition region approximately $2mm$ in length. The plaque, because of its chemical composition and structure, is considered to be a wholly different material than the thread, and will not be discussed heavily in this thesis. However, the plaque, and the adhesive gel which it secretes, are themselves the subject of much recent research (see [8]); the gel especially has been shown to demonstrate an unmatched adhesive ability.

The proximal thread section is elliptical in cross-section, with the major axis at least twice as long as the minor axis. The major axis ranges in length from approximately $250\mu m$ to $400\mu m$, with an average length of approximately $280\mu m$. The distal thread section is thinner with a circular cross-section. The diameter of the distal thread section ranges from approximately $60\mu m$ to $180\mu m$, with an average diameter of approximately $110\mu m$.

Surrounding the entire thread is a cuticle or sheath, which, like the plaque, has become the subject of much recent research (see Figure 6) [13] [12] [14]). Again, in this study, the cuticle is not heavily discussed. However, as will be discussed in the mechanical testing section of this thesis, in several tests of the proximal thread section, the cuticle was found to withstand larger stretches than the thread itself i.e. the core of the thread failed, while the cuticle remained intact to significantly higher strain. This finding supports work by Holten-Andersen et. al. (Holten-Andersen et. al., 2007), which demonstrates the remarkable nature of these coatings, namely that they can be more extensible than the threads themselves.

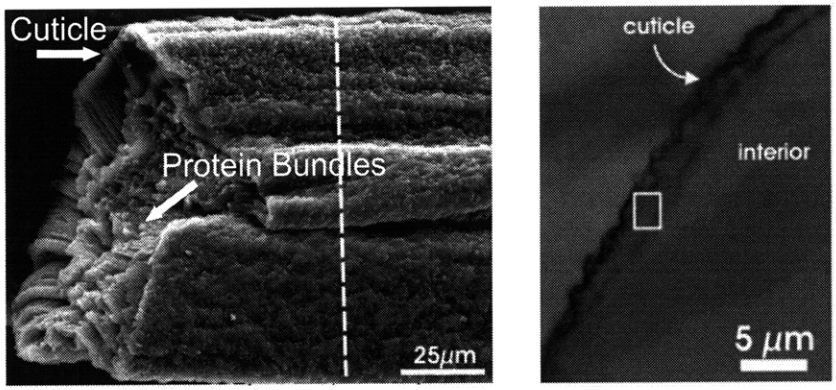

Figure 6: 3-D Cross-section of distal section of mussel byssal thread, with cuticle and protein bundles highlighted (left). 2-D cross-section of byssal thread with cuticle and interior highlighted (Holten-Andersen et. al., 2008).

1.1.3 Chemical Composition and Micro-Structure of the Threads

Byssal threads consist primarily of water and proteins. Freshly collected threads are nearly 70% water by weight, while protein represents approximately 96% of the dry weight [30]. The most significant single protein in the thread is collagen, which represents approximately 50% of the protein contribution in the distal thread section and approximately 33% in the proximal thread section.

Three collagenous proteins, known as 'pre-pepsinized collagens' or preCOL's make up the bulk of the thread core [29]. Two of these preCOL's (preCOL^2 -P, and -D) provide

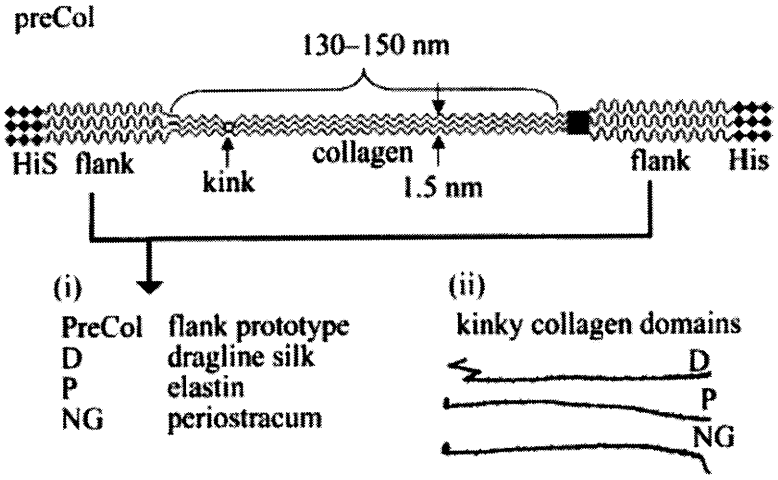

Figure 7: Single preCOL molecule. The interior collagen region is approximately $130 - 150nm$ in length, with flanking regions approximately $75 - 85nm$ in length. The diameter of a single bundle is approximately $1.5nm$. The different types of flanking regions are shown below in (i) and (ii). Taken from Waite [10]

the major load-bearing capabilities of the thread. Both are bent-core i.e. banana-shaped structures and share similar collagen backbones, but they differ with respect to their ends; the preCOL-D molecules are flanked with domains resembling silk, while the preCOL-P molecules are flanked with elastin-like domains. In both cases the flanking domains fold over onto themselves multiple times, increasing the overall stiffness of the domain, and 'hiding' their true length. During loading these folded domains unfold freeing up excess stretchable length; this mechanism will be discussed in detail in following sections. The other major difference between the preCOL-P and preCOL-D molecules is their location within the thread. The density and distribution of these molecules vary down the length of the thread, with the proximal section consisting primarily of preCOL-P, and the distal section consisting primarily of preCOL-D (see Figure 8).

Each preCOL molecule binds with nearby molecules forming a protein bundle, consisting of 7 individual molecules. These bundles form into one of two shapes, either a flower shape, with the bent ends facing off at 360°, or a banana shape, with all the bent ends facing in

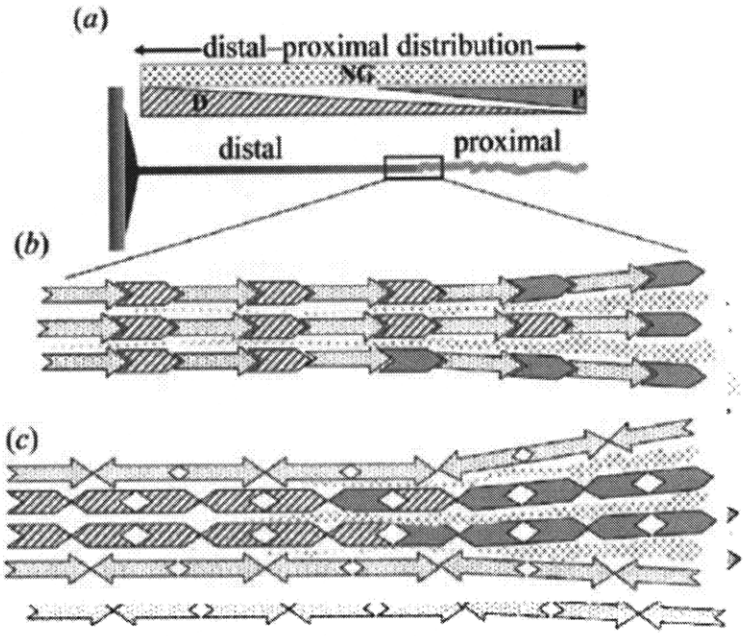

Figure 8: Schematic of the preCOL gradient in a thread. In the proximal thread section, preCOL-P molecules predominate, while in the distal preCOL-D's dominate. In between the proximal and distal thread section, the density of preCOL's transition smoothly. Taken from Waite et. al. [30].

the same direction (see Figure 9). The vast majority of preCOL bundles in mussel byssal threads are arranged in the banana configuration [11].

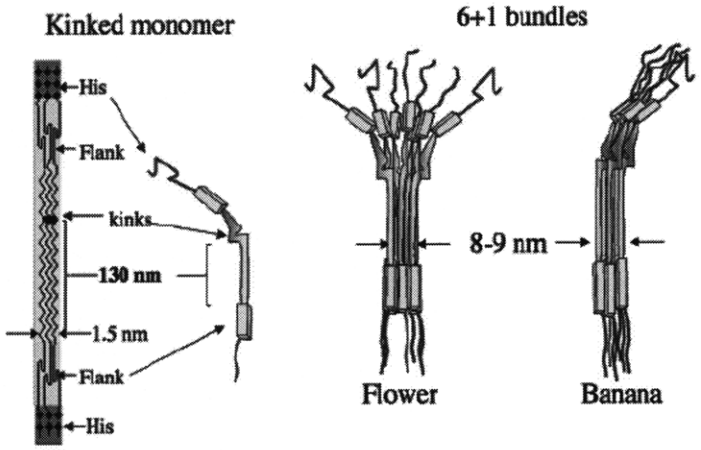

Figure 9: Structure of protein molecule bundles, with chemical breakdown of constituent preCOL and the preCOL in the bent configuration (a), flower-shaped bundle (b), and banana-shaped bundle (c). The majority of preCOL bundles in mussel byssal threads are banana-shaped bundles. Taken from Hassenkam et. al. [11]

These bundles further organize into linear arrays. The bundles align end to end, with the head of one preCOL bundle bonding to the tail of a neighboring bundle. These arrays consist of tens to hundreds of individual bundles, tilted at an angle of approximately 25° to the thread axis (in the distal section, in the proximal section these arrays are randomly aligned). As the thread is loaded, the bundles rotate to align with the axis of the fiber, forming long continuous sheets of preCOL bundles (see Figure 10).

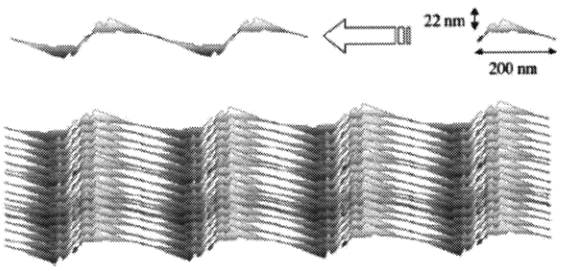

Figure 10: A linear assembly of preCOL bundles. Initially these arrays are tilted at an angle of 25° to the axis of the thread, but as they are loaded, they straighten into continuous sheets. Taken from Hassenkam et. al. [11]

Surrounding these preCOL bundles is a water and protein based matrix. The relative amount of matrix to preCOL varies significantly from proximal to distal section, implying that the density of preCOL's increases from the organism to the attachment surface. Further, the proximal region demonstrates a much lower amount of cross-linking between bundles than in the distal section [11]. Together, these factors contribute heavily to the differences in the overall stress-strain behavior of the thread, which will be discussed thoroughly in the experimental results section of this thesis.

1.2 Molecular Response to Loading

Since these preCOL bundles provide the bulk of the material's load-bearing capacity, it is essential to understand their response to mechanical loading. Recent improvements in mechanical testing at small length-scales (down to the micro- and nano-scale), have made it possible to isolate and test individual protein molecules. Methods such as single-molecule

force spectroscopy and optical tweezers have been used to stretch titin, the giant multi-domain protein found in muscle [27]. This protein is similar in structure and composition to the multi-domain preCOL's found in mussel byssal threads, and so its mechanical behavior is taken as a model for the mechanics of these preCOL's.

The evolution of the protein's structure during loading is shown in Figure 11. Initially the protein is at rest in its bent configuration with flanking domains fully folded. As the protein is loaded, the molecule stretches, with both the unfolded inner domain, and the folded flanks stretching. Although the folded domains stretch, the load on the region is not yet high enough to break the bonds holding the folds together. As the force increases, the folded domains' weakest bonds break, freeing up excess tension-free length. As this excess length stretches, the force again increases until it is high enough to break the next weakest bonds, and the process repeats until all the folded domains have unfolded. If loading is continued beyond the point of complete unfolding, both the inner domain and flanks will stretch until the load becomes high enough to break the molecule completely.

In the case of a single molecule, this unfolding phenomenon gives rise to a 'sawtooth' loading curve, with the force on the molecule dropping suddenly when a bond is broken (see Figure 12 left). Because a slightly higher force is required to break each successive bond, the peaks of the sawtooth curve increase with extension. This behavior is also highly rate dependent, with the magnitude of the peak loads increasing with increased strain rate [24] [19]. In the byssal threads these molecules do not exist as single entities, but rather bundle into the banana-shaped 7-protein bundles, which form the linear arrays, and the protein sheets (as discussed in the previous section). This grouping of proteins serves to smooth the sawtooth loading curve into a more continuous loading curve (see Figure 12 right).

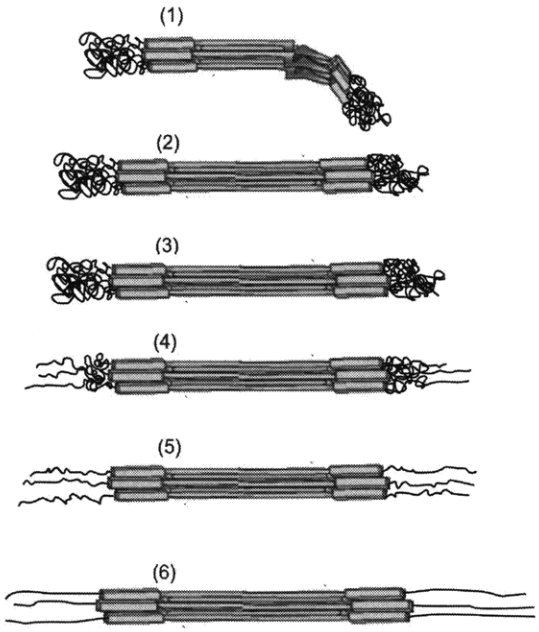

Figure 11: Structural evolution of a preCOL bundle during loading: (1) bundle at rest in the folded and bent configuration (2) initial loading straightens the bend, but folded domains remain folded (3) collagen region stretches, and the force on the bundle builds (4) folded domains begin to unfold (5) folded domains completely unfold (6) collagen region and flanks stretch.

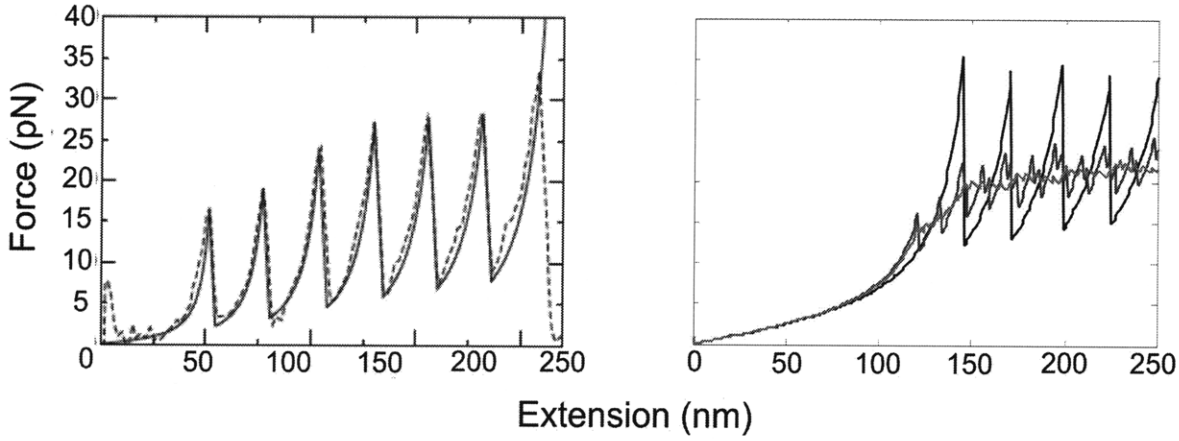

Figure 12: (left) Experimental results for the loading of a single molecule of titin (Taken from Staple, et. al. [27]), and (right) smoothing effect from loading multiple bundles (Taken from Qi, et. al. [23]).

1.3 Thesis Objectives and Outline

Although several of the microstructural and macrostructural characteristics of these threads (as well as many of the mechanical properties) have been studied, neither a comprehensive

constitutive model for the stress-strain behavior of these threads nor a model of the thread itself has been developed. These models are important on several levels. A constitutive model provides a method for modeling the unfolding and refolding of segmented proteins (proteins with stiff regions and folded domains), and a method for modeling protein unfolding and refolding in a network. A full thread model provides insight into how graded structures (graded with respect to mechanical properties and physical geometry) share and transmit load, particularly with respect to transitioning from adhering a relatively soft compliant structure (the stem) to a stiff structure (the rock). The following thesis outlines the development of a micro-structurally informed constitutive model for the mechanical behavior of mussel byssal threads and applies that model to a full thread finite element model.

In order to have a consistent set of data with which to compare the results of the constitutive model, a wide array of tension tests was conducted both on individual thread regions (proximal and distal separately), and on the thread as a whole. These tests included monotonic loading at different nominal strain rates and several different types of cyclic loading, including multiple cycles to the same strain, cycles to increasing strain, and cycles to the same strain with a hold time in between cycles. Video monitoring equipment was used during testing to investigate the evolution of the thread macrostructure, and to ensure valid results.

Two separate but related models were developed for the stress-strain behavior of the proximal and distal thread sections. A detailed discussion of the process of model development is provided, highlighting the inability of some commonly used models to accurately capture the unfolding/refolding phenomenon in byssal threads. In both cases the experimental results were used to validate the models.

These material models were implemented into a finite element model of the entire thread (using ABAQUS), and simulations of loading the entire thread were conducted. The geometry of the model, as well as the material properties, were graded as in actual byssal threads.

Again, experimental results from full-thread tests were used to validate these simulations. In the sections to follow, the experimental results will be shown, the material model will be outlined, and results both from the material model, and from the simulations will be presented.

2 Mechanical Testing

2.1 Mechanical Properties Background

The most basic properties of mussel byssal threads have been known since the 1970's when Smeathers and Vincent first began testing these threads [26]. This study highlighted many of the mechanical properties of the threads (including ultimate strain, ultimate stress, Young's modulus, and break energy), as well as discussing the overall stress-strain behavior including yield and hysteresis. Further, this study investigated the differences in properties and behavior between the different thread sections (here separated as corrugated section, smooth section, and full thread), and the differences in properties between wet threads and dry threads. Most notably, the strain to failure (mean value) was measured to be 1.22 in the corrugated (proximal) region, 0.66 in the smooth (distal) region, and 0.44 for the full thread [1]. These values were significantly lower for dry threads. The mean failure load and ultimate tensile stress (of the full thread) were measured to be $0.25N$ and $21MPa$ respectively, while the initial Young's modulus and modulus after yield were measured to be $85MPa$ and $32MPa$ respectively. A smooth rollover-type 'yield' behavior was also noted (see Figure 13), and the material was observed to undergo a hysteresis with cyclic softening (a more compliant behavior upon reloading). Finally, this study noted that the material demonstrated an ability to 'recover' i.e. if a specimen that had been used for cyclic test were allowed to relax over several hours and then stretched again, the reloading curve would follow the initial loading curve more closely than reloadings prior to the rest.

Although the work of Smeathers and Vincent demonstrated some of the remarkable

[1]This result seems counterintuitive. For a full thread consisting only of a proximal and distal thread section, the full thread should (on average) fail at a strain intermediate to the failure strain of the proximal and distal thread separately. There is no explanation for this phenomenon in the Smeathers and Vincent paper. Most likely the threads are failing in a transition region between the proximal and distal thread sections. This is discussed more fully later in this thesis, when the experimental results for full thread tests, and the finite element simulations of full thread loading are shown.

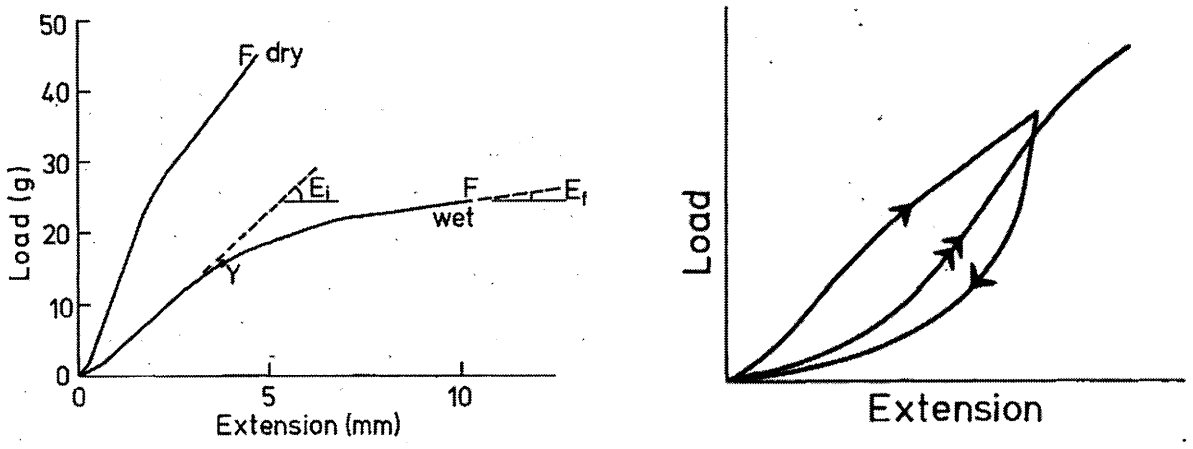

Figure 13: (left) Load-extension curve for full threads, wet and dry, showing moduli and yield point. (right) Load-extension curves for cyclic loading tests on full threads, showing cylic softening. Single arrow represents initial load/unload, while double arrow respresents reloading. Figures taken from the Smeathers and Vincent study (1979).

mechanical properties of mussel byssal threads, these threads remained largely uninvestigated for twenty years. The next major work in characterizing the mechanics of mussel threads came from Bell (name changed to Carrington), beginning in 1995 and continuing to the present [2], [20], [7], [6], [5]. This work investigated the stress-strain behavior of full threads, and the individual thread sections, noting major differences between the proximal and distal thread sections (Figure 14). Notably (as in the case of the Smeathers study) the proximal region was found to exhibit a lower initial Young's modulus, a lower ultimate stress, a higher ultimate strain, and a less-pronounced 'yield' relative to the distal region. This work also quantified this data in the case of several different mussel species (*M. Californianus*, *M. Trossolus*, *M. Galloprovincialis*, *M. Modiolus*, *B Thermophilus*, *D. Polymorpha*, *G. Demissa*, and *M. Edulis*), demonstrating that Smeather's and Vincent's findings held true in every case, though the actual values of ultimate stress, ultimate strain, etc. varied from species to species.

In the case of full threads, Bell not only reproduced curves similar to those of Smeathers and Vincent, but also used the load-displacement response of the individual thread regions

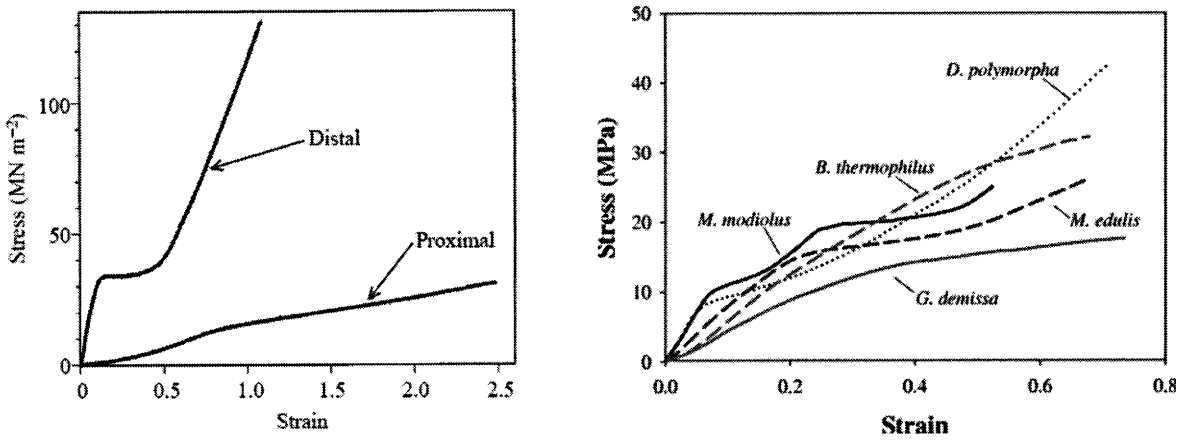

Figure 14: Stress-strain curves for the proximal and distal thread regions of *Mytilus Californianus*, stretched at an extension rate of 10 $mm\ min^{-1}$ (left) (Taken from Bell and Gosline 1996). Stress-strain curves for full threads of several different mussel species (right) (Taken from Brazee and Carrington 2006).

to predict the behavior of each section during full thread loading. Specifically, they broke the full thread load-displacement curve into three distinct regions (Figure 15). They predict that extension in the first phase of the force-displacement curve would be accommodated by stretching primarily in the proximal region. The 'yield' in the the full thread curve arises from the 'yield' in the distal thread section, with most of the stretching in this region accommodated by the distal thread section. Finally, as the distal region stiffens, loading will again be accommodated by the proximal thread region, until the ultimate tensile stress in the proximal region is reached, at which time the thread fails.

Bell also looked at the hysteretic behavior of the material, the material's ability to recover, strain-rate dependence, and variation in the mechanical properties of the threads with season. In terms of seasonal-strength dependence, Bell noted that spring threads are over 60% stronger and over 83% more extensible than summer, fall, or winter threads (Carrington (Bell) 2004). In terms of hysteresis, Bell noted that in the distal thread section the amount of hysteresis increased with the strain from which the specimen was unloaded. If the specimen was unloaded prior to yield, the material behaved almost perfectly elastically, with very little hysteresis. For specimens unloaded post-yield, dissipation increased with strain

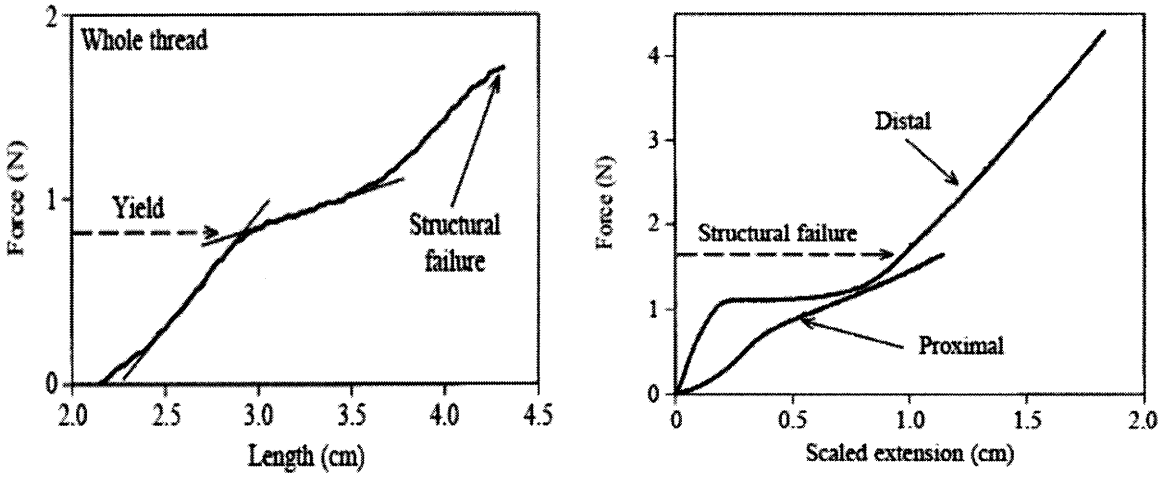

Figure 15: Load-displacement curve for a full thread, with the three individual loading regions marked with lines (Left). The corresponding load-displacement curves for the distal and proximal thread sections individually (Right). These curves were used to predict the behavior of each individual thread section during full thread loading. Note that full thread failure occurs at the load corresponding to failure in the proximal region. (Taken from Bell and Gosline 1996)

from approximately 25% of the total work for specimens unloaded immediately after yield to over 70% for specimens unloaded just prior to failure (see Figure 16). Bell was also able to repeat Smeathers' recovery results, demonstrating that (in the distal thread region) having a hold time between cycles increased the material's stiffness during reloading. Further, Bell showed that if the material is cycled twice (load/unload/reload/unload) then held at zero strain for some non-zero amount of time, although the first load after the hold will be stiffer than the previous reload, any additional cycles without a hold will follow the first reload (see Figure 17). Finally, Bell noted that the material is highly strain-rate dependent, with stress increasing with strain rate (see Figure 18).

A third research group (the Waite group, UCSB) has also investigated the mechanical properties of mussel byssal threads, though their primary focus area is on the chemical composition of the threads. Aside from noting several of the properties discussed previously, and doing a more in-depth study of the material's recovery properties from a micro-scale/chemical composition point of view, Waite also looked at the behavior of the material when cycled

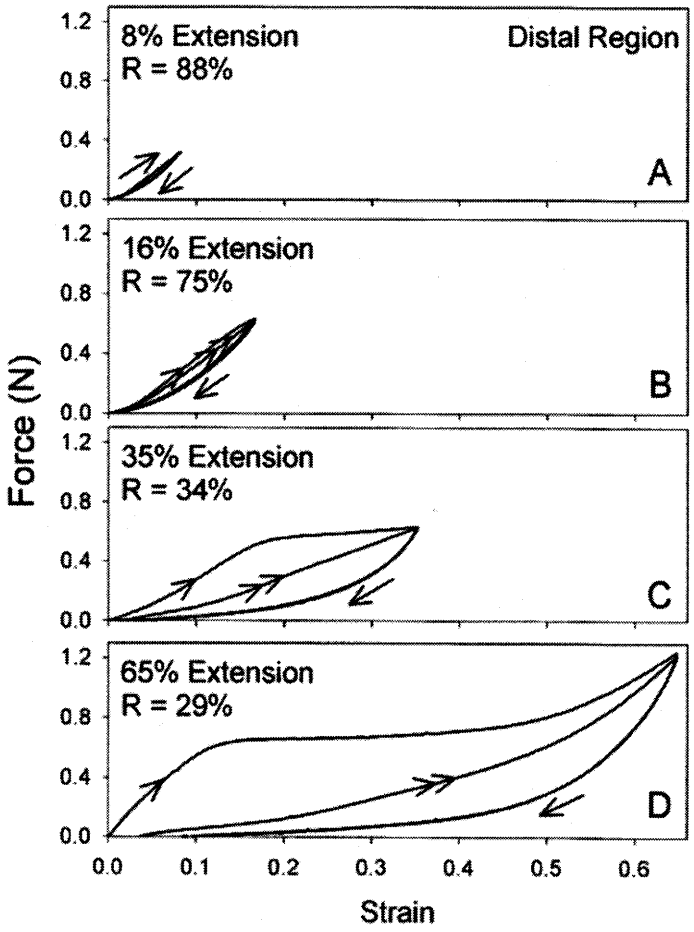

Figure 16: Cyclic loading (load/unload/reload) for distal thread section. For cycles prior to 'yield' and immediately post 'yield', the material demonstrates very little hysteresis. Hysteresis increases significantly for unloading from strains increasingly beyond initial yield. (Taken from Bell and Gosline 2004).

multiple times, to a slightly higher strain each time (See Figure 19) [10], [28]. He noted a 'second yield' for cycles beyond the material's initial yield point i.e. if the material is loaded to a strain beyond yield, then unloaded and reloaded, the material will not rejoin the initial loading curve, but rather will exhibit a rollover-type 'yield' just prior to the maximum initial strain. The stress in the material will then increase, but more slowly than originally, eventually achieving the maximum initial stress, but at a strain slightly higher than the maximum initial strain.

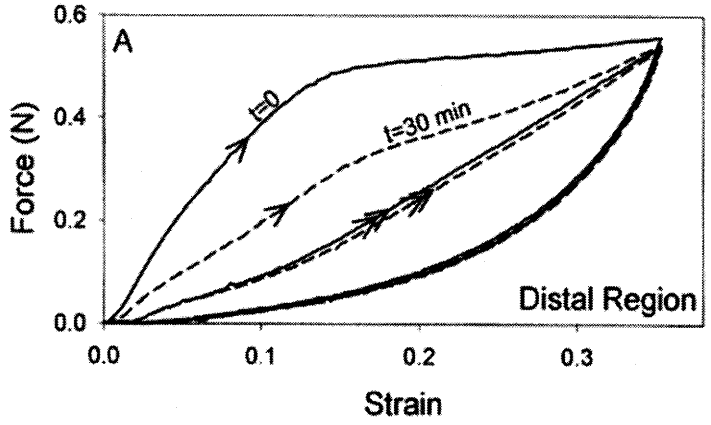

Figure 17: Recovery in distal thread section. Specimen was loaded, unloaded, reloaded, and unloaded again. The specimen was then left at rest for 30 min, before cycled again. Note that the reloading path for the first set of cycles and the reloading path for the second set of cycles follow the same curve. (Taken from Bell and Gosline 2004).

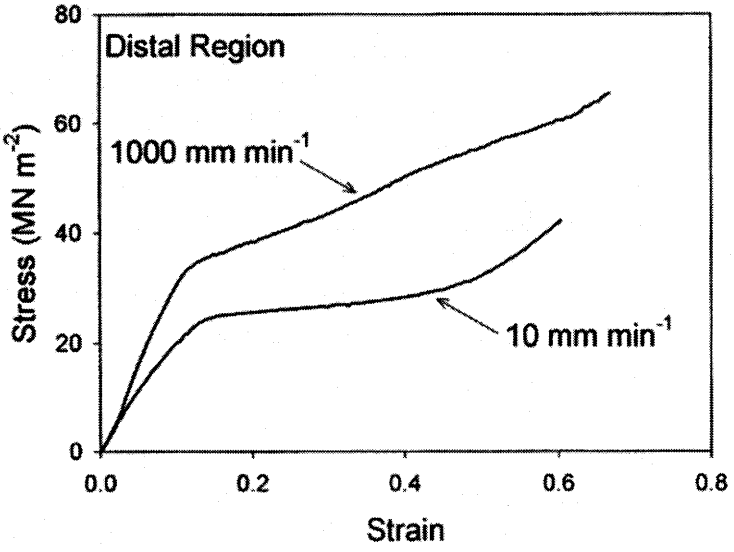

Figure 18: Strain rate dependence of distal thread section. Curves were for tests run at rates of 1000 $mm\ min^{-1}$, and 10 $mm\ min^{-1}$. Both specimens were taken from the same thread of *Mytilus Californianus*. (Taken from Bell and Gosline 2004).

2.2 Experimental Methods

2.2.1 Mussel Collection

As noted in the introduction, and in the previous section, there are many different species of mussels; they live in oceans, rivers, and lakes throughout the world, in both fresh and salt

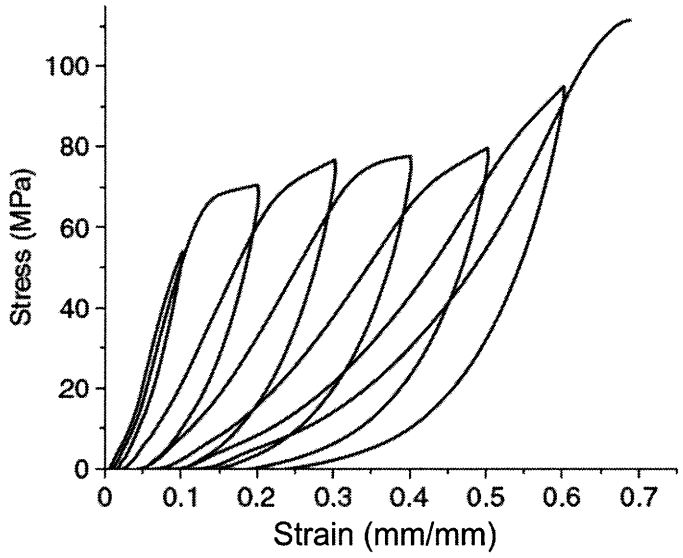

Figure 19: Stress-strain curve for cyclic loading of distal thread region. For each cycle the strain is increased slightly. (Taken from Harrington and Waite 2007).

water. The threads of many of these species have been studied, though the most commonly studied threads come from *Mytilus Californianus*, the California Mussel, and *Mytilus Edulis*, the Blue Mussel. This study looks exclusively at the threads of *Mytilus Edulis*, as these mussels are commonly found in the tidal zones near Boston, Massachusetts.

Mussels were collected at Georges Island in Boston Harbor, during the months of September - October, and were collected at Pigeon Cove in Gloucester, MA during the winter months. For solitary mussels, the threads were detached at the plaque with tweezers, ensuring that the threads were not stretched or damaged in the removal process. For bed mussels, or mussels that were attached to multiple different surfaces, it was impossible to detach individual fibers without damaging the stem, so threads were cut at the base of the stem. This allowed comparison between threads grown in the ocean and threads grown in the tank at MIT (the difference in mechanical properties between 'ocean' threads and 'tank' threads was found to be negligible). Mussels were transported from Georges Island or Red Rock in small coolers filled with ocean water, and were placed in the tank at MIT immediately upon returning to the lab.

Figure 20: Mussel holding tank.

The holding tank at MIT is a Stark live lobster tank (see Figure 20). The salt concentration in the tank is kept at approximately 34 parts per thousand, and the water temperature at approximately $38°F$, roughly equivalent to spring conditions in Boston Harbor. The mussels, whose threads had been cut during collection usually regrew a full byssal apparatus (at least 20 threads) within 48 hours, and most mussels (over 90%) survived indefinitely after transplantation from their natural habitat. Those mussels that did die from transplantation usually died within five days.

2.2.2 Experimental Specimens

Prior to testing, a portion of the stem was cut from live mussels (these mussels were returned to the tank to regrow threads), and whole threads were removed from the stem as shown in Figure 3. These threads were then either tested whole or separated into distal and proximal sections (note that the difference in diameter between the proximal and distal sections is noticeable with the naked eye). For whole threads, each end of the thread was attached to a small piece of cardstock with cyanoacrylate glue. Due to the limited range of the

testing apparatus (stroke of 12mm), only shorter threads (length less than 1.5cm) were tested whole. Distal and proximal specimens were cut to approximately 6mm in length, and attached to cardstock holders with cyanoacrylate glue. These holders were rectangular pieces of cardstock, approximately 1cm wide by 2cm long, with a small 'window' approximately 2mm by 6mm (see Figure 21). Thus, the gage length of distal/proximal specimens was equal to the width of the 'window' i.e. approximately 2mm, while the gage length of full thread specimens was equal to the length of the thread.

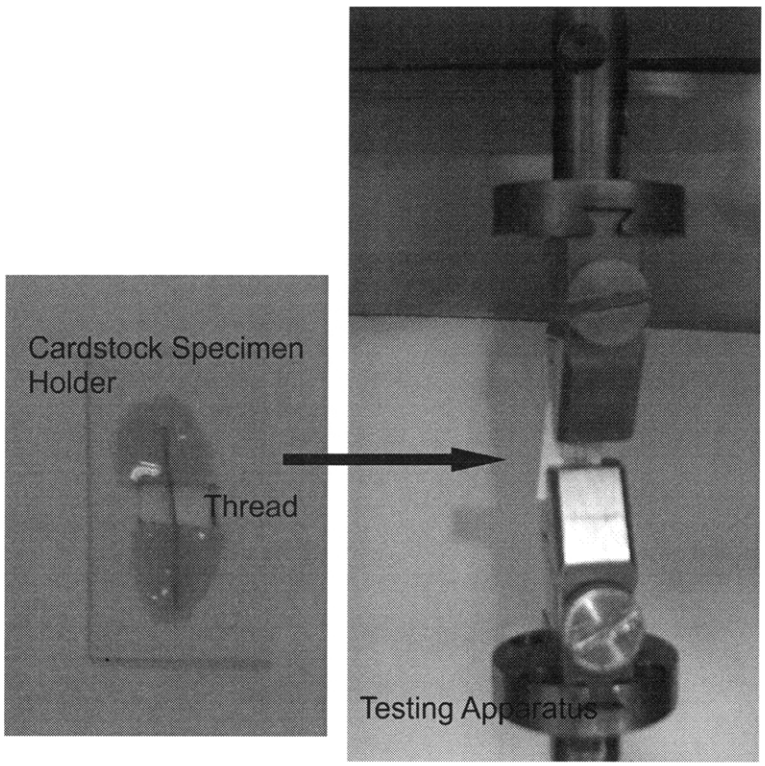

Figure 21: A proximal thread section attached to a cardstock specimen holder (left), and that same specimen placed in the grips of the testing machine (right). Note that the sides of the cardstock are cut after mounting the specimen in the grips and prior to testing.

Prior to testing specimens were dried, then rehydrated, and the diameter was measured. First, the cyanoacrylate glue was allowed to dry for approximately fifteen minutes, ensuring a strong bond between the threads and the cardstock. Specimens were then soaked in saltwater for approximately five minutes to ensure that they were fully hydrated prior to testing. Last, the diameter of each specimen was measured in this fully hydrated state;

measurements were taken using the optical microscope and scale on a Leintz micro-hardness tester. The distal thread sections were roughly circular in diameter, with diameter ranging from approximately $80\mu m$ to $150\mu m$. The average distal diameter was approximately $120\mu m$. The proximal thread sections were elliptical in cross section, with the minor axis of the ellipse approximately equal to the diameter of the distal section i.e. approximately $120\mu m$ in length. The major axis of the ellipse ranged from approximately $160\mu m$ to approximately $300\mu m$, with an average length of approximately $240\mu m$.

2.2.3 Tensile Testing

Once the specimens had been prepared, a wide array of uniaxial tension tests, both monotonic and cyclic, were conducted at constant nominal strain rates from $0.01/s$ to $1/s$. All tests were conducted on a BOSE EnduraTEC Electroforce 3200 (see Figure 22), and were monitored during testing using a UNIMAC microscope (0.7X to 4.5X magnification) connected to a Sony HDR-HC9 Camcorder (system supplied by Martin Microscope Company, and shown in Figure 23).

This video system was used to monitor threads during tests, ensuring that tests in which threads twisted or slipped out of the grips could be discounted (these issues were extremely problematic prior to the utilization of imaging equipment). The tests were also videotaped so that each test could be reviewed if the accompanying stress-strain curve yielded dubious results. This allowed for the disproval of several outlying curves, which did not follow the norms seen in the majority of tests. For example, some specimens (especially proximal specimens) were prone to 'soaking' up the cyanocrylate glue. This stiffened the glue-saturated region, effectively decreasing the gage length of the specimen. Recording also helped in determining the macroscopic evolution of the specimens during testing.

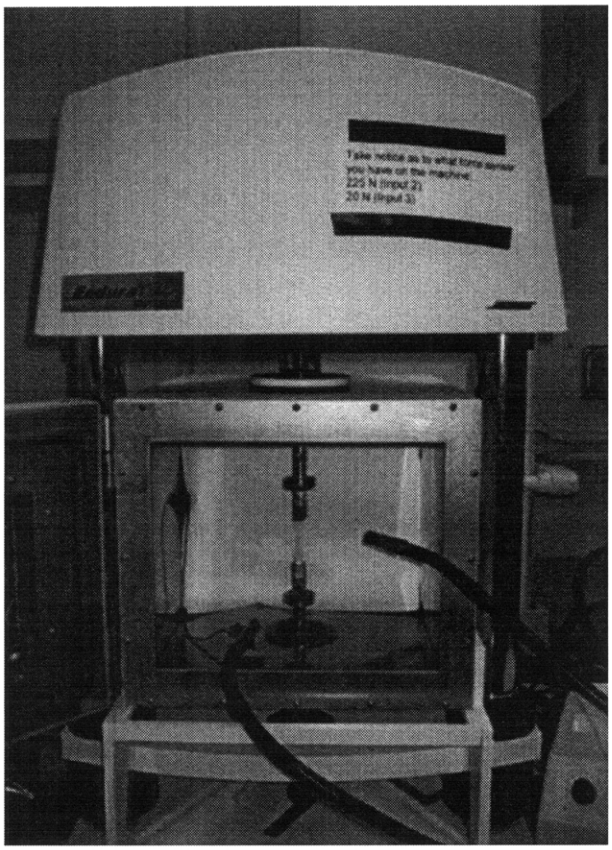

Figure 22: BOSE Enduratec Electroforce 3200 testing apparatus.

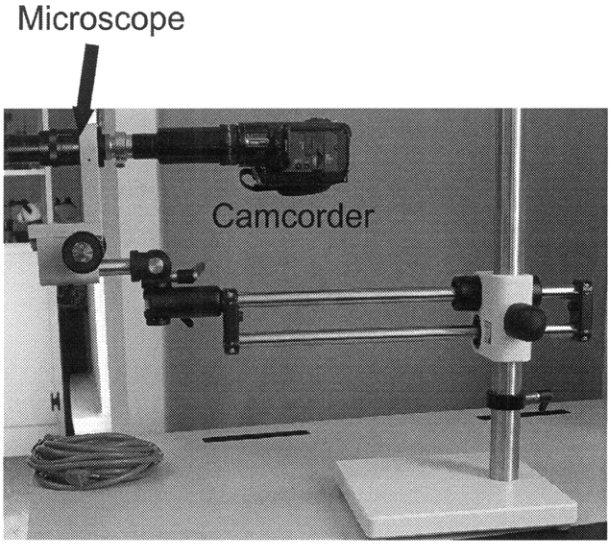

Figure 23: Microscope apparatus used for test monitoring

2.3 Experimental Results and Discussion

2.3.1 Distal Behavior

Monotonic Loading Tension tests to high strain were performed on the distal thread section at three nominal strain rates ($1s^{-1}$, $0.1s^{-1}$, and $0.01s^{-1}$). The corresponding true stress-true strain curves are shown in Figure 24, where the upper left plot shows the stress-strain response for true strain less than 0.25, the upper right plot shows the stress-strain response for true strain less than 0.5, and the lower plot shows the stress-strain response to a true strain of 0.9. As can be seen, the stress-strain behavior of the distal thread section is characterized by an initially stiff region, followed by a rollover-type 'yield' event and a stress plateau. As strain increases, this plateau gives way to a region of significant strain hardening.

The effect of strain rate on the material's stress-strain behavior changes significantly throughout loading. Prior to yield, the material response is primarily elastic (this is further evidenced in the cyclic loading results), and independent of strain rate; the initial Young's modulus of the material is approximately $300MPa$. Conversely, the 'yield' event, and the material's post-'yield' response is highly rate-dependent, with the 'yield stress' and 'yield strain' increasing with strain rate. Further, the material's stress magnitude (at a given strain value) increases with increasing strain rate, and the 'flatness' of the post-yield plateau decreases with strain rate. For high strains (strains higher than approximately 0.7), the stress-strain curves become parallel.

The curves shown in Figure 24 are 'characteristic' stress-strain curves. Because these threads are natural materials, they exhibit much larger variance in their mechanical behavior than synthetics. Figure 25 shows all statistically significant tests for monotonic loading of the distal thread section at a nominal strain rate of $1s^{-1}$. As can be seen the variance in stress (at a given strain) increases with strain, with a very small variance in the initial linear

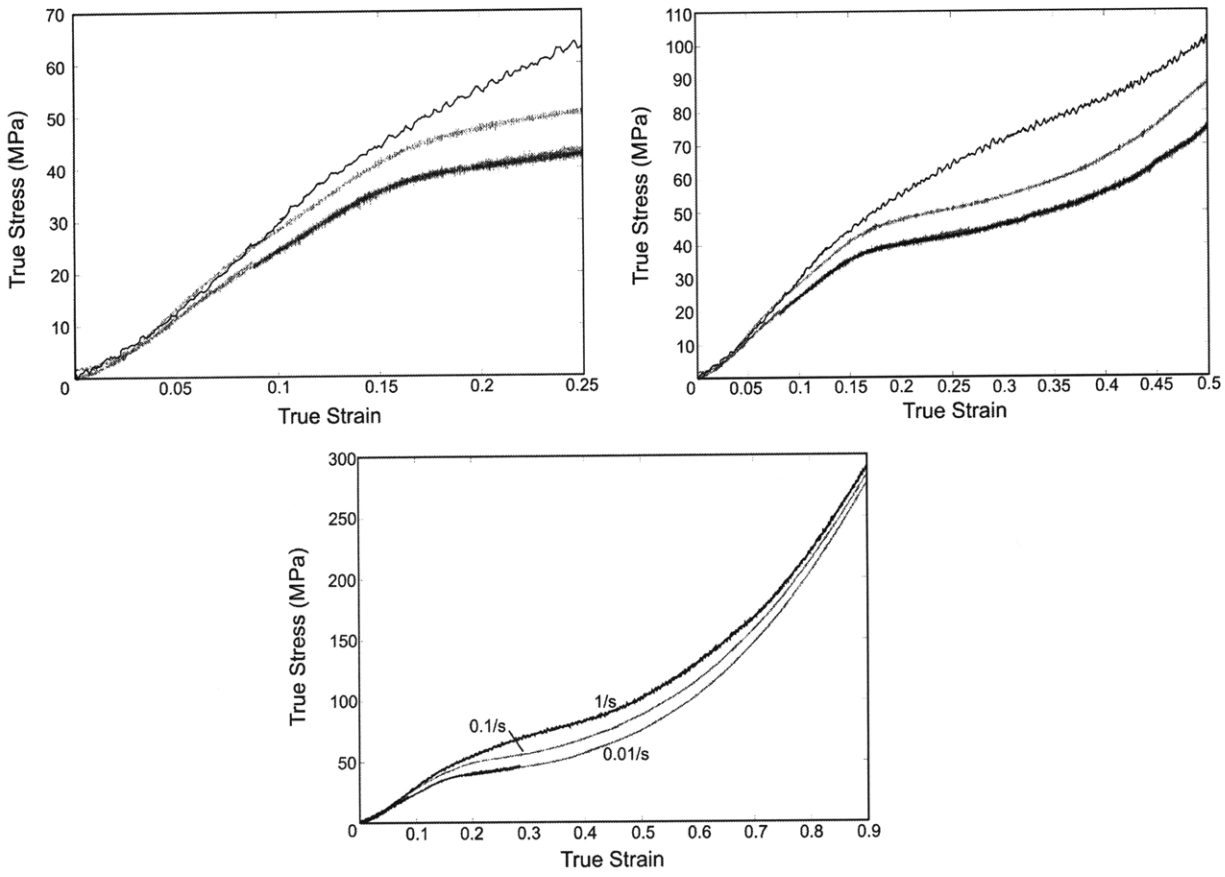

Figure 24: Stress-strain curves for monotonic loading of the distal thread region at three nominal strain rates ($1s^{-1}$, $0.1s^{-1}$, and $0.01s^{-1}$).

elastic region, increasing to a significant variance at high strains (strain greater than 0.8). Similarly, the failure strain, failure load, and failure stress all vary from thread to thread. Table 1 gives the mean values and standard deviations for failure strain, failure load, and failure stress in the distal thread section.

Failure Stress (MPa)		Failure Load (N)		Failure Strain	
Mean	Standard Deviation	Mean	Standard Deviation	Mean	Standard Deviation
289.3	80.2	1.51	0.43	0.88	0.16

Table 1: Statistics of failure in the distal thread section. The mean values and standard deviations of the failure stress, failure load, and failure strain for the distal thread section loaded at a nominal strain rate of $1s^{-1}$ are shown.

As can be seen in Table 1, the failure event is highly variable in the distal thread section. The standard deviation in failure strain is approximately 18% of the average, while the

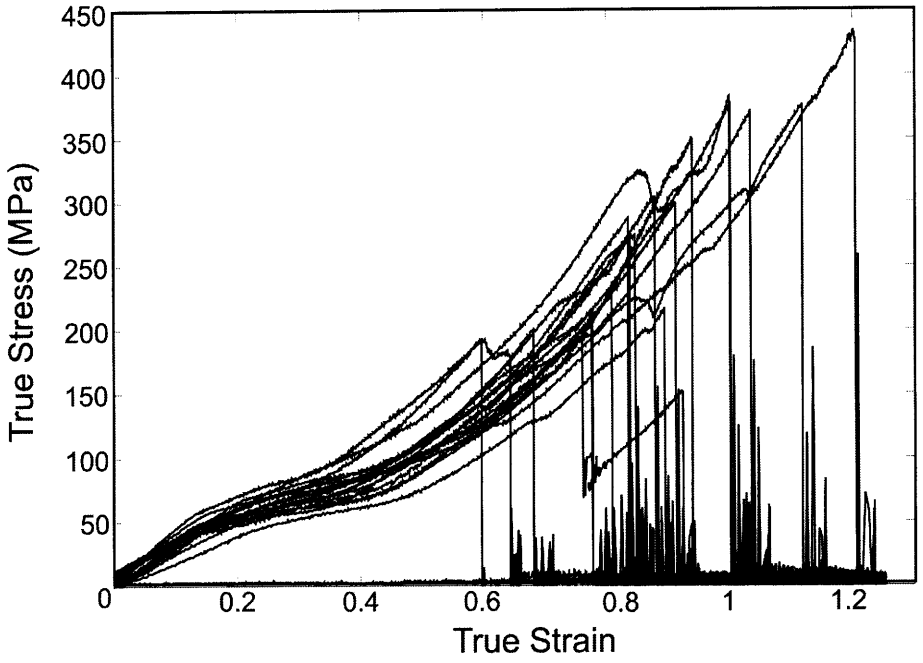

Figure 25: All statistically significant tests for monotonic loading of the distal thread section at a nominal strain rate of $1s^{-1}$.

deviation in the failure stress and failure load are both approximately 28% of the average. In spite of this high variance in failure, the actual stress-strain curves overlap quite nicely, as 18 curves are shown in Figure 25, all of which demonstrate a similar shape, similar yield strain (approximately 0.2), similar yield stress (approximately $55 - 70MPa$), and similar length of the post-'yield' stress plateau.

Cyclic Behavior Multiple cycle tests were performed at nominal strain rates of $1s^{-1}$ and $0.01s^{-1}$. For these tests, specimens were loaded to three different strain levels (the first in the initial elastic strain region, the second in the stress plateau region, and the third in the post-plateau hardening region), then unloaded by returning to a strain of zero, and then reloaded to the maximum strain, repeating this cycle three times. The corresponding stress-strain plots are shown in Figure 26.

As can be seen, the material exhibits hysteresis throughout loading, with the amount of hysteresis increasing significantly with strain. The material also demonstrates a small

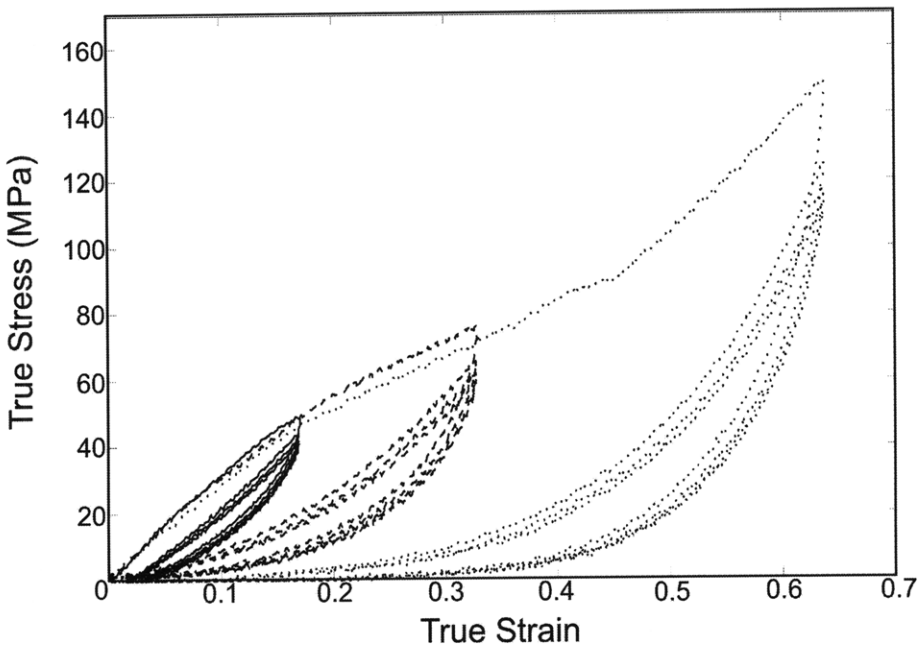

Figure 26: Stress-strain curve for cyclic loading of distal thread region. For each strain level, the specimen is loaded to a given strain (here 0.17, 0.33, or 0.64), then unloaded to a strain of zero, and reloaded to the maximum strain value three times. Hysteresis and cyclic softening increase with strain, though the majority of the softening occurs during the first cycle.

residual strain after the first load cycle (with the magnitude of this residual strain increasing with the strain from which the specimen was unloaded), as well as a more compliant response on reloading, until the stress-strain curve during reloading rejoins the initial loading curve upon reaching the strain from which unloading began. After the second cycle, there is little additional residual strain and the reloading and unloading is nearly identical to the first reload/unload cycle. This phenomenon (also observed in elastomers where it is referred to as the Mullins Effect (Mullins 1969), is well-documented in elastomers and rubbers, and implies that the majority of structural evolution with loading occurs in the first cycle [21].

The amount of hysteresis can be quantified by measuring the work applied to the material, and the work per unit volume (work density) dissipated in cyclic loading. Here, work density is calculated as:

$$w = \int_0^{\epsilon_f} \boldsymbol{\sigma} d\boldsymbol{\epsilon} \tag{1}$$

which can be calculated from the experimental data as the area under the stress-strain curve. In this sense, the work density applied to the material is the area under the initial loading curve, and the work density released with unloading is the area under the unloading curve, which gives a measure of the energy density stored during loading. Figure 27 shows a plot giving a visual representation of the different work density quantities with regards to two cycle loading. The total work density applied in each cycle, the work density stored in each cycle, and the work density dissipated in each cycle are all highlighted.

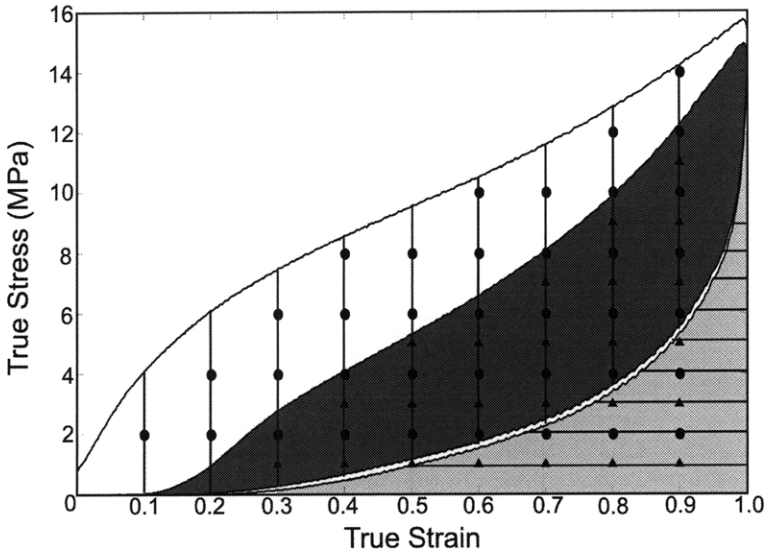

Figure 27: Relative amounts of work density for each cycle (stress strain curve for an ethylene methacrylic acid with butyl acrylate copolymer). The area with dots corresponds to the total work applied in the first cycle. The area with triangles corresponds to the total work applied in the second cycle. The area with vertical lines corresponds to the work dissipated in the first cycle. The area with horizontal lines corresponds to the work stored in the first cycle. The dark gray area corresponds to work dissipated in the second cycle. The light gray area corresponds to work stored in the second cycle.

Figure 28 shows these work density values for the case of the distal thread section. As can be seen, the total work density applied to the material in both the first and second load cycles increases non-linearly with strain. For the first load cycle, this work density increases from zero strain, while in the second load cycle, the work density remains zero until reaching a non-zero strain due to there being a residual strain after the first load cycle; the amount of residual strain increases with an increase in the maximum strain applied. The

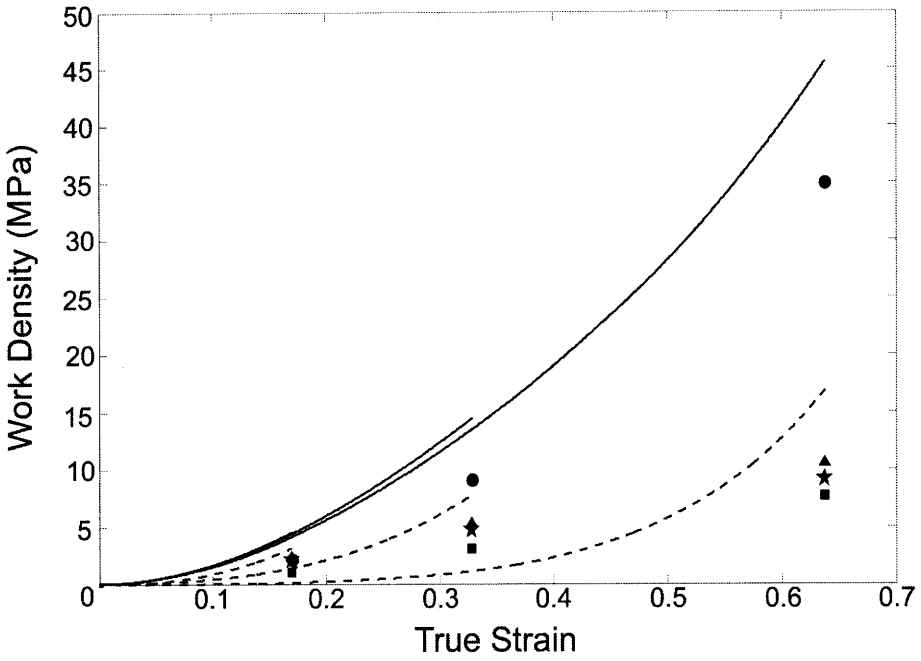

Figure 28: Work density vs. strain for the distal thread section in cyclic loading. Solid lines correspond to the total amount of work applied in the first load cycle. Dashed lines correspond to the total amount of work applied in the second load cycle. Circles correspond to the amount of work dissipated during loading to the given strain in the first load cycle. Triangles correspond to the amount of work stored during loading to the given strain in the first load cycle (as calculated by measuring the unloading response). Squares correspond to the amount of work dissipated during loading to the given strain in the second load cycle. Stars correspond to the amount of work stored during loading to the given strain in the second load cycle.

work density dissipated in the first cycle also increases non-linearly with strain in roughly the same manner as observed for the total work density evolution. The stored work density in both the first and second cycle appears to increase linearly (though, as can be seen in Figure 30, the increase is actually slightly non-linear). This stored work density is roughly equivalent in both the first and second load cycle, a result of the nearly overlapping stress-strain behavior in unloading for all cycles. The work density dissipated in the second load cycle increases in a similar manner to the work density stored in both cycles, and is lower in magnitude than the work density stored in the second cycle. The relative amounts of stored work and dissipated work are given in Table 2

A final type of cyclic test, where the maximum strain is increased for each cycle, was also performed, and a characteristic stress-strain curve is shown in Figure 29 (note that the strain

Strain	Cycle 1			Cycle2		
	Total (MPa)	Dissipated (MPa)	Stored (MPa)	Total (MPa)	Dissipated (MPa)	Stored (MPa)
0.17	4.55	2.21 (49)	2.34 (51)	3.1	1.00 (32)	2.10 (68)
0.33	14.5	9.20 (63)	5.31 (37)	7.76	3.08 (40)	4.69 (60)
0.64	45.61	35.0 (77)	10.6 (23)	16.84	7.71 (46)	9.14 (54)

Table 2: Values of stored and dissipated work at three different strain levels for two-cycle loading of the distal thread section. The actual values of work density (total, stored, and dissipated) are given in the table, with the percentage of the total that is stored and dissipated shown in parentheses.

rate for this test was $1s^{-1}$). Here the initial unloading is from a strain less than 0.1, well

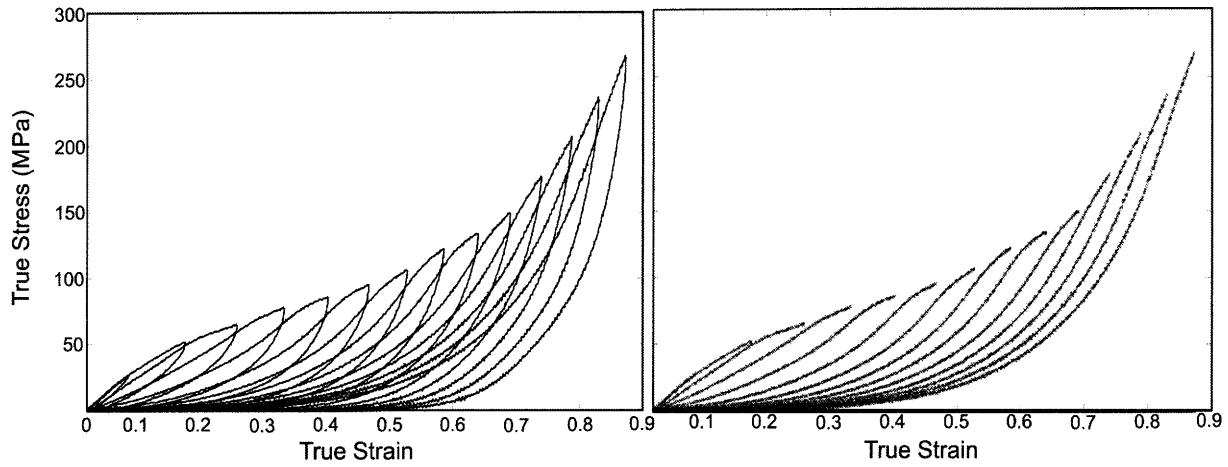

Figure 29: Stress-strain curve for cyclic loading of distal thread region. Here the specimen is loaded to a certain strain value, then unloaded to a strain of zero, and reloaded to a higher strain, with the incremental increase in strain being approximately 0.05. The plot on the left shows both unloading and reloading for each cycle, while the plot on the right shows loading alone.

within the initial elastic region; very little hysteresis is seen at this strain level, and there is no noticeable softening/Mullins Effect i.e. the reloading curve follows the initial loading curve exactly. This test serves to better highlight how much the hysteresis and residual strain increase with strain.

Figure 30 shows the amount of total work density applied to the material (in both the first and second cycle), the amount of work density stored in the first cycle, and the amount of work density dissipated in the first cycle for the increasing cyclic test shown in Figure 29. As can be seen, the total amount of work density dissipated in the first cycle increases non-

linearly throughout loading (as was already discussed with regards to Figure 28). Here, the non-linearity of the stored work density vs. strain curve is more apparent. As can be seen, the stored work density increases relatively quickly at low strain, then reaches a 'plateau' at a strain of approximately 0.25 (corresponding to the strain at which the stress plateau begins). The amount of work stored then increases slowly until a strain of approximately 0.5, at which point the stored work density begins to increase more rapidly with strain (again, the end of the stored work density plateau corresponds to the end of the stress plateau). This plateau is also present in the total work density applied in the second load cycle. Results for stored work density and dissipated work density are not shown in this figure, because only one cycle was conducted at each strain. However, the amount of stored work density in the second cycle should be similar to the amount of stored work density in the first load cycle (as was seen in Figure 28), and so it can be assumed that the amount of stored work density would be non-linear, giving a more linear appearance to the work density dissipated in the second cycle vs. strain curve.

Material Recovery A third subset of cyclic tests was performed, where the specimen was loaded and unloaded, then held at zero strain for times ranging from 3 minutes to 40 minutes, then reloaded and again unloaded. Stress-strain curves for these tests at three different strain levels (0.17, 0.28, and 0.37) are shown in Figure 31. As can be seen, the amount of recovery and time constant for recovery are heavily dependent on strain. For low strains i.e. strains in or near the initially elastic regime, full recovery happens extremely quickly. In Figure 31, the upper left plot shows full recovery occurring in three minutes. Although the actual time for full recovery is different for each thread, for strains in this regime, full recovery almost always occurs between 3 and 5 minutes. The next figure (upper right) shows cyclic loading to a strain of approximately 0.25 (a strain within the post-'yield' unfolding strain regime), with a hold time between cycles of 5 minutes and 25 minutes. For

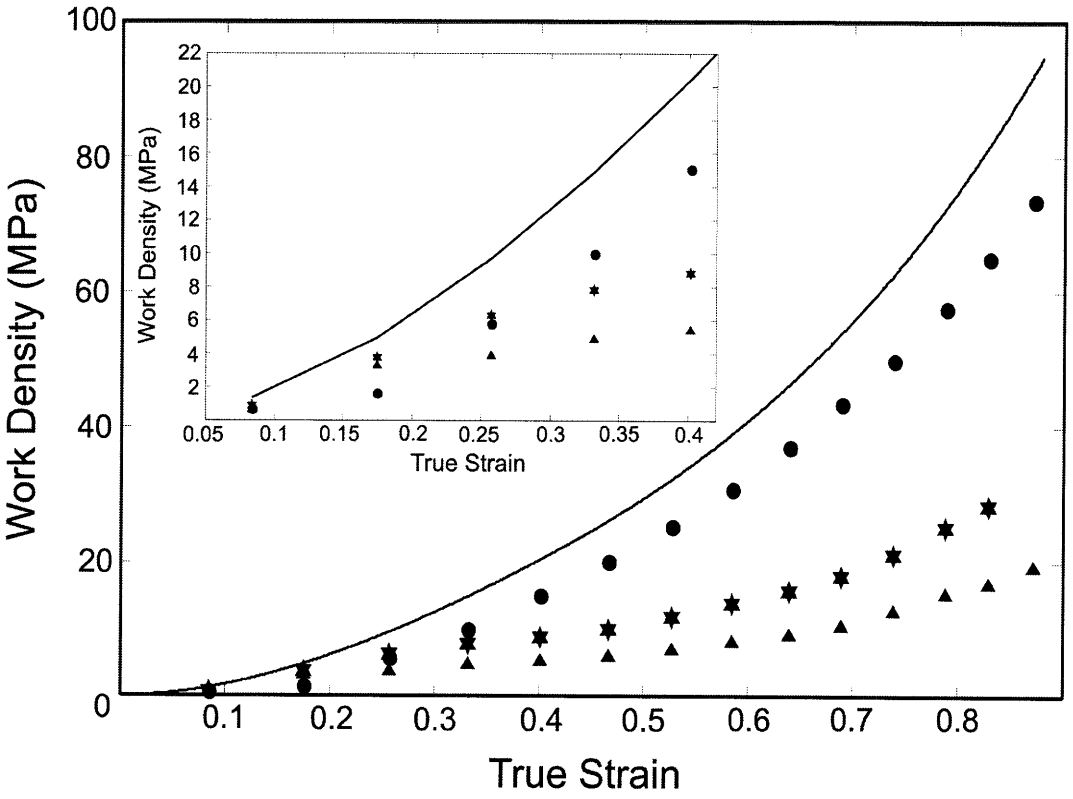

Figure 30: Work density vs. strain for the distal thread section, during cyclic loading in increasing strain increments (stress-strain curve for this test is shown in Figure 29. The solid line corresponds to the work density applied in the first load cycle (this curve is extrapolated from the broken curve of Figure 29 by assuming a solid curve of the same shape). Circles correspond to the amount of work density dissipated during loading to the given strain in the first load cycle. Triangles correspond to the amount of work density stored during loading to the given strain in the first load cycle. Hexagrams correspond to the total work density applied to the material in reloading to the given strain.

threads in this regime, full recovery takes significantly longer than in the low strain regime, and does not occur in all cases. In general, for strains in the unfolding regime, the time required for full recovery varies a great deal. The minimum observed full recovery time was 20 minutes, and some threads did not fully recover in 40 minutes. In all cases, the majority of the recovery occurred in the first $5-10$ minutes of hold, as is shown in the upper right plot of Figure 31. Finally, the bottom plot shows cyclic loading with hold from the post-unfolding regime, where the material begins to harden. For threads loaded to this strain regime, full recovery is not observed. Shown here are curves for reloading after a hold of 5 minutes and 20 minutes. Again the majority of the recovery occurs in the first 5 minutes. The curve

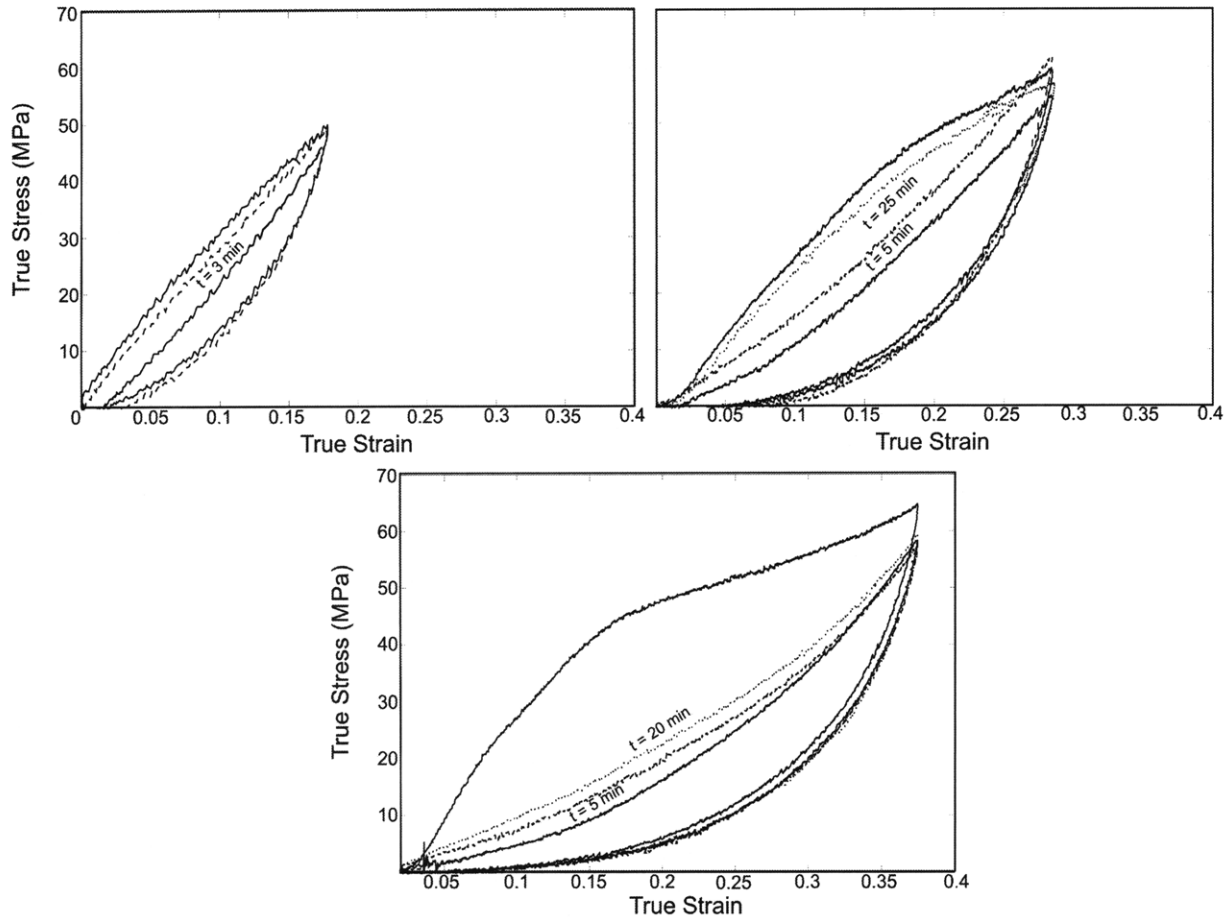

Figure 31: Stress-strain curves for cyclic loading of distal thread regions to different strains, and with different hold times between cycles.

here corresponding to a hold time of 20 minutes is a good average curve for the maximum amount of recovery possible in this strain regime.

2.3.2 Proximal Behavior

Monotonic Loading Tension tests to high strain were also conducted on the proximal thread sections at nominal strain rates of $1s^{-1}$, $0.1s^{-1}$, and $0.01s^{-1}$, with the results plotted in Figure 32. For the proximal thread section, the stress-strain response is characterized by an initially compliant region, where the stress increases slowly at first but begins to increase more quickly as the strain increases. The effect of strain rate on the material's stress-strain behavior is apparent throughout loading, with the value of stress for a given

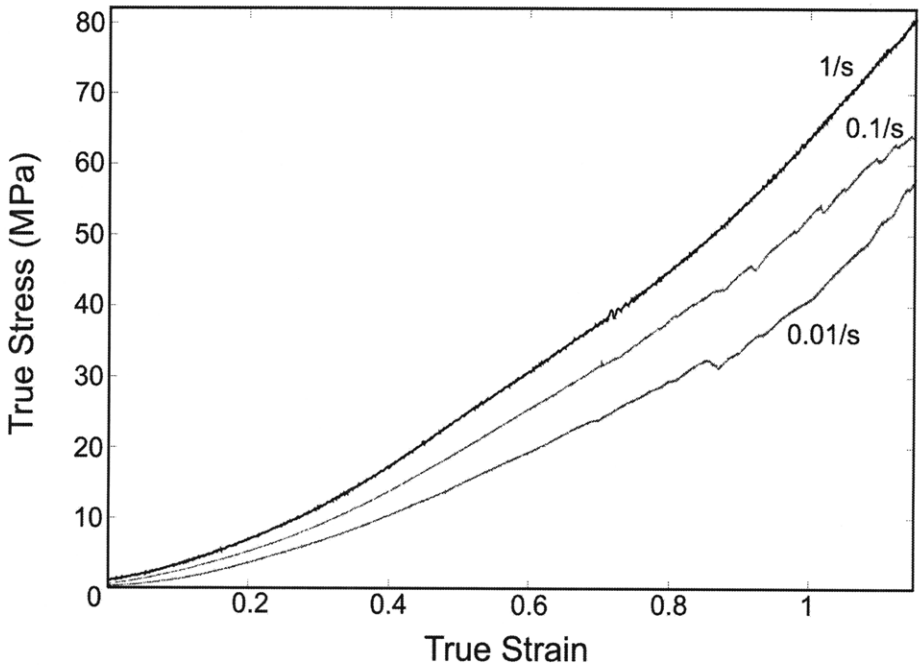

Figure 32: Stress-strain curves for monotonic loading of the proximal thread region at three nominal strain rates ($1s^{-1}$, $0.1s^{-1}$, and $0.01s^{-1}$).

strain increasing with strain rate. The material strain-rate dependence increases with strain, with the difference in the three curves of Figure 32 almost negligible for strains below 0.2. For intermediate strains (strains between 0.2 and 0.7) the difference increases significantly, so that at high strain (strains above 0.7) the strain-rate dependence is quite dramatic. In this high strain regime (as in the distal section), the stress-strain curves are nearly parallel.

As in the case of the distal section, there is a large amount of variability from specimen to specimen. Figure 32 shows three characteristic curves, while Figure 33 shows all statistically significant proximal thread specimens tested to failure at a nominal strain rate of $1s^{-1}$. Again the variance in stress (at a given strain) is relatively small at low strains (except for a few outliers) and increases with strain. Material failure is also quite variable (as in the distal section), with specimens failing at strains as low as 0.75 and as high as 1.4. Table 3 gives the mean values and standard deviations for failure strain, failure load, and failure stress in the proximal thread section.

There is a final feature that can be observed in loading of the proximal thread section to

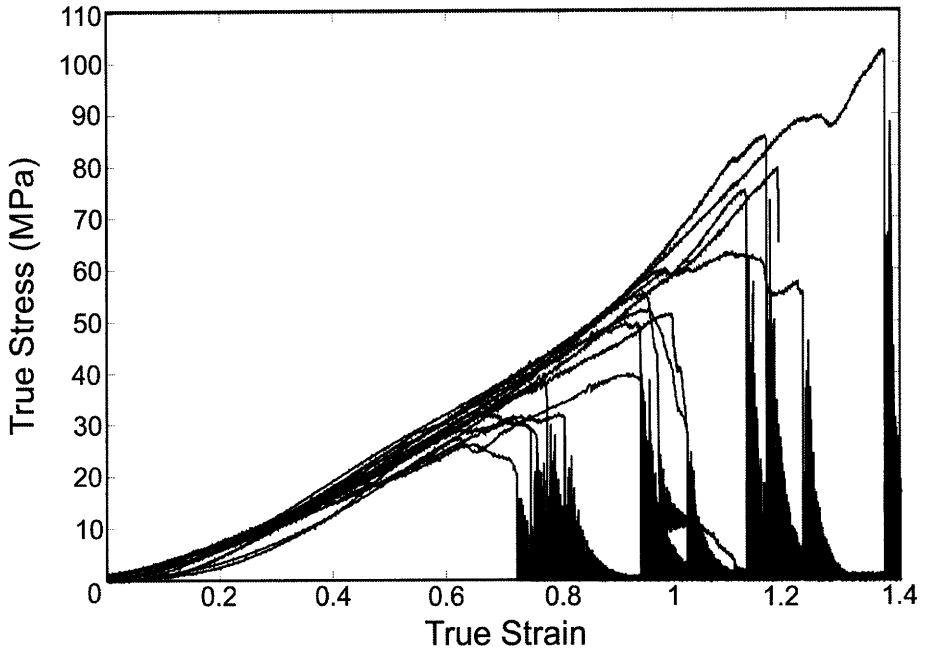

Figure 33: All statistically significant specimens for monotonic loading of proximal thread sections at a nominal strain rate of $1s^{-1}$.

Failure Stress (MPa)		Failure Load (N)		Failure Strain	
Mean	Standard Deviation	Mean	Standard Deviation	Mean	Standard Deviation
57.3	22.97	0.81	0.23	0.95	0.17

Table 3: Statistics of failure in the proximal thread section. The mean values and standard deviations of the failure stress, failure load, and failure strain for the proximal thread section loaded at a nominal strain rate of $1s^{-1}$ are shown.

failure (though it occurs mainly at lower strain rates), namely that in some cases the core of the thread will fail, while the cuticle remains intact. Figure 34 shows a stress-strain curve for a test of the proximal thread section at a nominal strain rate of $0.1s^{-1}$, during which the core fails at a strain of approximately 0.95, while the cuticle remains intact to a strain greater than 1. This is evidenced in the stress-strain behavior by a small constant stress (usually a stress less than $5MPa$), which extends beyond the sudden stress drop associated with core failure. In this case the cuticle only remains intact for an additional strain of approximately 0.075, though in some cases the cuticle can achieve strains up to 1.5 times greater than the maximum strain achieved by the core. This highly extensible character of the cuticle has been investigated and outlined by several other researchers [14] [12] [13].

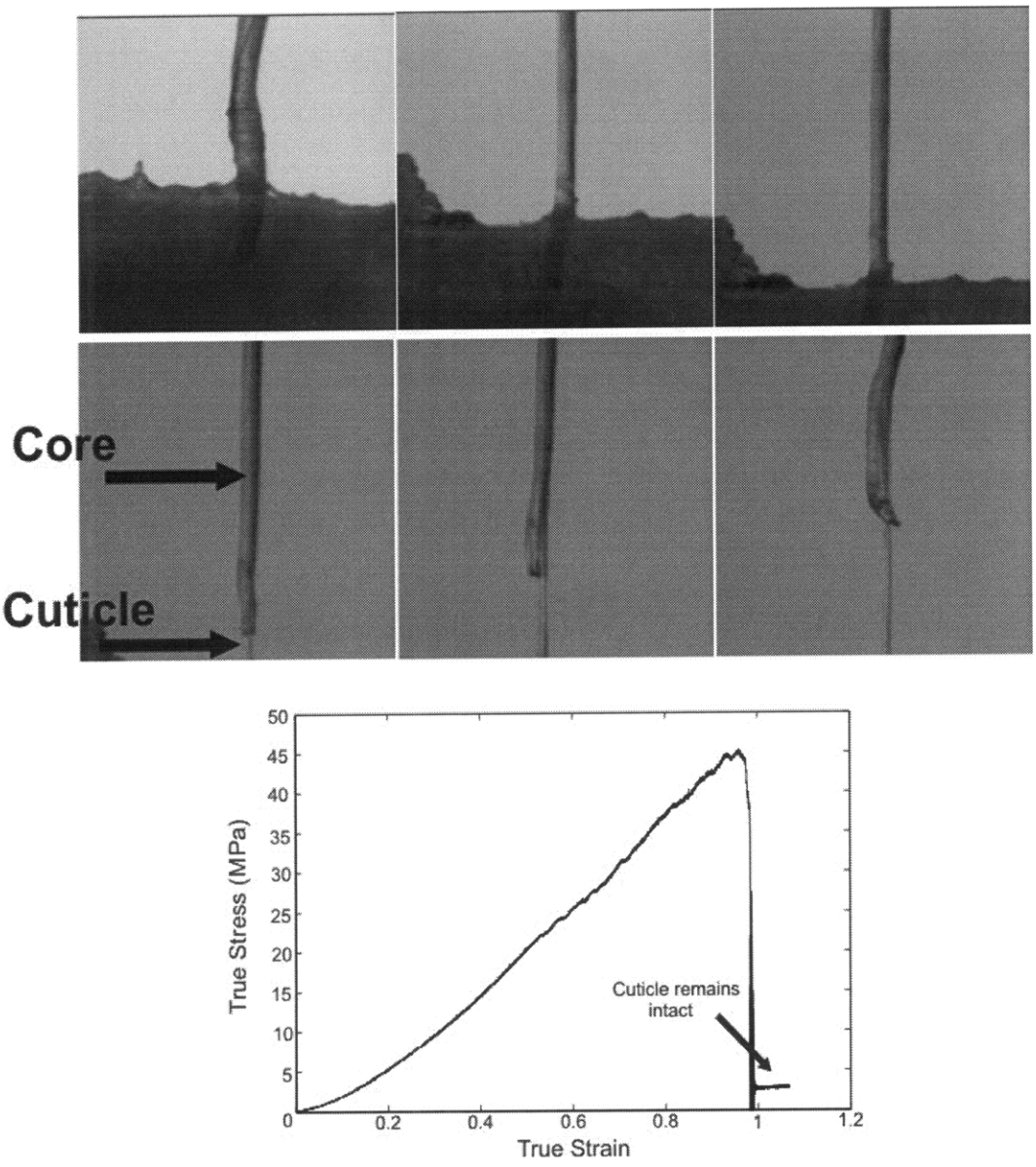

Figure 34: Monotonic loading of a proximal thread section at a nominal strain rate of $0.1s^{-1}$. Top shows the strain history imposed upon the specimen. Prior to stretching, the cuticle is wrinkled. As the specimen stretches, the core stretches and smooths out. With continued deformation, the core of the thread breaks, while the cuticle remains intact. The cuticle continues to stretch, with small cracks forming in the cuticle (Holten-Andersen 2007). In the final two frames, the core appears to stick out (presumably through one of these cracks). Bottom shows the stress-strain curve accompanying this test. The small constant stress region (for strains above 0.95) corresponds to continued loading beyond core failure, while the cuticle remains intact.

Cyclic Behavior Multiple cycle tests were performed at a nominal strain rate of $1s^{-1}$. For these tests, specimens were loaded to four different strain levels (in true strain increments of roughly 0.2), then were unloaded, reloaded, and unloaded again. The corresponding

stress-strain plots are shown in Figure 35.

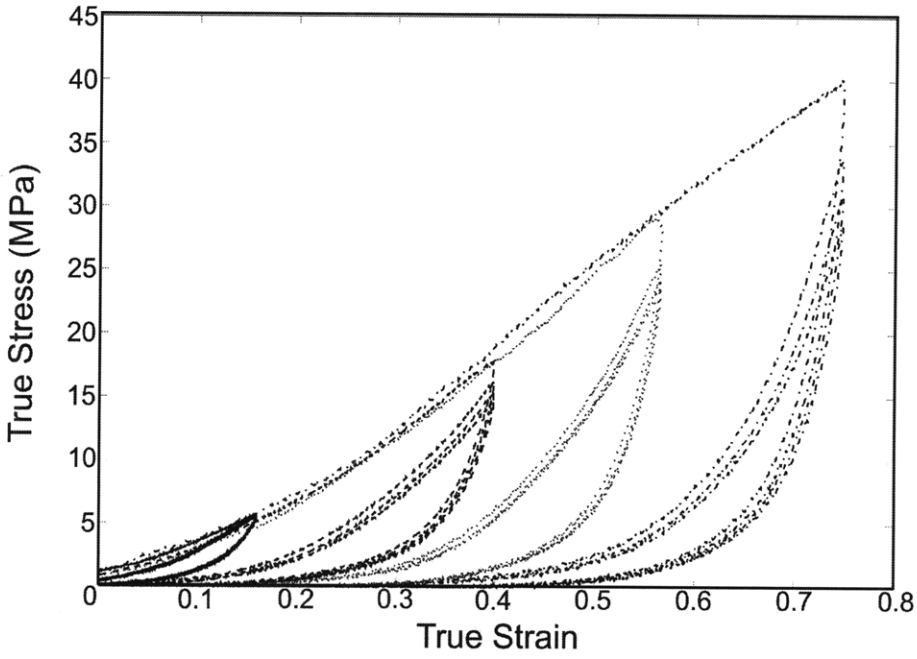

Figure 35: Stress-strain curves for cyclic loading of proximal thread regions to different strains (approximately 0.15, 0.4, 0.55, and 0.75). For each test, the specimen was loaded to the given strain value, unloaded to zero strain, reloaded to the same value, unloaded to zero strain, etc., with a total of four cycles. In general, hysteresis and cyclic softening increase with strain, though the majority of hysteresis and softening occur in the first load cycle.

The material exhibits hysteresis throughout loading, with the amount of hysteresis increasing significantly with strain. The material also demonstrates a residual strain after the first load cycle, which is relatively unnoticeable for the smallest strain test, and increases to approximately 0.35 for the largest strain test (roughly 50% of the maximum strain for this test). The cyclic softening (Mullins Effect) also increases dramatically with strain, where in the lowest strain test the reloading almost follows the initial loading, while in the largest strain test the reloading is far more compliant.

The amount of hysteresis can again be quantified via the method highlighted in Figure 27 above. Figure 36 shows the total work density applied to the material for loading to the four strains of Figure 35, as well as discrete values for the dissipated work density and the stored work density in each cycle.

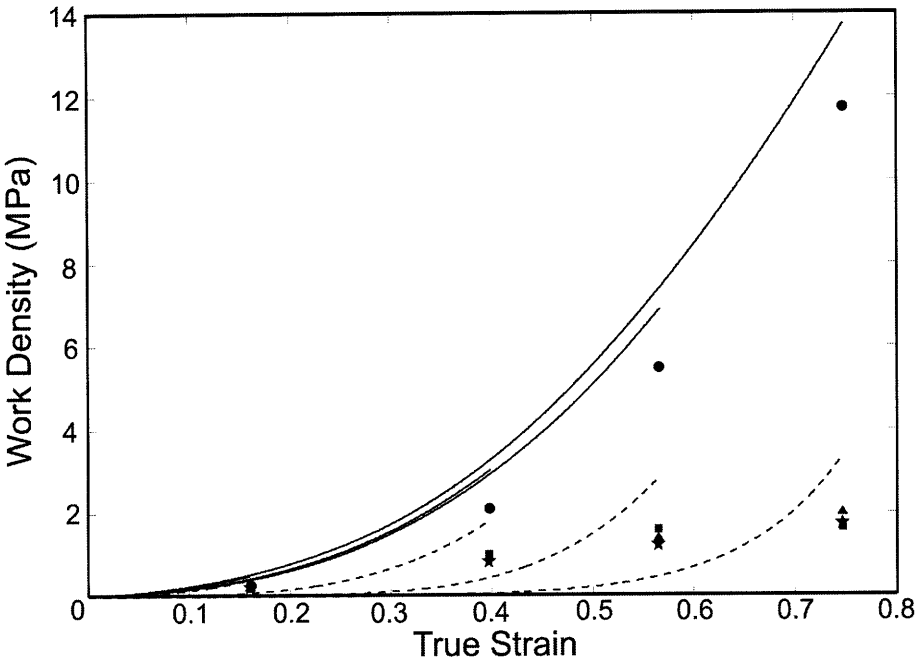

Figure 36: Work density vs. strain for the proximal thread section in cyclic loading. Solid lines correspond to the total work density applied in the first load cycle. Dashed lines correspond to the total work density applied in the second load cycle. Circles correspond to the amount of work dissipated during loading to the given strain in the first load cycle. Triangles correspond to the amount of work stored during loading to the given strain in the first load cycle. Squares correspond to the amount of work dissipated during loading to the given strain in the second load cycle. Stars correspond to the amount of work stored during loading to the given strain in the second load cycle.

As can be seen, the total work density required to deform the material is highly non-linear, and increases with strain for both the first and second load cycle. For the first load cycle, this work density increases from zero strain, while in the second load cycle the work density remains zero until reaching a non-zero strain (the residual strain). As in the distal thread section, the residual strain increases with strain, as is evidenced by the increasing non-linearity of the total work density curves (for the second load cycle). The work density dissipated in the first load cycle is also highly non-linear and increases with strain in roughly the same manner as observed for the total work density evolution. The stored work density in both the first and second cycle increases linearly (this is more apparent in Figure 38). Again, the stored work density is roughly equivalent in both the first and second load cycle, because of the overlapping unloading curves. The work density dissipated in the second

load cycle increases in a similar manner to the work density stored in both cycles, but is greater in magnitude than the work stored in the second cycle for all strains, and is greater in magnitude than the work stored in the first cycle for all but the highest strain (strain of approximately 0.75). The relative amounts of stored work density and dissipated work density are given in Table 4.

Strain	Cycle 1			Cycle2		
	Total (MPa)	Dissipated (MPa)	Stored (MPa)	Total (MPa)	Dissipated (MPa)	Stored (MPa)
0.16	0.48	0.27 (56)	0.21 (44)	0.39	0.19 (48)	0.20 (52)
0.4	3.04	2.11 (70)	0.92 (30)	1.82	1.00 (55)	0.82 (45)
0.57	6.88	5.50 (80)	1.38 (20)	2.83	1.60 (57)	1.23 (43)
0.75	13.76	11.8 (85)	2.00 (15)	3.36	1.64 (49)	1.72 (51)

Table 4: Values of stored and dissipated work at four different strain levels for two-cycle loading of the proximal thread section. The actual values of work density (total, stored, and dissipated) are given in the table, with the percentage of the total that is stored and dissipated shown in parentheses.

As in the case of the distal thread, cyclic tests where the maximum strain is increased for each cycle were performed. A characteristic stress-strain curve is shown in Figure 37. Again, this result serves to highlight the evolution of hysteresis and softening with strain, giving a sense of these behaviors at smaller strain increments than in Figure 35. It also demonstrates the full elasticity of the material at very small strains, as the initial cycle (below a true strain of 0.1 shows no noticeable hysteresis).

Figure 38 shows the amount of total work density applied to the material (in both the first and second cycle), the stored work density in the first cycle, and the dissipated work density in the first cycle for the increasing cyclic test shown in Figure 37. As can be seen, the total dissipated work density in the first cycle increases non-linearly throughout loading (as was already discussed with regards to Figure 35). Here, however, the dramatic rate of increase of the dissipated work density in the first cycle is more noticeable, as the dots corresponding to dissipated work density fall only slightly below the total work density curve. Further, unlike in the distal section, the stored work density in the first cycle and the total work density

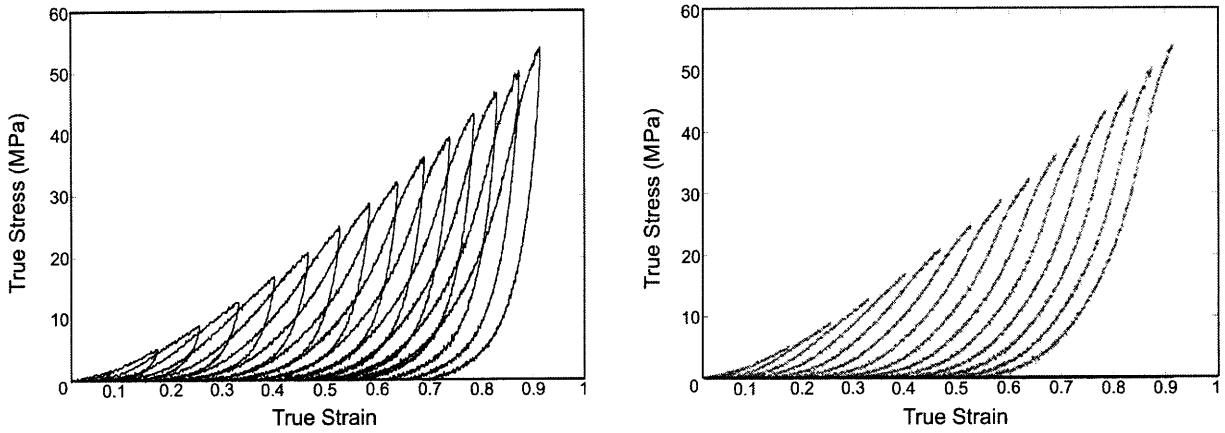

Figure 37: Stress-strain curve for cyclic loading of proximal thread region. Here the specimen is loaded to a certain strain value, then unloaded to a strain of zero, and reloaded to a higher strain, with the incremental increase in strain being approximately 0.05. The plot on the left shows both unloading and reloading for each cycle, while the plot on the right shows loading alone.

in the second cycle are shown to increase linearly with respect to strain. Again, because of the nature of this test, dissipated and stored work densities in a second load cycle cannot be calculated. However, assuming that the stored work density in the second cycle would be roughly equivalent to the stored work density in the first cycle (as it is in Figure 36), the dissipated work density in the second cycle can be estimated to increase roughly linearly with strain.

Material Recovery As in the case of the distal thread section, tests with hold times at zero strain were performed. In this case hold times of 5 minutes and 20 minutes were applied. Stress-strain curves for these tests at three different strain levels (approximately 0.3, 0.6, and 0.8) are shown in Figure 39. As in the distal section, the amount of recovery and the time constant for recovery are heavily dependent on strain. For low strains i.e. strains below and up to 0.3, the lowest value of strain, the material will fully recover given a long enough hold time. The stiffness recovered in 5 minutes is shown; for a hold time of 20 minutes the material recovers completely. For higher strains, recovery is much slower. At a strain of 0.6, the material recovers some amount in 5 minutes and slightly more in 20 minutes.

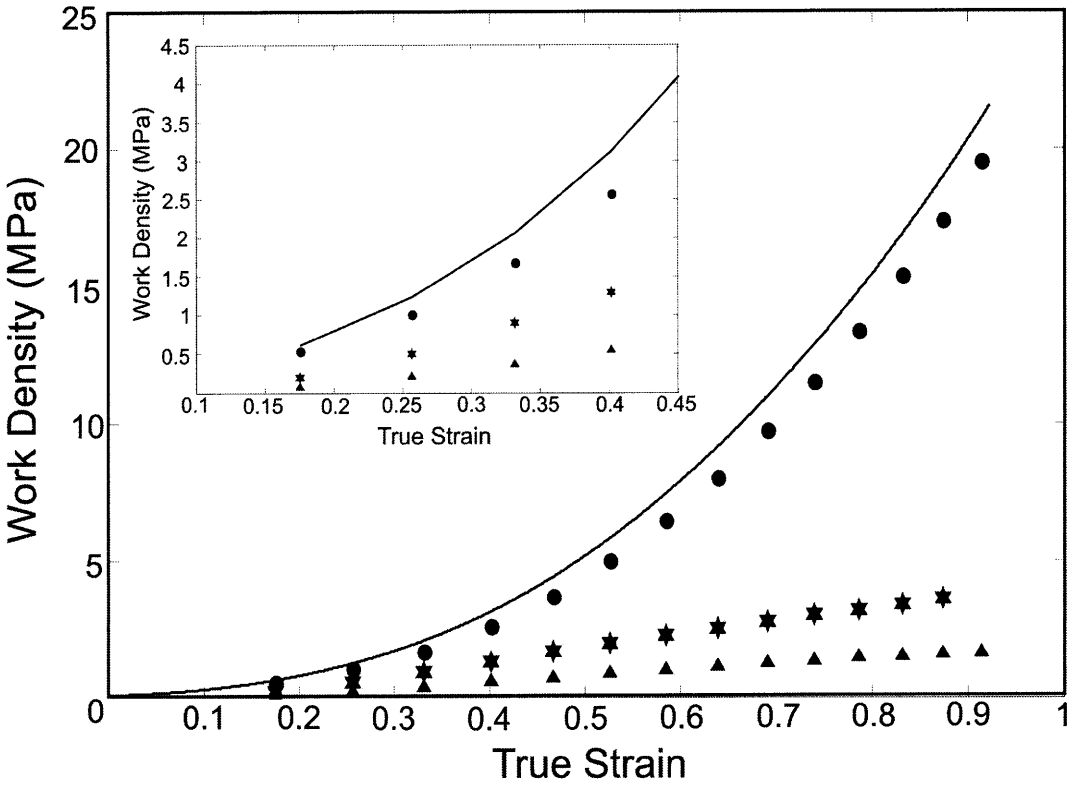

Figure 38: Work density vs. strain for the proximal thread section, during cyclic loading in increasing strain increments (stress-strain curve for this test is shown in Figure 37. The solid line corresponds to the work density applied in the first load cycle (this curve is extrapolated from the broken curve of Figure 37 by assuming a solid curve of the same shape). Circles correspond to the amount of work density dissipated during loading to the given strain in the first load cycle. Triangles correspond to the amount of work density stored during loading to the given strain in the first load cycle. Hexagrams correspond to the total work density applied to the material in reloading to the given strain.

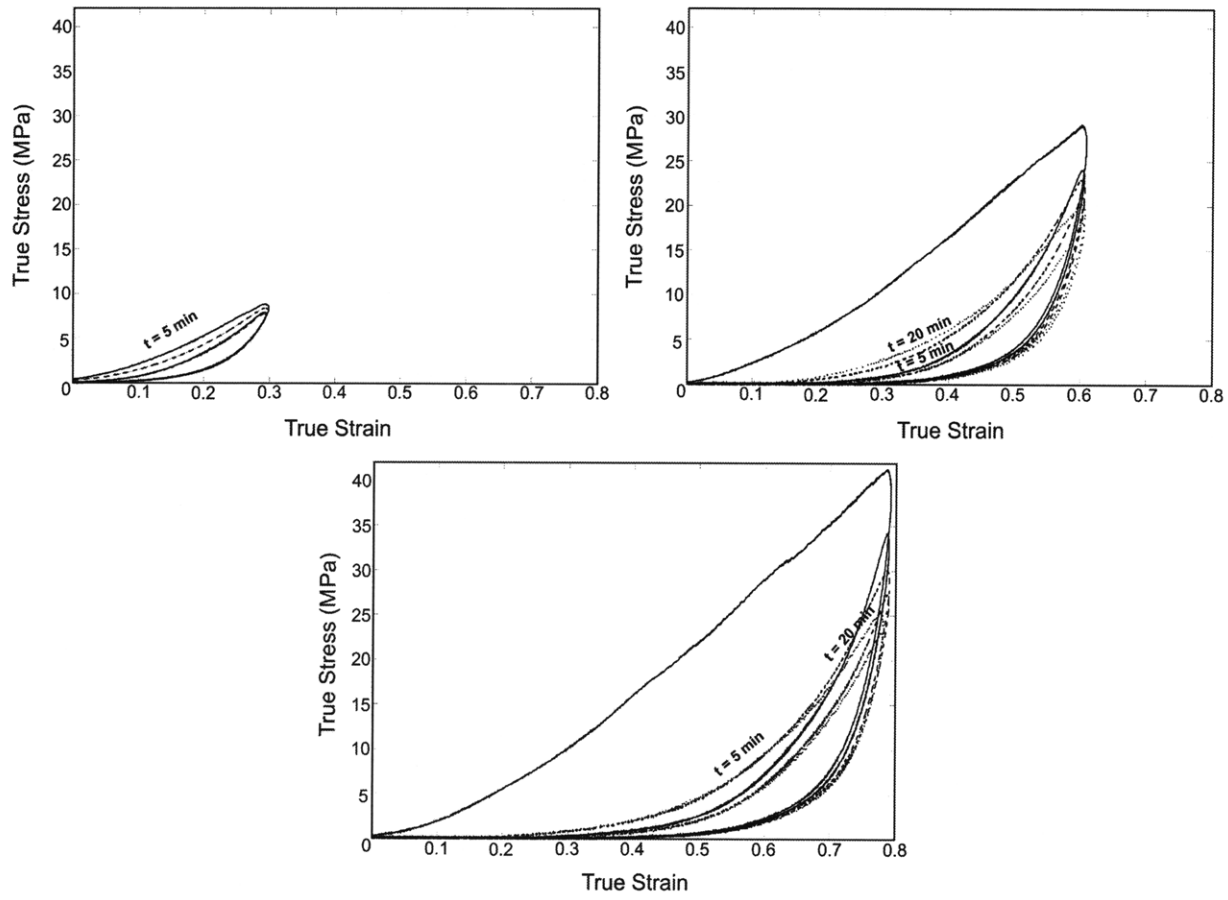

Figure 39: Stress-strain curves for cyclic loading of proximal thread regions to different strains, and with different hold times between cycles.

2.3.3 Comparison of the Distal and Proximal Section Behavior

Looking at the proximal and distal stress-strain curves separately can be deceiving, giving the impression that the distal thread section will carry a much larger load, and consequently that failure (in full thread loading) will always occur in the proximal section. In reality this is not the case, since the cross-sectional area of the two regions is different; the cross-sectional area of the distal thread region ranges from 2800 to 25,000 square μm with an average value of approximately 9500 square μm, while the cross-sectional area of the proximal thread region ranges from approximately 21,000 to 35,000 square μm with an average value of approximately 24,000 square μm. Figure 40 shows the load-strain behavior of the two thread regions plotted together (characteristic curves are used). As can be seen, the load carried

by both sections is similar, with the proximal section failing at a load of approximately 1.2N and the distal section failing at a load of approximately 1.6N. Remember from the previous discussion of the sections individually, that most specimens do not survive to these high strains. Tables 1 and 3 give the average failure strains of the distal and proximal thread sections to be 0.88 and 0.95 (true strain) respectively; these values correspond to nominal strains of approximately 1.4 and 1.6 respectively.

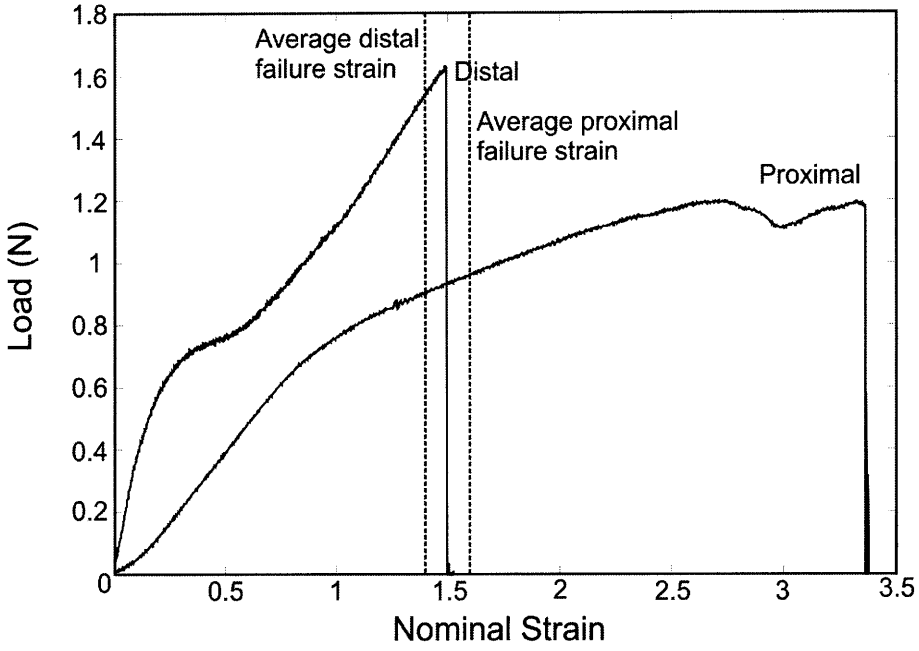

Figure 40: Load vs. nominal strain for proximal and distal thread sections. Vertical dashed lines show the normal strain for failure in each section.

Figure 41 shows load-strain curves for multiple proximal and distal thread sections loaded at a nominal strain rate of $1s^{-1}$. Since the cross-sectional area of these threads can vary to such a high degree, the actual load carried in each thread section is highly variable. Thus, although the proximal thread section may fail at a much lower stress than the distal section, it is found to exhibit failure loads similar to those of the distal section.

The cyclic load-strain behavior of the two sections is shown in Figure 42. As can be seen, the unloading load-strain curves are similar for both materials, with the distal unload curve demonstrating a slightly steeper initial slope. The amount of residual strain in each section

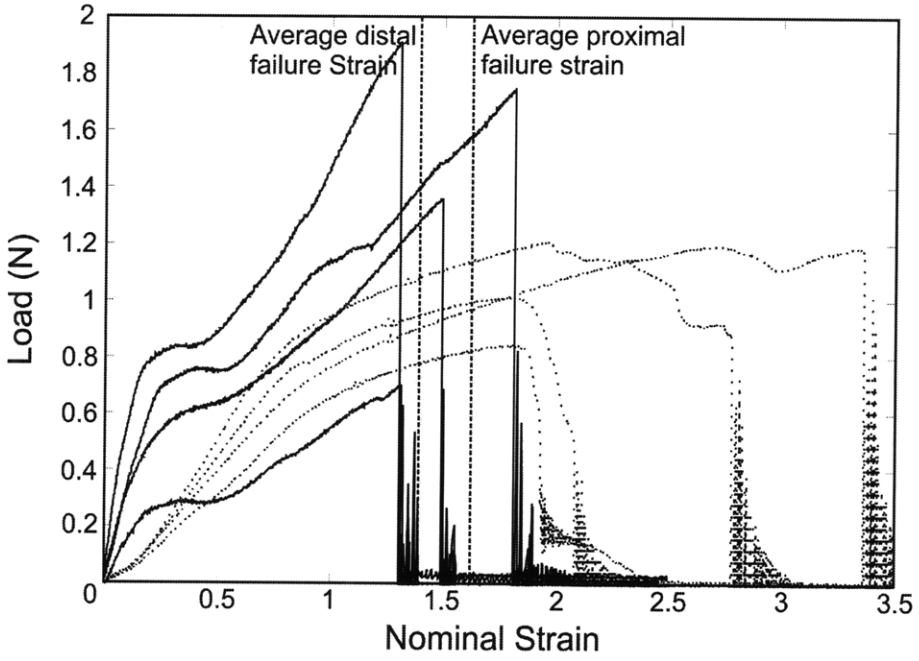

Figure 41: Load vs. nominal strain for proximal (dotted) and distal (solid) thread sections. Because of the high variability in cross-sectional area of individual threads, the load carried in a thread prior to failure can vary significantly, giving rise to the large differences in magnitude between load-strain curves for different specimens.

is also similar, with the distal section having a residual strain of 0.25 after loading to a strain of 0.8, and the proximal section having a residual strain of 0.5 after loading to a strain of approximately 1.2. The cyclic softening in each section is also similar, as is the number of cycles required to reach a stable equilibrium path.

2.3.4 Stem Behavior

As discussed above, the interaction between the proximal thread section and the stem is extremely interesting from an engineering standpoint. Thus, the properties of the stem were investigated via tension testing. The stem was dissected into several different sections, the threads were removed, and the stem was affixed to the same cardboard holder as the proximal and distal thread sections. Thus, the gage length of stem specimens was approximately $2mm$. The stem was roughly circular in diameter with a diameter ranging between $0.8mm$ and $1mm$. Thus, the cross sectional area of the stem specimens ranged between $0.5mm^2$

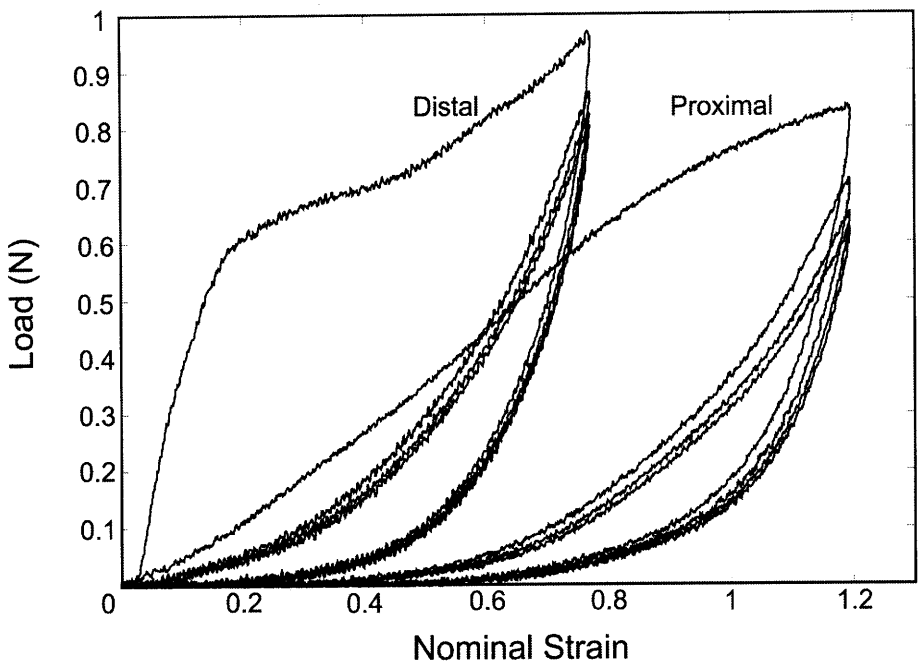

Figure 42: Load vs. nominal strain for proximal and distal thread sections in cyclic loading. Specimens were loaded and unloaded four times, with zero hold time between cycles.

and $0.8mm^2$. Results of monotonic loading of the stem at a nominal strain rate of $1s^{-1}$ are shown in Figure 43.

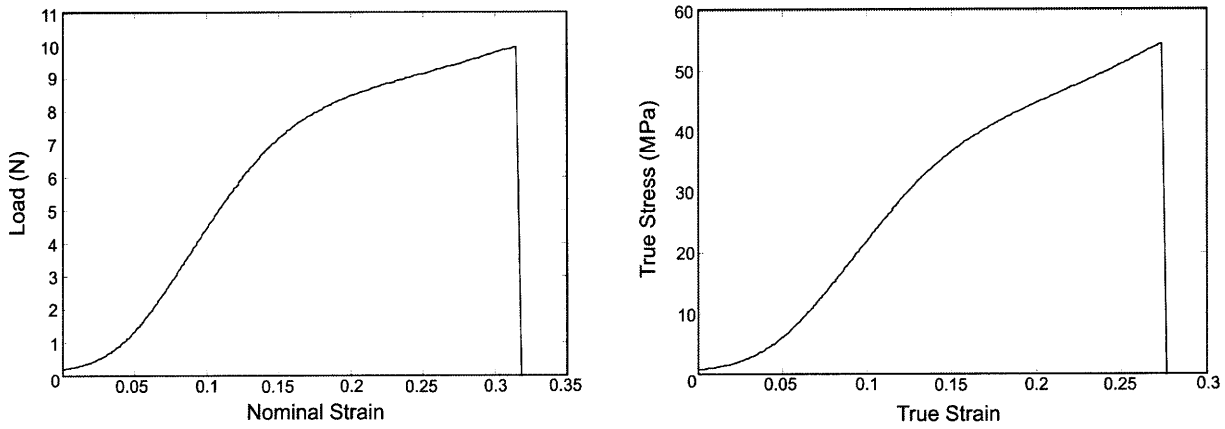

Figure 43: Load vs. nominal strain (left) and true stress vs. true strain (right) for the mussel stem. The specimen was loaded until failure.

The stem has a small initially compliant toe region. At a low strain (approximately 0.07) the stiffness increases rapidly, such that the stiffness of the stem in this strain regime is similar in magnitude to the initial stiffness of the distal thread region. The stem then demonstrates

a 'rollover' type yield, and a more compliant response post-'yield'. The material fails at a true strain of approximately 0.3, much less than either the distal or proximal thread region.

Figure 44 compares the load-strain and stress-strain behavior of the stem to load-strain and stress-strain behavior of the distal thread region. Because the cross-sectional area of the stem is so much larger, the stem is capable of withstanding a much greater load prior to failure than the threads themselves. In Figure 44 (left), the load carried in the stem is approximately $10N$, while that carried in the distal thread section is less than $1N$. In general, the stem can carry between 8 and 15 times the load carried in the thread. Figure 44 (right) shows the stress-strain curves for the same two specimens. As can be seen, the stem is initially much more compliant than the distal thread section, though the stiffness and the 'yield' phenomenon are similar for both materials. The distal thread section (as well as the proximal thread section and the full thread) are far more extensible than the stem.

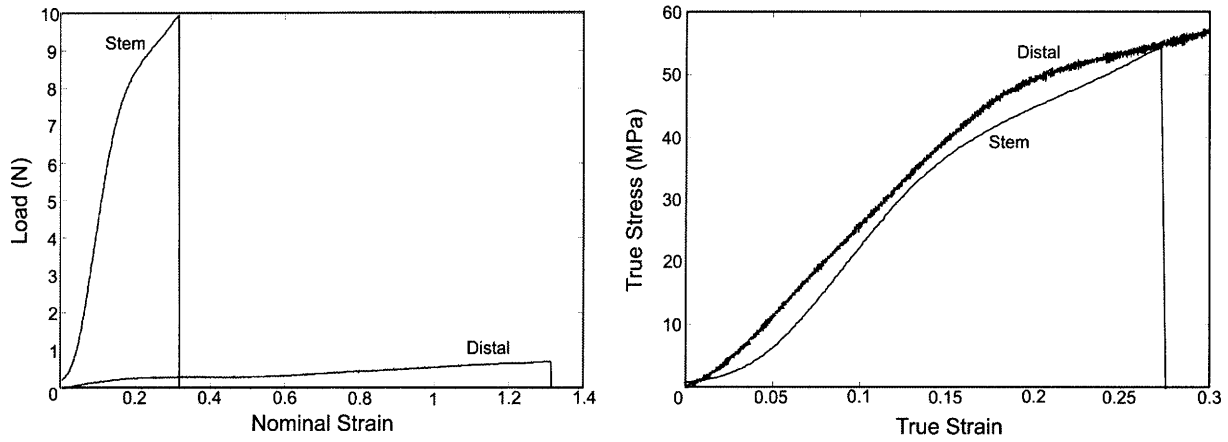

Figure 44: Load vs. nominal strain (left) and true stress vs. true strain (right) for distal thread section and stem. As can be seen the stem is initially much more compliant than the distal thread section, but the stiffness of the two regions are similar, as is the yield behavior.

2.3.5 Full Thread Response

Full threads were also tested in monotonic and cyclic loading, with the corresponding load-strain curves shown in Figures 45 and 47 respectively. The full thread specimens tested were collected at a different time of year and a different location than the full threads from

which the distal and proximal specimens were sectioned. As a result, the full threads are stiffer than would be expected from investigating proximal and distal sections separately (the seasonal variation in mussel thread strength has been investigated and is documented - see [20]); this phenomenon will be discussed in greater detail below and in the simulations section of this thesis. For full thread specimens, the ends of the specimens were glued directly to cardstock and mounted in the grips of the testing apparatus (small specimen holders with the $2mm$ gage length window were not used). Thus, the gage length of the specimens varied. Shorter specimens were used so that high strains could be achieved. The average length of full thread specimens was $18.03mm$ with a standard deviation $3.54mm$; the average length of the proximal section was $4.9mm$ with a standard deviation of $1.4mm$; the average length of the distal section was $9.9mm$ with a standard deviation of $1.8mm$; the average length of the transition section was $3.3mm$ with a standard deviation $0.8mm$.

Monotonic loading behavior As can be seen in Figure 45, the mechanical behavior of the full thread is characterized by an initial stiff region, followed by a gradual rollover-type 'yield'. The material stress-strain response is more compliant post-'yield' with a nearly constant tangent stiffness. The 'yield' in the full thread is similar to that seen in the distal section, and is correlated to the distal yield. As the distal section 'yields', the full thread becomes more compliant. However, the 'yield' in the full thread is not as sudden or as sharp as the 'yield' in the distal thread section, because the stress is still increasing at the same rate (with respect to strain) in the proximal thread section. Load-strain curves for the full thread as well as the proximal and distal thread sections are shown in Figure 49, after which the other load-strain features of each section are compared with the full thread.

The statistics of failure in the full thread were also tabulated and are given in Table 5 (the failure loads and failure strains for the proximal and distal thread sections are also shown in this table). The average failure strain for the full thread is 0.36 with a standard

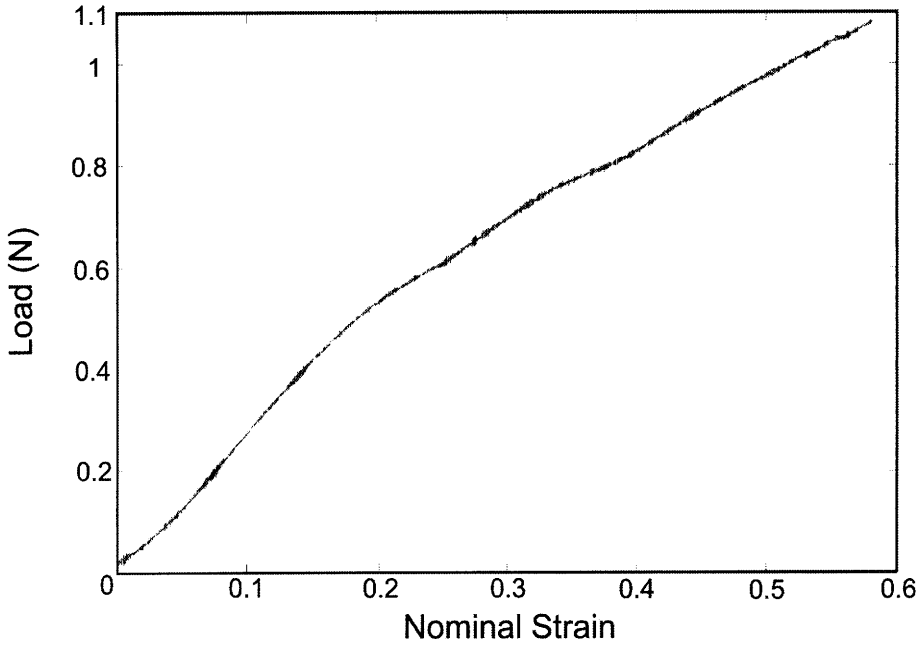

Figure 45: Load vs. nominal strain for a full mussel byssal thread in monotonic loading at a nominal strain rate of approximately $1s^{-1}$. Note that the load is different for every test, as the cross-sectional area of each thread is different. The curve shown is a curve that falls near the center of the spectrum. Figure 46 below shows all load-strain curves for full thread tests.

deviation of 0.12, while the average failure load is $0.86N$ with a standard deviation of $0.24N$. Thus, although the average failure strain of the full thread is much less than the average failure strain of either the proximal or distal thread section, the average failure load of the full thread is between the failure loads in the distal and proximal thread sections separately (though closer to the average failure load in the proximal section). This result implies that failure is occurring somewhere in the transition region, most likely close to the proximal section. A comparison of the proximal, distal, and full thread failure statistics are given in Table 7.

Failure Load (N)		Failure Strain	
Mean	Standard Deviation	Mean	Standard Deviation
0.86	0.24	0.36	0.12

Table 5: The statistics of failure for the full thread. The mean values and standard deviations of the failure load and failure strain are shown (all values are for tests conducted at a nominal strain rate of $1s^{-1}$).

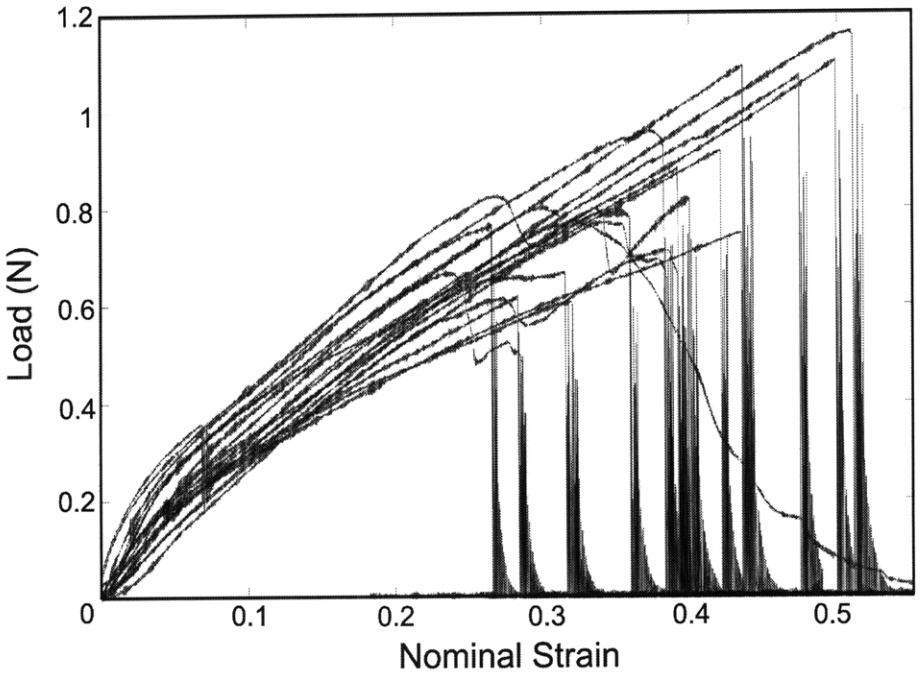

Figure 46: Load vs. nominal strain for full mussel byssal threads. Threads fail between strains of 0.25 and 0.55, with an average failure strain of 0.36. The average failure load is $0.86N$.

cyclic loading behavior The cyclic behavior is similar to that seen in the distal and proximal regions. In the initial stiffness regime the hysteresis exhibited in unloading is relatively small, with a reloading that is close to the initial loading. There is also some cyclic softening in this low strain region, though the amount of softening is relatively small. As the strain increases the hysteresis and cyclic softening increase. The amount of softening in subsequent cycles also increases with strain, where at low strain the third and fourth loadings follow the second loading almost exactly, at intermediate strain the fourth loading follows the third almost exactly, though both are slightly softer than the second, and at high strains cyclic softening continues (though at a decreasing rate) through four cycles.

The total amount of work applied to the material, the amount of work stored, and the amount of work dissipated can again be quantified. In this case, since no stress can be calculated, the work must be calculated using the force-displacement curves. Thus, instead of calculating the work density applied, stored, and dissipated in the material, the work is

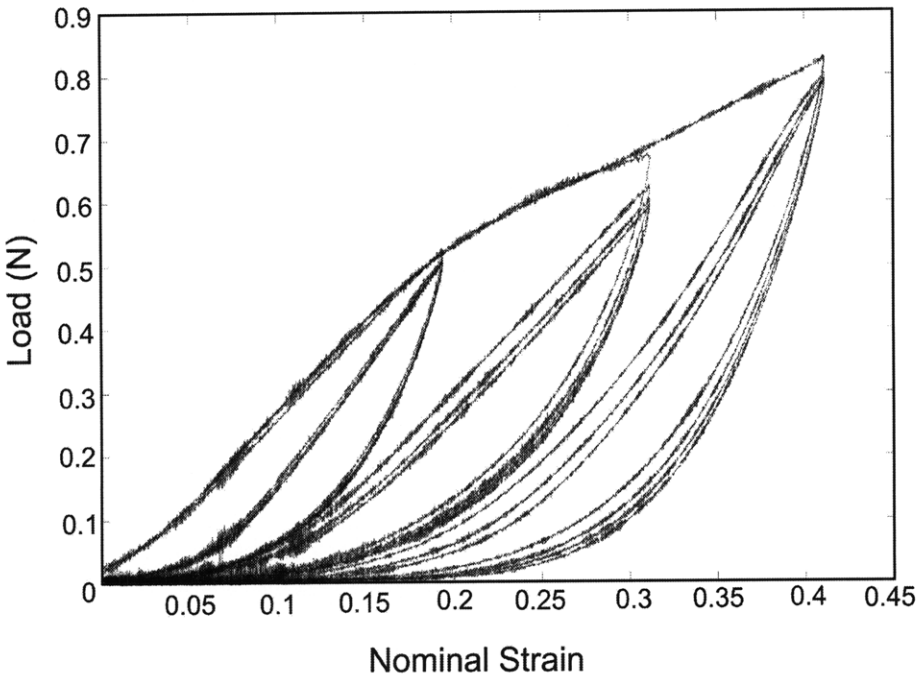

Figure 47: Load vs. nominal strain curves for a full mussel byssal thread in cyclic loading at a nominal strain rate of approximately $1s^{-1}$. Again, the load is different in each specimen, as the cross-sectional area of each thread is different. The curves shown here are from three separate threads taken from the same byssus. They represent good average value curves.

calculated.

$$W = \int_0^{x_f} f dx \tag{2}$$

The values of work applied, stored, and dissipated in the first two cycles at each strain level are given in Table 6, and plotted in Figure 48.

As can be seen in Figure 48 the amount of stored and dissipated work in each cycle increases with displacement, with the amount of work dissipated in the first cycle increasing the most quickly. The work dissipated in the first cycle increases roughly linearly with displacement, while the other work values increase slightly non-linearly with the rate of increase decreasing with strain. This is the same as in the proximal and distal sections, since the dissipated work in the first cycle for the individual sections increased non-linearly with true strain (what would be a linear increase with displacement), and the other stored and dissipated work values increased roughly linearly with true strain (what would be a

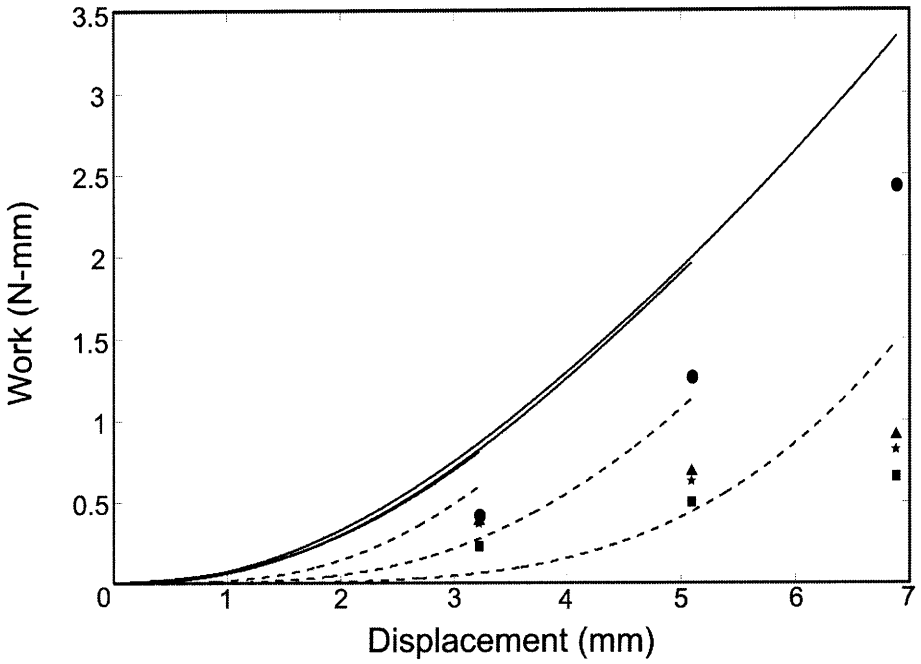

Figure 48: Work vs. displacement curves for a full mussel byssal thread in cyclic loading at a nominal strain rate of approximately $1s^{-1}$. Solid lines correspond to the total amount of work applied to the material in the first load cycle. Dashed line correspond to the total amount of work applied to the material in the second load cycle. Circles correspond to the amount of work dissipated in the first load cycle. Triangles correspond to the total amount of work stored in the first load cycle. Squares correspond to the total amount of work dissipated in the second load cycle. Stars correspond to the total amount of work stored in the second load cycle.

non-linearly slowing increase with displacement).

The disparity between stored and dissipated work is different in each cycle, but for both cases increases with strain. At low strain, in both the first and second cycle this disparity is quite small. At intermediate strain, in the first cycle, the amount of dissipated work begins to heavily outweigh the amount of stored work, with the amount of dissipated work nearly twice the amount of stored work. At intermediate strain in the second cycle, the amount of stored work begins to outweigh the amount of dissipated work. Again, the disparity is not large (stored work is only approximately 1.2 times greater than the amount of dissipated work), but the disparity is certainly larger than at low strains. For high strains, the same trends are observed, with the disparity between stored and dissipated work increasing. In the first cycle, the amount of work dissipated is almost three times the amount of stored work, while in the second cycle the amount of stored work is approximately 1.3 times greater than the amount of dissipated work.

Displacement	Cycle 1			Cycle2		
	Total (N-mm)	Dissipated (N-mm)	Stored (N-mm)	Total (N-mm)	Dissipated (N-mm)	Stored (N-mm)
3.22	0.81	0.43 (53)	0.38 (47)	0.60	0.23 (38)	0.37 (62)
5.09	1.96	1.27 (65)	0.69 (35)	1.13	0.50 (45)	0.63 (55)
6.89	3.35	2.44 (73)	0.91 (27)	1.48	0.66 (44)	0.82 (56)

Table 6: Values of total, stored, and dissipated work at three different displacement levels for two-cycle loading of the full thread. The actual values of work (total, stored, and dissipated) are given in the table, with the percentage of the total that is stored and dissipated shown in parentheses.

Comparison of load-strain behavior in proximal and distal sections and the full thread Figure 49 shows several load-strain curves for the proximal thread section, the distal thread section, and the full thread. The yield in the full thread is correlated with the yield in the distal section (as discussed above), and the overall shape of the full thread curve seems to correlate well with the curves of the individual sections i.e. the full thread is initially stiff, as it primarily samples the stiffness of the proximal thread section, after yield

the full thread is more compliant, as it samples the stiffness of the distal section's stress plateau. In general the threads fail in this strain regime (corresponding to the post-'yield' stress plateau in the distal section), though some post-plateau hardening should occur for the full thread with continued loading. As noted above, the full thread is stiffer than would be expected (see inset plot).

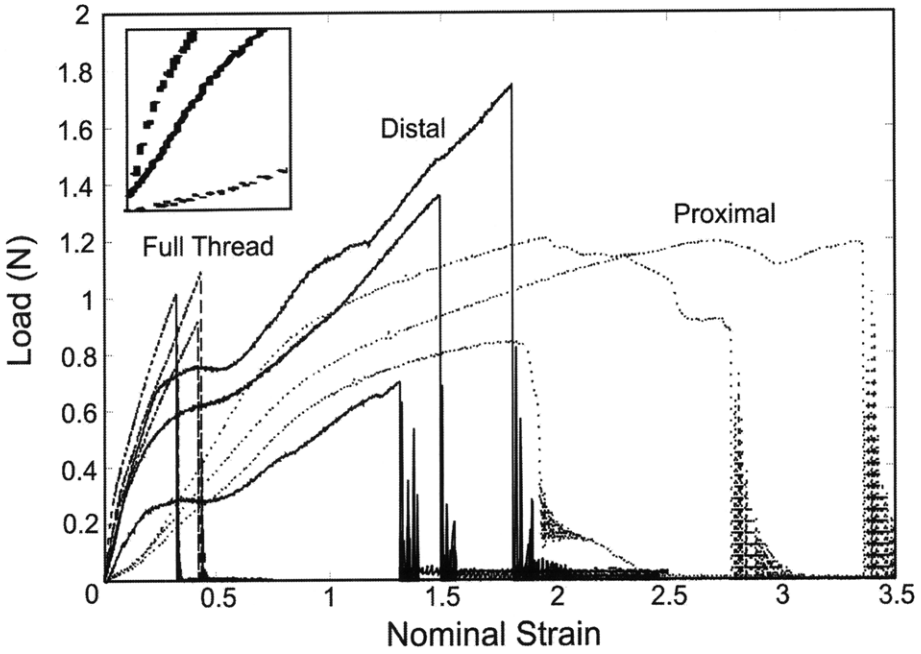

Figure 49: Load-displacement curves for the proximal section, distal section, and full thread. The inset shows the initial stiffness of the distal (solid line), proximal (dotted line), and full thread (dashed line). The proximal sections fail at the highest strain, the distal sections fails at an intermediate strain, and the full thread fails at the lowest strain. The failure load is similar in all materials.

The most likely reason for the discrepancy in stiffness, is that the threads used for distal and proximal specimens, and the threads tested whole were collected at different times of the year. All of the specimens used for testing the distal and proximal behavior of these materials were collected from Georges Island in Boston Harbor during the late summer/early fall (late August through early October). The specimens used in full thread tests were collected from a different location (Pigeon Cove in Gloucester, MA) and at a different time of year (mid-March). As discussed in Moeser and Carrington (2006), the stiffness of blue mussels is heavily dependent on season, with the strongest (stiffest) threads produced in

late winter/early spring, and the weakest threads produced in late summer [20]. For the mussels investigated in the Moeser and Carrington study (blue mussels from Rhode Island - the same species as the mussels used in this study), winter threads lost as much as 60% of their stiffness by late summer. Thus, if the stiffness of the full thread results (results from late winter threads) is reduced by 60% to account for this seasonal variation, the load-strain curves become as expected i.e. at a given strain, the load in a full thread is greater than the load in the proximal section alone, but less than the load in the distal section alone. This is shown in Figure 50

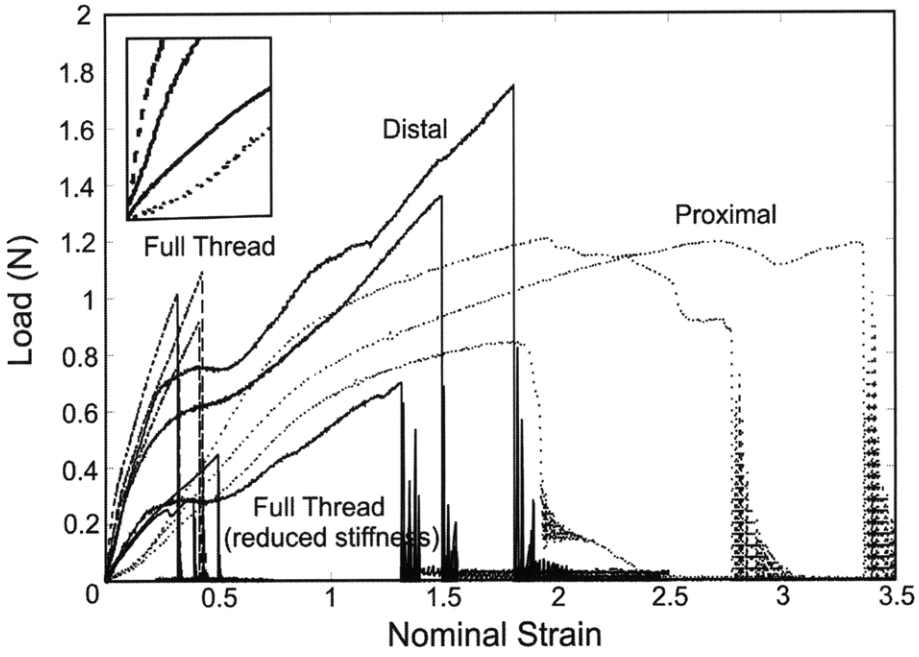

Figure 50: Load-displacement curves for the proximal section, distal section, full thread, and reduced full thread. The inset shows the initial stiffness of the distal (stiffer solid line), proximal (dotted line), full thread (dashed line), and reduced stiffness full thread (more compliant solid line). The reduced stiffness full thread performs as expected i.e. the stiffness is intermediate to the distal proximal section stiffness. The un-reduced full thread is more stiff than is to be expected.

Table 7 gives the values of failure strain and failure load for the proximal section, distal section, and full thread, though the failure loads of the full thread tested and those of the proximal and distal cannot be compared, since they correspond to threads collected in different seasons. As can be seen (both in Figure 49 and in Table 7), the average failure

strain of the full thread is much lower than the average failure strain of the proximal and distal thread sections separately (again these values should not be compared directly, but since a lower failure strain in the full thread relative to the failure strains in the individual sections was described in the Smeathers and Vincent study, it can be assumed that the failure strain would be lower in summer threads as well). Thus lower failure strain in the full thread suggests a localized strain in either the proximal or distal section of the full thread, likely at the transition, where the elevated local strain reaches the failure strain of the section.

Material	Failure Load (N)		Failure Strain	
	Mean	Standard Deviation	Mean	Standard Deviation
Summer Proximal Section	0.81	0.23	0.95	0.17
Summer Distal Section	1.51	0.43	0.88	0.16
Winter Full Thread	0.86	0.24	0.36	0.12
Approximated Summer Thread	0.52		0.36	

Table 7: Comparison of the statistics of failure for the summer proximal thread section, the summer distal thread section, the winter full thread, and an approximation for a summer full thread. The mean values and standard deviations of the failure load and failure strain are shown (all values are for tests conducted at a nominal strain rate of $1s^{-1}$). The summer full thread's failure load will likely be substantially lower (due to the lower stiffness), while the failure strain will likely be the same.

As discussed in the introduction, the protein density in the proximal thread section is much less than in the distal thread section. Thus, the protein density, as well as the cross-section must transition in this region. Further, the mechanical properties of the protein filaments must transition, with regards to fiber orientation, fiber stiffness, and the constants of folding. Thus, we postulate that the area/density/mechanical properties of the transition section are not as robust as in the proximal or distal section separately, and that failure occurs in this region at a relatively low strain. The simulations, which will be discussed later in this thesis, support this conclusion.

Strain in distal and proximal sections It is possible to monitor the strain in the proximal and distal regions separately during loading. To do this, the specimen is marked with black ink stripes, and the distance between stripes is measured during loading. This way,

the strain in the proximal and distal sections can be monitored and plotted as discrete points along with the overall strain (which is measured directly by the testing machine). Figure 51 plots the strains (proximal, distal, and overall) against time, and the strain in each section against macroscopic strain. For this test, the thread used is fairly representative, in that the proximal section is approximately $\frac{1}{2}$ of the length of the distal section (here the proximal section is $3.2mm$, the transition is $6.6mm$, and the transition section is $1.7mm$).

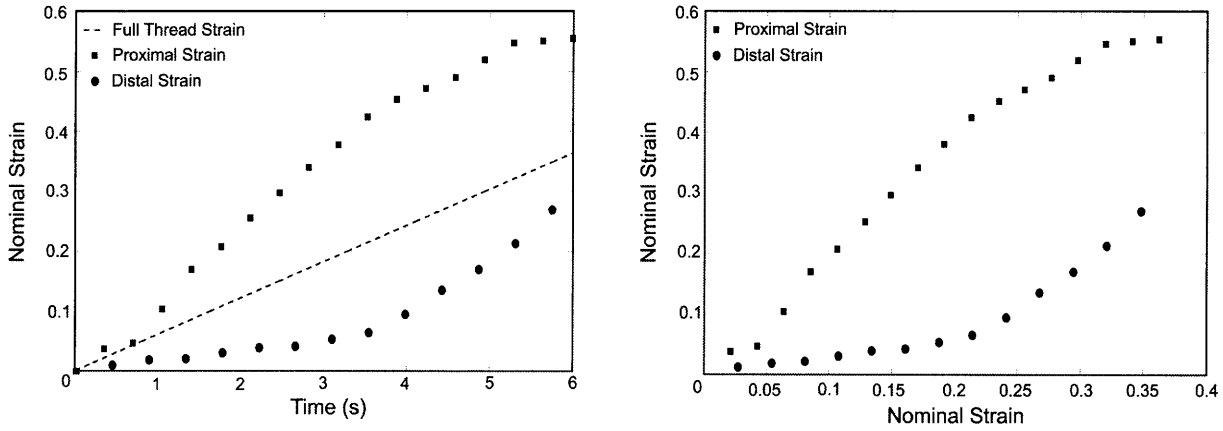

Figure 51: The strain in the proximal (squares) and distal (circles) thread sections as well as the overall strain in the thread (dashed line) vs. time (left). Strain in the proximal (squares) and distal (circles) thread sections vs. the overall strain in the thread (right). Data is taken from a monotonic loading test to failure.

As can be seen, initially the majority of the strain is accommodated by the strain in the proximal thread section, as is hypothesized above. As loading increases, the distal section increases in strain slowly, while the proximal strain increases rapidly. At an overall thread nominal strain of approximately 0.2, the rate of increase of strain in the distal section increases quickly, and the rate of increase of strain in the proximal section decreases quickly. This change corresponds to the yield in the distal thread section. At yield, the distal section becomes much more compliant than the proximal section, thus accommodating the majority of the thread strain. Again, theoretically for continued loading, the distal thread section would get past the 'stress plateau' in the stress-strain curve, and would stiffen, but all of the specimens tested failed prior to this post-plateau hardening.

Although the interaction between the distal thread section and the plaque was not specif-

ically investigated in this thesis (nor has it been discussed heavily), this result suggests that the stress level the distal section transmits to the adhesive plaque is, at most, equal to the stress plateau ($\sim 50MPa$). Essentially, this suggests that the unfolding event in the distal thread section (which gives the stress plateau and rapid strain increase) limits the distributed stress level transmitted to the plaque.

Section Pairing and Load Sharing There are two final observations that need to be stated regarding the experimental results. First, it is apparent from Figure 49 that the load-strain curves of the individual sections can be very different, in spite of the fact that the stress-strain curves overlap (since stress is load divided by area). Further, since the unfolding event in the distal thread section is a force-activated event, it is important that the load in the thread reach a certain level to force the distal thread section to yield. If a compliant proximal section is paired with a stiff distal section, the yield will never occur (or occur at very high macroscopic strain). Conversely, if a compliant distal section is paired with a stiff proximal section, the yield will occur at a low macroscopic strain. In the former case, the full thread will exhibit the yield very late (at a high strain), while in the latter the full thread will yield very early (at low strain). This could account for the larger variation in yield strain seen in the full thread results (Figure 46) relative to the variation in yield strain seen in the distal results. This 'sectional pairing' is also important from a structural mechanics point of view, as it dictates the load-sharing capability of the threads.

The load-sharing capability, especially with regard to the yield, of the thread is itself extremely important to the mussel's ability to remain attached to the rocks of its habitat. The yield in the full thread regulates the amount of stress that is transmitted both to the stem and to the adhesive plaque. If the distal section does not yield (and consequently the thread does not yield), the strain in the proximal thread section will continue to increase linearly. Consequently, the stress will continue to increase, and the amount of stress applied

to the stem may become too large, ripping the connective hoop. Conversely, if the distal section yields too soon, it may prematurely pass through the stress-plateau region and stiffen. Thus, the stress applied to the adhesive plaque may become too large, tearing the thread at the plaque-thread interface. It is likely that the mussel compensates for this itself, only pairing the 'appropriate' proximal and distal sections, but a more in-depth study of this phenomenon would certainly provide valuable insight into the mechanics of load sharing in these threads.

2.4 Summary of Mechanical Experimental Results

Several key features of the mechanical behavior of the mussel byssal apparatus (threads and stem) have been highlighted in this section:

- The large deformation non-linear stress-strain (and/or load-strain) behavior of the proximal and distal sections separately, of the full thread, and of the stem (Figures 24 32 45, 43).
  - The distal thread section exhibits an initially stiff region, followed by a rollover-type 'yield', followed by a post-'yield' stress plateau, and strain hardening at high strains. The 'yield' occurs at a true strain of approximately $50MPa$ (at a nominal strain rate of $1s^{-1}$. Failure occurs at an average true strain of 0.81 and an average load of $1.51N$.
  - The proximal thread section exhibits an initially compliant toe region, followed by a region of roughly constant tangent stiffness. Failure occurs at an average true strain of 0.95 and an average load of $0.88N$.
  - The full thread exhibits a small initially compliant toe region, followed by a relatively stiff region. A gradual rollover-type 'yield' event occurs at strains of approximately 0.2, and the yield is followed by a more compliant region with

roughly constant tangent stiffness. Full threads fail at an average strain of 0.36 and an average load of $0.86N$.

  - The stem demonstrates a fairly large initial toe region, followed by a stiff region (stiffness comparable to the distal thread section). At strains of approximately 0.2 the stem exhibits a rollover-type 'yield', which is quickly followed by failure. The stem fails at strains of approximately 0.25 and loads of approximately $9N$.

- The cyclic loading behavior of the proximal and distal sections separately, and of the full thread (Figures 26 35 47).

  - The distal thread section exhibits small hysteresis at low strain, with the hysteresis increasing with strain. The material also demonstrates cyclic softening, and a large amount of dissipation.

  - The proximal thread section exhibits significant hysteresis throughout loading, with the majority of the work density applied to the material dissipated for all strain levels. The proximal section also shows significant cyclic softening.

  - The full thread demonstrates a similar cyclic response, with a hysteresis increasing with strain. The hysteresis of the full thread is less than the proximal section, but greater than the distal. Again, the material demonstrates significant cyclic softening.

- The recovery seen in the proximal and distal thread sections (Figures 31 39).

  - The distal section's ability to recover is heavily dependent on strain. Prior to yield, the material recovers fully within 3 minutes. In the post-yield stress plateau region, the material will recover fully, but the process can take up to (or greater than) 25 minutes. After the plateau, when the material has hardened, full recovery does not occur.

- The proximal section recovers similarly to the distal section. At small strain, the material recovers fully within minutes. For intermediate strain the material will recover fully, though the time required for full recovery can be very long. For high strain, the material will not recover.

- The dissipative behavior seen in the proximal and distal sections separately, and in the full thread (Figures 28 36 48, and Tables 2 4, and 6).

  - In the distal section the majority of the work applied in the first cycle is dissipated, while the majority of the work applied in the second cycle is stored. The amount of stored work in each cycle is similar, and the amount of dissipated work in the second cycle is much lower than that dissipated in the first.

  - In the proximal section the majority of the work applied in the first cycle is dissipated, as is the majority of the work applied in the second cycle (for all but the highest strain tested). The amount of stored work in each cycle is similar, and is similar to the amount of work dissipated in the second cycle. The amount of work dissipated in the first cycle is far greater than any of the other quantities.

  - In the full thread, the majority of work in the first cycle is dissipated, while the majority of work in the second cycle is stored. For the full thread, there is larger variation in the amount of work stored in the first and second cycle, though they are still similar, and are similar to the amount of work dissipated in the second cycle. Again, the amount of work dissipated in the first cycle is far greater than any other work quantity.

These results will be used in the following chapters to validate the material constitutive model and the full thread finite element simulations.

3 A Micro-structurally-informed Constitutive Model of the Stress-Strain Behavior of Mussel Byssal Threads

As discussed in the introduction of this thesis, the microstructure of mussel byssal threads consists primarily of protein filaments suspended in a jelly-like matrix. In recent years, the mechanical behavior of protein molecules (as well as other biological molecules and long chain synthetic molecules) has become an increasingly popular area of research, and several models have been developed to capture the stress-stretch behavior of these molecules. Recently, much of this work has focused on capturing the unfolding of large folded domains within these molecules, as well as modeling how these molecules behave in multi-molecule networks. In most cases the proteins are modeled either as freely-jointed chains, with their mechanical response captured with the inverse Langevin function [23], or as worm-like chains, with their mechanical response captured with the equations developed by Marko and Siggia [18] and MacKintosh [17].

3.1 The Bertoldi Model for the Mechanical Behavior of Mussel Byssal Threads

Bertoldi (2007) proposed a constitutive model for the mechanical behavior of the distal section of mussel byssal threads, modeling the material as a network of folded protein molecules in parallel with a Neo-Hookean matrix (see Figure 52) [1].

In this model, eight protein filament bundles are arranged into the eight chains of an eight-chain orthotropic unit cell (as described in Bischoff et. al. [3] [4]). As can be seen in Figure 53 the dimensions of the unit cell are a, b, and c, where:

$$a = c = \sqrt{2} r_0 \sin\theta_0, \qquad b = 2 r_0 \cos\theta_0 \tag{3}$$

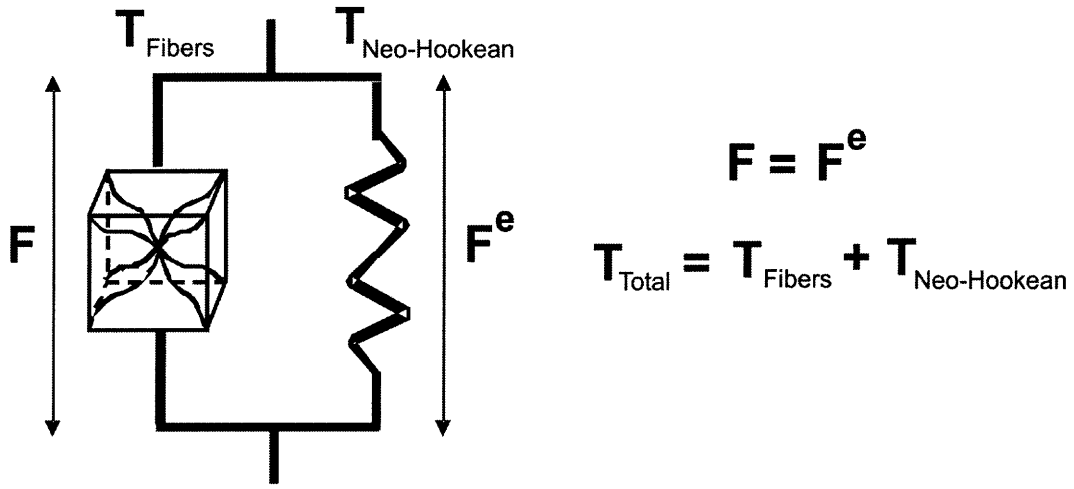

Figure 52: A rheological description of the Bertoldi constitutive model. Here the material is modeled as an eight-chain protein network in parallel with a Neo-Hookean matrix. The matrix is linear (modeled as a spring). Note that the strain on each element i.e. the deformation gradient will be the same, while the stresses will be different. The stresses sum to give the total stress in the material.

and the vector orientations of the filament bundles are:

$$\begin{aligned}
\mathbf{v}_0^{(1)} &= -\mathbf{v}_0^{(5)} = \nu_1\hat{e}_1 + \nu_2\hat{e}_2 + \nu_1\hat{e}_3 \\
\mathbf{v}_0^{(2)} &= -\mathbf{v}_0^{(6)} = \nu_1\hat{e}_1 + \nu_2\hat{e}_2 - \nu_1\hat{e}_3 \\
\mathbf{v}_0^{(3)} &= -\mathbf{v}_0^{(7)} = \nu_1\hat{e}_1 - \nu_2\hat{e}_2 + \nu_1\hat{e}_3 \\
\mathbf{v}_0^{(4)} &= -\mathbf{v}_0^{(8)} = \nu_1\hat{e}_1 - \nu_2\hat{e}_2 - \nu_1\hat{e}_3
\end{aligned} \tag{4}$$

where:

$$\nu_1 = \frac{1}{\sqrt{2}}\sin\theta_0, \qquad \nu_2 = \cos\theta_0 \tag{5}$$

and $\hat{e}_1$, $\hat{e}_2$, and $\hat{e}_3$ are unit vectors in the directions of the coordinate axes. The long, continuous nature of the fibers permits the assumption of affine deformation, giving the fiber stretch $\lambda_f^{(i)}$ of the i-th fiber to be:

$$\lambda_f^{(i)} = \sqrt{\mathbf{v}_0^{(i)} \cdot \mathbf{C}\mathbf{v}_0^{(i)}} = \sqrt{\mathbf{I}_4^{(i)}} \tag{6}$$

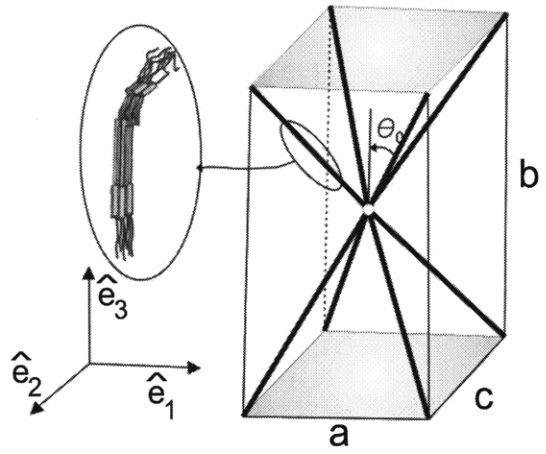

Figure 53: Protein filament bundles are arranged as the eight legs of an eight-chain orthotropic unit cell. The dimensions of the cell are a, b, and c. The unit vectors $\hat{e}_1$, $\hat{e}_2$, and $\hat{e}_3$ are shown.

where $\mathbf{I}_4$ is a measure of the fiber stretch, and is invariant.

3.1.1 Fiber Force-Stretch Behavior

In order to determine the stress-strain behavior of the material, it is necessary to determine the force-stretch behavior of an individual fiber bundle. To do this, a fiber bundle is idealized as two long stiff rods (L_1 and L_2) joined by a bend (α), and flanked by two folded domains (see Figure 54). The stretch on a bundle is then given by $\lambda_f = \frac{r}{r_0}$, where r is the end-to-end distance of the bundle at any point in time, and r_0 is the end-to-end distance in the un-stretched configuration. The fiber stretching can then be multiplicatively decomposed, following a Kroner-Lee decomposition [15] [16], into a stretch from the unbending of the bundle and a stretch from the stretching of the bundle (note that the unfolding of the folded flank domains is here lumped in with the stretching contribution to the overall fiber stretch):

$$\lambda_f = \lambda_f^s \lambda_f^u \tag{7}$$

where λ_f^u is the stretch accommodated by unbending, and λ_f^s is the stretch accommodated by unfolding and stretching. This stretch decomposition is calculated using fiber force equi-

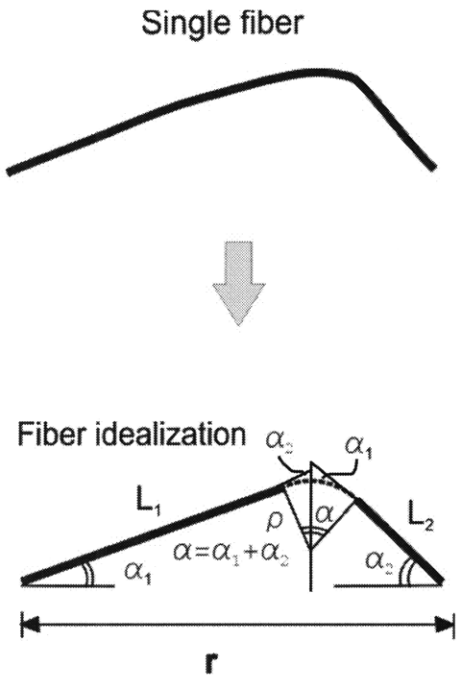

Figure 54: Fiber bend idealization. Legs L_1 and L_2 are idealized as stiff rods joined by a bend angle α.

librium (namely that $F_f^s = F_f^u$) and the relations between these forces and the individual stretches (λ_f^s and λ_f^u).

Fiber Force and Strain Energy Due to Unbending: The strain energy in a bent rod as it unbends is given by:

$$w_f^u = \frac{1}{2} EI \left(\Delta\kappa\right)^2 \rho_0 \alpha_0 \tag{8}$$

where the change in curvature $\Delta\kappa$ is:

$$\Delta\kappa = \left(\frac{1}{\rho} - \frac{1}{\rho_0}\right) = \frac{\alpha - \alpha_0}{\rho_0 \alpha_0} \tag{9}$$

where the length of the bend is approximated to be constant, $\rho\alpha = \rho_0\alpha_0$. Thus, in order to determine the strain energy in the fiber as a function of the portion of stretch accommodated by unbending, it is necessary to determine the bend angle (α) as a function of the unbending stretch $\left(\lambda_f^u\right)$. First, assume that the contour length of the kink is fixed (this assumption is

valid since the stretching in the kink is negligible relative to the stretching in the straight rods L_1 and L_2). Thus:

$$\rho\alpha = \rho_0\alpha_0 \tag{10}$$

Next, note from compatibility (and referring to Figure 54):

$$L_1 \sin\alpha_1 = L_2 \sin\alpha_2 \tag{11}$$

and the stretch from unbending is related to the lengths of the stiff rods (L_1 and L_2) and their angles (α_1 and α_2) as:

$$\lambda_f^u = \frac{L_1\cos\alpha_1 + L_2\cos\alpha_2}{r_0} \tag{12}$$

where $r_0 = L_1\cos\alpha_0 + L_2\cos\alpha_0$. Thus, α_1 and α_2 are related to λ_f^u as follows:

$$\begin{aligned}
\alpha_1 &= \arcsin\left[\frac{\sqrt{4L_2^2\left(\lambda_f^u\right)^2 r_0^2 - \left(\left(\lambda_f^u\right)^2 r_0^2 + L_2^2 - L_1^2\right)^2}}{2\lambda_f^u r_0 L_1}\right] \\
\alpha_2 &= \arccos\left[\frac{\left(\lambda_f^u\right)^2 r_0^2 + L_2^2 - L_1^2}{2\lambda_f^u r_0 L_2}\right]
\end{aligned} \tag{13}$$

Thus, since the overall angle (α) is given by $\alpha = \alpha_1 + \alpha_2$, the force in the fiber due to unbending is given by:

$$f_f^u = \frac{2EI}{\alpha_0\rho_0}\frac{\lambda_f^u r_0\left(\alpha - \alpha_0\right)}{\sqrt{4L_2^2\left(\lambda_f^u\right)^2 r_0^2 - \left[\left(\lambda_f^u\right)^2 r_0^2 + L_2^2 - L_1^2\right]^2}} \tag{14}$$

Fiber Force and Strain Energy Due to Stretching/Unfolding: The strain energy in a rod as it stretches is given by:

$$w_f^s = \frac{EA}{2L_u} L_0^2 \left(\lambda_f^s - \frac{L_u}{L_0} \right)^2 \tag{15}$$

where L_u is the tension-free length of the fiber and L_0 is the rod's original contour length. Thus, the force on the fiber due to stretching is given by:

$$f_f^s = \frac{EA}{L_u} L_0 \left(\lambda_f^s - \frac{L_u}{L_0} \right) \tag{16}$$

The fiber unfolding is captured by allowing the tension-free length of the fiber to evolve, with the rate of evolution increasing with the force on the filament. In order to also capture the rate-dependence of the unfolding, an Eyring-type model is used [9]:

$$\dot{L}_u = \alpha_u \left(L_{max} - L_u \right) \exp \left[\frac{f_f^s x_u}{K_B \Theta} \right] \tag{17}$$

where L_{max} is the maximum contour length of the filament, α_u is related to an activation frequency, $\dot{\alpha}$, and an activation energy $\dot{\alpha} \exp\left(\frac{\Delta G}{K_B \Theta}\right)$ and x_u is the activation length, K_B is the Boltzmann constant, and Θ is absolute temperature. Thus, at any time during the loading, the tension free length can be determined by the current rate of evolution $\dot{L}_u$, and the amount of time that has elapsed since loading began Δt:

$$L_u = \dot{L}_u \Delta t + L_{u0} \tag{18}$$

3.1.2 Material Stress-Strain Behavior

Stress-Strain Behavior of the Fiber Network With the force-stretch behavior of the protein fibers known, the overall stress-strain behavior of the fiber network can be calculated.

Since a single protein fiber bundle sits as each leg of the eight-chain orthotropic unit cell, the strain energy of the cell is given by the sum of the strain energies of each of the constituent bundles, where many fibers, say N, are in each bundle:

$$W_{cell} = 2N \sum_{i=1}^{4} w\left(\lambda_f^{(i)}\right) \tag{19}$$

Similarly, the strain energy density is given by the strain energy of all of these fibers divided by the volume they occupy, V,

$$W_{ani} = \frac{W_{cell}}{V} = \frac{\nu}{4} \sum_{i=1}^{4} w\left(\lambda_f^{(i)}\right) \tag{20}$$

where ν is the fiber density, $\frac{N}{V}$.

The First Piola-Kirchoff stress is calculated as:

$$\mathbf{S}_{ani} = 2\mathbf{F}\left(\frac{\nu}{4} \sum_{i=1}^{4} \frac{\partial w_f}{\partial \mathbf{I}_4^{(i)}} \frac{\partial \mathbf{I}_4^{(i)}}{\partial \mathbf{C}}\right) \tag{21}$$

Defining $\mathbf{v}^{(i)}$ to be $\mathbf{F}\mathbf{v}_0^{(i)}$, and with $\frac{\partial \mathbf{I}_4^{(i)}}{\partial \mathbf{C}} = \mathbf{v}_0^{(i)} \otimes \mathbf{v}_0^{(i)}$ and $\frac{\partial w_f}{\partial \lambda_f^{(i)}} = fr_0$ known, S_{ani} is found to be:

$$\mathbf{S}_{ani} = \frac{\nu}{4} \sum_{i=1}^{4} \frac{1}{\lambda_f^{(i)}} \left[\frac{EA}{L_u} r_0^2 \left(\lambda_f^{s(i)} - 1\right)\right] \mathbf{v}^{(i)} \otimes \mathbf{v}_0^{(i)} \tag{22}$$

and therefore the Cauchy stress for the fiber network is:

$$\boldsymbol{\sigma}_{ani} = \frac{\nu}{4J} \sum_{i=1}^{4} \frac{1}{\lambda_f^{(i)}} \left[\frac{EA}{L_u} r_0^2 \left(\lambda_f^{s(i)} - 1\right)\right] \mathbf{v}^{(i)} \otimes \mathbf{v}^{(i)} \tag{23}$$

Stress-Strain Behavior of the Neo-Hookean Matrix As noted above, the jelly matrix that surrounds the protein fibers, is modeled as a nearly incompressible Neo-Hookean

material. The strain energy for such a material is given by:

$$W_{iso} = \frac{\mu}{2}(\mathbf{I}_1 - 3) - \mu \log J + \frac{K}{2}(J-1)^2 \tag{24}$$

where μ and K denote the shear and bulk modulus respectively. The Cauchy stress for such a material is given by:

$$\boldsymbol{\sigma}_{iso} = \frac{\mu}{J}(\mathbf{B} - \mathbf{I}) + K(J-1)\mathbf{I} \tag{25}$$

Overall Material Stress-Strain Behavior Because the model elements lie in parallel (see Figure 52), the stresses in the two components sum to give the overall stress in the material.

$$\boldsymbol{\sigma} = \boldsymbol{\sigma}_{iso} + \boldsymbol{\sigma}_{ani} \tag{26}$$

Or, more specifically:

$$\boldsymbol{\sigma} = \frac{\mu}{J}(\mathbf{B} - \mathbf{I}) + K(J-1)\mathbf{I} + \frac{\nu}{4}\sum_{i=1}^{4} \frac{1}{\lambda_f^{(i)}} \left[\frac{EA}{L_u} r_0^2 \left(\lambda_f^{s(i)} - 1\right)\right] \mathbf{v}^{(i)} \otimes \mathbf{v}^{(i)} \tag{27}$$

3.2 Results of the Bertoldi Model

The Bertoldi model is compared to experimental data in Figure 55; the values of the different parameters used are given in Table 8. Although the Bertoldi model captures the 'yield' in the material, as well as the material rate dependence, it fails to capture the material behavior at high strains (strains above approximately 0.5). The model also fails to capture the non-linearity in unloading and hence also fails to capture the large hysteresis. A comparison of the Bertoldi model's results to experimental results is shown in Figure 55.

The reason that this model overestimates the stiffness of the material at high strains (and fails to accurately capture the hysteresis) is because the length evolution equation does not accurately capture the protein unfolding event. Because of the exponential dependence on

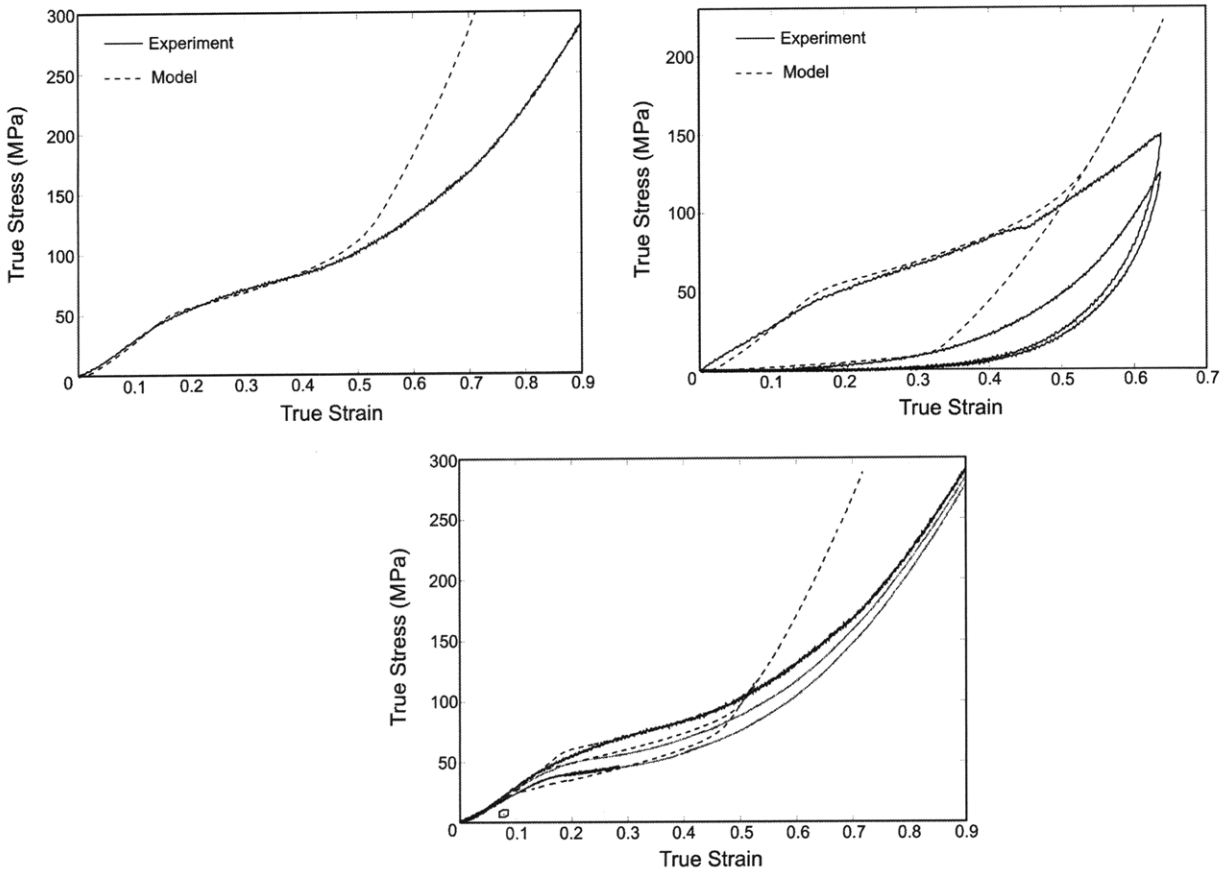

Figure 55: Comparison of the Bertoldi model to experimental data from distal byssal threads. The model captures the initial stiffness, yield, and rate dependence, but overestimates the stiffness at high strain. The model also fails to capture the material's hysteresis at high strain.

force, the rate of unfolding increases very rapidly at a certain force (in this case a force of approximately 1.2 mN), then decreases slowly as the contour length increases. For contour length values approaching the L_{max}, the rate of unfolding decreases rapidly to zero, and the contour length remains fixed at the L_{max} value. The evolution of the rate of unfolding as well as the evolution of the contour length and force are shown in Figure 56.

When this final state is reached ($L_u = L_{max}$), the f_f^u term becomes essentially 'infinitely stiff', and λ_f^u remains constant. This requires that all further stretching be accommodated by λ_f^s, and the fiber acts as a straight chain, with a stiffness given by EA (the relative values of λ_f^s and λ_f^u are shown in Figure 57). As can be seen, this is also true after the initial bend angle has been 'unbent' and prior to unfolding. For this reason, the stress-strain behavior

$\mu\,[MPa]$	3.5	$K\,[MPa]$	173.8	θ_0	25°
$E\,[GPa]$	45	$L_{10}\,[nm]$	200	$L_{20}\,[nm]$	100
$H_0\,[nm]$	22	$d\,[nm]$	9	$L_{max}\,[nm]$	380
$\alpha_u\,[s^{-1}]$	$7.5 \cdot 10^{-9}$	$x_u[nm]$	$1.9 \cdot 10^{-4}$		

Table 8: Parameters used in the Bertoldi model to achieve the fit corresponding to Figure 55. μ is the shear modulus of the matrix, K is the bulk modulus of the matrix, θ_0 is the initial fiber orientation, E is the fibers' Young's Modulus, L_{10} is the initial length of the longer leg of the protein filament, L_{20} is the initial length of the shorter leg of the protein filament, H_0 is the initial fiber center-to-center distance, d is the fiber diameter, L_{max} is the maximum contour length, α_u is the activation energy, and x_u is the activation length.

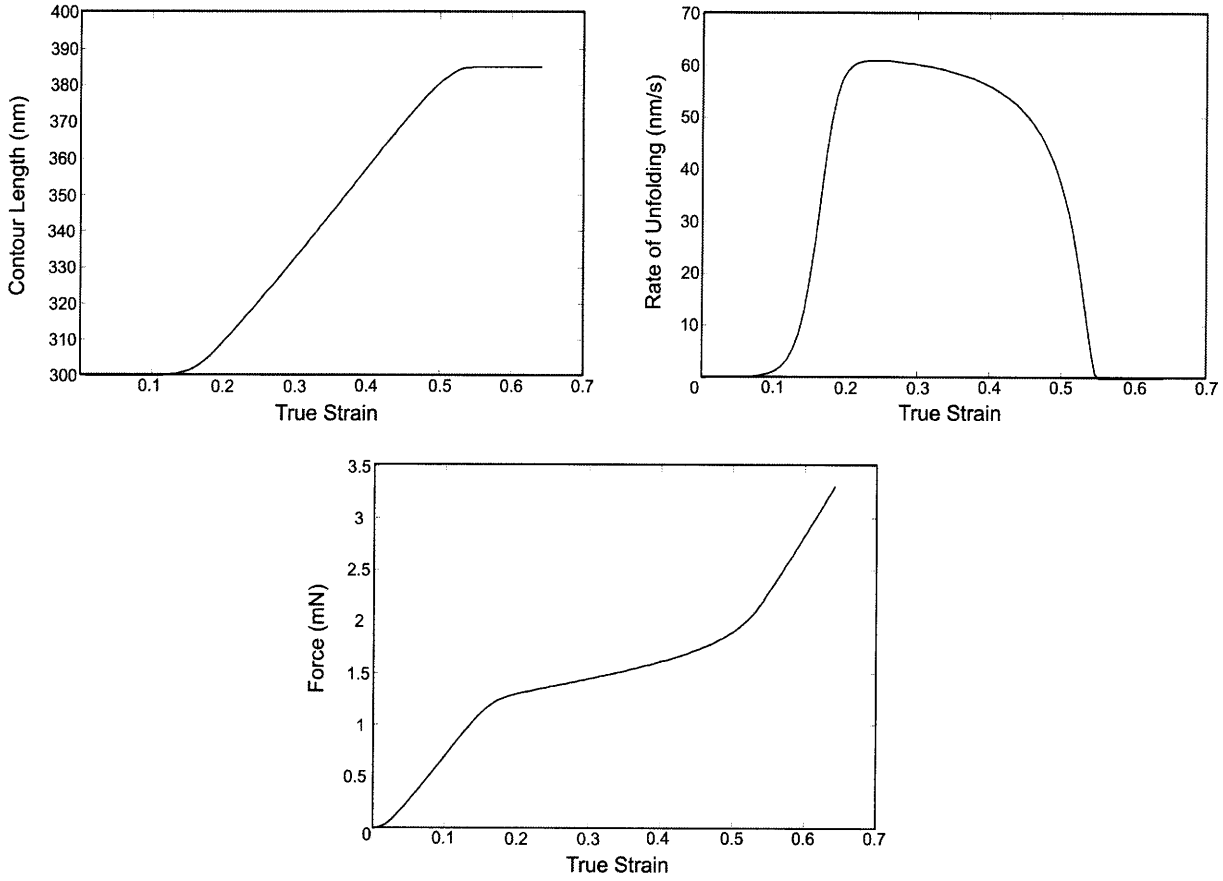

Figure 56: Force and length evolution of the protein fibers predicted by the Bertoldi model. The contour length remains constant up to a strain of approximately 1.25, then increases roughly linearly to the maximum value of 385 nm, and remains constant at the maximum value for increasing strain (upper left). The rate increases rapidly at a strain of approximately 1.25, then decreases slightly until a strain of approximately 0.45, then drops suddenly to a value of zero (upper right). The fiber force increases linearly until unfolding begins, this increases the compliance dramatically. As the contour length reaches the maximum value, the force again begins to increase linearly (bottom).

of the material prior to unfolding and after unfolding will be the same, giving the same stiffness in each region. This is not the behavior seen in the experimental results. This is

also why the model cannot predict the hysteresis in the material (the model predicts that for high strains, the unloading curve will follow the loading curve until it returns to the 'unfolding region' - see Figure 55) i.e. since all the stretching in this strain regime is due to λ_f^s the material behaves as a linear elastic material (the f_f^s and EA effects are essentially the behavior of a spring). Further, the model predicts a sharp transition from stiff to compliant behavior in unloading, due to the unbending of the bent protein filaments. During unloading, the filaments first un-stretch. At some force the filaments stop un-stretching and begin to unbend. The unbending requires a small force, which decreases much more slowly than the un-stretching. This gives rise to the sudden increase in compliance.

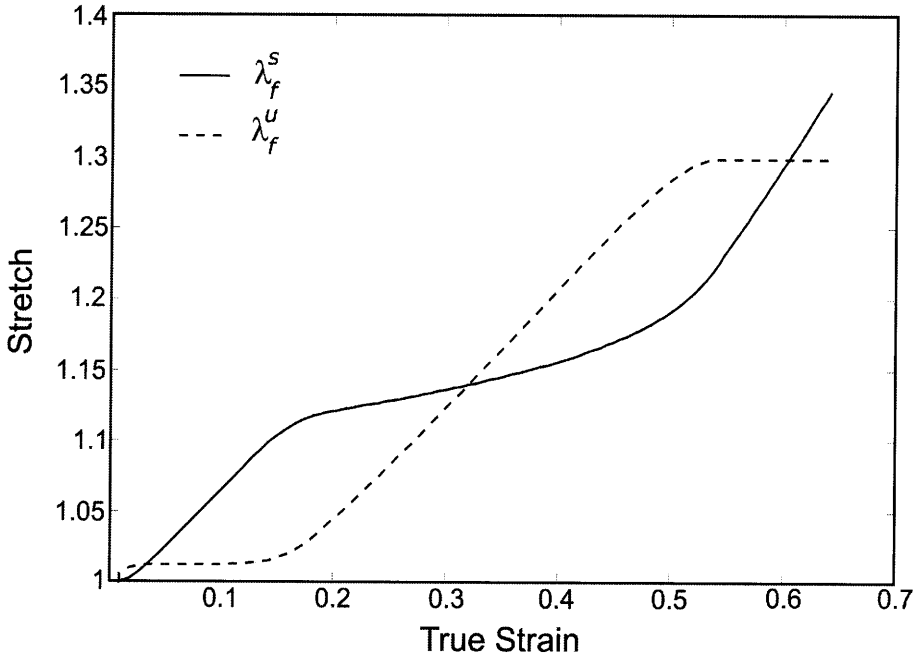

Figure 57: Relative contributions of stretching and unbending to the overall fiber stretch. The solid line shows the stretching/unfolding contribution λ_f^s, while the dotted line shows the unbending contribution λ_f^u.

There are several possible explanations for the disparities between the experimental results and the model's predictions. First, the model assumes that the effective stiffness (the EA) of the protein fibers is uniform down the length of the fiber. However, as noted in the introduction, the chemical composition of the folded fiber ends is different from that of the interior 'bent rod' section, and so it is possible (if not likely) that these two regions will

have different effective stiffnesses. Although a stiffness difference will 'correct' the problem of overestimating the material stiffness at high strains i.e. if the folded domains are modeled as more compliant than the interior region then the model can fit the experimental results in loading, the stiffness difference alone will not capture the material behavior in unloading. A second possible cause of this disparity is the degradation and failure of some protein filaments during loading. Thus, although the majority of the protein filaments remain intact, some fail, effectively decreasing the number density (ν in the model) of protein filaments in the material. This again would give rise to a more compliant response at high strains, but would not capture the hysteresis. The final possibility, and the only that will capture the material's hysteretic behavior is that the protein filaments never attain their maximum contour length, and hence are not being directly axially stretched.

3.3 A Parametric Study of the Fiber Contour Length Evolution Equation

There are several ways to vary the parameters in order to change the rate of increase of contour length. First, the equation can be made non-linear with respect to the $(L_{max} - L_u)$ term:

$$\dot{L}_u = \alpha_u \left(L_{max} - L_u\right)^n \exp\left[\frac{f_f^s x_u}{K_B \Theta}\right] \tag{28}$$

where n can vary over all real numbers. Next, the width of the activation barrier i.e. x_u can vary with fiber contour length. In order to keep the argument of the exp term non-dimensional, the length must be normalized, thus the argument can be multiplied by $\frac{L_u}{L_{max}}$:

$$\dot{L}_u = \alpha_u \left(L_{max} - Lu\right) \exp\left[\frac{f_f^s x_u \left(\frac{L_u}{L_{max}}\right)}{K_B \Theta}\right] \tag{29}$$

where the argument can either be linearly dependent on this term, or non-linearly dependent on this term i.e. $\left(\frac{L_u}{L_{max}}\right)^n$.

Both these methods to alter the rate of increase of contour length were attempted, with little difference in the overall stress-strain behavior of the material. In the first case, the non-linearization served to change the point fiber force at which unloading began, increasing the load required for unfolding for n-values greater than 1, and decreasing the load required for unfolding for n-values between 0 and 1. In the second case, the load required to initiate unfolding was again altered depending on the n-value chosen, while the flatness of the stress-plateau increased (a result of a greater initial jump in $\dot{L}_u$).

The second case (evolving the activation barrier with loading) gives insight into how to achieve the desired shape of the stress-strain curve. In this case, the shape becomes worse, with the angle between stress-flattening and post-yield hardening decreasing. In order to increase this angle, and get a smoother transition, the argument of the exp term needs to decrease with loading (to counteract the force term, which increases with loading). To achieve this, the equation can be multiplied by the difference between the max contour length and the current contour length:

$$\dot{L}_u = \alpha_u \left(L_{max} - L_u\right) \exp\left[\frac{f_f^s x_u}{K_B \Theta}\left(\frac{L_{max} - L_u}{L_{max} - L_{u0}}\right)^n\right] \tag{30}$$

Thus, by varying n the shape of the stress-strain curve can be significantly altered (see Figure 58). Using this form of the contour length evolution equation, the experimental results were fitted (shown in Figure 59). Cyclic loading is also shown with corresponding experimental results (Figure 60).

Thus, the material behavior in loading, as well as the large hysteresis at high strains is captured with this model. However, the model fails to capture the 'smoothness' of the unloading curve, predicting that the unloading will change compliance sharply at low stress,

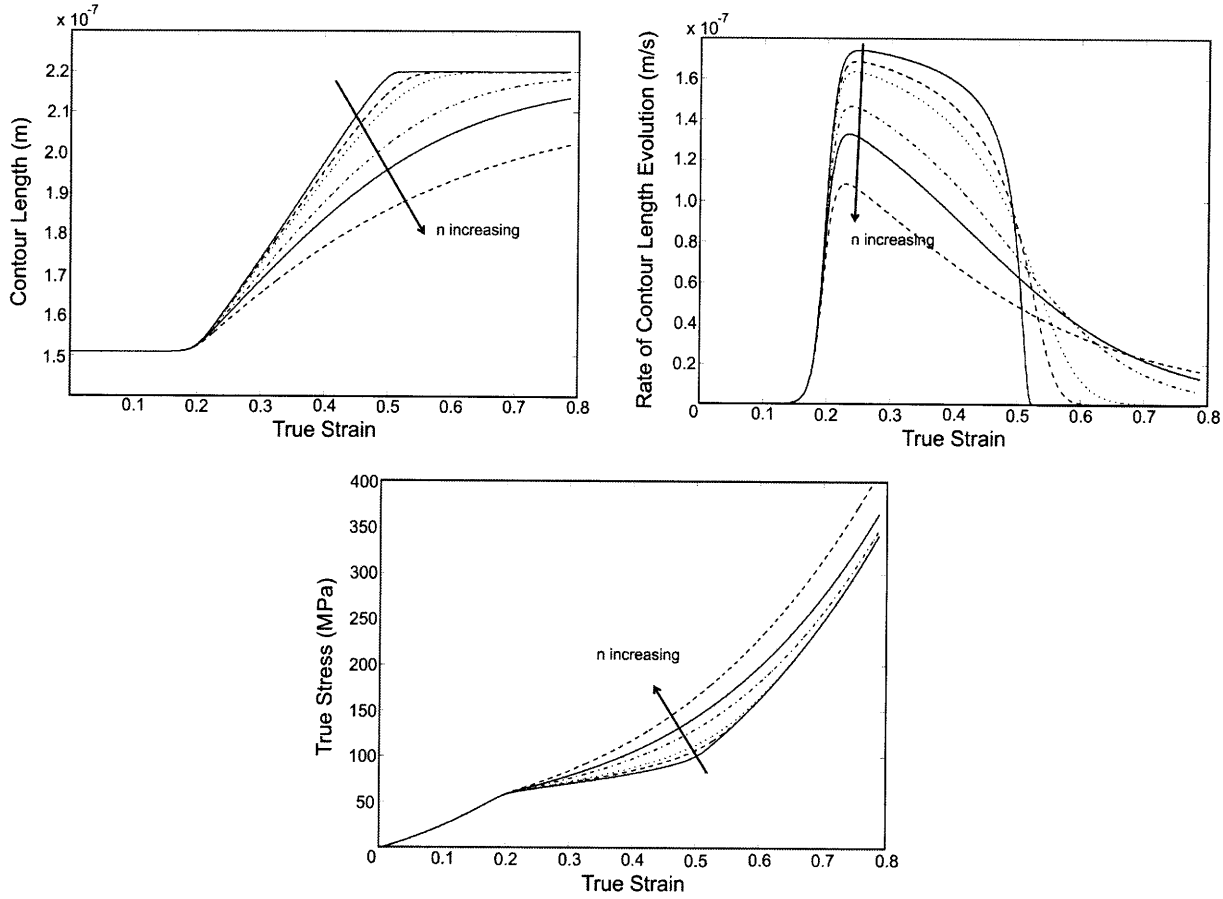

Figure 58: Contour length vs. true strain (upper left), rate of contour length evolution vs. true strain (upper right), and true stress vs. true strain (bottom). Arrows show the directions of n increasing from 0 to 0.9. The actual n values shown are 0, 0.05, 0.1, 0.3, 0.5, and 0.9.

as opposed to the smooth curve shown in Figure 55.

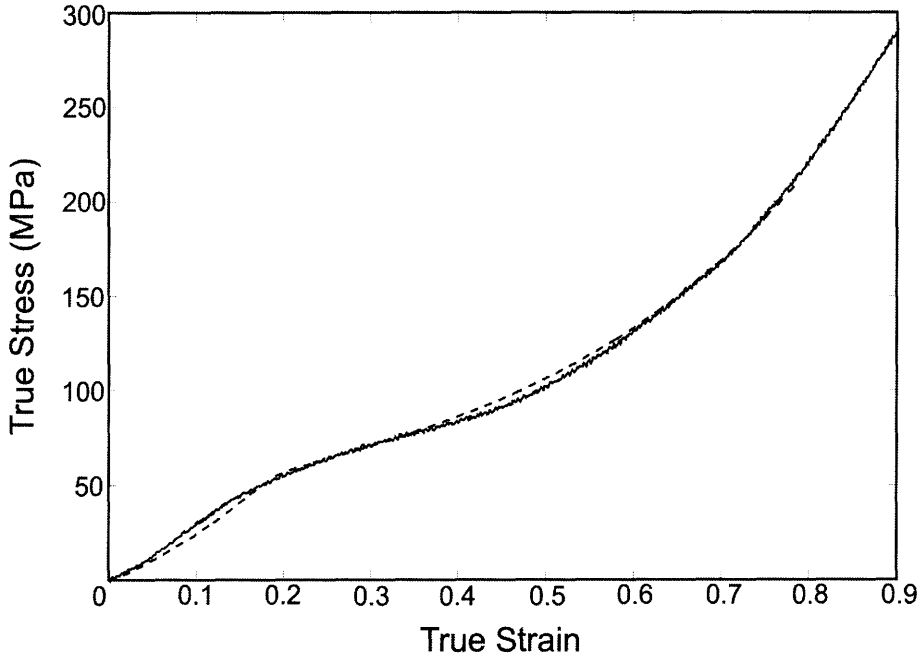

Figure 59: True stress vs. true strain for distal mussel byssal threads at a nominal strain rate of 1/s. Solid line corresponds to experimental data; dashed line corresponds to the model's fit. The value of the n parameter chosen here is 0.5.

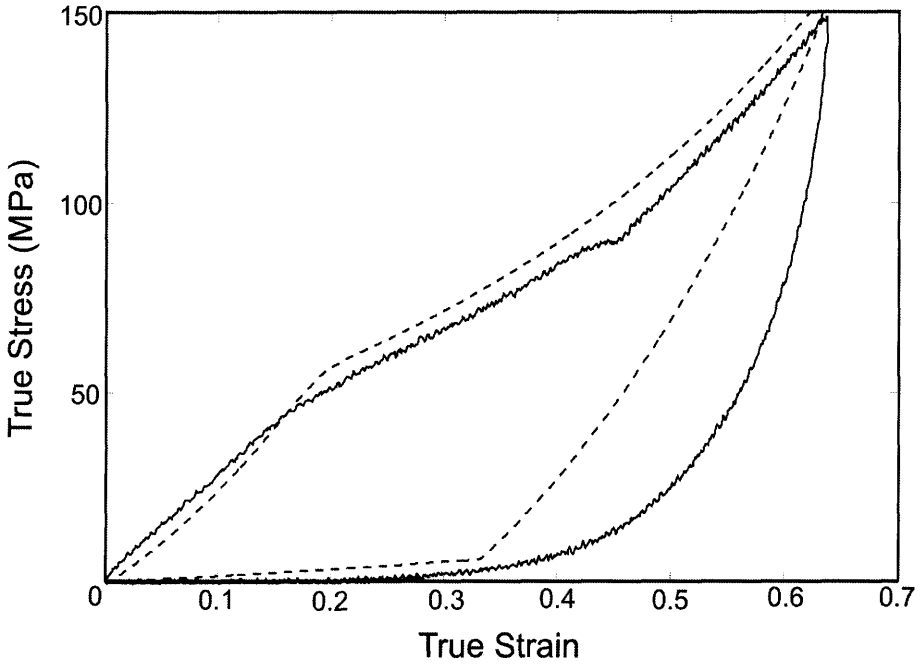

Figure 60: True stress vs. true strain for cyclic loading of distal mussel byssal threads at a nominal strain rate of 1/s. Solid line corresponds to experimental data; dashed line corresponds to the model's fit.

3.4 Modeling the Proteins as Worm-like Chains to Capture the Non-linearity in Unloading

Similar models for the mechanics of protein unfolding have been developed to model the stress-strain behavior of protein networks [23]. However, unlike the Bertoldi model, which is an energetic (enthalpy-based) model, these models are statistical (entropy-based). The two most commonly used models for the force-extension behavior of single molecules are the worm-like chain (WLC) model and the freely-jointed chain (FJC) model; both were implemented into the fiber network model discussed above. These models have each also been augmented with an unfolding model. The two models can be shown to both provide the same benefits (slightly greater hysteresis and increased ability to capture the non-linearity in unloading), but both also have the same problems (non-zero force at zero strain). The WLC will be discussed here to highlight these benefits and problems. The FJC is discussed in Appendix 8.

3.4.1 General Forms of the WLC Model

In general the WLC model is used to model the mechanical behavior of molecular chains where the end-to-end distance of the chain is less than the contour length of the chain. Figure 61 shows a typical molecule that could be modeled with the WLC. In this case the end-to-end distance is given by r and the contour length of the chain (the total length of the chain in its fully straightened configuration) is given by L_c. A third important chain quantity, the persistence length l_p, measures the bending stiffness of the chain.

There are several forms of the WLC force-stretch equation, each of which models a different filament stiffness regime. Figure 62 shows the physical description of each model. For $L_c \gg l_p$ the molecular chain is considered flexible and the force-stretch equation developed

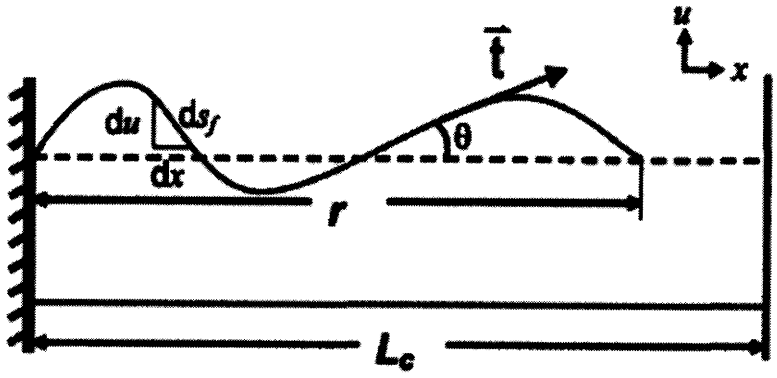

Figure 61: A typical molecule that could be modeled with the WLC model. The molecule end-to-end distance at any point during loading is given by r, while the overall contour length of the molecule is given by L_c. Figure taken from Palmer PhD thesis [22].

by Marko and Siggia is most often used [18]. The form of this equation is:

$$f_f^{WLC} = \frac{K_B\Theta}{l_p}\left[\frac{r}{L_c} + \frac{1}{4\left(1-\frac{r}{L_c}\right)^2} - \frac{1}{4}\right] \tag{31}$$

The end-to-end distance at zero force for the flexible chain is zero, $r_{f=0} = 0$. For $L_c \sim l_p$, the chain is considered semi-flexible and the MacKintosh model is the most common [17]. The form of this equation is:

$$f_f^{WLC} = \frac{K_B\Theta}{l_p}\left(\frac{1}{4\left(1-\frac{r}{L_c}\right)^2}\right)\left(\frac{\frac{L_c}{l_p} - 6\left(1-\frac{r}{L_c}\right)}{\frac{L_c}{l_p} - 2\left(1-\frac{r}{L_c}\right)}\right) \tag{32}$$

The end-to-end distance at zero force for the semi-flexible chain is $r_{f=0} = L_c\left(1-\frac{L_c}{6l_p}\right)$.

3.4.2 The WLC Model as it Applies to Mussel Byssal Threads

In the case of the protein filaments in the mussel byssal threads, the WLC is only applicable to the folded domains at the end of the filament. The central filament region remains stiff

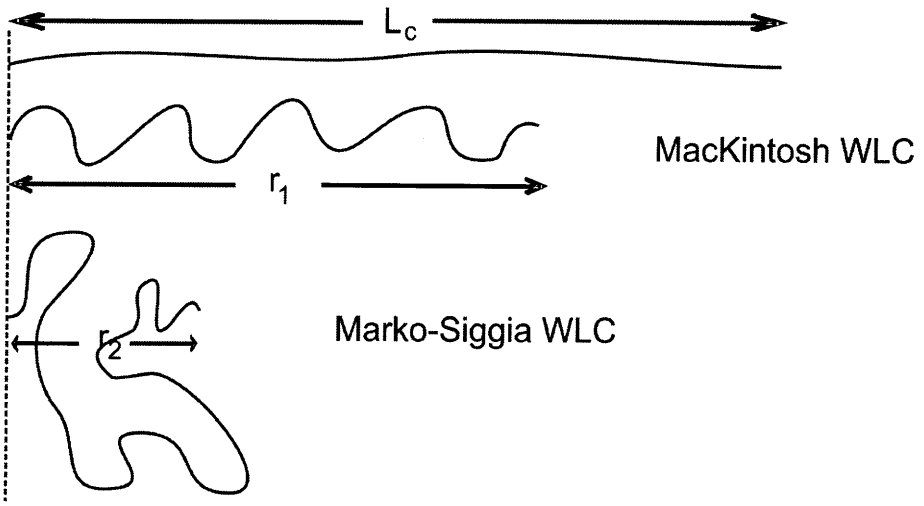

Figure 62: A physical representation of the types of molecules that can be modeled with the MacKintosh WLC model and the Marko-Siggia WLC model.

and is modeled as a straight stretching rod (the same as in the Bertoldi model). Further, the folded domain does not act as a traditional WLC, because as more and more folded domains unfold, it transitions from a semi-flexible to a flexible molecule and, when all domains unfold, the backbone begins to stretch. A model for an extensible semi-flexible WLC was developed by Palmer in his PhD thesis [22], and is more directly applicable to this situation.

In the extensible semi-flexible WLC model, the overall stretch on the molecule is decomposed via a multiplicative decomposition into a stretch from unbending and a stretch from stretching (the same decomposition used for unbending and stretching in the Bertoldi model).

$$\lambda_f = \lambda_f^s \lambda_f^u \tag{33}$$

In this case, the force due to stretching, f_f^s, is given by:

$$f_f^s = \frac{EA}{L_c} r_0 \left(\lambda_f^s - 1\right) \tag{34}$$

and the force due to unbending, f_f^u, is given by the MacKintosh WLC force (Equation 32). Thus, the force-stretch behavior can be determined iteratively.

This model is applied to the folded domains at the ends of the mussel proteins, while the internal section is modeled as a stiff rod (see Figure 63). Thus, the overall length of the fiber (L_f) is broken down into the length of the middle section (L_m) and the length of the end sections (L_e).

$$L_f = L_m + L_e \tag{35}$$

With the length of the fiber as well as the lengths of the middle and end sections known, the stretch in each region can be determined:

$$\lambda_f = \frac{L_f}{L_{f0}} = \frac{(L_m + L_e)}{(L_m + L_e)_0} \tag{36}$$

where the stretch in the middle section is given by $\lambda_m = \frac{L_m}{L_{m0}}$ and the stretch in the ends is given by $\lambda_e = \frac{L_e}{L_{e0}}$. Noting that λ_e is the overall stretch on the WLC section, λ_e can be used in the stretch decomposition equation (Equation 33), and force equilibrium can be used to determine the relative amounts of λ_e that are due to stretching and unbending. The force on the middle section can be determined by:

$$f_m = EA\,(\lambda_m - 1) \tag{37}$$

which (due to fiber equilibrium) is equal to the forces from stretching and unbending in the folded ends.

$$f_m = f_e^s = f_e^u \tag{38}$$

Again, the force-stretch behavior can be determined iteratively.

For this model, the length evolution i.e. unfolding is taken to occur only in the WLC section. Thus, the contour lengths of the end sections evolve instead of the overall fiber length. In this case, varying the activation length, X_u, by $\left(\frac{L_c}{L_{cMax}}\right)^n$ captured the unfolding

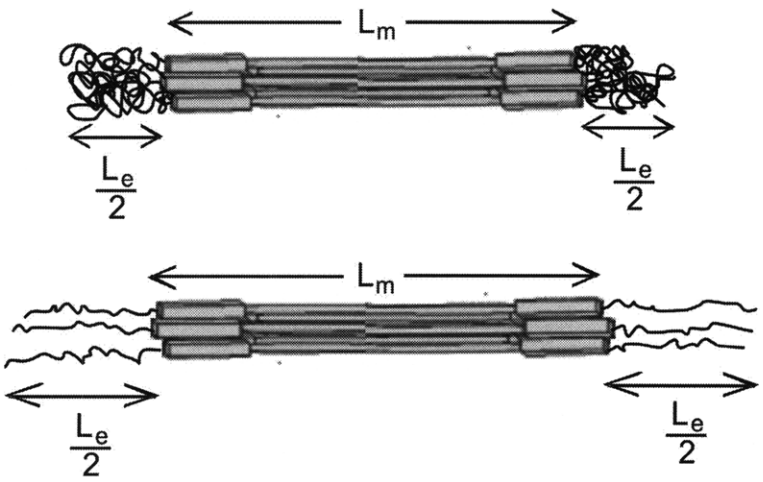

Figure 63: WLC idealization of a protein filament during loading. Initially the end sections L_e are fully folded and the middle section L_m is at rest. As the protein is stretched the end sections unfold and stretch while the middle section stretches.

$\mu\,[MPa]$	5	$K\,[MPa]$	248.3	θ_0	25°
$E\,[GPa]$	40	$L_{e0}\,[nm]$	150	$L_{m0}\,[nm]$	150
$L_{c0}\,[nm]$	151	$d\,[nm]$	9	$L_{cmax}\,[nm]$	280
$\alpha_u\,[s^{-1}]$	$3 \cdot 10^{-8}$	$x_u[nm]$	$1.8 \cdot 10^{-4}$	n	0.2

Table 9: Parameters used in the WLC model to achieve the fit corresponding to Figures 64 and 65. μ is the shear modulus of the matrix, K is the bulk modulus of the matrix, θ_0 is the initial fiber orientation, E is the fibers' Young's Modulus, L_{e0} is the initial length of the folded domain, L_{m0} is the initial length of the central rod-like domain, L_{c0} is the initial contour length, d is the diameter of the fiber, L_{cmax} is the maximum contour length, α_u is the activation energy, x_u is the activation length, and n is the exponential in the contour length evolution equation.

sufficiently.

$$\dot{L}_c = \alpha_u \left(L_{cMax} - L_c\right) \exp\left[\frac{f_e^s X_u \left(\frac{L_c}{L_{cMax}}\right)^n}{K_B \Theta}\right] \tag{39}$$

3.4.3 Results of the WLC Model

The new force relations determined by the WLC model described above were implemented into the overall material model. The stress-strain behavior was fit to the experimental results, and the resulting curves are plotted in Figures 64 (monotonic loading) and 65 (cyclic loading); the values of the parameters used in the fitting are given in Table 9.

As can be seen in Figure 64, the WLC model with the non-linear evolution equation,

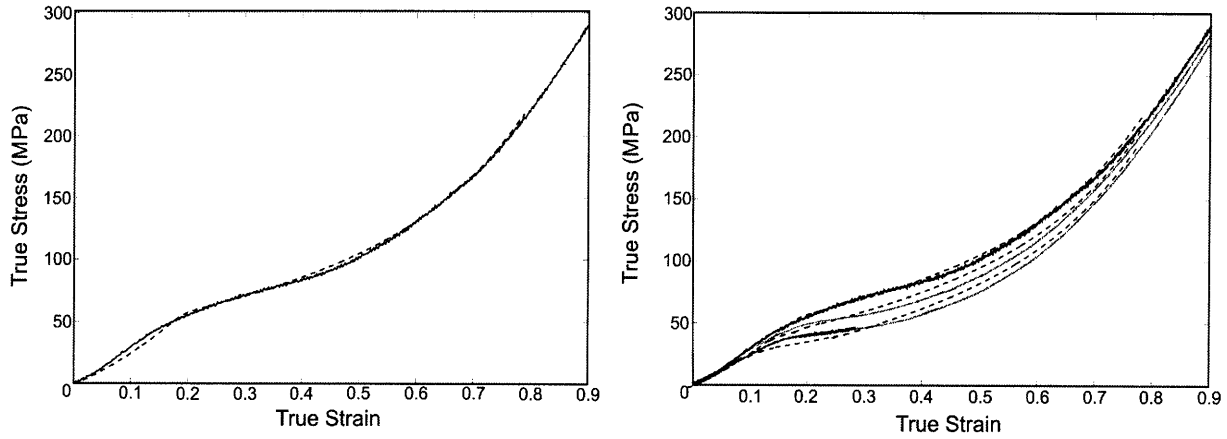

Figure 64: Monotonic loading results for the WLC model. Experimental results are shown with a solid line, while the model's results are shown with a dashed line. On the left, an isolated strain rate, $1s^{-1}$ is shown, while on the right three strain rates, $1s^{-1}$, $0.1s^{-1}$, and $0.01s^{-1}$ are shown.

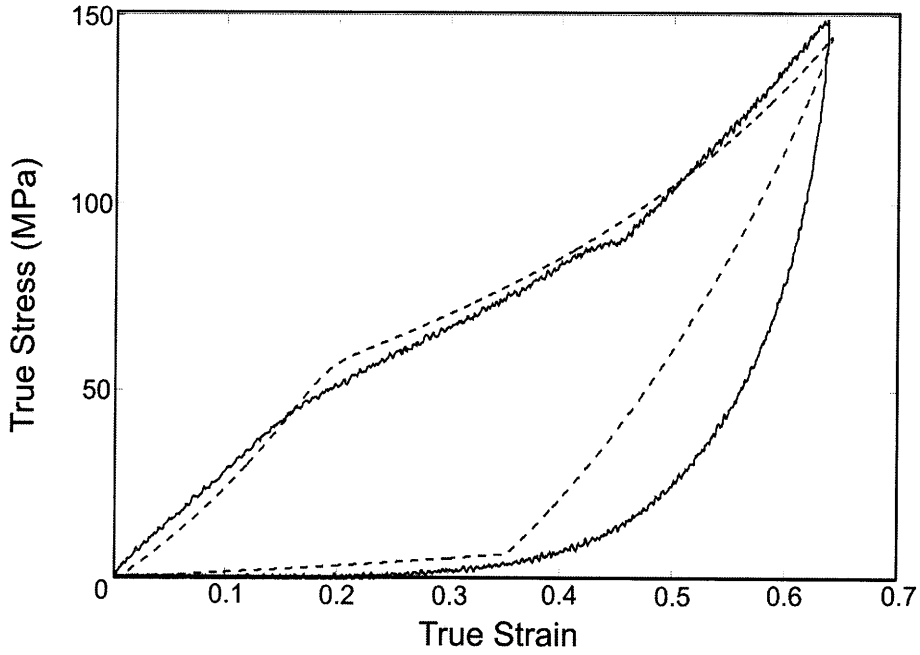

Figure 65: Cyclic loading results for the WLC model. Experimental results are shown with a solid line, while the model's results are shown with a dashed line.

captures the material 'yield', stress-plateau, and post-'yield' hardening quite well. The model also captures the material strain rate dependence well, capturing the different 'yields' when loading at different strain rates. The model also predicts the parallel nature of the stress-strain curves at high strain. The model fails to capture the full 'flatness' of the post-'yield' stress plateau, but in general gives a good fit to the experimental data.

Figure 65 shows the unloading path for the WLC model. As can be seen, the WLC model's prediction of the unloading response is quite similar to the Bertoldi model's prediction. The stiffness of the initial unloading is high (and similar to the stiffness of the Bertoldi model's unloading), and at a small stress (approximately $10MPa$) the compliance drops suddenly, giving a sharp corner to the stress-strain curve.

The sharpness of this corner can be altered by varying the persistence length. For a decreasing persistence length, the 'sharpness' of the unloading curve decreases. Thus, a 'smoothness' comparable to that seen in the experimental results can be achieved (see Figure 66). However, decreasing the persistence length gives rise to a non-zero force in the protein filament for a stretch of 1, which gives rise to a non-zero stress in the fiber network for a strain of zero. This is obvious when looking at the form of the f_f^{WLC} equation i.e. Equation 32. For this equation, there is one specific value of l_p that gives zero force in the chain in the initial configuration i.e. when $r = r_0$. From Equation 32, f_f^{WLC} equals zero only when $l_p = \frac{L_c}{6}\left(1 - \frac{r_0}{L_c}\right)^{-1}$. Thus, for any other value of l_p, in order for the material to be stress-free in the undeformed configuration, there must be an equal (in magnitude) compressive stress in the matrix. This phenomenon i.e. have a pre-stressed protein network in a slightly-compressed gel or matrix, is not uncommon in biological entities.

However, in this case, altering the persistence length, although it provides the desired 'smoothness' of the unloading curve, decreases the hysteresis at high strain. It also highlights a major problem with using the WLC model to model the folded domains in these particular protein filaments, namely that at different stages in loading the protein filaments are in different flexibility regimes. Initially the protein filaments are semi-flexible, with a persistence length on the order of the contour length. This continues throughout much of the loading cycle. However, as more and more domains unfold, the chain transitions to a flexible chain. Hence, during unloading the chain become very 'floppy', i.e. the protein filaments behave as a flexible WLC. Thus, neither the Marko-Siggia nor the MacKintosh model can accurately

capture loading and unloading of these filaments.

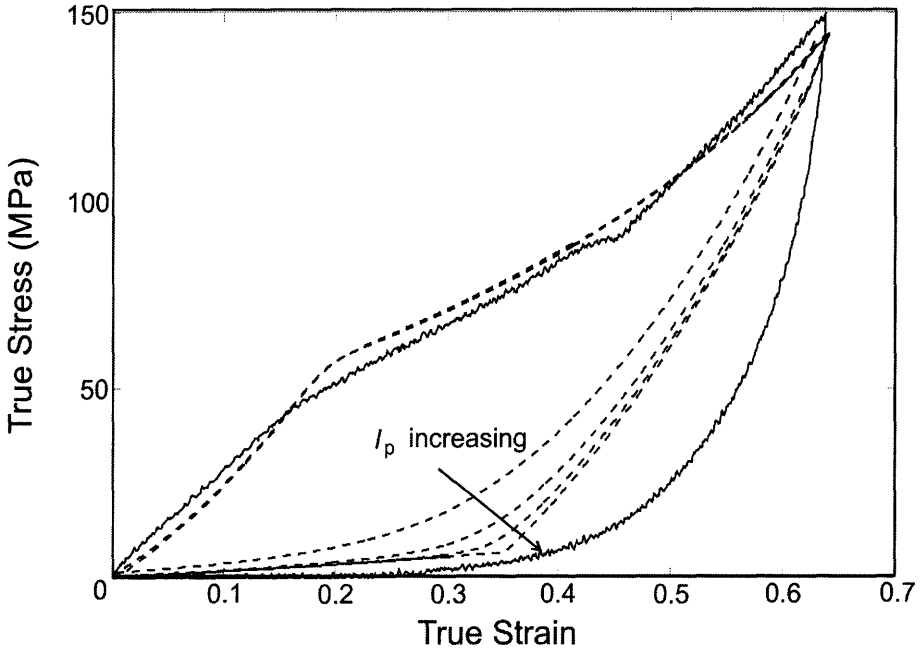

Figure 66: Cyclic loading results for the WLC model. Experimental results are shown with a solid line, while the model's results are shown with a dashed line. The smoothness of the unloading curve is increased by decreasing the persistence length. However, decreasing the persistence length also gives rise to a non-zero stress at a true strain of 0.

3.5 A Phenomenological Model for the Mechanical Behavior of Mussel Byssal Threads

Because of the inability of the Bertoldi model and the commonly used entropic models (FJC and WLC) to capture the unloading of the protein fibers in the mussel byssal threads, a phenomenological model, which is able to capture the loading, unloading, and reloading of the material was developed.

3.5.1 Force-Extension behavior of a single filament

The phenomenological model developed for the stress-strain behavior of mussel byssal threads is similar to the models discussed previously, in that it takes the stretching/unfolding of

protein filaments to be the major constituent of the overall material stress-strain behavior. Again the protein filaments are separated into two regions, the middle domain (straight rod domain) and the end domains (folded domains), as was shown in the protein domain schematic (Figure 63). The overall stretch on the fibers is additively decomposed using Equations 35 and 36, where the force on the internal section is again given by

$$f_m = EA\left(\lambda_m - 1\right) \tag{40}$$

Again, due to force equilibrium, the force in the middle (straight rod) domain equals the force in the end (folded) domains, where the force in the end domains will be taken to follow a nonlinear behavior given by the phenomenological equation:

$$f_e = c_0 \left(1 - \frac{\lambda_e}{\lambda_L}\right)^n \left(\lambda_e - 1\right) \tag{41}$$

where c_1 and n are constants, which take different values in the proximal and distal section, and λ_L is a locking stretch, which evolves with force. Force equilibrium and the fiber stretch decomposition are used to solve for the force on the fiber at a given macroscopic stretch; this is done iteratively via the bisection method.

3.5.2 Evolution of the locking stretch

The locking stretch λ_L is similar to the overall fiber contour length in the Bertoldi model and the WLC/FJC models, in that as the stretch on the folded domains λ_e approaches the locking stretch, the force begins to increase exponentially. The physical unfolding of folded domains within the protein is captured by evolving the locking stretch, using an Eyring-type evolution equation (similar to the contour length evolution equations discussed above). In this case, the locking stretch evolution equation is non-linear with respect to locking stretch.

$$\dot{\lambda}_L = \alpha_u \left(\lambda_{LMax} - \lambda_L\right)^{c_2} \exp\left[\frac{f_e X_u}{K_B \Theta}\left(\frac{\lambda_L}{\lambda_{LMax}}\right)^{c_3}\right] \tag{42}$$

Where λ_{LMax}, c_2, and c_3 are constants which differ in the proximal and distal thread sections. The evolution equation is solved using a forward Euler integration, which gives a discrete value for the locking stretch at any instant in time.

$$\lambda_L = \lambda_{LOld} + \dot{\lambda}_L \Delta t \tag{43}$$

Where λ_{LOld} is the value of locking stretch at the previous time step, and Δt is the time duration of that step. The load-strain, locking stretch-strain, and locking stretch evolution rate-strain behaviors for a single fiber bundle are shown in Figure 67. As can be seen, the load-strain curves are similar to those seen in the Bertoldi model (Figure 56). Further, the locking stretch evolves similarly to the contour length in the Bertoldi model. Figure 68 shows the load-stretch behavior for loading and unloading at two different strain rates (solid lines - $1s^{-1}$, dashed lines - $0.1s^{-1}$) and two different maximum strains.

3.5.3 Preliminary results of the constitutive modeling in the proximal and distal sections

The phenomenological form of the force-stretch equations were implemented in the overall material stress-strain model, using the material properties given in Table 12 (the methods for determining the material properties are highlighted in Appendix 6). The monotonic loading and unloading curves for both the distal thread section and the proximal thread section are shown in Figures 69 and 70 respectively. As can be seen, the model captures the materials' non-linear stress-strain behavior, including the initially stiff loading, the 'yield' in the distal section, and the post'-yield' stress plateau. The model also captures the stress-strain behavior in the proximal section, as well as the rate-dependence in both the proximal

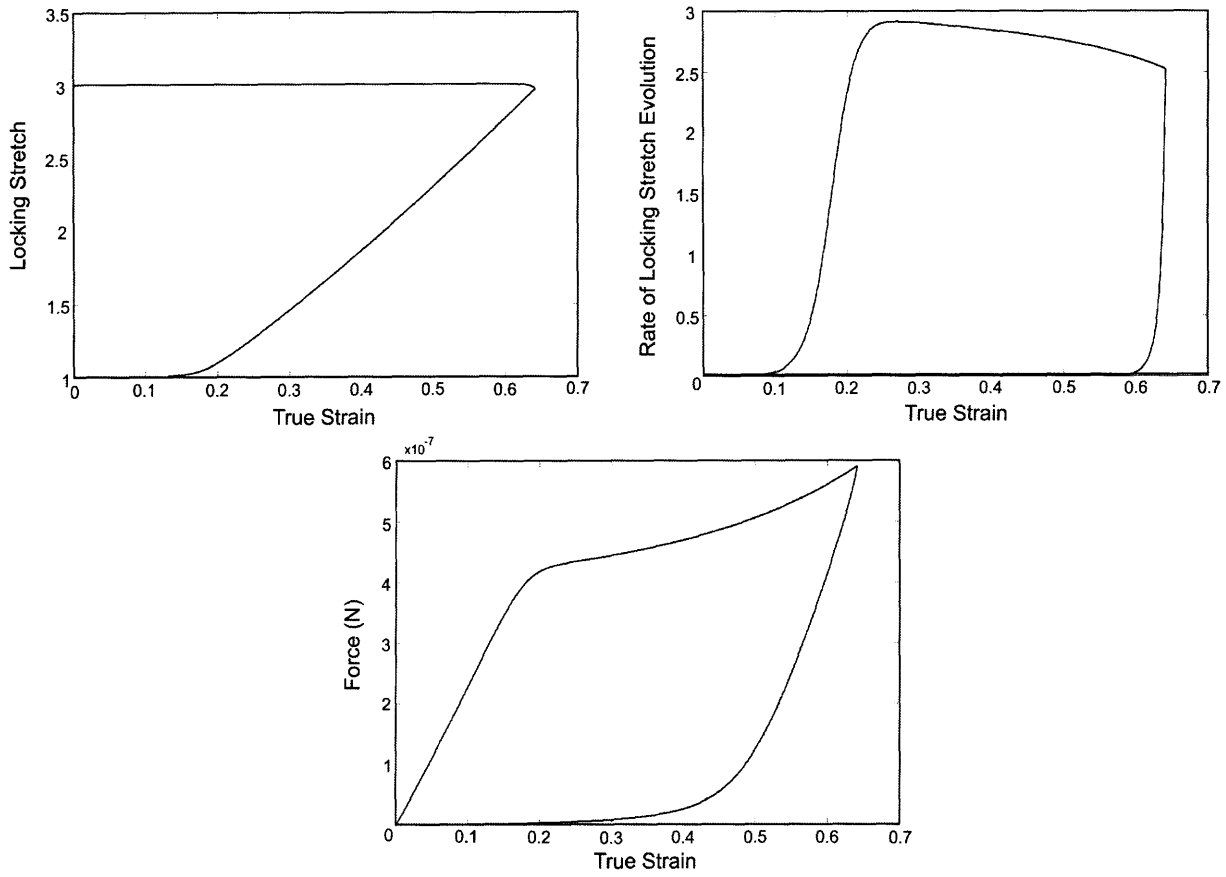

Figure 67: Locking stretch vs. strain (upper left), rate of evolution of locking stretch vs. strain (upper right), and force vs. strain (lower center) for the phenomenological model developed above in load-unload-reload. The rate of evolution of locking stretch is similar to the rate of evolution of contour length in the Bertoldi and WLC models.

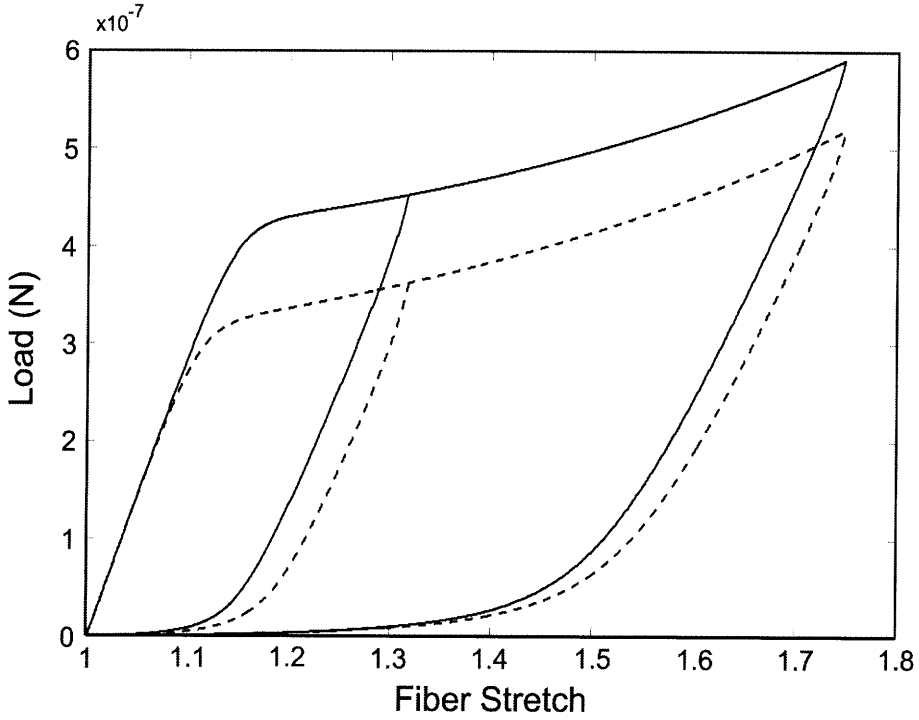

Figure 68: Force-stretch behavior for a single fiber bundle modeled using the phenomenological model developed above. Solid lines correspond to loading at a nominal strain rate of $1s^{-1}$, while dashed lines correspond to loading at a nominal strain rate of $0.1s^{-1}$.

and distal sections. In unloading, the model captures the large hysteresis and the non-linearity of the unloading curve. Unlike the other models, this model predicts a 'smooth' transition in compliance for unloading.

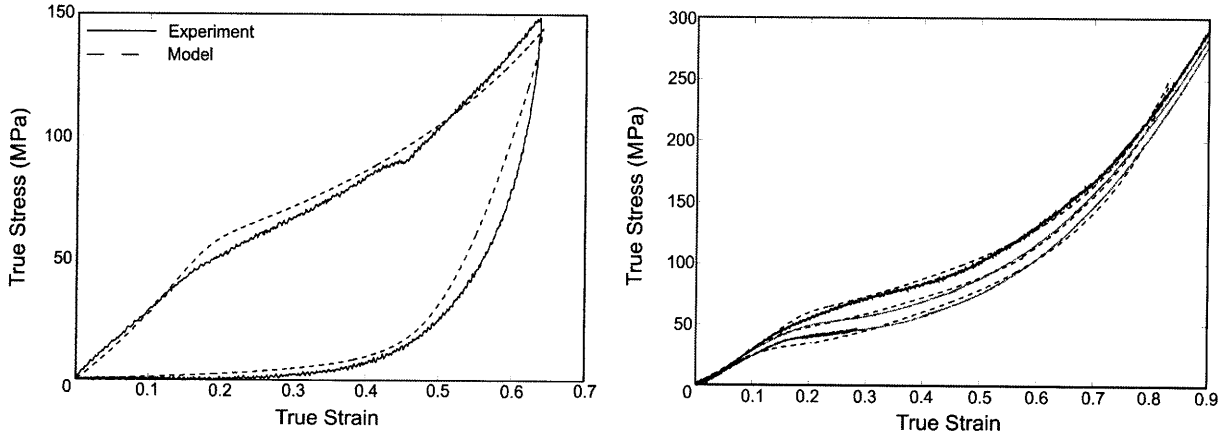

Figure 69: Stress-strain behavior of distal thread section in monotonic loading/unloading (left), and stress-strain behavior of distal thread section in monotonic loading at three nominal strain rates (right). The solid line corresponds to the experimental results; the dashed line corresponds to the model's results.

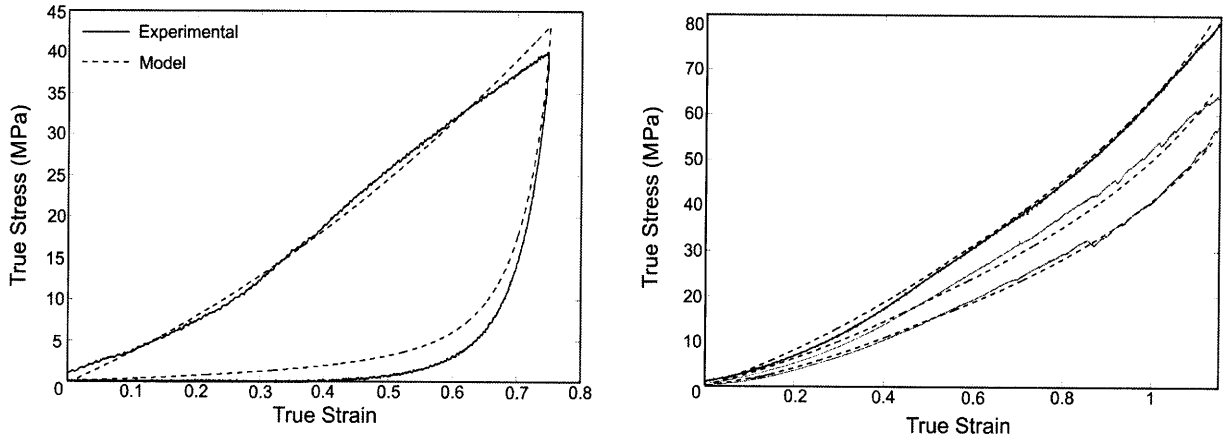

Figure 70: Stress-strain behavior of proximal thread section in monotonic loading/unloading. The solid line corresponds to the experimental results; the dashed line corresponds to the model's results (overall stress - matrix plus fibers); the dotted lines correspond to the model's results (matrix stress only).

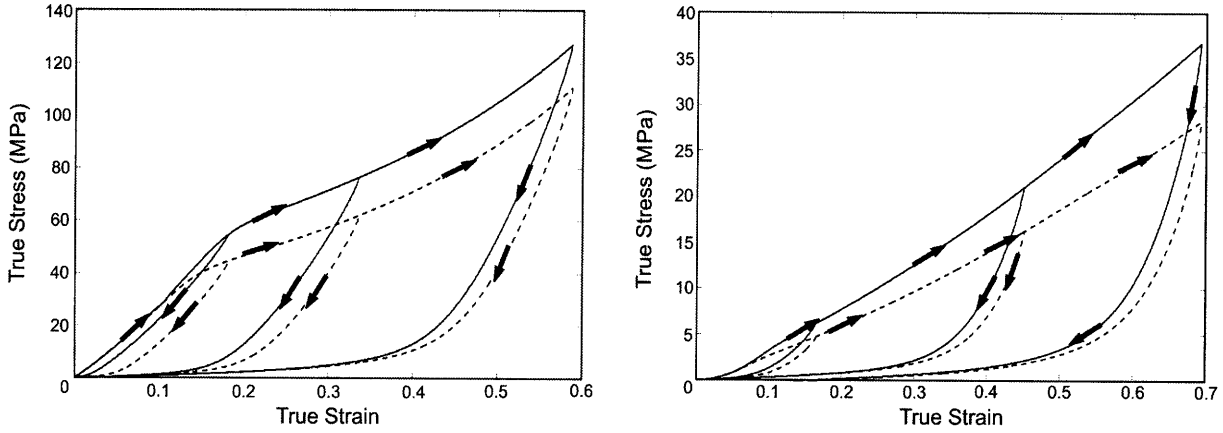

Figure 71: The model predictions of stress-strain behavior for cyclic loading of the distal (left) and proximal (right) thread sections to different maximum strains.

Figures 71 and 72 show the stress-strain behavior and the locking stretch evolution respectively of the proximal and distal thread sections at two different strain rates (solid lines correspond to a nominal strain rate of $1s^{-1}$ and dashed lines correspond to a nominal strain rate of $0.1s^{-1}$) and three different maximum strains. As can be seen, in the distal section, increasing the strain rate increases the stress and strain at yield, and decreases the amount of hysteresis. In the proximal section, increasing the strain rate increases the stress at a given strain throughout loading, and again decreases the amount of hysteresis. Increasing the strain rate also affects the evolution of the locking stretch. In the distal thread section,

increasing the rate of loading causes the locking stretch evolution to occur later (at a higher strain). For all strains beyond the initiation of locking stretch evolution, the rate of increase of locking stretch (the slope of the locking stretch vs. true strain curve) is the same for both strain rates. The delayed evolution of the locking stretch corresponds to the higher 'yield' stress for higher strain rates, while the parallel nature of the locking stretch vs. strain curves corresponds to the parallel nature of the stress-strain curves post-'yield'. In the proximal thread section, increasing the strain rate does not significantly affect the initiation of locking stretch evolution, as the evolution begins at approximately the same strain for both strain rates. However, increasing the rate of loading slightly decreases the locking stretch at a given strain. This corresponds to the higher stress at a given strain in the stress-strain curves.

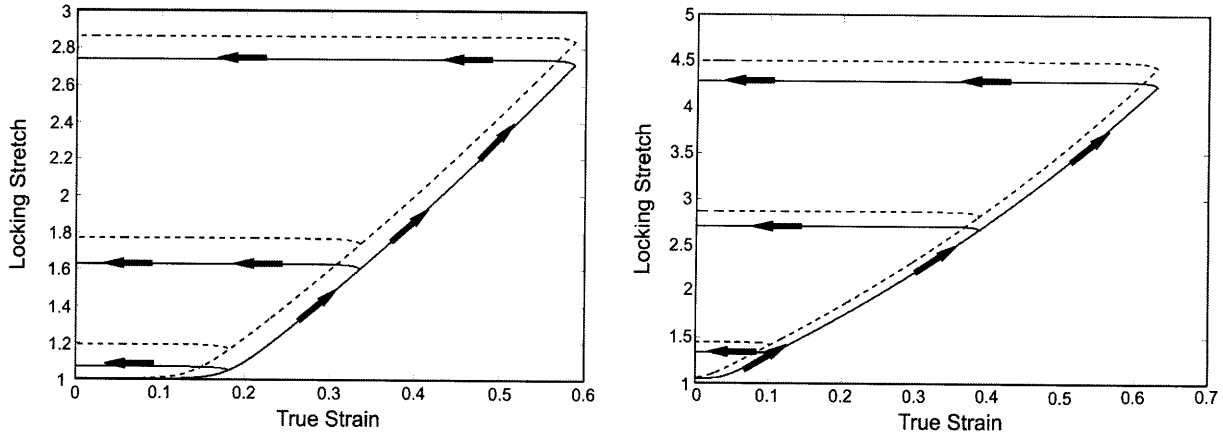

Figure 72: The model predictions of locking stretch evolution as a function of strain for the distal (left) and proximal (right) thread sections to different maximum strains.

Although the model captures many aspects of the material behavior, it fails to capture the residual strain in unloading, as well as the material stiffness in reloading, as is seen in Figures 73 and 74. The residual strain is most likely a visco-elastic effect, while the increased stiffness in reloading is most likely a result of protein refolding i.e. when the force holding the folded domains taut is removed, they tend to refold. These effects were implemented in the model by adding a visco-elastic element to the matrix to capture the residual strain, and by adding a reverse (refolding) process to the locking stretch evolution equation to capture

the increase in stiffness upon reloading. Note that the residual strain may be due to viscous or other slipping mechanisms in the fiber network; this effect was not implemented in the model but could be explored in the future.

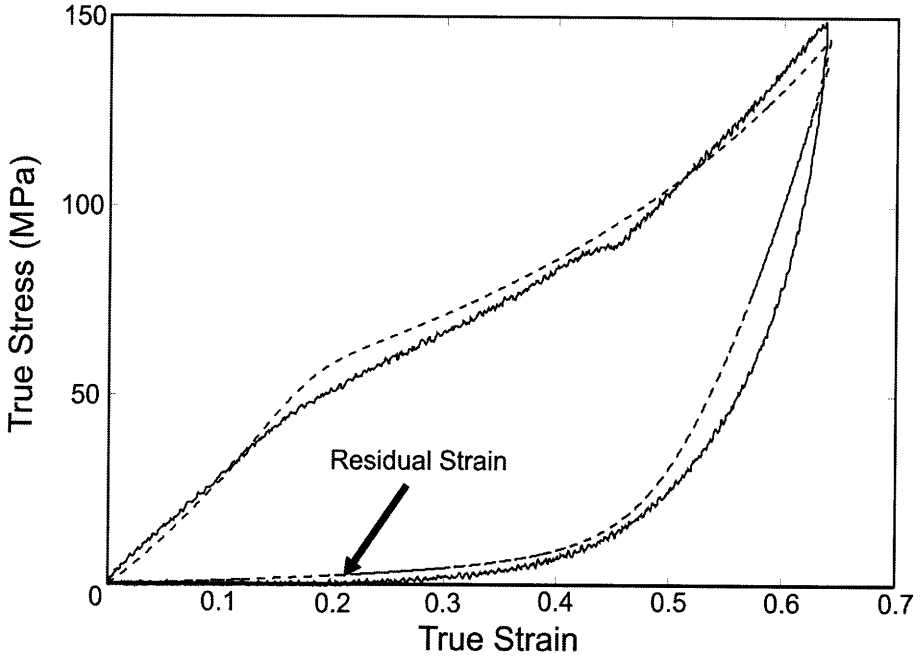

Figure 73: Load-unload-reload for distal thread section. Experimental results are shown with a solid line, while model results are shown with a dashed line. The model fails to predict the residual strain in the material, and the increased stiffness during reloading (the reloading curve for the model follows its own unloading curve exactly).

3.5.4 Adding visco-elasticity to the matrix

In order to capture the residual strain, a viscoelastic element was added in series with the Neo-Hookean matrix (See Figure 75). As can be seen in Figure 75, the overall deformation gradient $\mathbf{F}$ acts equally on the fiber network and the Neo-Hookean matrix

$$\mathbf{F} = \mathbf{F}_{Fibers} = \mathbf{F}_{Neo-Hookean} \tag{44}$$

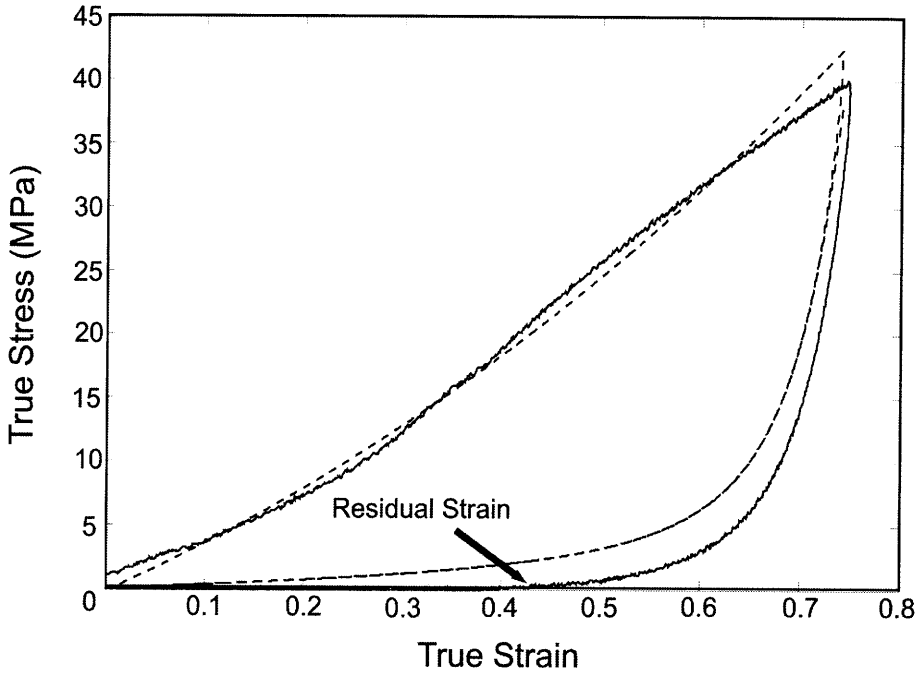

Figure 74: Load-unload-reload for proximal thread section. Experimental results are shown with a solid line, while model results are shown with a dashed line. The model fails to capture the residual strain in the material and the increased stiffness during reloading (the reloading curve for the model follows its own unloading curve exactly).

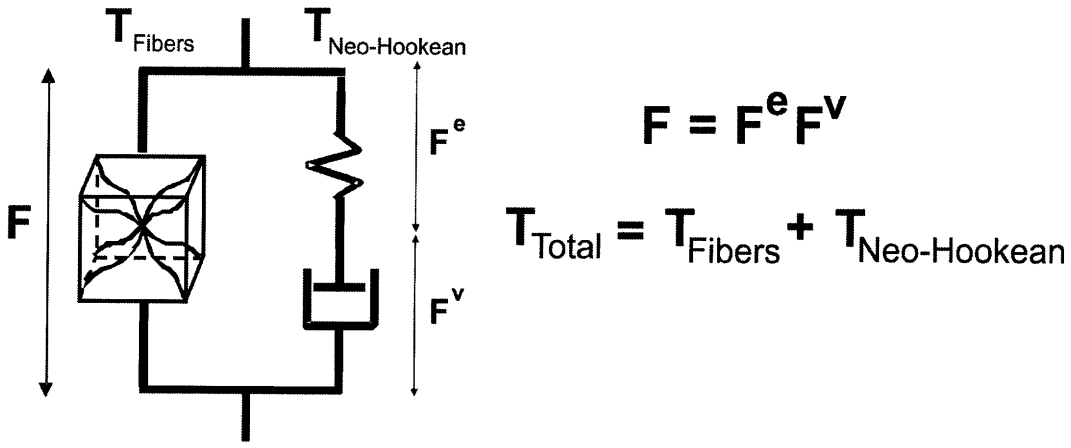

Figure 75: Rheological representation of the material constitutive model with the additional viscoelastic element (dashpot) in the Neo-Hookean matrix. As before the stresses in each leg of the model sum to give the total stress, while the deformation gradient is the same for each leg of the model. In the matrix, the deformation gradient is now multiplicatively decomposed into an elastic and viscous portion.

while the overall stress is the sum of the stresses acting on the network and the matrix.

$$\mathbf{T} = \mathbf{T}_{Neo-Hookean} + \mathbf{T}_{Fibers} \tag{45}$$

In the matrix the deformation gradient is multiplicatively decomposed into elastic and viscous contributions.

$$\mathbf{F}_{Neo-Hookean} = \mathbf{F}^e\mathbf{F}^v \tag{46}$$

The rate kinematics are described by the velocity gradient $\mathbf{L} = \dot{\mathbf{F}}\mathbf{F}^{-1}$, which can also be decomposed into its elastic and viscous contributions

$$\mathbf{L}^e = \dot{\mathbf{F}}^e\mathbf{F}^{e-1} \tag{47}$$

$$\mathbf{L}^v = \dot{\mathbf{F}}^v\mathbf{F}^{v-1} \tag{48}$$

where the overall velocity gradient is the sum of the elastic and viscous velocity gradients.

$$\mathbf{L} = \dot{\mathbf{F}}\mathbf{F}^{-1} + \mathbf{F}^e\dot{\mathbf{F}}^v\mathbf{F}^{v-1}\mathbf{F}^{e-1} = \mathbf{L}^e + \mathbf{F}^e\mathbf{L}^v\mathbf{F}^{e-1} \tag{49}$$

$$\mathbf{L} = \mathbf{L}^e + \tilde{\mathbf{L}}^v \tag{50}$$

where $\tilde{\mathbf{L}}^v = \mathbf{F}^e\mathbf{L}^v\mathbf{F}^{e-1}$.

Thus, the viscous velocity gradient is the sum of the rate of spin tensor and the rate of stretching tensor, with the rate of spin tensor for the viscous component taken to be equal to zero.

$$\tilde{\mathbf{L}}^v = \tilde{\mathbf{D}}^v \tag{51}$$

This leads to an expression for the rate of change of the viscous deformation gradient,

$$\dot{\mathbf{F}}^v = \mathbf{F}^{e-1}\tilde{\mathbf{D}}^v\mathbf{F}^e\mathbf{F}^v \tag{52}$$

and all that remains is to determine the viscous rate of stretching tensor through a constitutive equation.

Because visco-elasticity is a shear-driven phenomenon, the viscous rate of stretching tensor can be determined from the magnitude of the shear stress τ, the driving direction of shear $\mathbf{N}^v$, and an effective viscoelastic shear strain rate $\dot{\gamma}$. The magnitude of the shear stress is calculated using the deviatoric part of the stress.

$$\tau = \sqrt{\frac{1}{2}\mathbf{T}' : \mathbf{T}'} \tag{53}$$

while the driving direction of shear is calculated by normalizing the shear stress by its magnitude.

$$\mathbf{N}^v = \frac{\mathbf{T}'}{\tau} \tag{54}$$

The effective shear strain rate is determined from the viscous deformation mechanism of the material, and can take many forms. For the case of linear viscoelasticity, the shear strain rate is modeled by the following.

$$\dot{\gamma} = \frac{\tau}{\eta} \tag{55}$$

where η, a constant, is the material viscosity. In the case of large deformations many materials demonstrate non-linear viscoelasticity, and several models for the shear strain rate have been proposed. In this case, an Eyring-type viscosity model is used

$$\dot{\gamma} = \dot{\gamma}_0 \left[\exp\left[\frac{-(\Delta G - \tau\Omega)}{K_B\Theta} \right] - \exp\left[\frac{-(\Delta G + \tau\Omega)}{K_B\Theta} \right] \right] \tag{56}$$

where $\dot{\gamma}_0$ is a material constant which captures a reference attempt frequency, ΔG is the activation energy, K_B is the Boltzmann constant, Θ is the absolute temperature, τ is the magnitude of the shear stress, and Ω is the width of the activation barrier. The first term in the exponential can be lumped into the material constant, which gives a reduced form of

the equation

$$\dot{\gamma} = \dot{\gamma}_0 \sinh\left(\frac{\tau\Omega}{K_B\Theta}\right) \tag{57}$$

which, because of the nature of the hyperbolic sin function, captures both the forward and reverse processes. Thus, the viscous rate of stretching tensor can be calculated

$$\tilde{\mathbf{D}}^v = \dot{\gamma}\mathbf{N}^v \tag{58}$$

and the rate of change of the viscous deformation gradient $\dot{\mathbf{F}}^v$ can be determined from Equation 52.

With the rate of change of the viscous deformation gradient known, the viscous and elastic components of the deformation gradient can be determined.

$$\mathbf{F}^v = \mathbf{F}^v_{old} + \dot{\mathbf{F}}^v \Delta t \tag{59}$$

where $\mathbf{F}^v_{old}$ is the viscous deformation gradient in the previous step and Δt is the duration of the step. Computationally, this is solved using a forward Euler integration. The elastic contribution is

$$\mathbf{F}^e = \mathbf{F}\mathbf{F}^{v-1} \tag{60}$$

which is used to solve for the stress in the material.

$$\mathbf{B} = \mathbf{F}^e\mathbf{F}^{eT} \tag{61}$$

$$\boldsymbol{\sigma}_{iso} = \frac{\mu}{J}(\mathbf{B} - \mathbf{I}) + K(J-1)\mathbf{I} \tag{62}$$

With the addition of the viscoelastic element, the model was able to capture the residual strain in both the proximal and distal section (see Figures 76 and 77). In the distal section,

the model predicted the amount of residual strain nicely for all but the lowest strain value. In the proximal section, the model predicted the amount of residual strain in the highest strain regime, while still failing to capture the residual strain in the low and intermediate strain regimes.

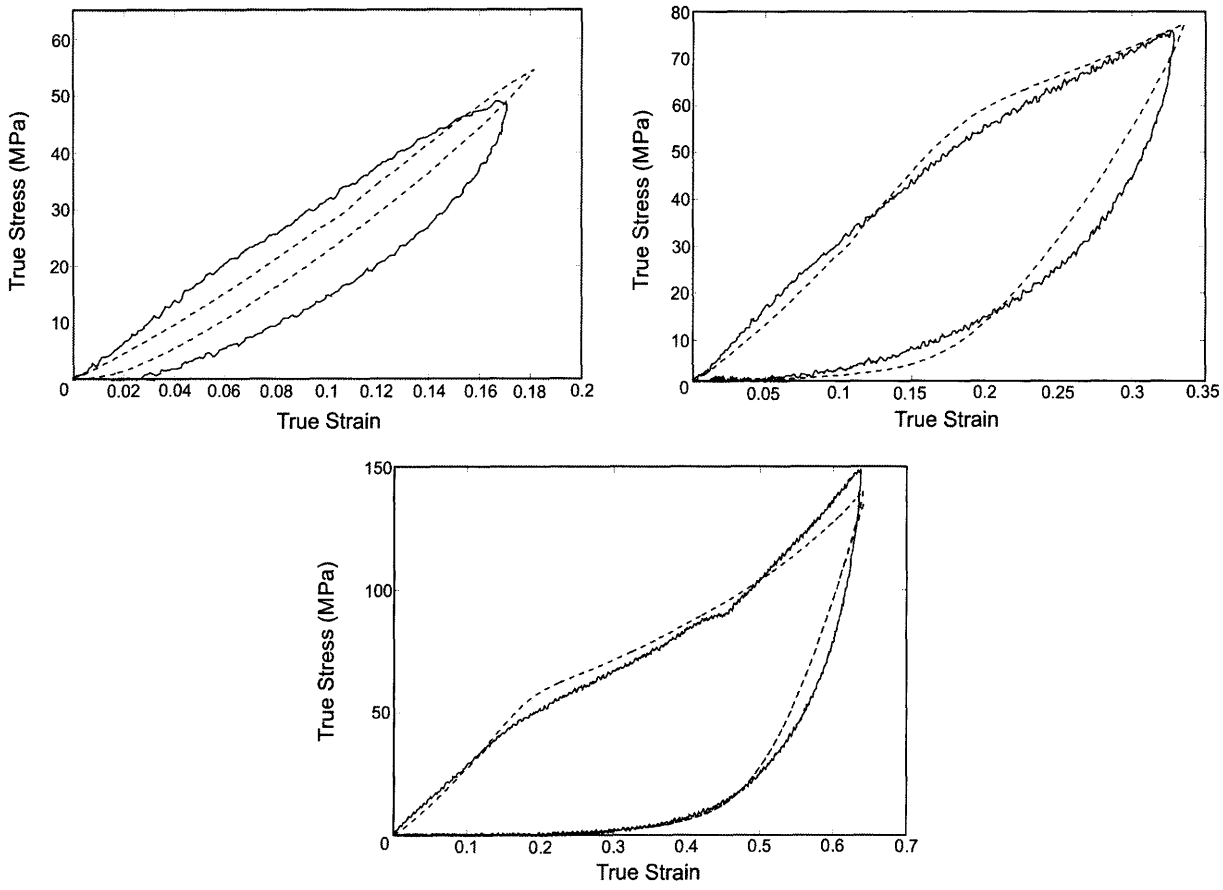

Figure 76: Experimental and model (with viscoelastic matrix) results for load-unload of distal thread section. The model predicts the residual strain for all but the lowest strain case (upper left).

A direct comparison of the model with and without the visco-elastic matrix is shown in Figure 78. As can be seen, the effect of the viscoelasticity increases with strain. In the lowest and intermediate strain case, the effect is unnoticeable. However, for the high strain regime (in both the distal and proximal thread section), adding the viscoelastic element significantly increases the model's ability to capture residual strain.

Figure 79 shows the load-unload-reload-unload response of the material with the vis-

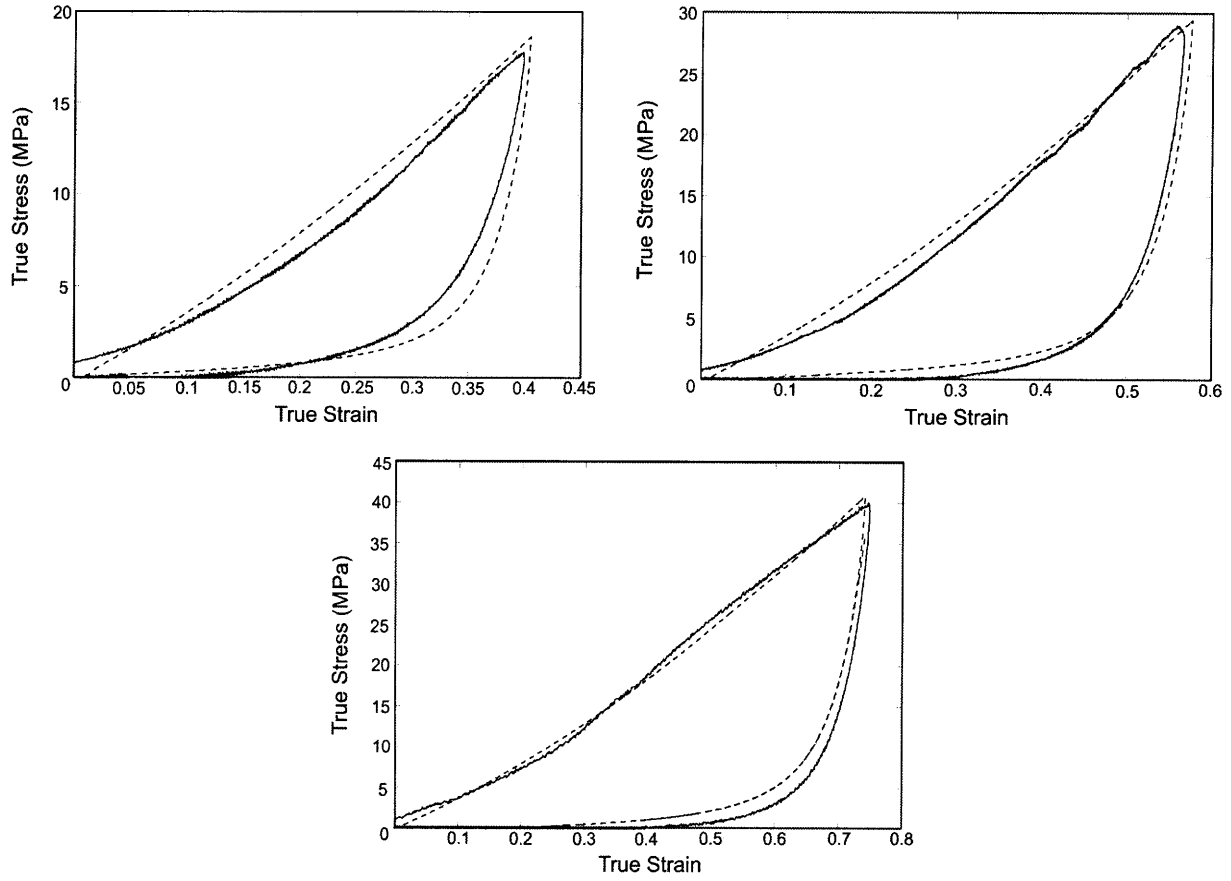

Figure 77: Experimental and model (with viscoelastic matrix) results for load-unload of proximal thread section. The model predicts some residual strain for all strain levels, though the magnitude of the residual strain in the experimental results is greater in all cases.

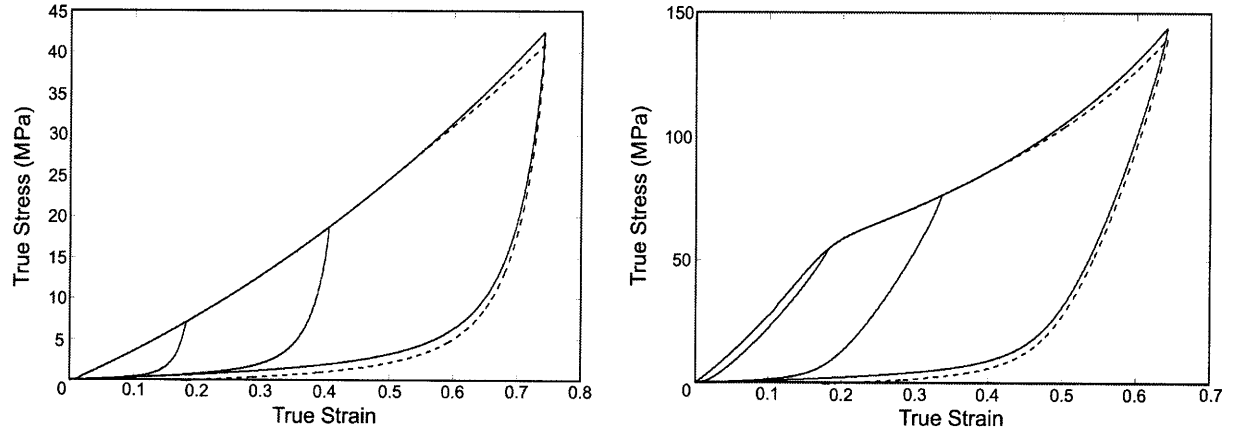

Figure 78: The model's prediction of the stress-strain behavior of the distal (left) and proximal (right) thread sections at a nominal strain rate of $1s^{-1}$. Solid lines show the model with a purely elastic matrix; dashed lines show the model with a visco-elastic matrix.

coelastic element (without the viscoelastic element, the reloading curve follows the unloading curve exactly). As can be seen, the model predicts a slightly more compliant response in reloading for both the distal and the proximal thread sections. The reason that the effect of the viscoelasticity on reloading is not large is because the relative magnitude of the matrix stress to the fiber network stress is small in both sections. A plot of the matrix stress, network stress, and overall stress is shown in Figure 80.

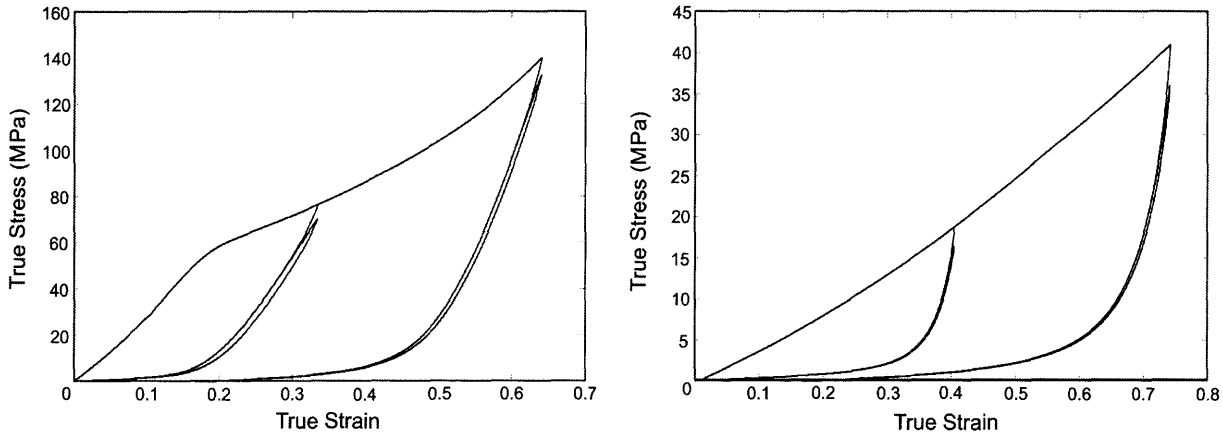

Figure 79: The model's (with the viscoelastic element included) prediction of the load-unload-reload-unload behavior of the distal thread section (left) and the proximal thread section (right).

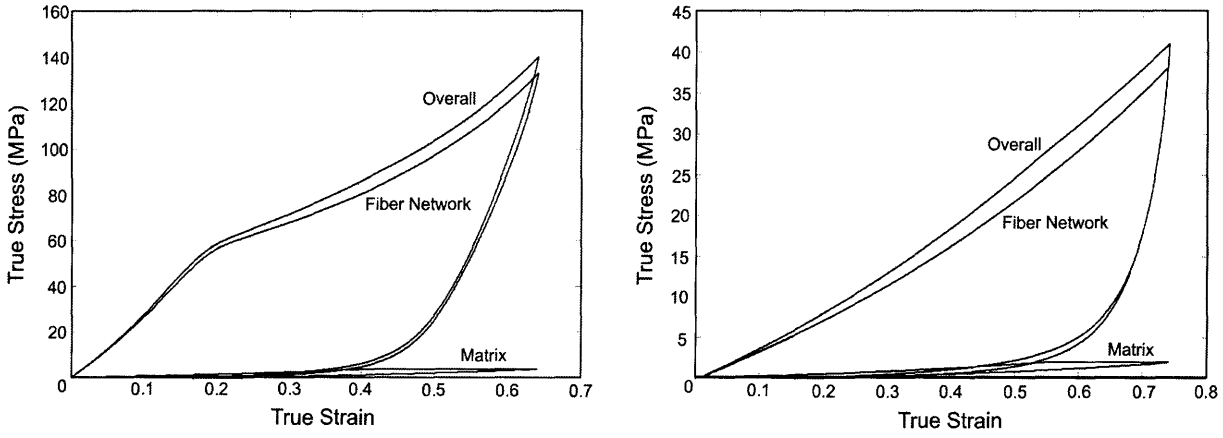

Figure 80: Overall stress, matrix stress, and fiber network stress for the model with viscoelasticity. In both cases the relative amount of matrix stress (compared to fiber network stress) is small.

The magnitude of this matrix stress can be varied by varying the shear modulus of the matrix. The amount of hysteresis can also be varied by changing the width of the activation

barrier, and/or the activation energy for viscoelasticity. Both the shear modulus and the width of the activation barrier were varied for both materials to demonstrate how this affected the residual strain and the overall mechanical behavior. Figure 81 shows these results. As can be seen, the overall stiffness of the material increases with the stiffness of the matrix; similarly, the overall material hysteresis increases with the hysteresis of the matrix. However, significantly altering the matrix properties negatively affects the 'smoothness' of the overall stress-strain curves.

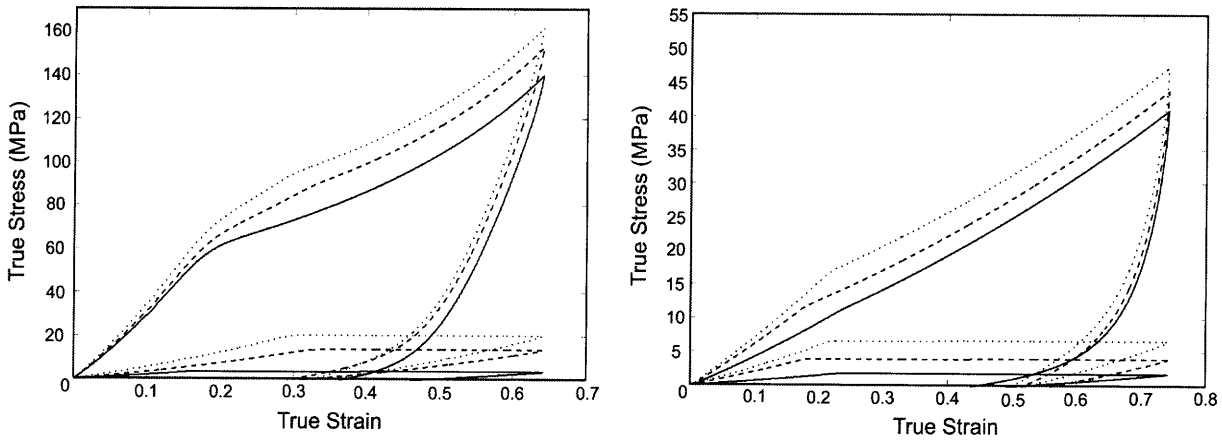

Figure 81: Overall stress and matrix stress for the distal (left) and proximal (right) models. Different curves correspond to different values of shear stress in the matrix and different widths of the activation barrier Ω. In the distal section (left), the solid lines correspond to a shear modulus of $9MPA$ and an activation barrier of $5.5(10^{-20})m$, the dashed lines correspond to a shear modulus of $15MPa$ and an activation barrier of $1.5(10^{-20})m$, and the dotted lines correspond to a shear modulus of $25MPa$ and an activation barrier of $1.0(10^{-20})m$. In the proximal section (right), the solid lines correspond to a shear modulus of $9MPa$ and an activation barrier of $5(10^{-20})m$, the dashed lines correspond to a shear modulus of $12MPa$ and an activation barrier of $3(10^{-20})m$, and the dotted lines correspond to a shear modulus of $15MPa$ and an activation barrier of $2(10^{-20})$. The properties of the fiber network were not varied in these plots.

Thus, although the viscoelastic element significantly increases the model's ability to capture the residual strain, even with the viscoelastic element, the model remained unable to capture the material stiffness in reloading. In order to capture this stiffness recovery, a reverse (refolding) process was added to the locking stretch evolution equation.

Adding a reverse process to the locking stretch evolution In general, a thermally-activated process such as that captured by an Eyring-type model involves a forward and

reverse process. The application of force (stress) then biases the process in the direction of the force i.e. biases the forward process; hence when a force is applied to the protein filaments, the folded domains begin to unfold with the exponential relation giving unfolding at a rate-dependent critical force level. The reverse process, meaning folding or refolding, is highly unlikely when a force is applied close to the critical force levels. However, refolding can occur when the force level is reduced to a low enough level. In the previous sections the reverse process was neglected, because it was assumed that the time scale for refolding would be much greater than the time scale for unfolding. However, when comparing the experimental results to the models' results it becomes apparent that such an assumption is not accurate, and it is likely that upon unloading, some refolding has occurred.

In its simplest form, the equation for the reverse process mirrors the equation for the forward process:

$$\dot{\lambda_L} = \alpha_r \left(\lambda_L - \lambda_{LMin}\right) \exp\left[\frac{-f_e X_r \frac{\lambda_L}{\lambda_{LMax}}}{K_B \Theta}\right] \tag{63}$$

where α_r and X_r are the activation energy and activation length for refolding, and λ_{LMin} is some minimum locking stretch, which evolves with deformation during loading. The minimum locking stretch, λ_{LMin}, must evolve with deformation in order to capture the time-dependent material recovery i.e. for small deformation loading the material recovers completely, and so $\lambda_{LMin} = \lambda_{L0}$, while for large deformation loading the material never completely recovers, so λ_{LMin} must be larger than the initial locking stretch. We postulate that after large enough stretches, complete refolding to the original length is hindered, since the domains will not refold precisely i.e. neighboring regions do not rebind to original neighbors (note that increasing temperature may help facilitate this). An equation of this form was attempted, with results shown in Figures 82 and 83.

As can be seen, the form of this equation is useful in capturing the initial stiffness recovered by the material in reloading. However, this equation significantly overpredicts the

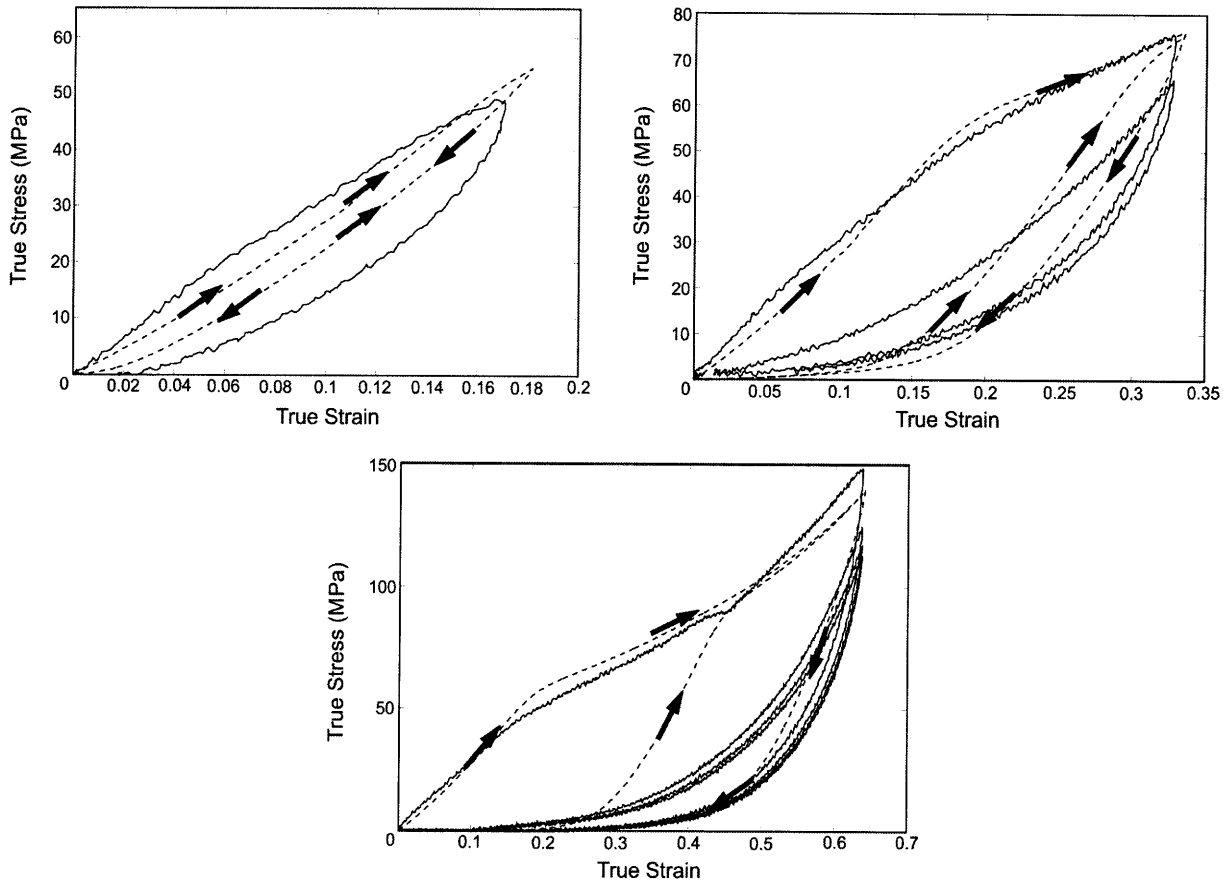

Figure 82: Experimental results (solid lines) and model (dashed lines)for load-unload-reload in the distal thread section. In this case the model includes a reverse process of the form shown in Equation 63.

material stiffness as the strain approaches the maximum strain in the previous load cycle. The reason for this is that the unfolding equation i.e. the forward process, remains the same in the first and second load cycle. Physically, this is certainly not the case.

New forward and reverse process equations When the primary bonds holding the folded domains together break in the initial load cycle, the folded domains unfold, and the protein uncoils randomly. During unloading the protein recoils, again randomly, and it is unlikely that two sites, which were adjacent in the protein's original conformation, would line up adjacent to each other in the protein's new conformation. Thus, the bonds that form during unloading will be considerably weaker than the bonds in the virgin material. Since the amount of primary bonds that are broken increases with the maximum strain in the first

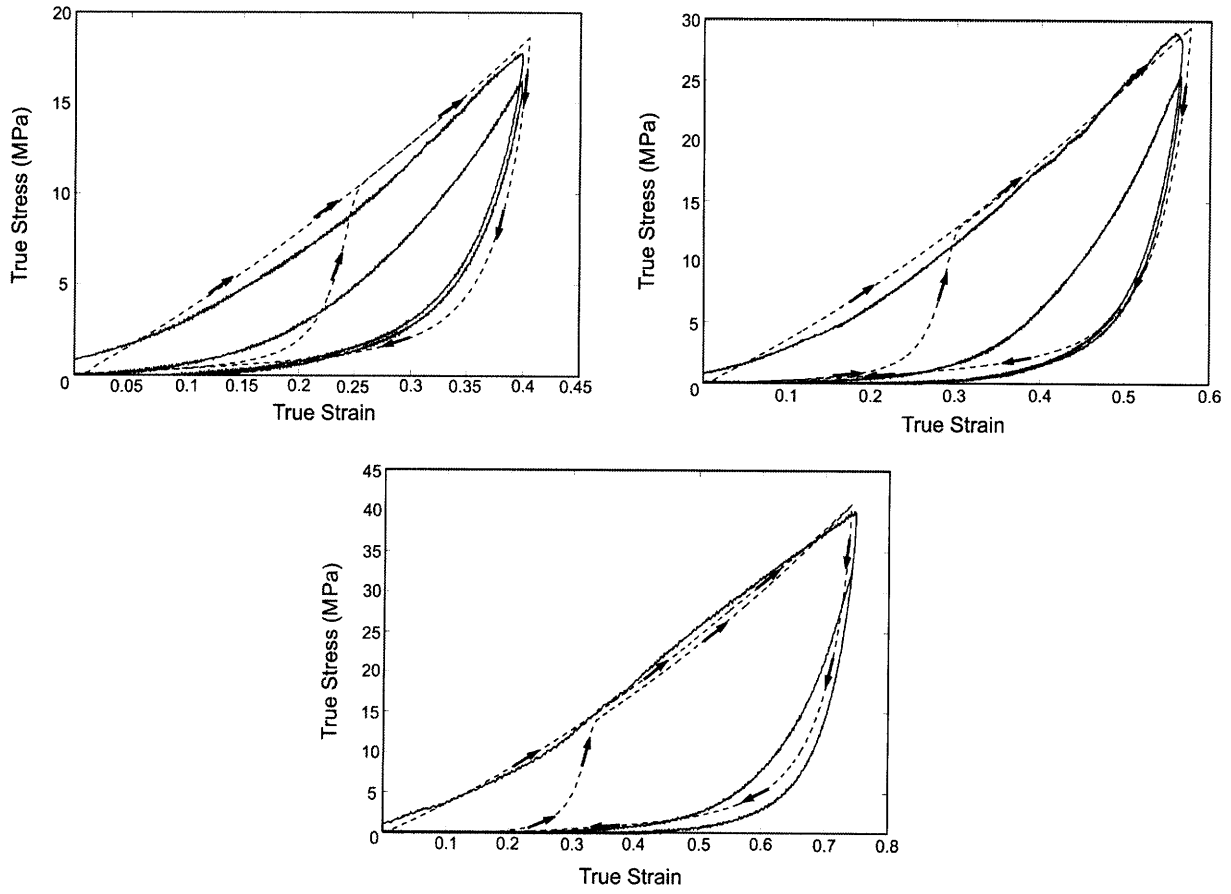

Figure 83: Experimental results (solid lines) and model (dashed lines) for load-unload-reload in the proximal thread section. In this case the model includes a reverse process of the form shown in Equation 63.

load cycle, a new parameter, the maximum locking stretch achieved during loading (λ_{Unload}), is introduced into the locking stretch evolution equation.

Again, the form of the locking stretch evolution equation can be either linearly or non-linearly dependent on this parameter. In this case, the best fit was achieved with a non-linear dependence, where the forward process takes the form:

$$\dot{\lambda_L} = \alpha_u \left(\lambda_{LMax} - \lambda_L\right)^{c_1} \exp\left[\frac{f_e X_u \left(\frac{\lambda_L}{\lambda_{LMax}}\right)^{c_2}}{K_B \Theta} \left(\frac{\lambda_{unload}}{\lambda_L}\right)^{c_3}\right] \tag{64}$$

and the reverse process takes the form:

$$\dot{\lambda_L} = \lambda_{unload}^{c_4} \alpha_r \left(\lambda_L - \lambda_{LMin}\right) \exp\left[\frac{-f_e X_u}{K_B \Theta}\right] \tag{65}$$

The forward and reverse processes sum to give the final form of the locking stretch evolution equation:

$$\begin{aligned} \dot{\lambda_L} &= \alpha_u \left(\lambda_{LMax} - \lambda_L\right)^{c_1} \exp\left[\frac{f_e X_u \left(\frac{\lambda_L}{\lambda_{LMax}}\right)^{c_2}}{K_B \Theta} \left(\frac{\lambda_{unload}}{\lambda_L}\right)^{c_3}\right] \\ &- \lambda_{unload}^{c_4} \alpha_r \left(\lambda_L - \lambda_{LMin}\right) \exp\left[\frac{-f_e X_u}{K_B \Theta}\right] \end{aligned} \tag{66}$$

where c_1, c_2, c_3, and c_4 are constants, f_e is the force on the protein, α_u and α_r are the activation energies for unfolding and refolding respectively, X_u and X_r are the activation lengths for unfolding and refolding respectively, λ_{LMax} is the maximum locking stretch, λ_{LMin} is the minimum locking stretch, λ_{unload} is the maximum locking stretch in the first load cycle, K_B is the Boltzmann constant, and Θ is the absolute temperature. This new evolution equation was implemented in the overall stress-strain framework; results are plotted in Figures 84 and 85.

The evolution of the locking stretch and the rate is plotted vs. strain (for the model including the reverse process) in Figure 86. As can be seen, after initiation of locking stretch evolution, the locking stretch increases rapidly. In unloading, the locking stretch remains relatively constant until the force on the fibers approaches zero. After a small force is reached, rapid refolding occurs, and continues for reloading in the small force regime. For continued loading, the locking stretch again increases until it reaches the previous maximum value at the previous maximum strain. Thus, with the updated locking stretch evolution equation, the model captures the material response to cyclic loading very well.

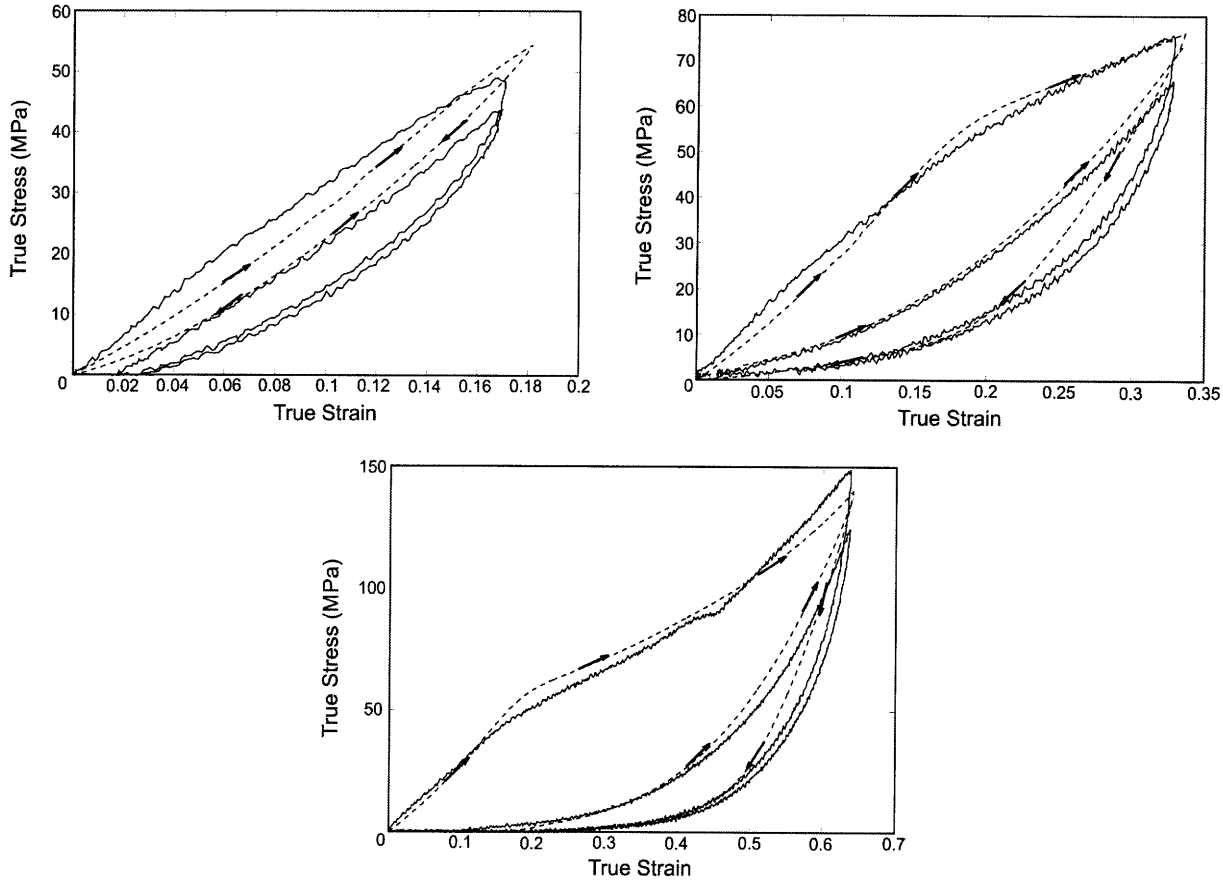

Figure 84: Load-unload-reload for distal thread sections using the locking stretch evolution equation that depends on the maximum locking stretch in the first load cycle (Equation 66).

Increasing cyclic loading Earlier, cyclic loading tests where the strain was increased slightly for each cycle were reported in Figures 29 and 37. Simulation results for similar tests are reported in Figures 87 and 88. As can be seen, the model does a good job of predicting the cyclic loading results at all strains. The model captures the hysteresis, cyclic softening, and residual strain. The model also captures the fact that in cyclic loading to increasing strains the material will rejoin the original loading curve for strains higher than the maximum strain in the previous load cycle.

The locking stretch was also monitored during increasing cyclic loading, and is shown in Figures 89 (for the distal thread section) and 90 (for the proximal section). As can be seen, in the distal section the locking stretch remains constant for low strain. As strain increases

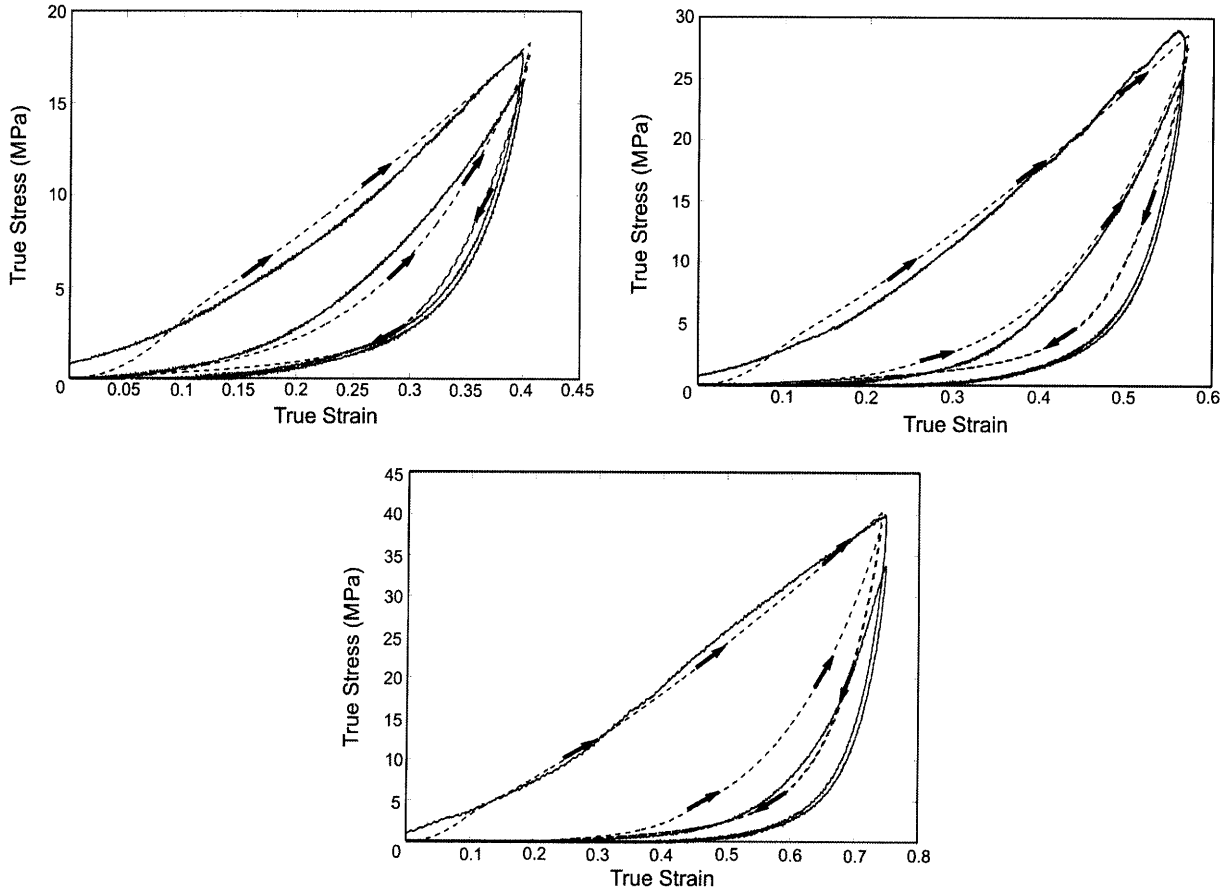

Figure 85: Load-unload-reload for proximal thread sections using the locking stretch evolution equation that depends on the maximum locking stretch in the first load cycle (Equation 66).

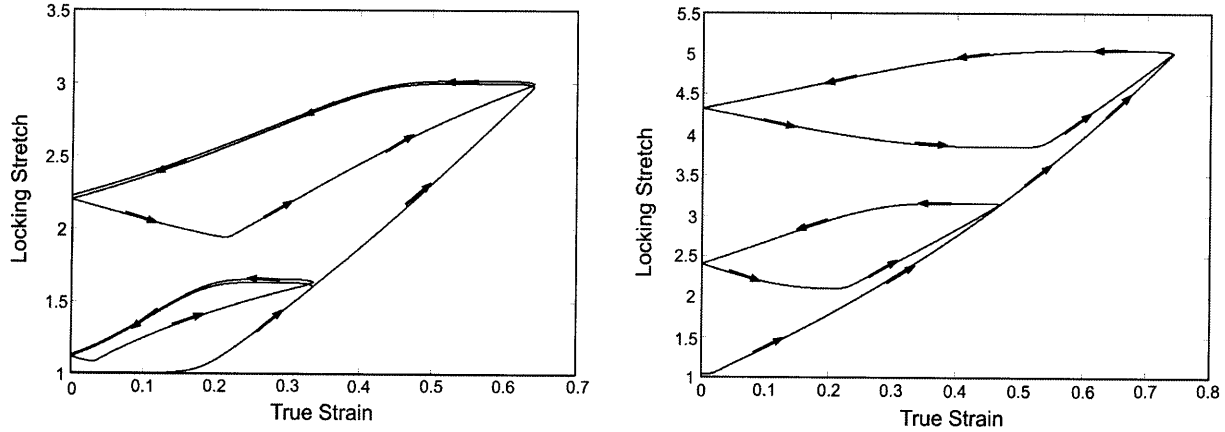

Figure 86: Locking stretch evolution with strain; distal curves are plotted on the left, proximal curves are plotted on the right.

beyond 0.15 the locking stretch increases quickly to slightly above 1.5. At this strain (corresponding to the first unload cycle) the locking stretch remains relatively constant for a small

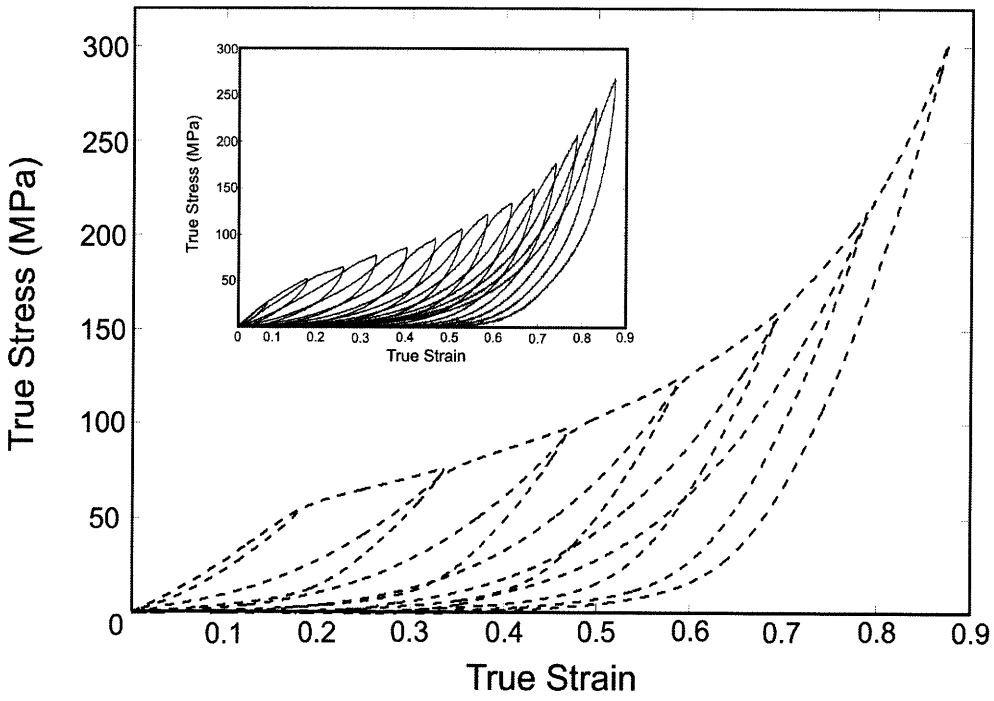

Figure 87: Increasing cyclic loading of distal byssal threads. Model results are shown in the foreground with dashed lines. Experimental results are shown inset.

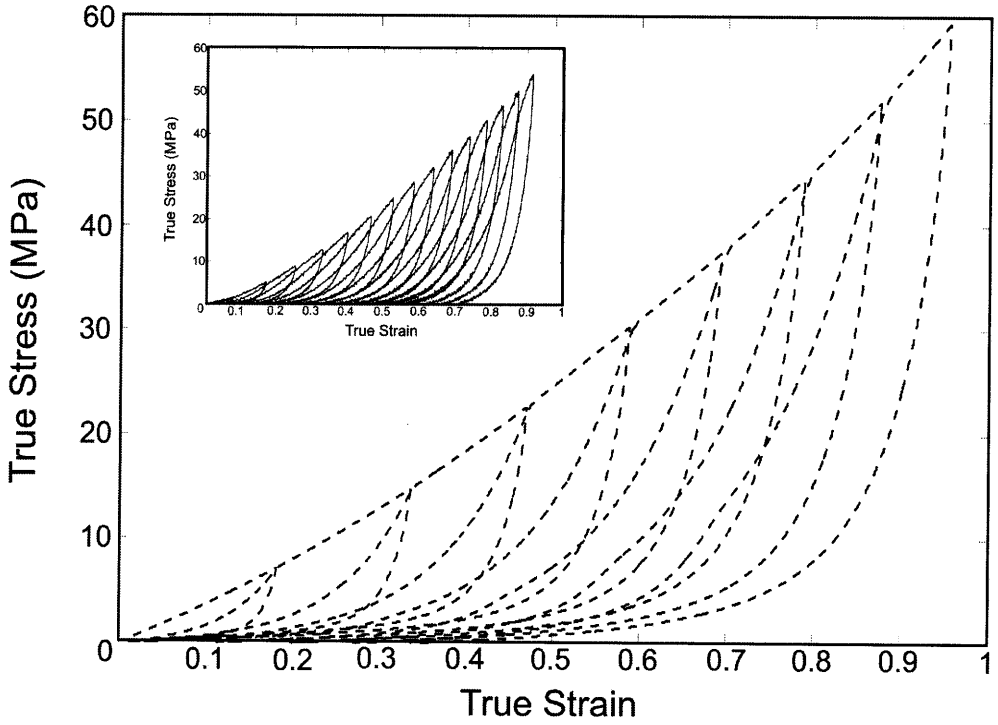

Figure 88: Increasing cyclic loading of proximal byssal threads. Model results are shown in the foreground with dashed lines. Experimental results are shown inset.

amount of strain in unloading, before decreasing to approximately 1.4. During reloading, the locking stretch continues to decrease, hitting a minimum value of approximately 1.3 at a true strain of approximately 0.11. As loading continues the locking stretch again increases slowly. As loading continues to the maximum strain in the previous cycle, the locking stretch rejoins the original curve, and again increases rapidly. This continues until the next unload-reload cycle, when the process is repeated. In none of the cycles, does the minimum locking stretch decrease beyond the level of the maximum locking stretch in the previous cycle. A similar behavior is seen in the proximal thread section, with the exception that unfolding begins right away, and the minimum locking stretch in a given unload-reload cycle does dip below the maximum locking stretch in the previous cycle.

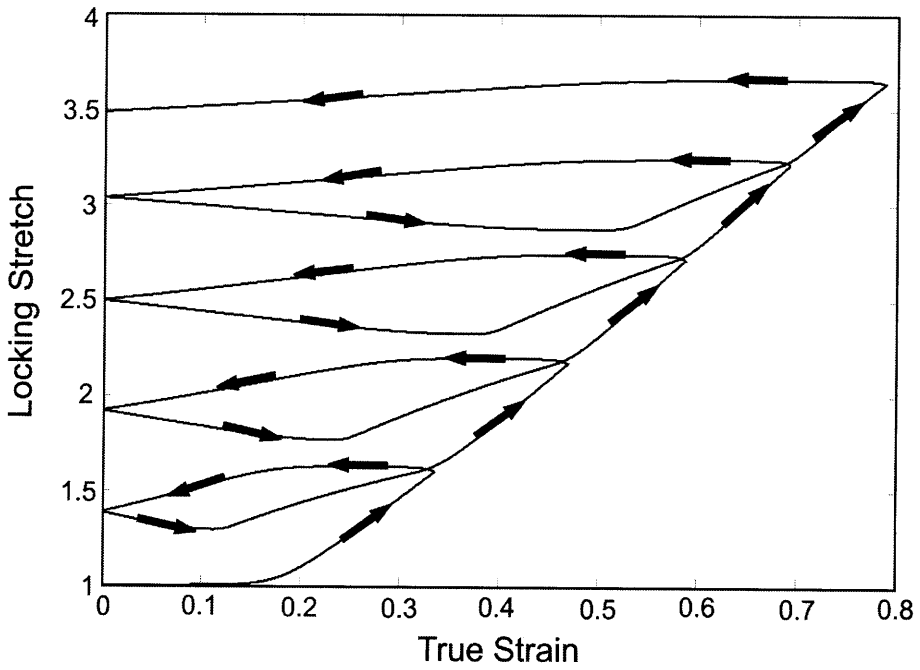

Figure 89: Locking stretch vs. strain for simulations of increasing cyclic loading of the distal thread section at a nominal strain rate of $1s^{-1}$.

These simulations were also conducted at a slower strain rate to investigate the rate-dependence of the refolding equation. Stress-strain results are shown in Figures 91 (distal) and 92 (proximal). In the distal thread section, at this slower rate, a sharper transition from stiff to compliant behavior in unloading is apparent, as well as a reduced amount of residual

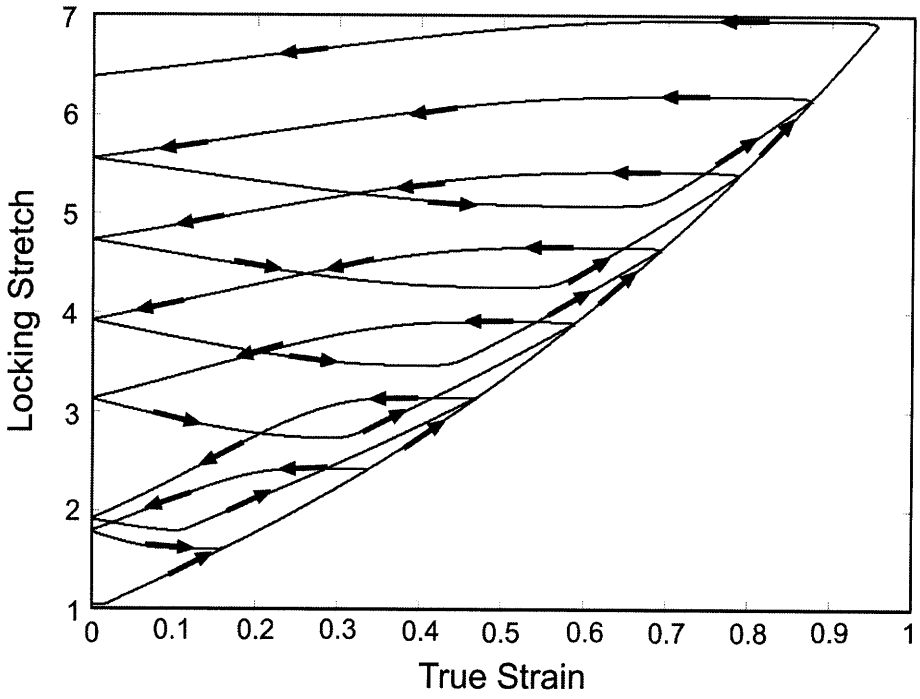

Figure 90: Locking stretch vs. strain for simulations of increasing cyclic loading of the proximal thread section at a nominal strain rate of $1s^{-1}$.

strain, especially at low strain. However, these effects are, in general, small, implying that the refolding equations are not overly sensitive to applied strain rate. This is important, because it implies that the model should continue to capture the material behavior well for slower and faster applied loadings. In the proximal section, decreasing the strain rate has no noticeable effect on the smoothness of the unloading curves or the residual strain.

The locking stretch vs. strain curves for these two simulations are shown in Figures 93 (distal) and 94 (proximal). The same basic behavior is seen in these tests as in the tests at higher rates. In this case, the locking stretch decreases more during the unloading cycle (in the distal section, the minimum locking stretch in a given unload-reload cycle dips below the maximum locking stretch in the previous unload-reload cycle), which is to be expected, since more time elapses between unloading and reloading. In the proximal section, the decrease in locking stretch is even more dramatic, with the locking stretch decreasing to less than half of its initial value in each unload-reload cycle.

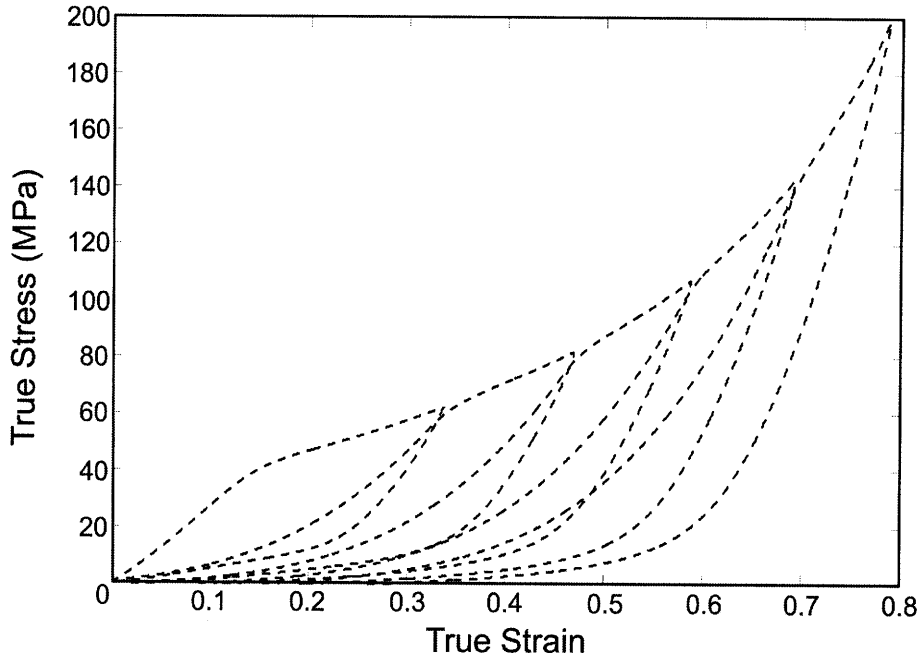

Figure 91: Stress vs. strain for increasing cyclic loading of the distal thread section at a nominal strain rate of $0.1s^{-1}$.

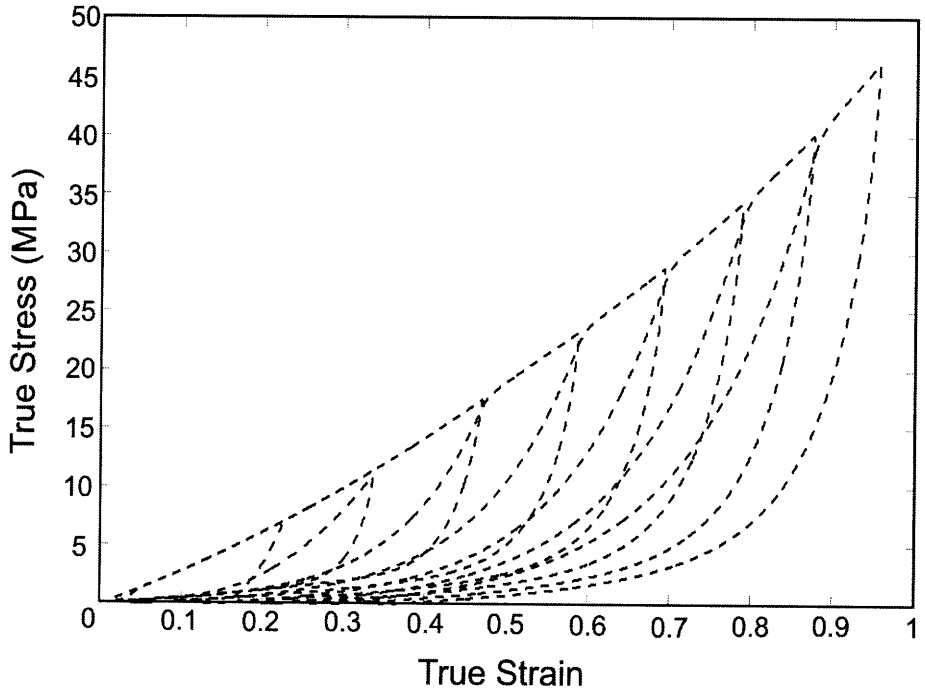

Figure 92: Stress vs. strain for increasing cyclic loading of the proximal thread section at a nominal strain rate of $0.1s^{-1}$.

Work Density As discussed above with regards to the experimental results, the dissipation during deformation can be examined in plots of work density vs. strain. Plots comparing

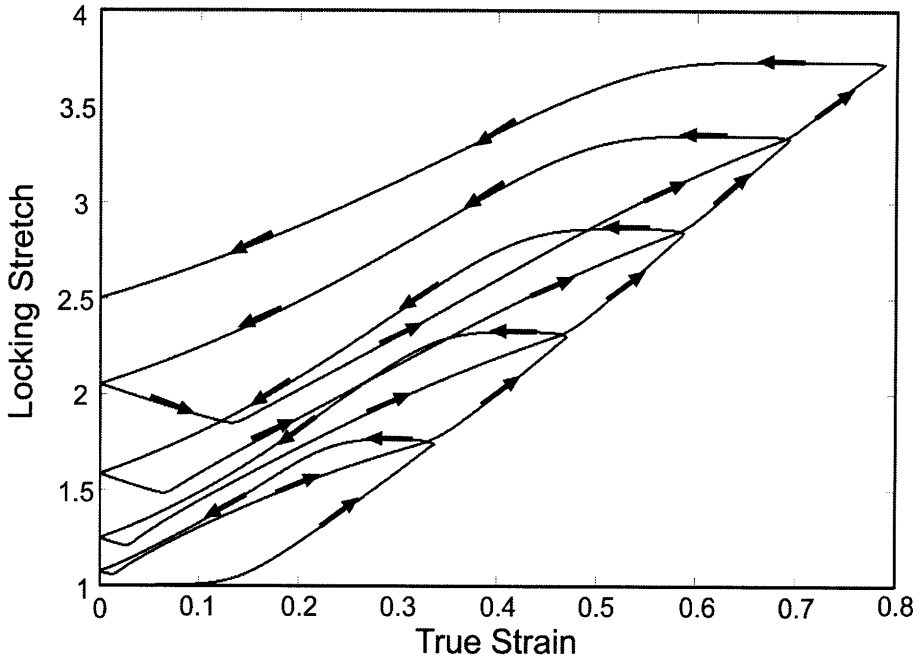

Figure 93: Locking stretch vs. strain for increasing cyclic loading of the distal thread section at a nominal strain rate of $0.1s^{-1}$.

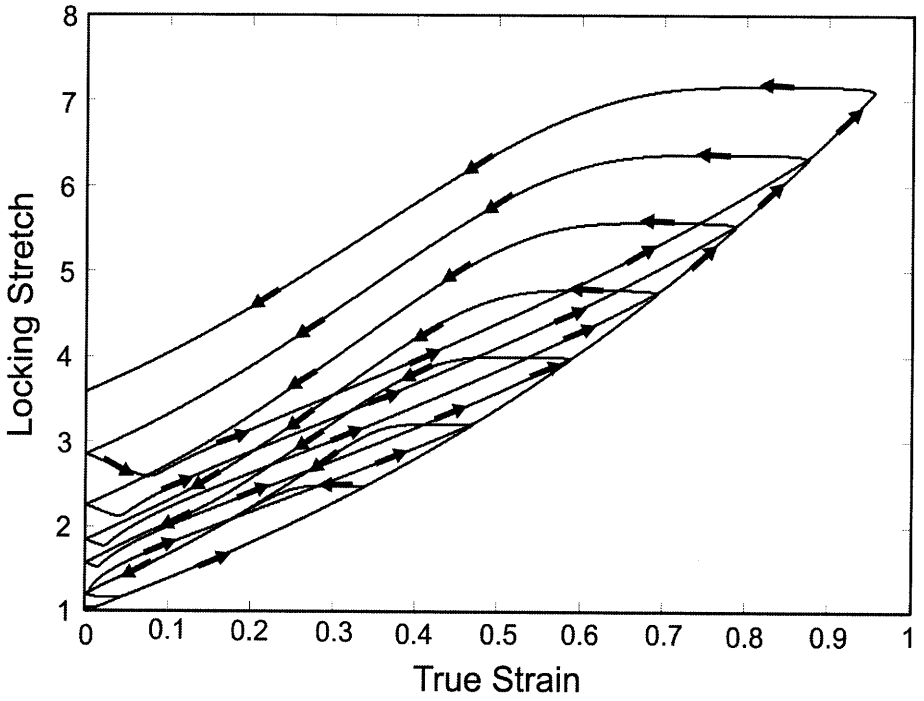

Figure 94: Locking stretch vs. strain for increasing cyclic loading of the proximal thread section at a nominal strain rate of $0.1s^{-1}$.

the total work density applied to the material in the first and second load cycles for the experimental results and the model are shown in Figures 95 and 96 for the distal and proximal

sections, respectively.

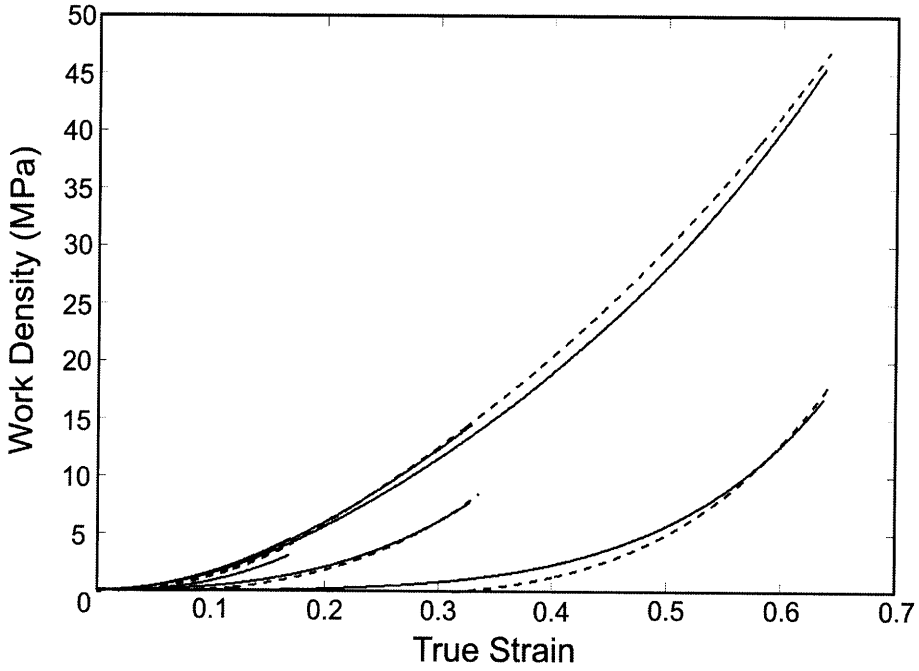

Figure 95: Work density vs. true strain for two cycle loading of the distal thread section (experimental results shown in solid lines) and the model of the distal thread section (the model's predictions are shown in dashed lines). Curves shown are for total work density applied to the material.

As can be seen, the model predicts the work density applied to the material in the first loading cycle for both the distal and the proximal models well. The model also captures the difference in total work density applied in the first and second loading cycles for both models. In all cases, the model captures the slope of the work density-strain curves well, only slightly overpredicting the slope of the work density strain curve at high strains in the proximal section. The actual values of work density applied are also accurate for both models in all (except the highes strain in the proximal section) cases.

Figures 97 and 98 show the experimental results and model's predictions of the amounts of work stored and dissipated for the distal and proximal sections respectively. Again, the model accurately predicting the experimental results in both cases. For the distal section, the model underpredicts the amount of work dissipated in the first load cycle at small strains, but predicts the amount of work dissipated well for intermediate and high strains.

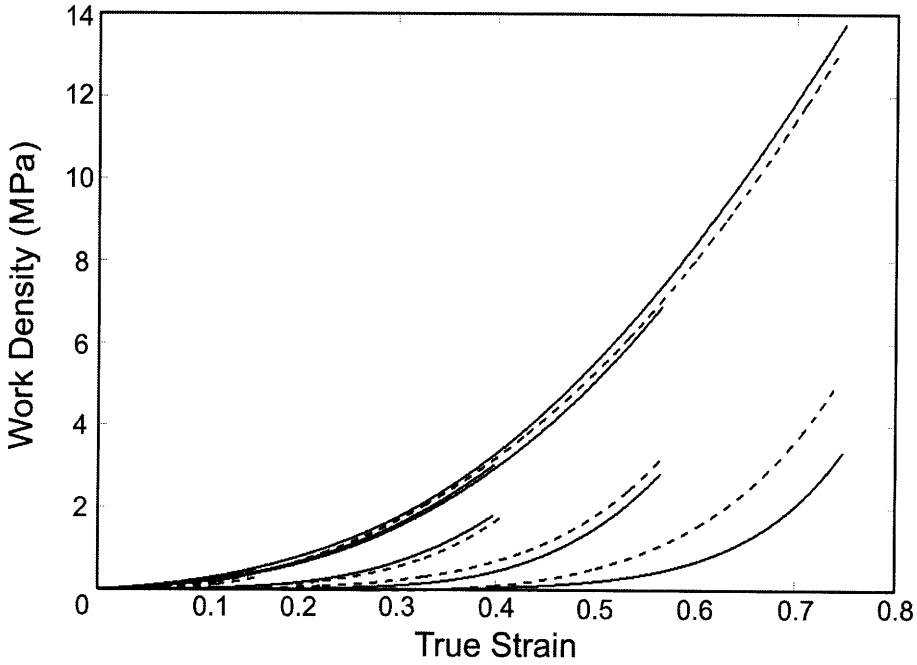

Figure 96: Work density vs. true strain for two cycle loading of the proximal thread section (experimental results are shown in solid lines) and the model of the proximal thread section (the model's predictions are shown in dashed lines). Curves shown are for total work density applied to the material.

Consequently, the model slightly overpredicts the amount of work stored in the first load cycle at all strains. For the second load cycle, the model slightly underpredicts the amount of work dissipated at all strains, consequently overpredicting the amount of work stored at all strains, though again, in all cases, the predictions are quite accurate. For the proximal section, the model predicts the experimental behavior at all strains, though slightly underpredicts the amount of work dissipated in the first load cycle, with the percent error increasing with strain. Consequently the model overpredicts the amount of work stored in the first load cycle, again with the percent error increasing with strain. The model's prediction of work dissipated in the second load cycle is quite accurate, with the the model underpredicting the amount of work dissipated at low and intermediate strains and slightly overpredicting the work dissipated at high strains. Consequently, the model overpredicts the amount of work stored at all strains, with the percent error again increasing with strain. The values for total, stored, and dissipated work density for the distal and proximal thread sections (both

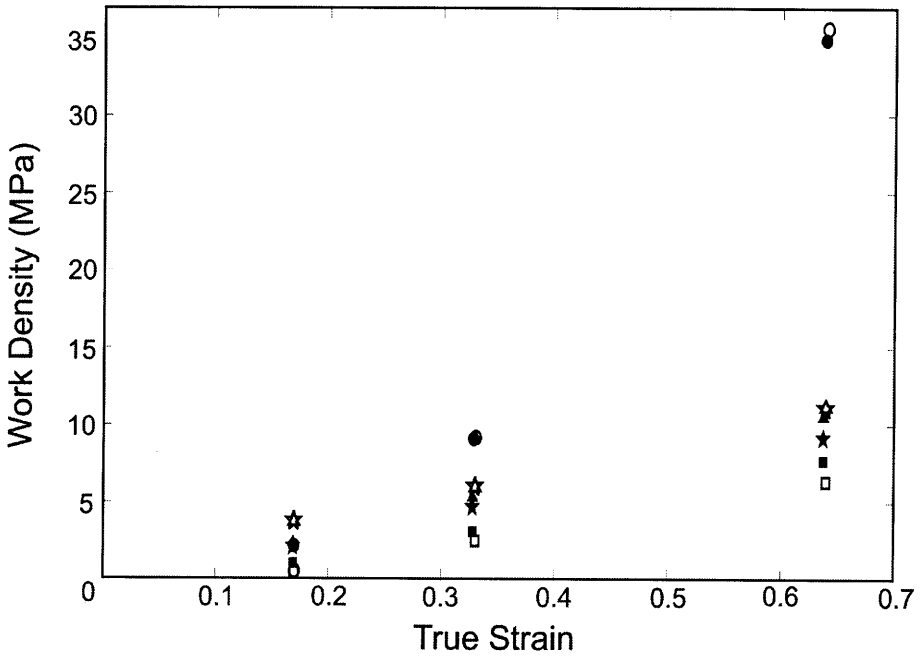

Figure 97: Work density vs. true strain for two cycle loading of the distal thread section (experimental results are shown in filled symbols) and the model of the distal thread section (the model's predictions are shown in unfilled symbols). Circles correspond to the amount of work dissipated during loading to the given strain in the first load cycle. Triangles correspond to the amount of work stored during loading to the given strain in the first load cycle (as calculated by measuring the unloading response). Squares correspond to the amount of work dissipated during loading to the given strain in the second load cycle. Stars correspond to the amount of work stored during loading to the given strain in the second load cycle.

experimental values and the model's predictions) are given in Tables 10 and 11 respectively. These results serve as another way to show that that the final model captures the cyclic behavior of these materials.

Strain		Cycle 1			Cycle2		
		Total (MPa)	Dissipated (MPa)	Stored (MPa)	Total (MPa)	Dissipated (MPa)	Stored (MPa)
0.17	Experimental	4.55	2.21 (49)	2.34 (51)	3.1	1.00 (32)	2.10 (68)
0.17	Model	4.31	0.56 (13)	3.74 (87)	4.16	0.45 (11)	3.71 (89)
0.33	Experimental	14.5	9.20 (63)	5.31 (37)	7.76	3.08 (40)	4.69 (60)
0.33	Model	15.23	9.27 (61)	5.97 (39)	8.49	2.51 (30)	5.98 (70)
0.64	Experimental	45.61	35.0 (77)	10.6 (23)	16.84	7.71 (46)	9.14 (54)
0.64	Model	46.98	35.8 (76)	11.2 (24)	16.67	5.62 (34)	11.1 (66)

Table 10: Values of total, stored, and dissipated work at four different strain levels for two-cycle loading of the distal thread section (experimental results and the model's predictions). The actual values of work (total, stored, and dissipated) are given in the table, with the percentage of the total that is stored and dissipated shown in parentheses.

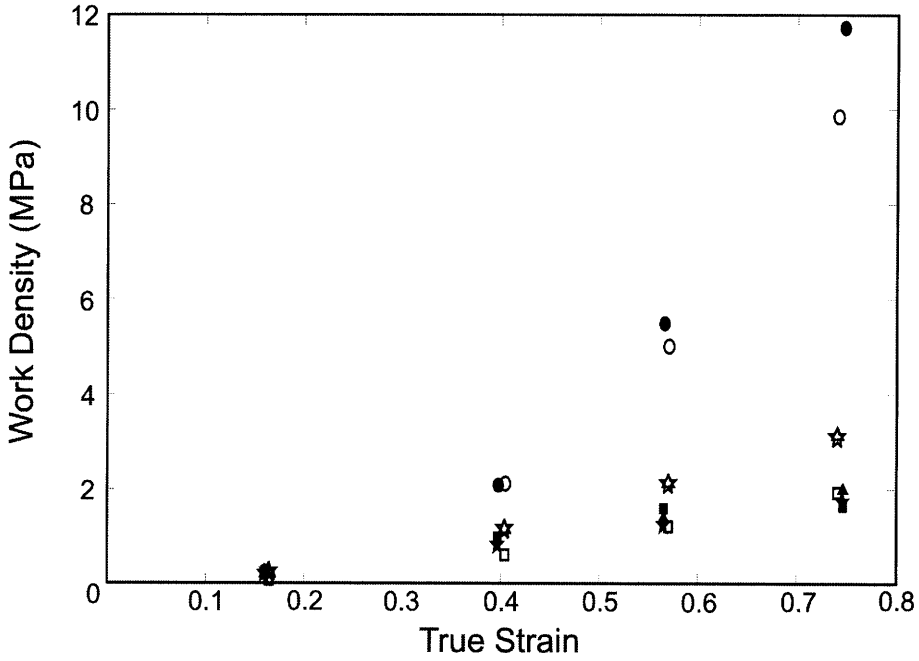

Figure 98: Work density vs. true strain for two cycle loading of the proximal thread section (experimental results are shown in filled symbols) and the model of the distal thread section (the model's predictions are shown in unfilled symbols). Circles correspond to the amount of work dissipated during loading to the given strain in the first load cycle. Triangles correspond to the amount of work stored during loading to the given strain in the first load cycle (as calculated by measuring the unloading response). Squares correspond to the amount of work dissipated during loading to the given strain in the second load cycle. Stars correspond to the amount of work stored during loading to the given strain in the second load cycle.

Strain		Cycle 1			Cycle2		
		Total (MPa)	Dissipated (MPa)	Stored (MPa)	Total (MPa)	Dissipated (MPa)	Stored (MPa)
0.16	Experimental	0.48	0.27 (56)	0.21 (44)	0.39	0.19 (48)	0.20 (52)
0.16	Model	0.42	0.17 (40)	0.25 (60)	0.32	0.08 (25)	0.24 (75)
0.4	Experimental	3.04	2.11 (70)	0.92 (30)	1.82	1.00 (55)	0.82 (45)
0.4	Model	3.28	2.12 (65)	1.16 (35)	1.75	0.61 (35)	1.14 (65)
0.57	Experimental	6.88	5.50 (80)	1.38 (20)	2.83	1.60 (57)	1.23 (43)
0.57	Model	7.16	5.01 (70)	2.15 (30)	3.31	1.21 (37)	2.10 (63)
0.75	Experimental	13.76	11.8 (85)	2.00 (15)	3.36	1.64 (49)	1.72 (51)
0.75	Model	13.03	9.88 (76)	3.14 (24)	5.01	3.08 (61)	1.93 (49)

Table 11: Values of total, stored, and dissipated work at four different strain levels for two-cycle loading of the proximal thread section (experimental results and the model's predictions). The actual values of work (total, stored, and dissipated) are given in the table, with the percentage of the total that is stored and dissipated shown in parentheses.

Material Recovery As a final check on the robustness of the constitutive model, simulations of cyclic loading with hold time (like the experimental data shown in Figures 31 and 39) were conducted. Results of the simulations are shown in Figures 99 and 100. As can be seen, the model captures the general behavior i.e. for load-unload-hold-reload-unload, the material exhibits an initially stiffer response upon reloading than for the same test without a hold time. However, the time scale for stiffness recovery is significantly accelerated. Whereas in the experimental data, in the intermediate/high strain regime (the strain regime shown in Figures 99 and 100), the maximum recovery was seen to take as long as 25 minutes, the simulation predicts a recovery to this level in less than 3 minutes. So, although the general trend is correct, the values of the parameters for the refolding equation (the α_r, X_r, and exponents) are not adequate to get the most accurate fit to all experimental results.

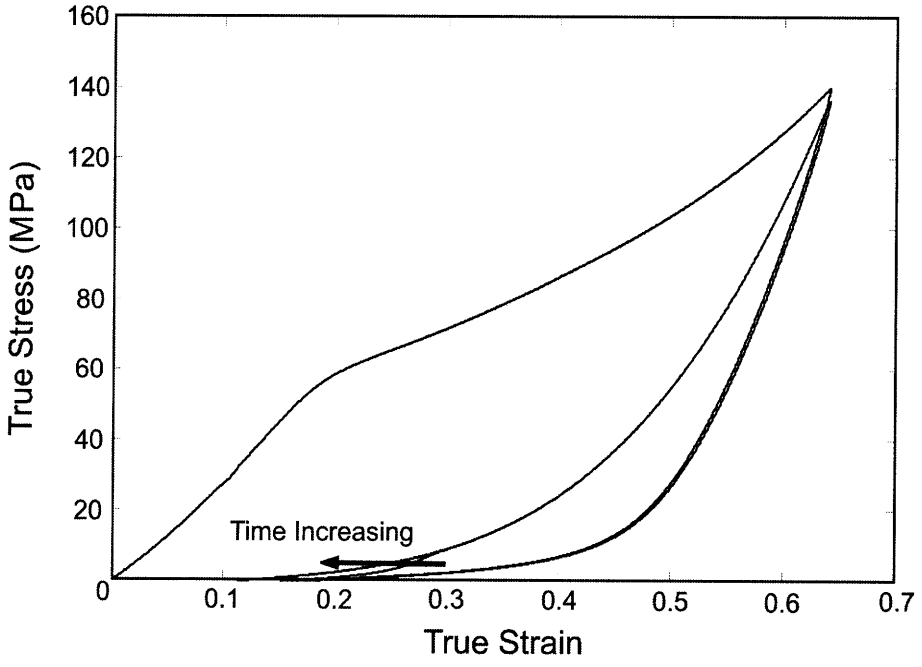

Figure 99: Stress-strain curves for simulations of load-unload-hold-reload of distal thread section loaded at a nominal strain rate of $1s^{-1}$. The arrow shows the simulation's prediction of the material response with increasing hold time. The hold time shown here is $300s$.

Note here that the stiffness recovery predicted by the model only occurs at very low strains. For higher strains, the reloading after hold curve follows the initial reloading curve

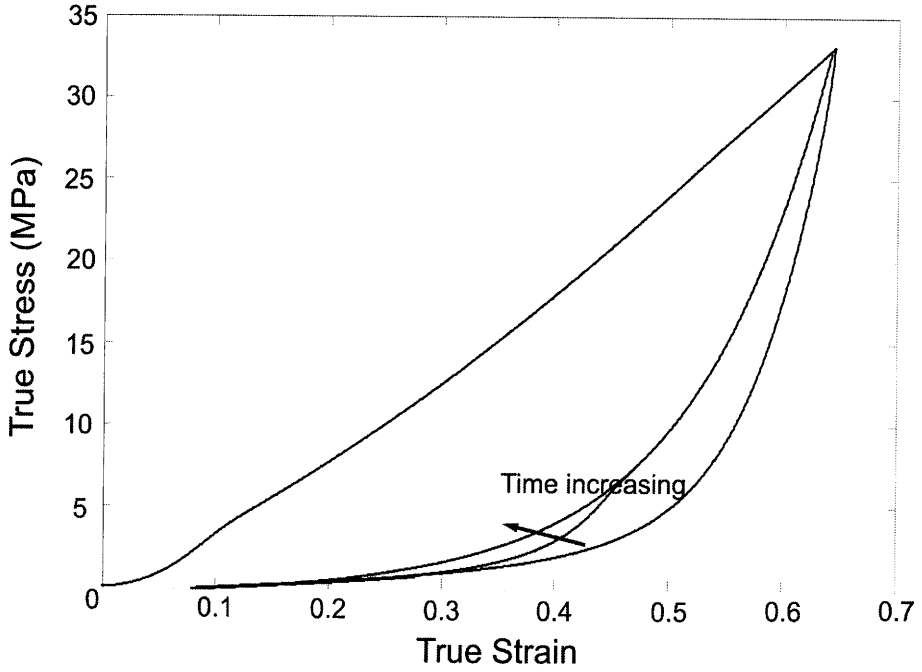

Figure 100: Stress-strain curves for simulations of load-unload-hold-reload or proximal thread section loaded at a nominal strain rate of $1s^{-1}$. The arrow shows the simulation's prediction of the material response with increasing hold time. The hold time here is $300s$.

exactly. This is because the unfolding occurs more quickly during reloading than in the virgin material (due to the exponential dependence on $\frac{\lambda_{unload}}{\lambda_L}$). The experimental results demonstrate that the material will be stiffer throughout the reload. This effect can be captured with the current model, but would require that the exponential on the $\frac{\lambda_{unload}}{\lambda_L}$ term i.e. c_3 evolve during the hold period. For example, if, as the hold time (t) goes to infinity ($t \rightarrow \infty$), the exponential term c_3 goes to zero, the material would fully recover, and the reloading curve would follow the initial loading curve. We do not postulate the actual form of such a time-dependent c_3 equation here.

3.6 Review of the final constitutive model

A brief review of the phenomenological model developed for the stress-strain behavior of mussel byssal threads is given here. The values of the mechanical properties used in the model are given in Table 12.

Material Property	Distal	Proximal	Material Property	Distal	Proximal
$d\,[nm]$	9	9	$E\,[GPa]$	23	300
$\theta_0\,[\circ]$	25	55	$\mu\,[MPa]$	3	1
ν	0.49	0.49	$x_u\,[nm]$	$9.1 \cdot 10^{-4}$	$1.3 \cdot 10^{-4}$
$\alpha_u\,[s^{-1}]$	$1 \cdot 10^{-6}$	$1 \cdot 10^{-4}$	$x_r\,[nm]$	$1 \cdot 10^{-4}$	$5 \cdot 10^{-5}$
$\alpha_r\,[s^{-1}]$	90	60	λ_{Lmax}	4	10
$\alpha_{ve}\,[s^{-1}]$	$1 \cdot 10^{-16}$	$1 \cdot 10^{-16}$	$\Omega\,[nm]$	$5.5 \cdot 10^{-4}$	$1.1 \cdot 10^{-4}$
n	-1.5	-2.5	c_0	$1.5 \cdot 10^{-9}$	$9 \cdot 10^{-9}$
c_1	0.8	5	c_2	-0.1	0.1
c_3	6	7	c_4	-3	-4

Table 12: Parameters used in the phenomenological model. d is the diameter of the fiber, E is the fibers' Young's Modulus, θ_0 is the initial fiber orientation, μ is the shear modulus of the matrix, ν is the Poissons ratio of the matrix, x_u is the activation length for unfolding, α_u is the activation energy for unfolding, x_r is the activation length for refolding, α_r is the activation energy for refolding, λ_{Lmax} is the maximum locking stretch, α_{ve} is the activation energy for the dashpot, Ω is the activation length for the dashpot, and n, c_0, c_1, c_2, c_3, and c_4 are constants in the fiber force and unfolding/refolding equations.

The constitutive model takes the protein filament bundles to be the major load bearing constituent in the material, with the force stretch behavior of the protein bundles given by:

$$f_e = c_0 \left(1 - \frac{\lambda_e}{\lambda_L}\right)^n (\lambda_e - 1) \tag{67}$$

in the folded domains, and:

$$f_m = EA\,(\lambda_m - 1) \tag{68}$$

in the straight rod domain. Force equilibrium requires that these forces be equal:

$$f_m = f_e \tag{69}$$

The stretch in each domain is additively decomposed from the overall fiber stretch:

$$L_f = L_m + L_e \tag{70}$$

$$\lambda_f = \frac{L_f}{L_{f0}} = \frac{L_m + L_e}{L_{f0}} \tag{71}$$

$$\lambda_f L_0 = \lambda_m L_{m0} + \lambda_e L_{e0} \tag{72}$$

The unfolding and refolding of the folded protein domains is given by the Eyring-type equation:

$$\begin{aligned} \dot{\lambda_L} &= \alpha_u \left(\lambda_{LMax} - \lambda_L\right)^{c_1} \exp\left[\frac{f_e X_u \left(\frac{\lambda_L}{\lambda_{LMax}}\right)^{c_2}}{K_B \Theta} \left(\frac{\lambda_{unload}}{\lambda_L}\right)^{c_3}\right] \\ &- \lambda_{unload}^{c_4} \alpha_r \left(\lambda_L - \lambda_{LMin}\right) \exp\left[\frac{-f_e X_u}{K_B \Theta}\right] \end{aligned} \tag{73}$$

The individual bundles are grouped into a network using the Bertoldi (Bertoldi and Boyce, 2007) network model, where each bundle is taken as one of the chains of an eight-chain orthotropic unit cell. The network stress is given by:

$$\boldsymbol{\sigma}_{ani} = \frac{\nu}{4J} \sum_{i=1}^{4} \frac{1}{\lambda_f^{(i)}} \left[E A r_0 \left(\lambda_m - 1\right)\right] \mathbf{v}^{(i)} \otimes \mathbf{v}^{(i)} \tag{74}$$

This network stress is summed with an isotropic matrix stress, which is described by the compressible Neo-Hookean constitutive model:

$$\boldsymbol{\sigma}_{iso} = \frac{\mu}{J} \left(\mathbf{B}^e - \mathbf{I}\right) + K \left(J - 1\right) \mathbf{I} \tag{75}$$

In this case, the matrix is taken to be non-linearly viscoelastic, where the deformation gradient is decomposed into elastic and viscous components, $\mathbf{F} = \mathbf{F}^e \mathbf{F}^v$, with the rate of

evolution of the viscous part of the deformation gradient given by:

$$\dot{\mathbf{F}}^v = \mathbf{F}^{e-1}\left(\dot{\gamma}_0 \sinh\left[\frac{\tau\Omega}{K_B\Theta}\right]\mathbf{N}^v\right)\mathbf{F}^e\mathbf{F}^v \tag{76}$$

The model captured all major aspects of the material mechanical behavior, including the non-linear monotonic loading behavior, material rate-dependence, hysteresis, and cyclic softening. Figures comparing the experimental data to the model for monotonic loading at different strain rates (Figures 101 and 102), and for cyclic loading (Figures 103 and 104) are shown here.

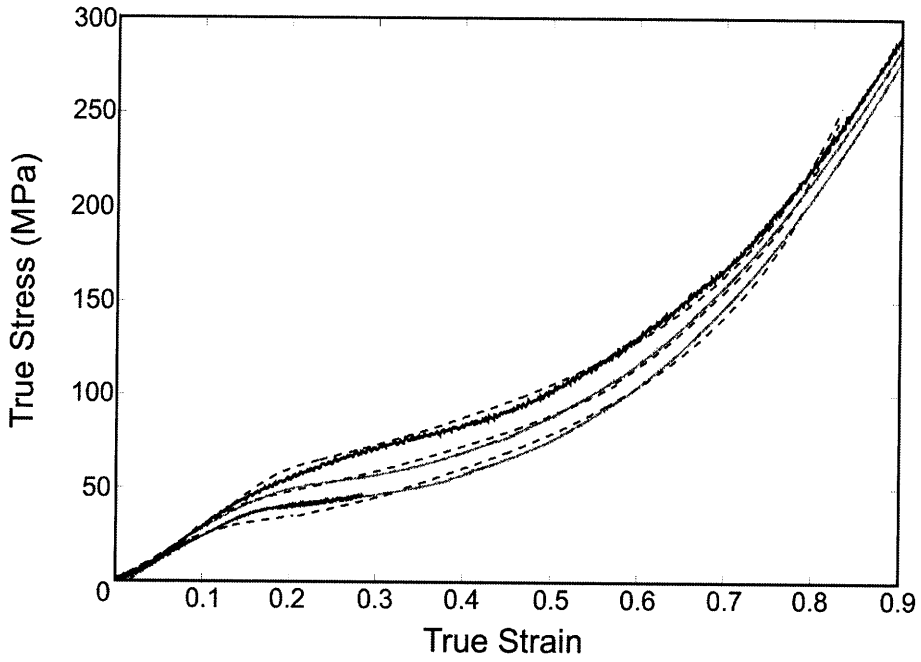

Figure 101: Stress-strain curves for monotonic loading of distal thread section at three nominal strain rates ($1s^{-1}$, $0.1s^{-1}$, and $0.01s^{-1}$). Experimental results are shown with solid lines; model results are shown with dashed lines.

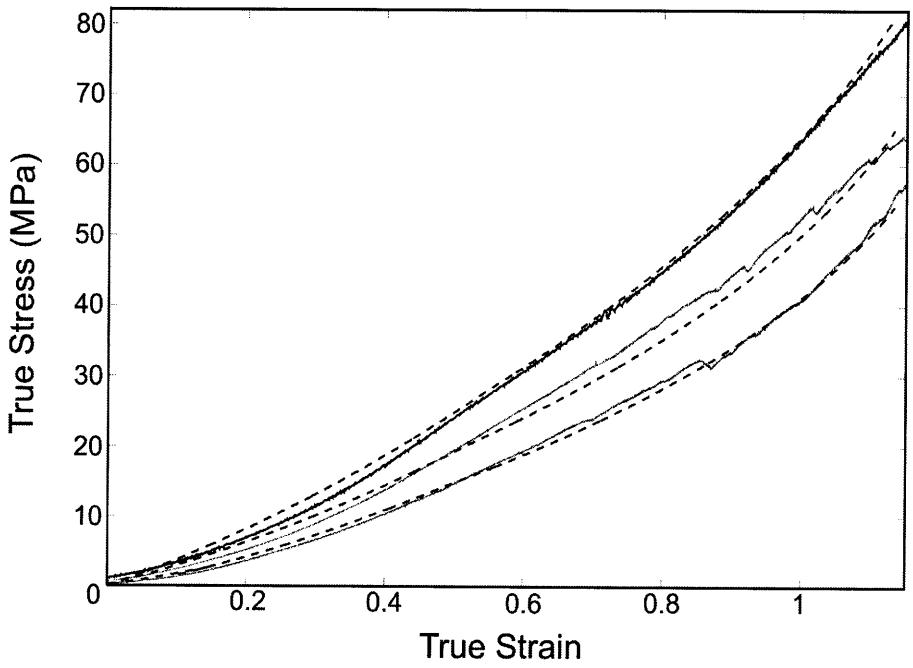

Figure 102: Stress-strain curves for monotonic loading of proximal thread section at three nominal strain rates ($1s^{-1}$, $0.1s^{-1}$, and $0.01s^{-1}$). Experimental results are shown with solid lines; model results are shown with dashed lines.

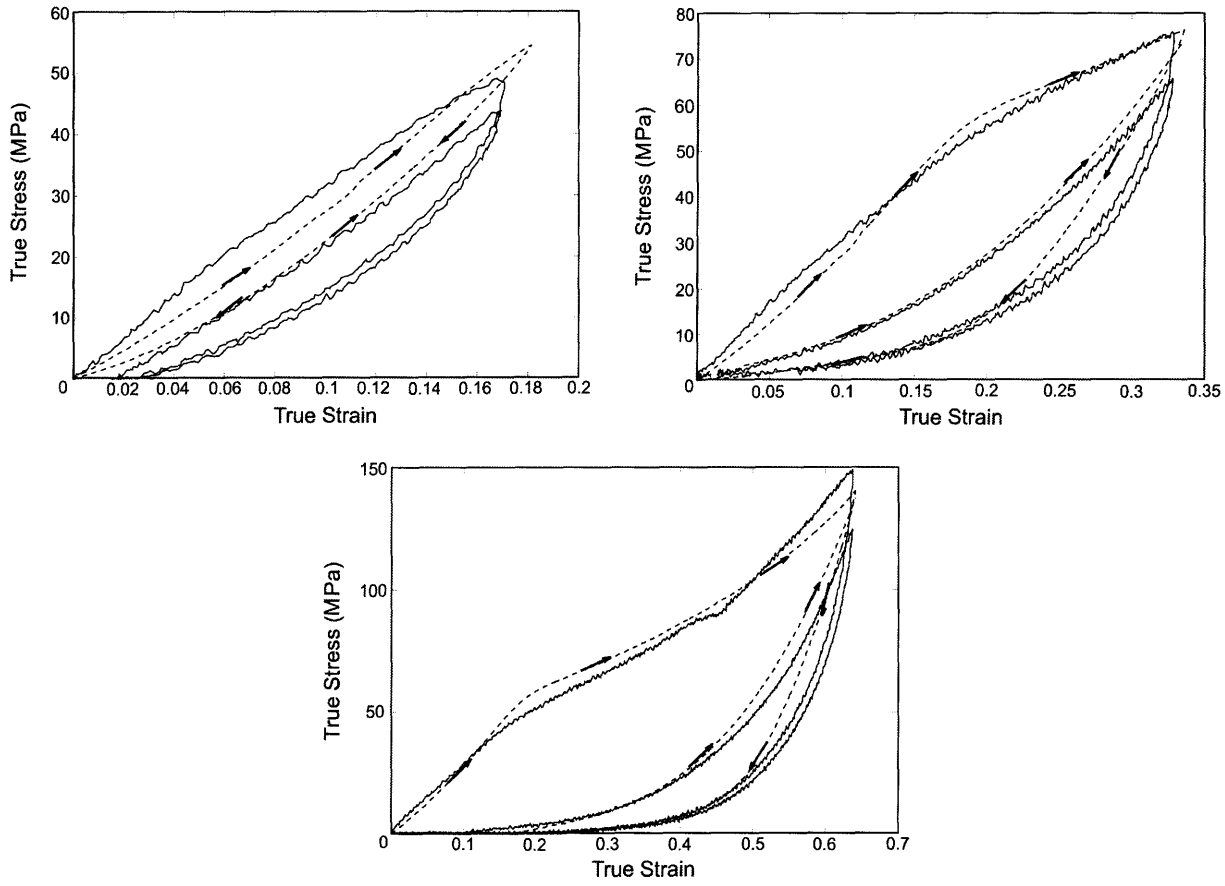

Figure 103: Stress-strain curves for load-unload-reload of distal thread section at three different strain levels. Experimental results are shown with solid lines; model results are shown with dashed lines.

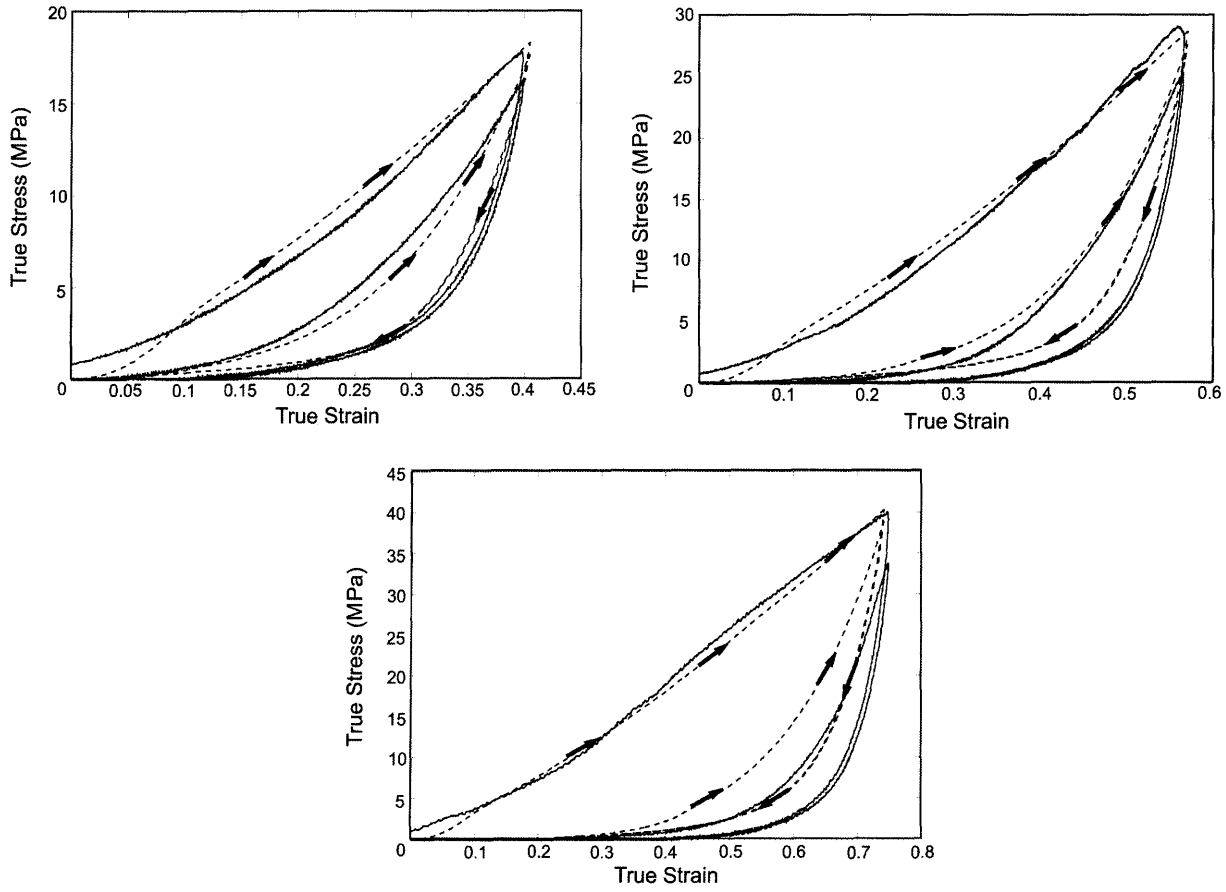

Figure 104: Stress-strain curves for load-unload-reload of proximal thread section at three different strain levels. Experimental results are shown with solid lines; model results are shown with dashed lines.

4 Full Thread Simulations

A three dimensional (3-D) model of the full thread was constructed using SolidWorks. The dimensions used for the full thread model were the average dimensions of the full threads after the adhesive plaque and the hoop connecting the proximal section to the stem were removed (proximal thread section $4.9mm$ in length, transition section $3.3mm$ in length, and distal section $9.9mm$ in length). The cross-section of the distal section was circular, with a diameter of $0.12mm$. The cross-section of the proximal section was elliptical, with a minor axis of $0.12mm$, and a major axis of $0.26mm$. In order to ensure a smooth transition in cross-section from the proximal to the distal thread section, the SolidWorks 'loft' feature was used to construct the transition section. The SolidWorks model was imported into ABAQUS, and the mesh was constructed using ABAQUS CAE.

The quarter symmetry of the thread was exploited in the model to reduce the model size, where only one quarter of the thread was modeled using 4325 elements of type $C3D8R$ (Figure 105 shows the meshed model as well as a plot of how the cross-sectional area of the model varies along the model's length). Appropriate boundary conditions were applied to the longitudinal sections to capture the symmetry i.e. the nodes on the faces were allowed to move radially and in the direction of loading, but were not allowed to move out of the plane. The material models developed in the previous chapter for the proximal and distal thread sections were used to simulate the stress-strain behavior of the related sections with a transition of these behaviors in the transition region.

4.1 Modeling the Thread's Transition Region

The transition section presents a problem with regards to simulating full thread loading, as it is difficult to mechanically test the properties of the transition region (a tension test would be unable to sample the stiffness at a specific point, and the short nature of the section

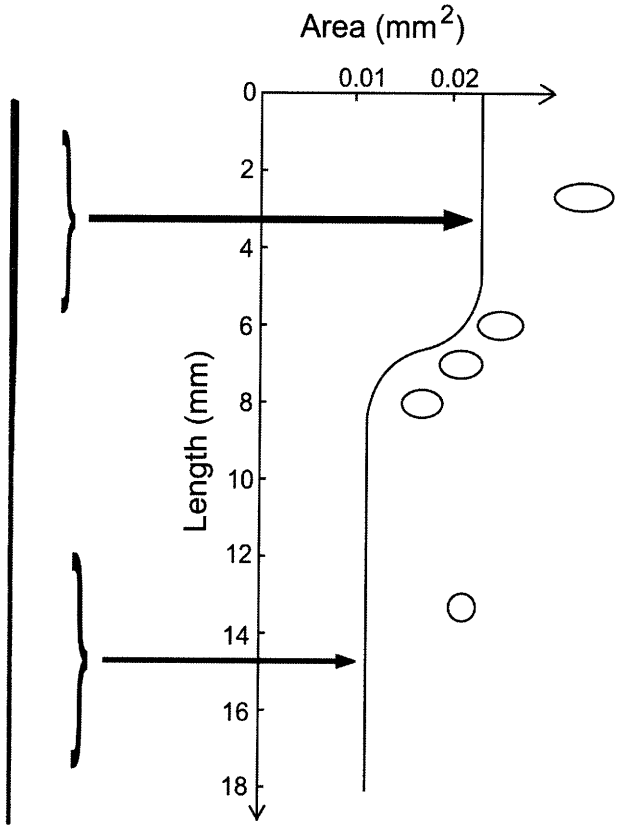

Figure 105: The 3-D meshed quarter geometry model of the full thread (left), and a plot of how the cross-sectional area of the thread model (full cross-section) varies along the model's length (right).

would give rise to gripping issues). It may be possible to ascertain some of the properties via nano-indentation, but such a technique was not utilized in this work. Thus, like the geometry, the mechanical properties are assumed to transition smoothly in the transition region. The transition region was divided into sections of equal length (either a discrete jump from proximal to distal with no section, one transition section, two transition sections, four transition sections, or eight transition sections), and the material properties used for each section were the appropriate fractions of the difference between the given material properties of the proximal and distal sections. For example, the value of c_3 (the exponent applied to $\frac{\lambda_{unload}}{\lambda_L}$ in the locking stretch evolution equation) in the proximal thread section is 7, while the value of c_3 in the distal thread section is 6; for the model with only one transition section, 6.5 was used for c_3.

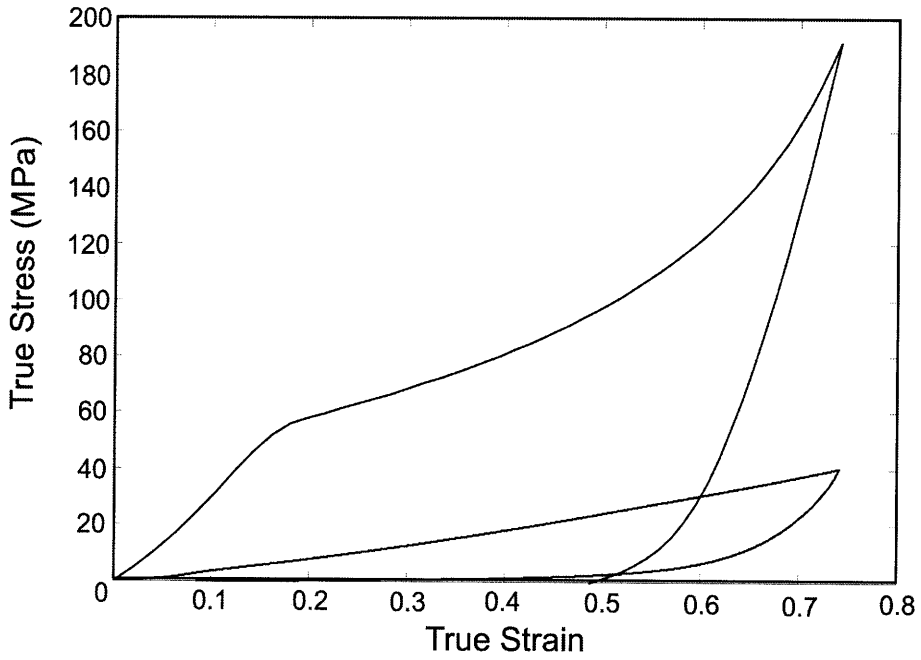

Figure 106: Stress-Strain behavior for the different thread sections when the thread is modeled as having no transition regions.

To show how the properties used for each section of the transition region acted to transition the behavior from proximal to distal, the resulting stress-strain curves are compared in Figures 106, 107, 108, 109, and 110. Additionally, the initial stiffness of each section

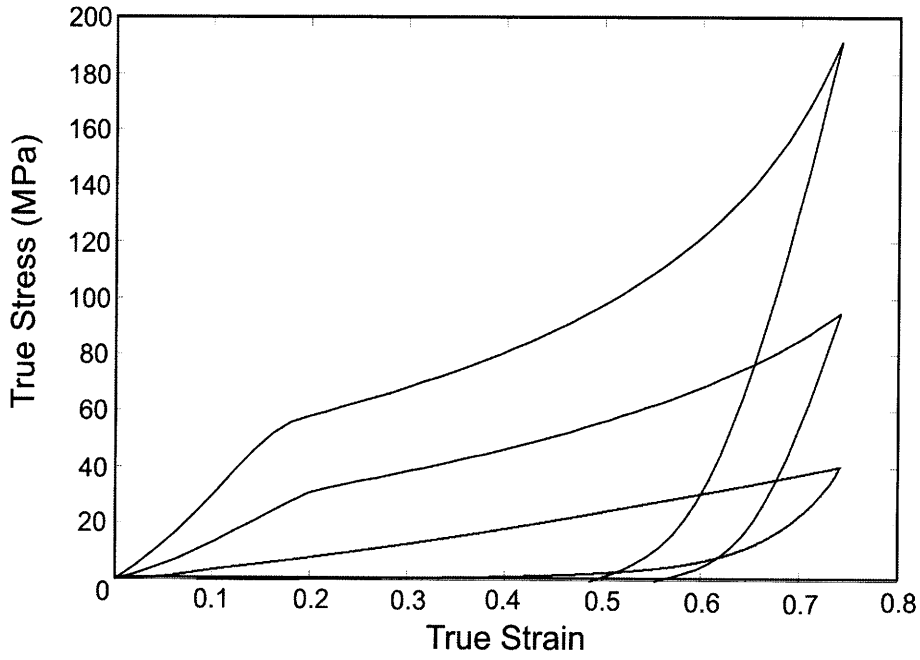

Figure 107: Stress-Strain behavior for the different thread sections when the thread is modeled as having one transition region.

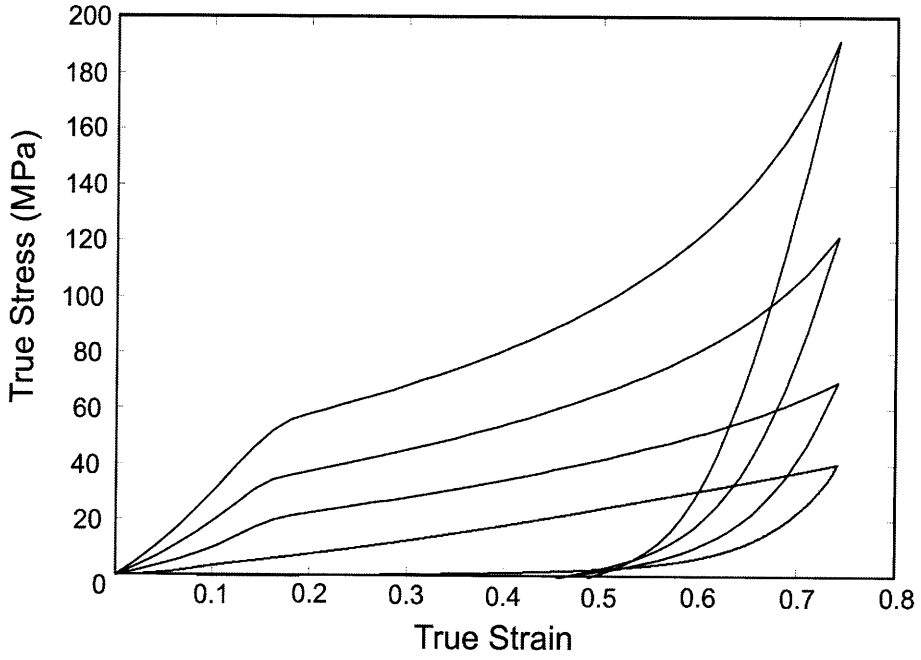

Figure 108: Stress-Strain behavior for the different thread sections when the thread is modeled as having two transition region.

(proximal, distal, and each transition section) is plotted as a function of length along the thread in Figure 111

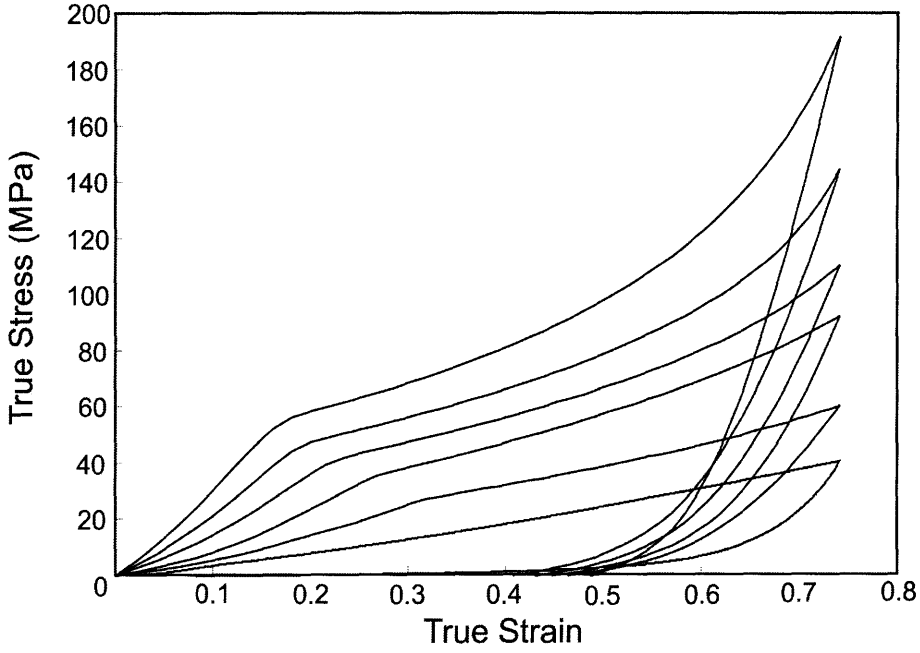

Figure 109: Stress-Strain behavior for the different thread sections when the thread is modeled as having four transition region.

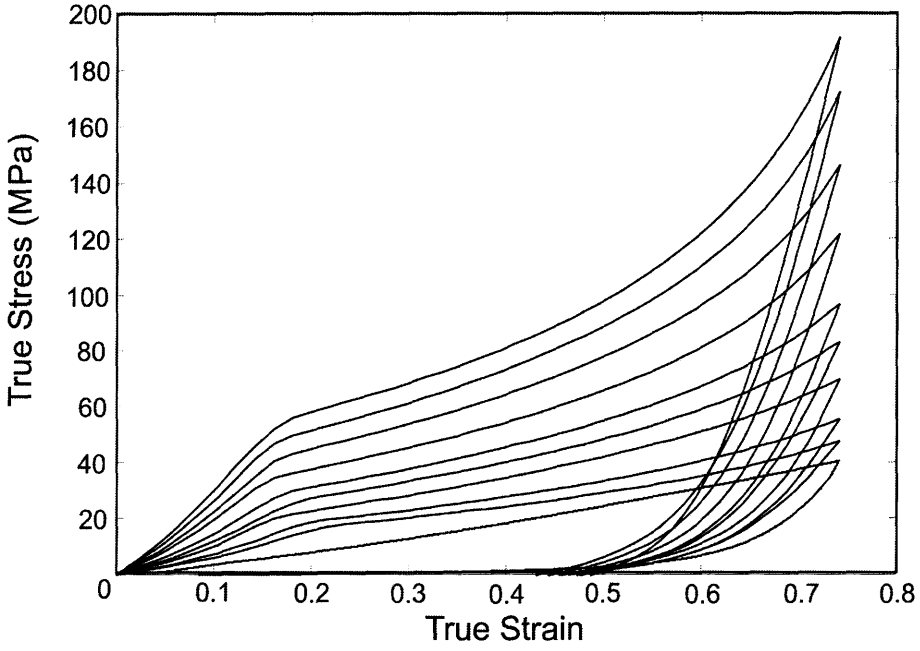

Figure 110: Stress-Strain behavior for the different thread sections when the thread is modeled as having eight transition region.

Finally, it is important to realize that the 'jumps' in material properties will give rise to strain concentrations, which will then lead to stress concentrations, since the straining

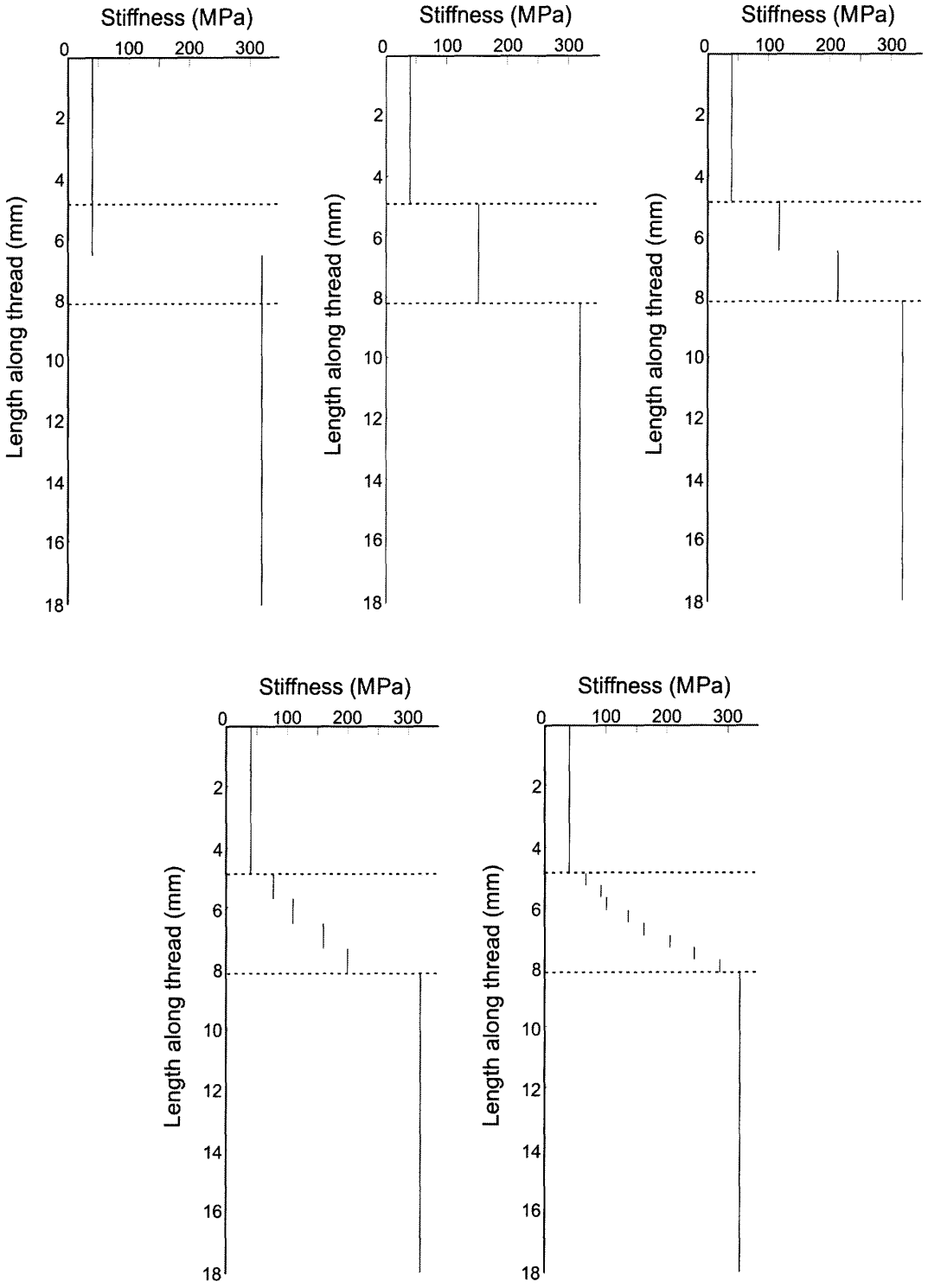

Figure 111: Stiffness as a function of distance along the thread for the quarter thread finite element model. All 'sectionings' of the transition section are shown, from the case where there is no transition region (upper left) to the case where there are eight transition regions (lower right).

will give localized changes in cross-section. Ideally, each individual row of elements in the transition region would be given its own mechanical properties to ensure a perfectly smooth transition, and even this would not give a truly smooth transition. One could then compare this ideal case (the case with a fully smooth transition) to the discrete transitioning that will be presented here. The trend towards this limit will be evident by the trend in increasing the number of transition sections.

4.1.1 Stress and strain contours

Stress and strain contours for the entire thread are difficult to show in this thesis, since the aspect ratio of the thread is such that the contours are difficult to see. In general, the stress and strain in the proximal and distal thread sections is uniform (because the cross-section and mechanical properties of these sections are uniform), while the gradients in the transition section can be quite large. The stress contours for the transition section at nominal macroscopic strains, i.e. the nominal strain applied to the overall thread, of 0, 0.08, 0.16, 0.24, 0.32, and 0.4 are shown in Figure 113 (Figure 112 shows the full thread with the transition section highlighted to provide a reference for the contour plots presented here and throughout this section). The strain contours for the transition section at the same nominal strains (leaving out the undeformed image) are shown in Figure 114.

As can be seen in Figure 113, the stress contours transition smoothly at small strains, but become more discrete in nature as strain increases. The reason for the apparent increasing discreteness is that the strain has localized in some of these regions leading to large axial gradients in the axial stress. Because of the nature of the uniaxial loading, the axial force is necessarily uniform along the thread's length. Because of the different constitutive relationships used in each thread section, a given stress will give rise to different strain in each region of the model. The difference in strain will cause the area of each section to change non-uniformly (if one section strains more than its neighbor, then its area will neck in more

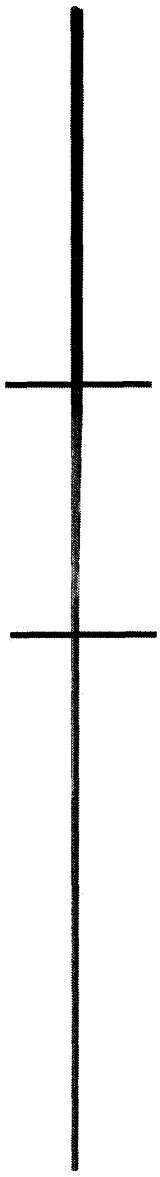

Figure 112: The full thread model during loading. As can be seen, the stress contours in the proximal and distal sections are homogeneous. In the transition section (highlighted with horizontal lines) the stress gradients can be large.

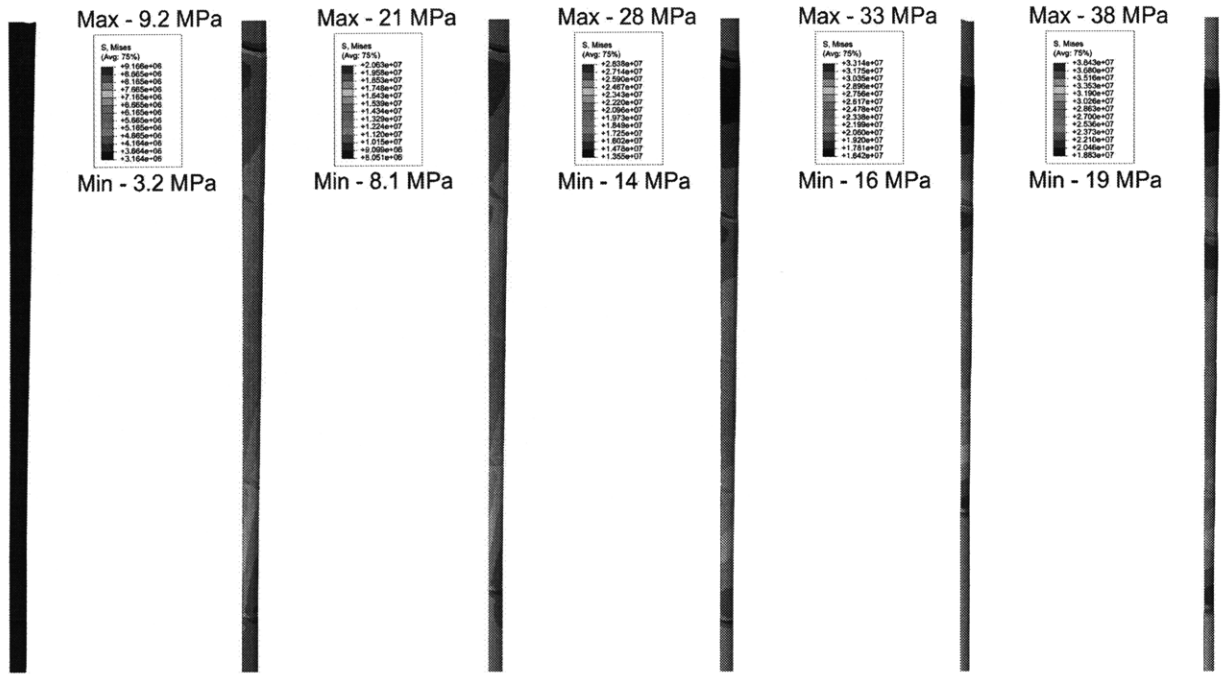

Figure 113: Mises Stress contours for the transition section at nominal macroscopic strain of 0, 0.08, 0.16, 0.24, 0.32, and 0.4. The number of sections within the transition region is 4 for this simulation.

than the neighbor). This will in turn lead to higher gradients in the stress fields, which will give even more localized strain fields. This effect is seen in Figure 114 which shows the strain contours in the model at the same discrete points in loading as were used for the stress contours in Figure 113.

Figures 115 and 116 show the stress and strain contours respectively for the case of no transition region in the thread (here shown at nominal macroscopic strains of 0.1, 0.2, 0.3, and 0.4). In this case, the effect discussed above is even more pronounced, due to the vastly different constitutive models used in each section. As can be seen, the proximal section (the more compliant section) necks considerably at the transition, giving rise to large gradients in the stress and jumps in strain values at the interface. These contours are extreme in the sense that for all other transition cases (one transition, two transitions, four transitions, and eight transitions) the stress and strain contours are much more uniform (following the same patterns as discussed above in the four section case), and although necks and jumps in

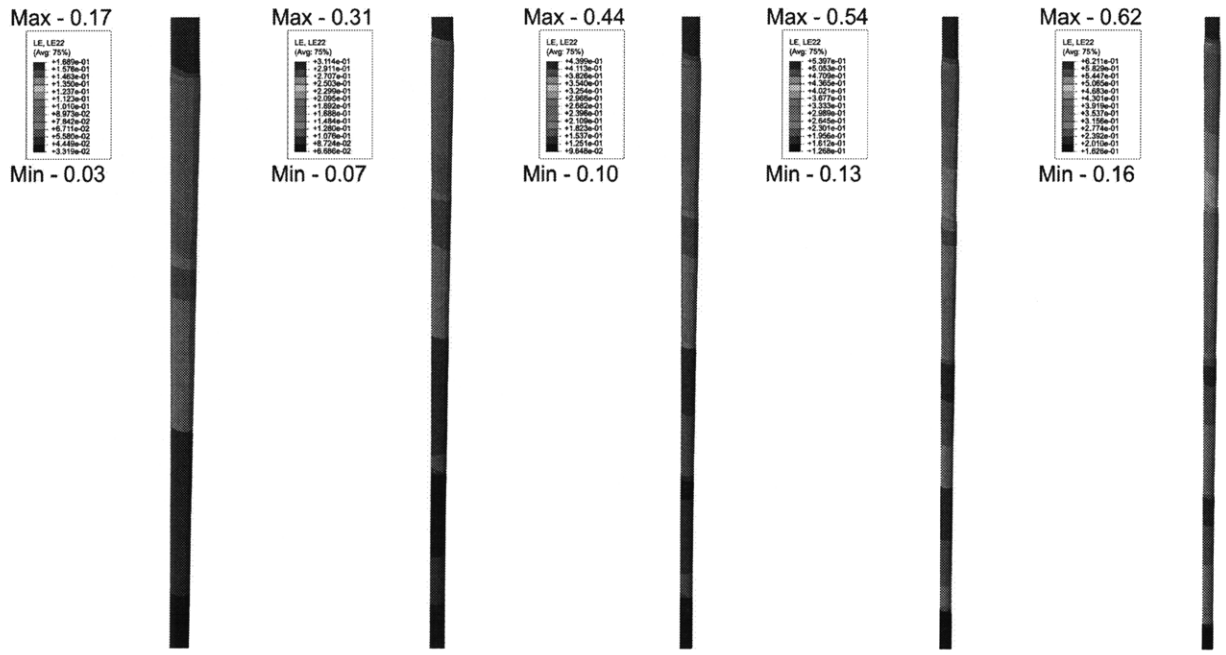

Figure 114: Strain contours for the transition section at nominal macroscopic strains of 0.08, 0.16, 0.24, 0.32, and 0.4. The number of sections within the transition region is 4 for this simulation. The elevated strain at the upper end of the contours reveals the strain concentration at the proximal-transition interface.

strain over interfaces are present, they are not as extreme. These results demonstrate that the 'smoothness' of the transition, both with regards to the transition in geometry and the transition in mechanical properties, is important for avoiding stress concentrations in the thread.

4.1.2 Stress, strain, and locking stretch variation along the thread

Just as the stiffness was plotted as a function of distance along the thread, so too can the local strain, local stress, and locking stretch be plotted as functions of the distance along the thread. As in the case of the stiffness, monitoring the evolution of local stress and local strain serve as a check on the smooth transitioning of mechanical properties in the transition regime; monitoring the evolution of the locking stretch determines whether or not structural evolution has begun (and when it begins) in each section. Figure 117 shows these values, as well as a normalized strain, $\hat{\epsilon} = \frac{\epsilon_{22}}{\bar{\epsilon}_{22}}$, taken at a point midway within each transition section

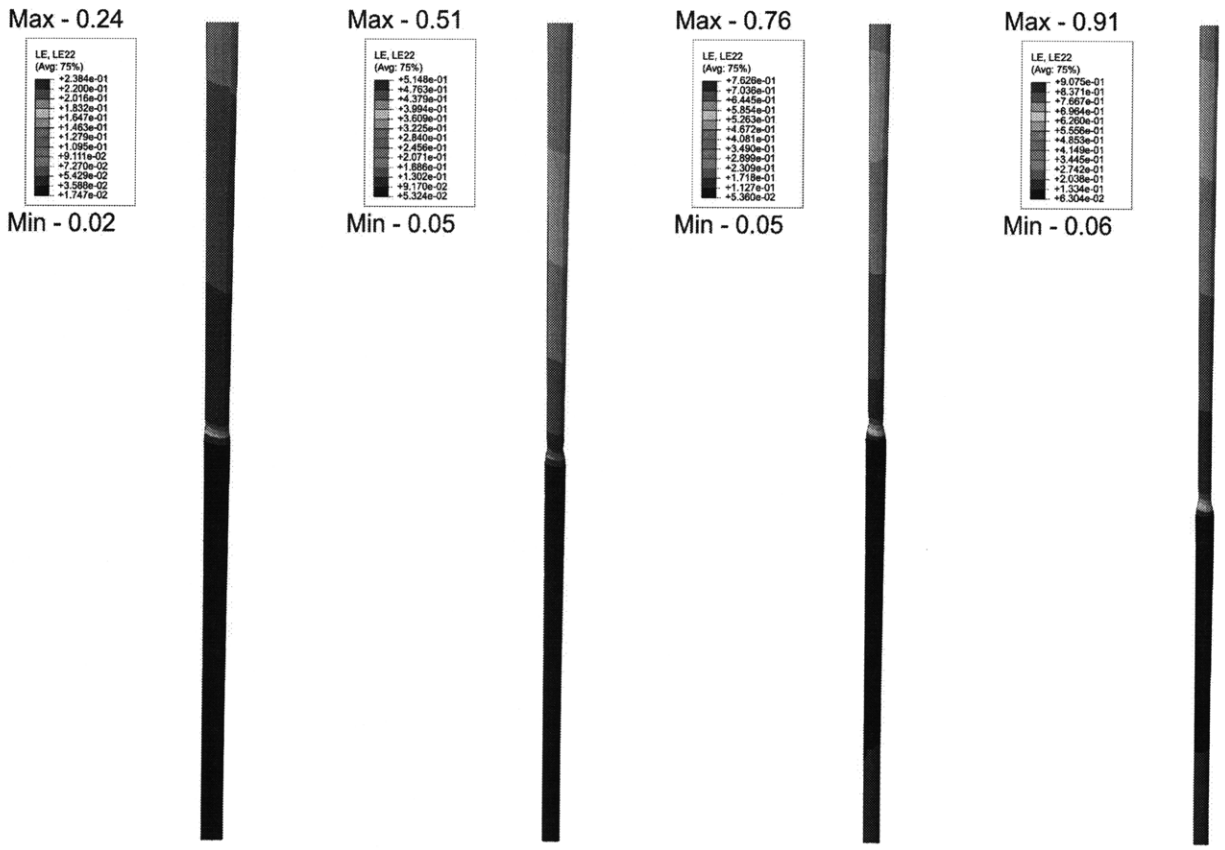

Figure 115: Strain contours for the transition section at nominal macroscopic strains of 0.1, 0.2, 0.3, and 0.4. There are no sections within the transition region for this simulation i.e. the distal section directly abuts the proximal section.

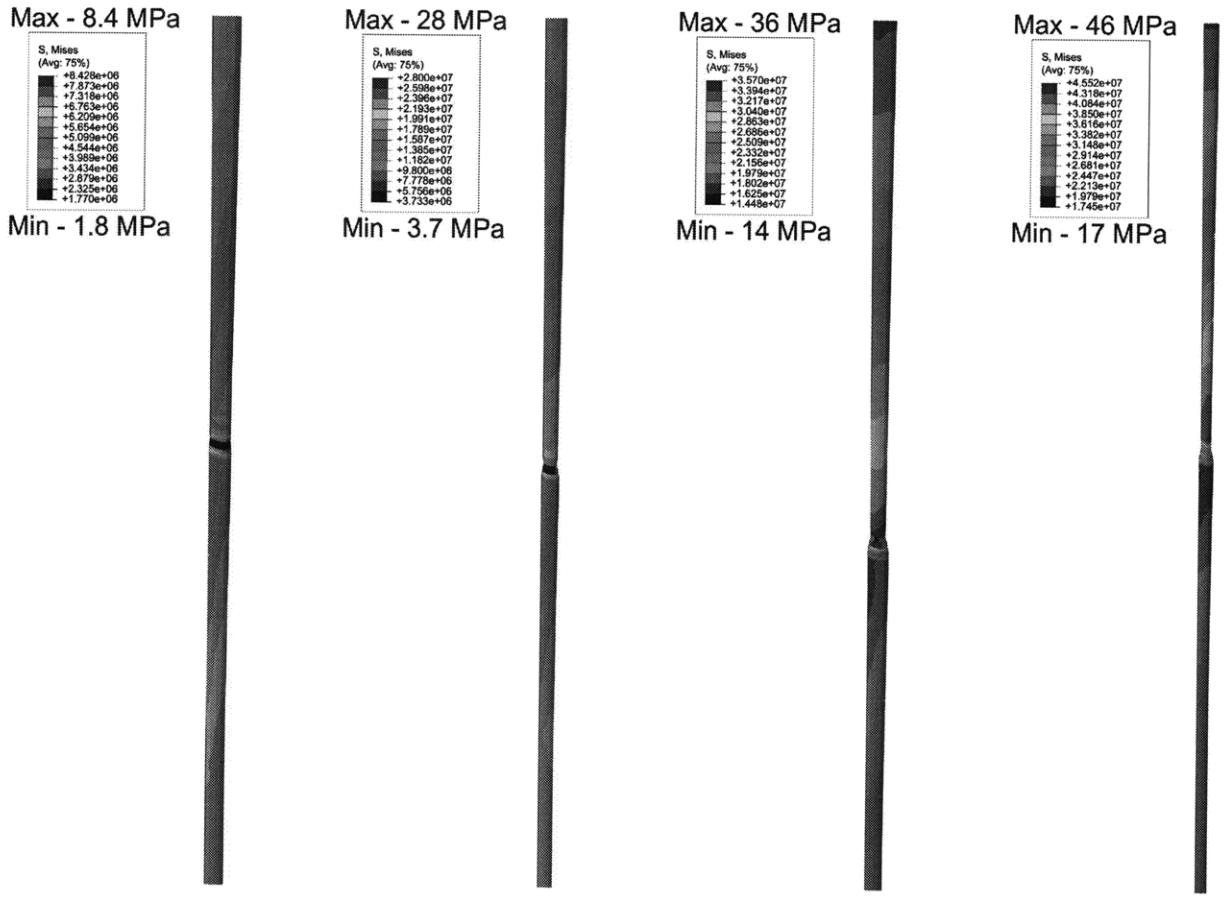

Figure 116: Mises stress contours of the transition section at nominal macroscopic strains of 0.1, 0.2, 0.3, and 0.4. There are no sections within the transition region for this simulation i.e. the distal section directly abuts the proximal section.

for the thread at a macroscopic strain of 0.1.

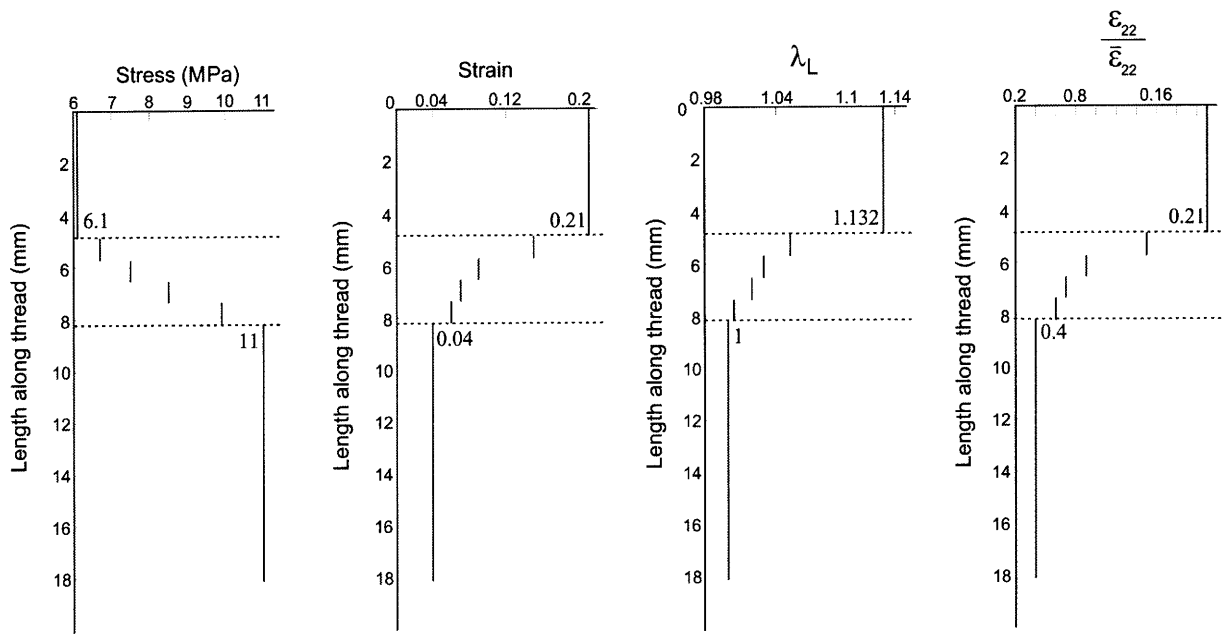

Figure 117: Local stress, local strain, normalized local strain, and locking stretch as a function of distance along the thread for loading at a macroscopic strain of 0.1. Horizontal dashed lines correspond to the points where the geometry begins to transition. Values shown are the values of the quantities in the distal and proximal sections.

As can be seen, the stress and strain contours transition relatively smoothly throughout the thread. The smoothest transition is seen in the stress, as is to be expected since the stress is simply the axial load on the thread divided by the cross-sectional area of the section. The strain contours transition smoothly (though less smoothly than the stress contours), with the majority of the initial strain (macroscopic strain less than 0.1) compensated by the proximal section and the transition section closest to the proximal section. For this low strain regime the distal section, and the three transition sections closest to the distal, experience relatively (relative to the strain in the proximal section) little strain, with the distal section experiencing almost zero strain. This result meshes well with what could be expected from the stiffness values of the different sections i.e. the most compliant regions (proximal and transition region closest to the proximal section) compensate the majority of the macroscopic strain.

Similarly, in the low strain case, the locking stretch does not significantly evolve in the distal and transition sections, while it begins to evolve in the proximal section (note that the locking stretch evolves a great deal in the proximal section relative to the distal and transition sections, but the magnitude of the locking stretch in the proximal section is still low - 1.1). This too is to be expected from the plots of locking stretch evolution shown in the constitutive modeling section of this thesis, since the locking stretch in the proximal section evolves at very low stresses (loads), while the locking stretch in the distal section does not significantly evolve until higher stresses. In the transition section, the evolution of locking stretch begins at intermediate stress levels (see Figure 109).

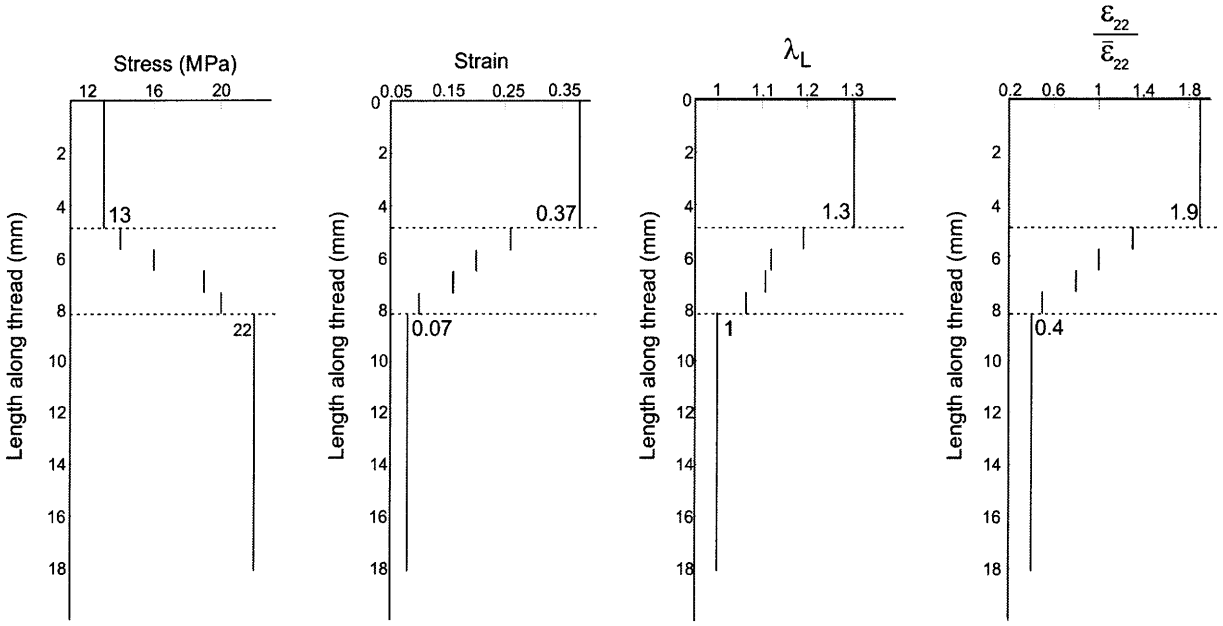

Figure 118: Local stress, local strain, normalized local strain, and locking stretch as a function of distance along the thread for loading at a macroscopic strain of 0.2. Horizontal dashed lines correspond to the points where the geometry begins to transition. Values shown are the values of the quantities in the distal and proximal sections.

Figures 118, 119, and 120 show similar plots for the same simulation (4 sections within the transition region), but for overall macroscopic strains of 0.2, 0.3, and 0.4. As can be seen, the stress continues to transition (relatively) smoothly throughout loading. For the two intermediate macroscopic strain cases (0.2 and 0.3), the stress appears to localize slightly

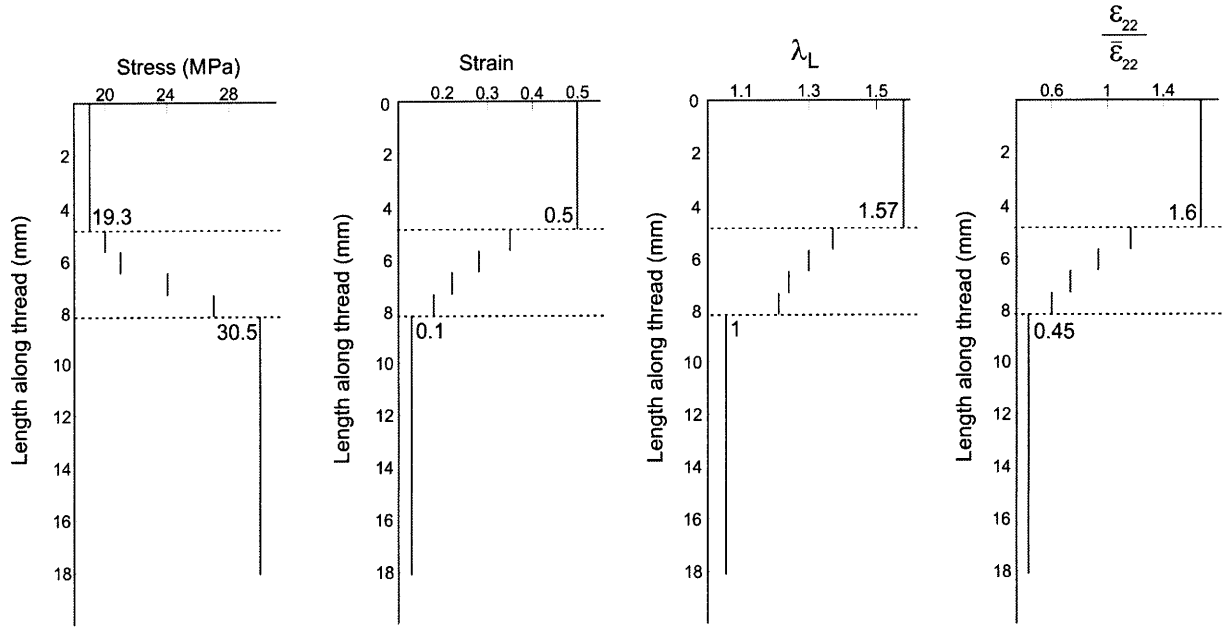

Figure 119: Local stress, local strain, normalized local strain, and locking stretch as a function of distance along the thread for loading at a macroscopic strain of 0.3. Horizontal dashed lines correspond to the points where the geometry begins to transition. Values shown are the values of the quantities in the distal and proximal sections.

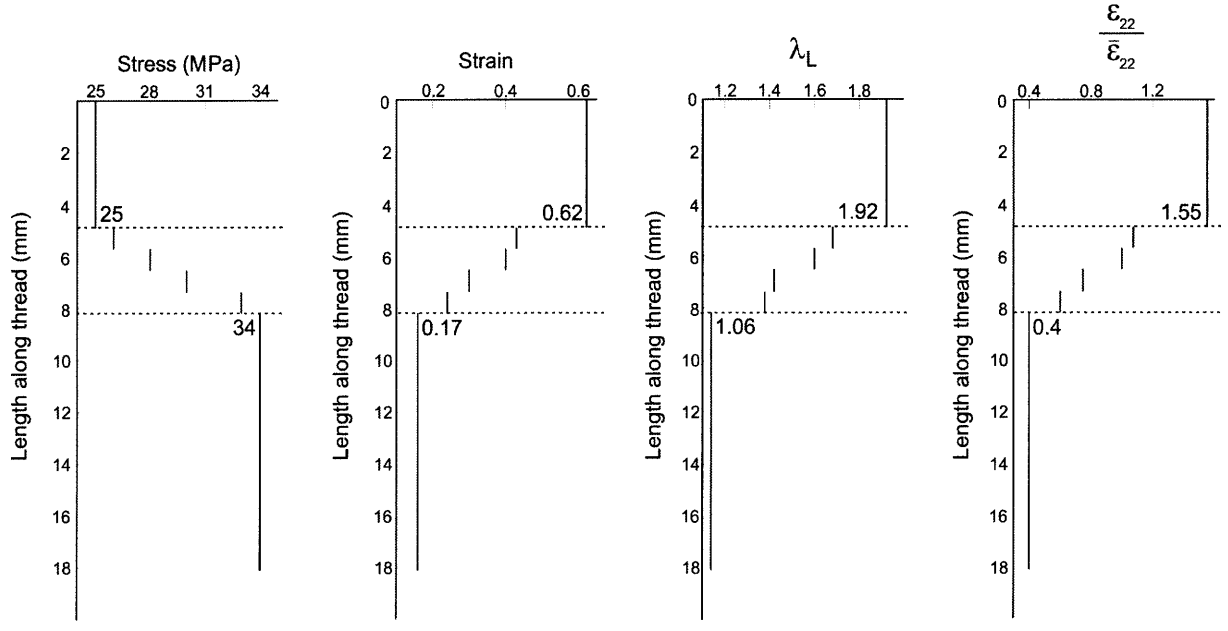

Figure 120: Local stress, local strain, normalized local strain, and locking stretch as a function of distance along the thread for loading at a macroscopic strain of 0.4. Horizontal dashed lines correspond to the points where the geometry begins to transition. Values shown are the values of the quantities in the distal and proximal sections.

(for the case of 0.2 macroscopic strain the stress localizes in the two transition regions closest to the proximal thread end, while for the case of 0.3 macroscopic strain the stress localizes in the two transition regions closest to the distal thread end). As discussed above, this result is not unexpected, as the localization of strain in the different thread sections will give rise to necking which will affect the stress in the section.

The strain contours in these intermediate macroscopic strain ranges begin to smooth out (from the skewed strain distribution seen at the lowest macroscopic strain), with the strain in the transition regions increasing. In spite of this smoothing, the 'jump' in strain from the proximal thread section to its nearest neighbor transition section is still quite large, while the 'jump' in strain from the distal thread section to its nearest neighbor transition section is relatively small.

For the case of a macroscopic strain of 0.2, the strain difference between the distal and its nearest neighbor transition section is especially low, while the strain difference between the proximal section and its nearest neighbor transition section is large (though smaller than in any of the other cases). Again, this corresponds well with the stress contours, since the stress is especially high in the proximal end of the transition section and especially low in the distal end of the transition section. For this strain, the locking stretch remains low in the distal section, though it increases in the transition and proximal sections, implying that microstructural evolution is occurring in the majority of the thread. Again, this result is to be expected from the stress-strain curves (Figure 109).

For the case of a macroscopic strain of 0.3, the strain difference between the proximal section and its nearest neighbor transition section is again quite high, while the difference between strain in the distal section and its nearest neighbor section is again low. In this case, the strains in the other transition sections are slightly closer to that seen in the distal section, which gives rise to the low stresses in the transition section for this macroscopic strain. For this macroscopic strain, locking stretch evolution (and consequently microstructural

evolution) has begun in all thread sections except the distal.

For the case of a macroscopic strain of 0.4 (the highest strain case), the straining in the distal region has now begun to more significantly contribute to the overall strain. As macroscopic strain (and overall load) increases, the thread begins to incrementally strain more evenly amongst sections. Here, the higher load magnitude has activated the microstructural evolution in all thread sections even the distal, where the small value of locking stretch in the distal section implies that the structural evolution in this section has only just begun.

It is important to realize that the values given above, and plotted in Figures 117 - 120, are the values of these properties taken at the midpoint of each section i.e. 'average values' in each section. Because the area transitions, the strain and stress in each section will not be constant, rather 'extreme' values of stress and strain will appear at the interfaces between sections. Looking at the 'extreme' strain value at the interface between the transition section and the proximal section and between the transition section and the distal section can lend insight into the lower-than-expected value of failure strain in the full thread. For the highest macroscopic strain case (macroscopic strain of 0.4), the strain at the proximal-transition interface is 0.62, while the strain at the distal-transition interface is 0.23. Although these values are less than the failure strain in either section individually, it is apparent that the values of strain at these interfaces (especially at the proximal-transition interface) are tending towards the failure strain of the individual sections rapidly. Note that this will also be heavily dependent on the number of transition sections used.

4.2 Load-Strain Behavior

From the previous section's discussion of the 'smoothness' of the transition of stress and strain in the thread (based on the number of discrete sections in the transition region), it is apparent that a smooth transition of mechanical properties is necessary in order to avoid strain and stress concentrations in the material. However, this analysis provides little insight

into how the smoothness of the transition of mechanical properties affects the load-strain behavior of the thread. To gain insight into this aspect of the thread's behavior, the load-strain response of the model for each simulation (0 transition sections, 1 transition section, 2 transition sections, 4 transition sections, and 8 transition sections) is plotted in Figure 121.

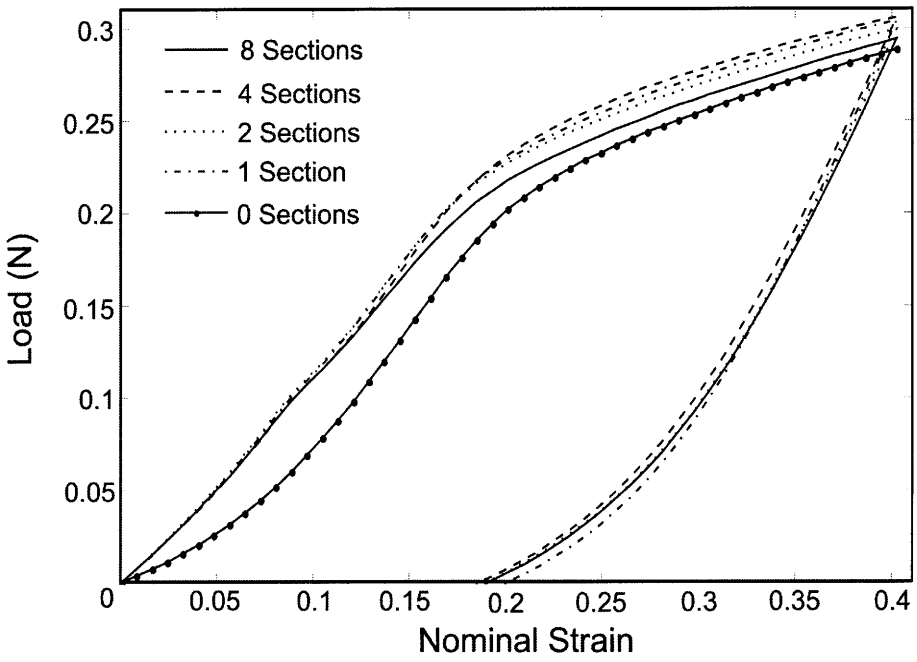

Figure 121: Load-strain curves for loading and unloading of mussel byssal threads at a nominal strain rate of approximately $0.1s^{-1}$. Solid line corresponds to 8 discrete sections in the transition, dashed line corresponds to 4 discrete sections in the transition, dotted line corresponds to 2 discrete sections in the transition, dotted-dashed line corresponds to 1 discrete section in the transition, and solid line with dots corresponds to zero section in the transition. Note that the test with no transition region does not show unloading, because for this test the large stress concentration at the transition caused a distorted mesh as unloading began.

As can be seen, the number of sections used to model the transition region does not have a major effect on the overall thread load-strain curves, with the exception that for the zero transition case, the model predicts a more compliant response throughout loading than in any of the other cases. The number of transition sections does slightly change the 'yield' stress in the simulations as well as the slope of the post-'yield' curve, though this is likely a result of the mechanical properties chosen for the transition sections as opposed to the actual number of sections, since there is no obvious pattern for the change in 'yield' stress

i.e. the yield stress is highest in the 4-section model, and lowest in the 8-section model, with the 1- and 2-section models falling in between.

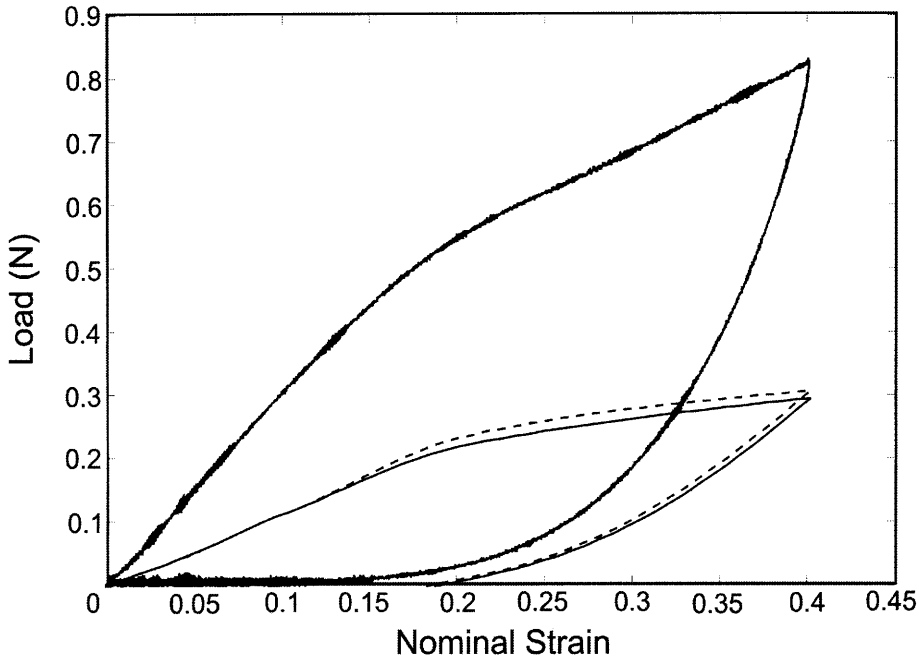

Figure 122: Experimental full thread load-strain curves (heavy black line), the load-strain curve predicted by the 4-section model (dashed line), and the load-strain curve predicted by the 8-section model (solid line).

Figure 122 shows the load-strain response for the 4- and 8-section case (dashed and solid lines respectively) compared to the experimental results (solid lines). As can be seen, the model significantly underpredicts the load for all strains. However, the curves are similar. In both cases (experimental results and both simulations) the load-strain curves exhibit an initially stiff response, followed by a smooth rollover-type 'yield', and a roughly constant post-'yield' tangent stiffness. In all cases the unloading is non-linear with a stiffness roughly equal to the initial stiffness.

The most likely reason for the discrepancy between the experimental results and the models' predictions is the time of year in which the specimens were collected. As discussed in the mechanical testing section of this thesis, the stiffness of blue mussels is heavily dependent on season, with the strongest (stiffest) threads produced in late winter/early spring, and the weakest threads produced in late summer [20]. Recall that the data on the distal and

proximal sections were collected on 'summer' mussels, while the data on the full threads was collected on 'winter' mussels. The constitutive models for the distal and proximal sections reflect 'summer' mussels and hence the full thread simulations reflect the behavior of the full threads of 'summer' mussels. The experimental curves reflect the behavior of the full threads of 'winter' mussels. However, noting that the stiffness of mussel threads decreased by approximately 60% from 'winter' mussels to 'summer' mussels in the Moeser and Carrington study, the experimental results can be scaled to account for this seasonal variation. The load-strain behavior for the scaled full threads are plotted against the results from the simulations in Figure 123. This result implies that seasonal variation in stiffness could certainly account for the discrepancy in stiffness highlighted in Figure 122.

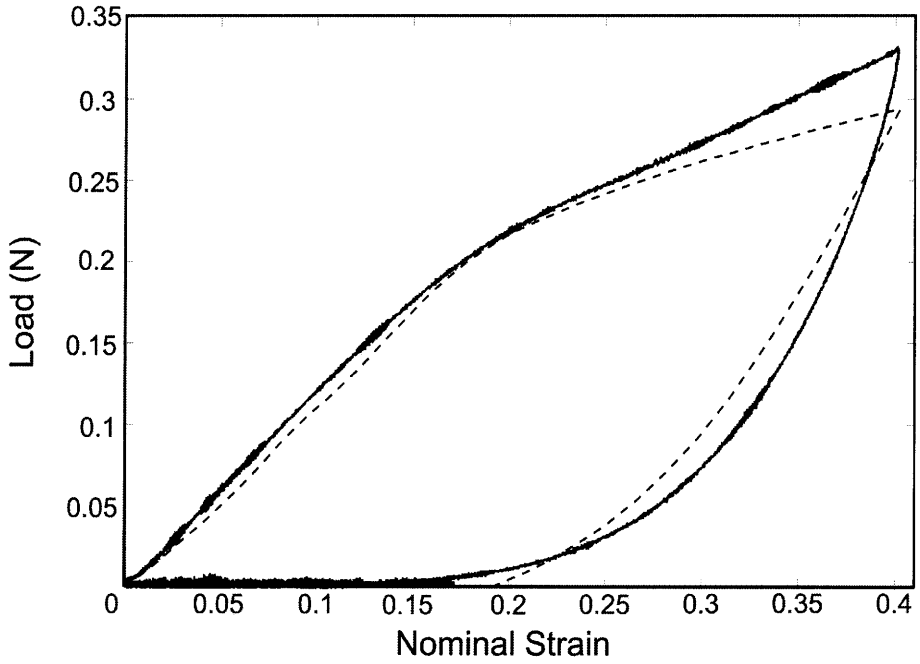

Figure 123: Load-strain curves for the experimental results taking into account the variation in stiffness from early spring to late summer i.e. at 40% the original stiffness, and for the simulation using the thread model with 8 sections in the transition region.

4.3 Evolution of Strain in the Proximal and Distal Thread Sections

As shown in Figure 51, the strain in each section (proximal and distal only, here the transition section is not shown since the strain varies throughout the transition) of the thread can be measured by videotaping the evolution in deformation during loading. Similarly, the strain in each section of the finite element model during loading can be monitored. Figure 124 shows the strain in each section of the model during loading. As can be seen, the strain in each section is roughly linear, with the strain in the proximal section much greater than the strain in the distal section. This result corresponds well with the previous discussion of relative stiffness in the two regions, as well as the discussion of locking stretch evolution in the distal section during loading. As highlighted in that discussion, initially the strain should be compensated by the proximal section, but after the distal section yields, the strain should be compensated by the distal section. As highlighted in the locking stretch evolution discussion, the locking stretch in the distal section of the model does not begin to evolve until the end of loading (only at the highest macroscopic strain is any evolution seen, and even at that highest macroscopic strain, the evolution is very slow). Thus, with no real yield in the distal section, no change in the slope of the local strain-macroscopic strain curves would be expected.

Strong agreement between the experimental results and the model's predictions are seen regarding the strain in the distal section vs. that seen in the proximal section up until a macroscopic strain of $\bar{\epsilon} = 0.2$. After this strain, the experiment and simulation depart, where the experiment reveals that the distal begins to significantly strain (suggesting that unfolding has begun), while the strain in the proximal section begins to taper off. The simulation has not yet reached this point, and the distal sections remains in its initial linear stiffness regime. Thus, the simulation predicts that the distal strain vs. macroscopic strain

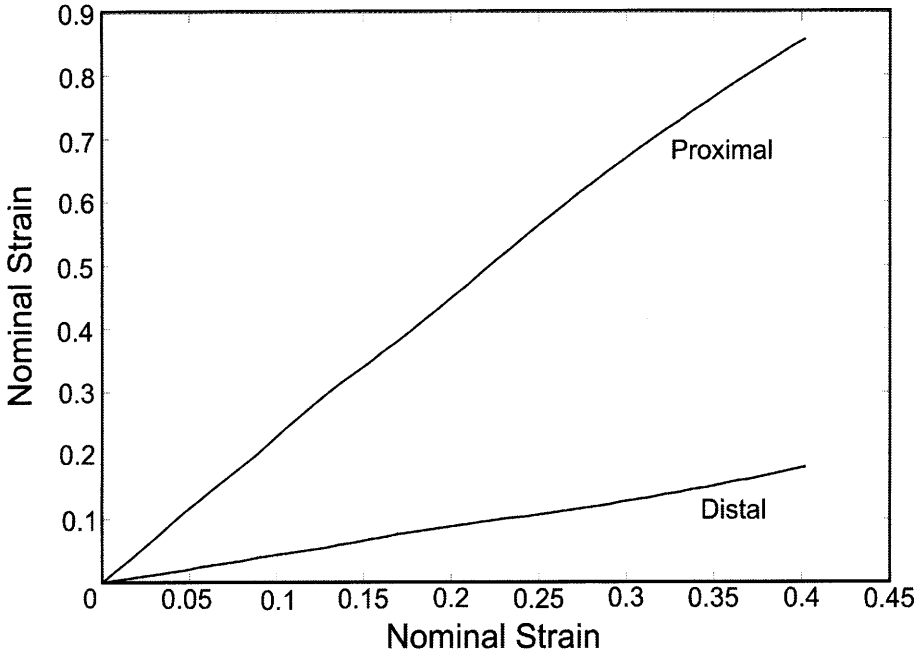

Figure 124: Local strain vs. macroscopic strain for the model (8 sections in the transition region).

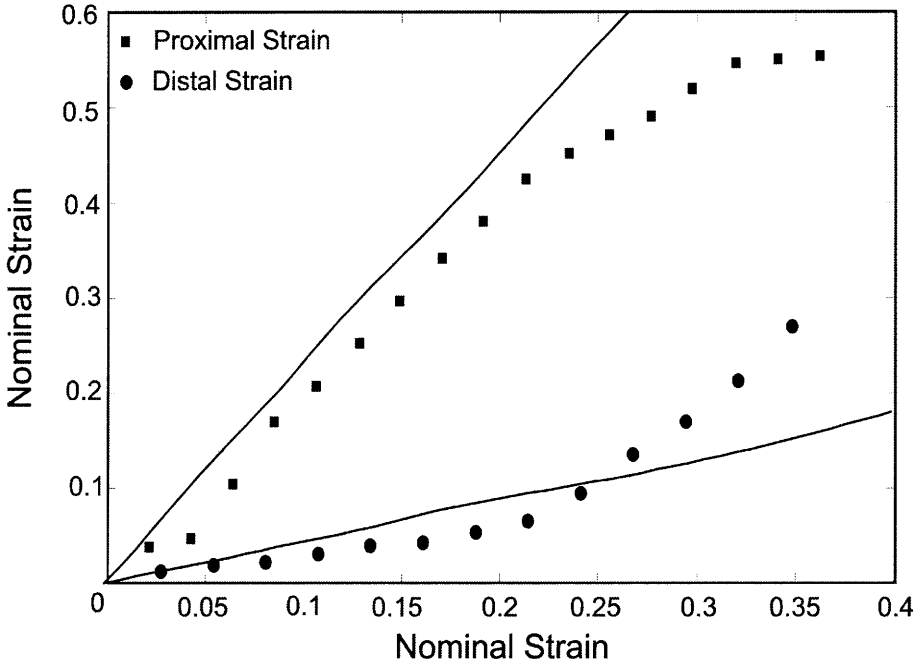

Figure 125: Local strain vs. macroscopic strain for loading simulations of the full thread model at a nominal strain rate of $0.1s^{-1}$.

(and consequently the proximal strain vs. macroscopic strain) curves remain roughly linear. However, the transition section has begun to unfold/evolve, which accounts for the yield

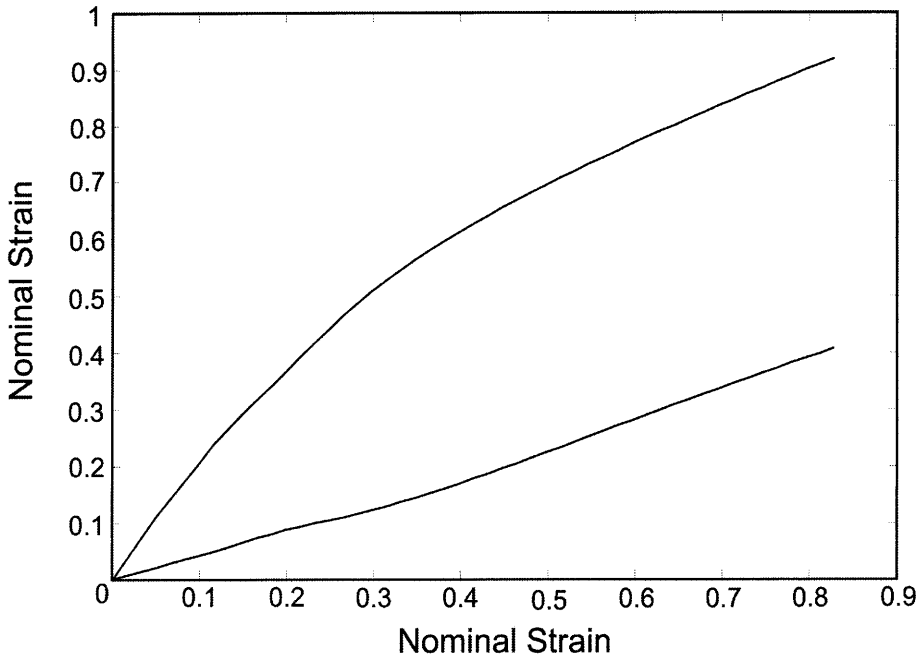

Figure 126: Local strain vs. macroscopic strain for loading simulations of the full thread model at a nominal strain rate of $0.1s^{-1}$ to a maximum macroscopic strain of 0.8

seen in the load-strain curve.

As stated above, the maximum macroscopic strain applied in this simulation corresponds to the macroscopic strain at which unfolding in the distal section begins. Thus, a simulation going to a higher strain should predict a change in the slope of the local strain-macroscopic strain curves similar to that seen in the experimental results. Figure 126 shows the local strain vs. macroscopic strain curves for a simulation going to a macroscopic strain of 0.8. As can be seen, at a strain of approximately 0.4 (the maximum macroscopic strain in the previous simulation) the model predicts that the strain will begin to increase more rapidly in the distal section and more slowly in the proximal section. However, even in this case, the sharpness of the change in slope of the distal section is not as prominent as in the experimental results.

Again, it is possible that this discrepancy is a result of the seasonal variation in the mechanical properties of the threads (if the distal section is stiffer in winter threads, and the unfolding event occurs at the same force, the yield will occur at a smaller strain). Indeed,

for a more compliant proximal section (the proximal section is much more compliant than the distal section regardless of season), the distal section will experience a smaller local strain than the macroscopic strain applied. Since the 'yield' event (as measured by the rapid increase in distal strain) occurs at a macroscopic strain of 0.2 - 0.25, which should correspond to a local strain in the distal section of less than 0.1, it is unlikely that the distal section yields at the same strain in winter and summer threads (note that the rollover in the simulation's load-strain curves is correlated with 'yield' in the transition region). It is not possible to account for a seasonal variation in the strain at unfolding in the same way as accounting for the stiffness of the thread. But, it is possible to change the geometry of the model so that the distal section yields earlier.

Another possible reason for this discrepancy is that the experimental results may really be sampling the strain in the transition region close to the distal section. As stated in the mechanical testing section of this thesis, because of the small size of the threads it can be difficult to pinpoint exactly where the distal (or proximal) section ends and the transition region begins.

This simulation also serves to highlight another point discussed above (that of 'extreme' local strain causing failure in the full thread). For this simulation the strain at the proximal/transition interface is approximately 0.95. Again, this strain is less than the average failure strain in the proximal thread section. However, it is close to the failure strain in the distal section (the failure strain in the distal section is 0.88, here the true strain is approximately 0.7), and could certainly be greater than the average failure strain in the transition section.

4.4 Varying the section lengths

One way to change the geometry so that the distal section yields prior to a macroscopic strain of 0.4 is to vary the lengths of the sections (proximal, distal, and transition). A full range

of simulations, varying the lengths of each section separately is not discussed in this thesis. However, to highlight this feature (changing section lengths gives different behaviors), the proximal and distal sections of the thread were shortened by $3mm$, giving an overall thread length of $12.1mm$. The load-strain curves comparing the results of these simulations with the results of the previous simulations and the experimental data are shown in Figure 127.

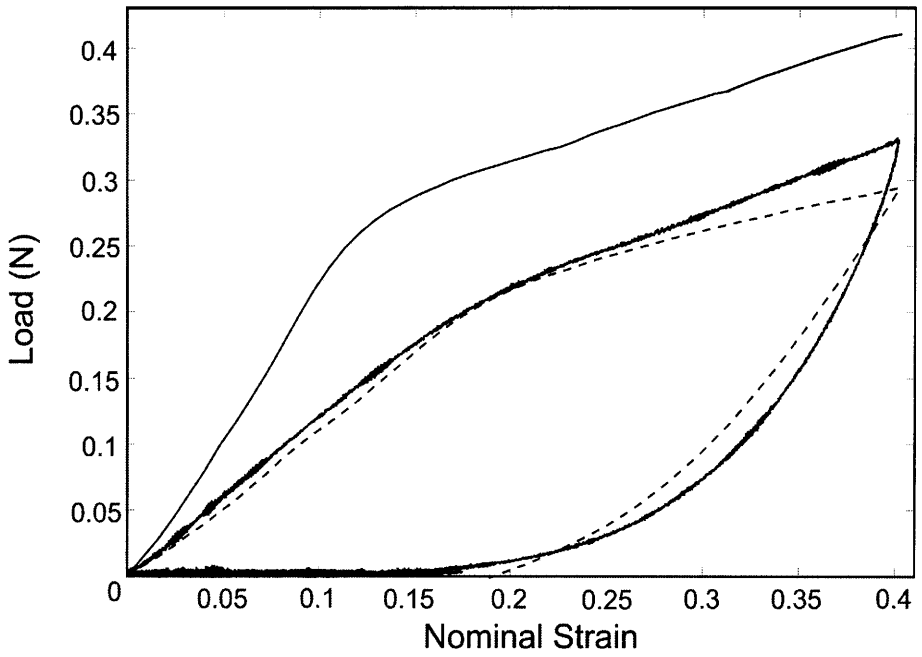

Figure 127: Load vs. nominal strain for full thread simulations and experimental results (with the reduced stiffness). The heavy black line corresponds to experimental results. The dashed line corresponds to the simulations using the average section lengths (8 transition sections). The light solid line corresponds to the simulation using the shortened proximal and distal section length (also with 8 transition sections).

As can be seen, the load-strain response of the shortened thread has a higher initial stiffness, a slightly lower 'yield' strain (higher 'yield' stress), and predicts a stiffer response post-'yield. This is to be expected, since in cutting $3mm$ off of the proximal section, 61% of the sections overall length is removed, while for a cut of the same length in the distal section, only 30% of its original length is removed. Essentially, this variation forces the entire thread to act more like the distal section.

Local strain vs. macroscopic strain curves for the experimental results, the 4-section long model, and the short model are shown in Figure 128. As can be seen, the short model does a

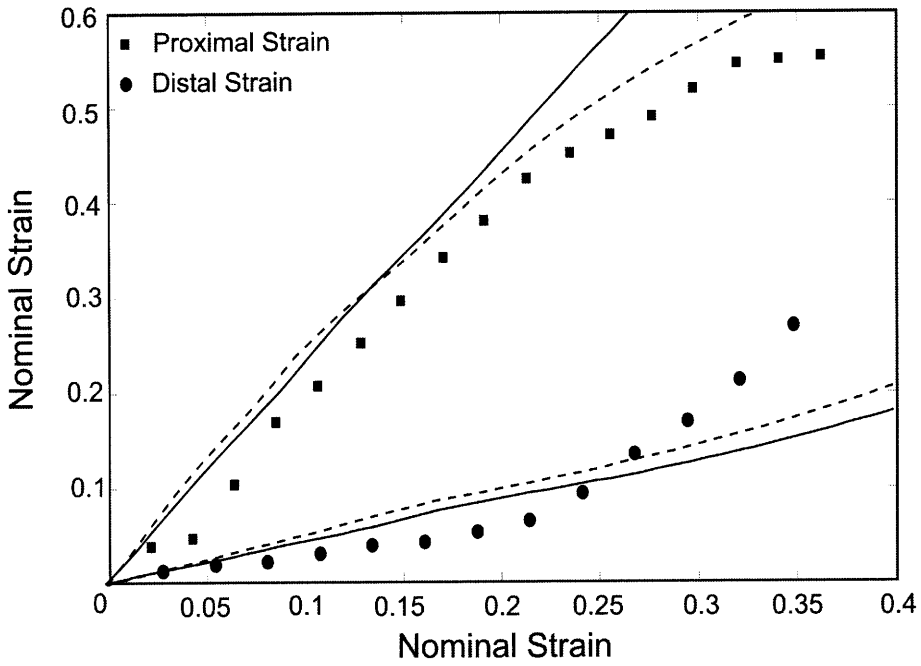

Figure 128: Local strain vs. macroscopic strain for experimental tests of the full thread (squares correspond to proximal strain, and circles correspond to distal strain), simulations using the 8-section long model (solid lines) and the short model (dashed lines).

much better job of predicting the strain in the proximal thread section throughout the range of loading (though again the prediction is slightly high for all strains). Again, the model fails to capture the strain in the distal thread section, underpredicting the local strain at high macroscopic strains. Such a result implies that the model is not capturing the dramatic nature of the 'yield'.

5 Conclusions and Future Work

A comprehensive set of uniaxial tensile tests was conducted on mussel byssal threads (individual thread sections and full threads) to characterize the mechanical behavior of this material. The stress-strain behavior was found to vary along the length of the thread, with the distal behavior characterized by a stiff, relatively rate-independent initial modulus, a rate-dependent 'yield' event, a post-'yield' stress plateau, and significant hardening at high strains. In unloading the distal behavior is characterized by a highly non-linear response, revealing the large post-yield deformation to be strongly dissipative with the proportion of energy dissipated increasing with an increase in the strain of the loading cycle. In reloading the distal behavior demonstrates a more compliant response (relative to the initial loading behavior), with the stiffness of the reloading behavior increasing with the amount of time between cycles. The proximal section demonstrates a much more compliant response characterized by a roughly linear true stress-true strain response up to high strains. Like the distal section, the proximal stress-strain behavior is highly rate-dependent, demonstrating increased stiffness for increasing applied strain rate at all strain levels. In unloading, the proximal section exhibits a highly nonlinear unloading behavior revealing the deformation to be highly dissipative, with the amount of dissipation increasing with the maximum strain of the loading cycle. Again, as in the distal section, in reloading the proximal behavior demonstrates a more compliant and highly nonlinear reloading response (relative to the initial loading behavior), with the stiffness of reloading increasing with the amount of time between load cycles. Full threads demonstrated an initially stiff response, with a soft 'rollover'-type yield (similar to that seen in the distal section, but with a gentler rollover). Like the proximal and distal thread sections, the full thread demonstrated a non-linear unloading response revealing a highly dissipative behavior.

Using the mechanical behavior together with microstructural descriptions of the material

collected from the literature, a microstructurally-informed constitutive model of each material (distal and proximal sections separately) was developed. The model, which is based primarily upon the behavior of protein networks and the unfolding of 'giant folded-domain proteins', captures the stretching and unfolding of proteins in a 3-D network. During the development of the final constitutive model, several models for the mechanical behavior of proteins (with special emphasis paid to the mechanics of protein unfolding) were investigated, and the merits and flaws of these models were discussed. The final model is able to capture all of the major components of the mechanical properties of both the distal and the proximal thread sections, including the initial stiffness, the rate-dependence, the 'yield' in the distal section, the non-linear unloading, the large hysteresis, the cyclic softening, and the time-dependent reloading behavior.

These material models were then implemented into a 3-D nonlinear finite element model of the full thread, and simulations of loading were conducted on this thread model. The model predicted the load-strain behavior of the full thread well, as well as the strain in each section of the thread during loading (as was acquired via video imaging of full thread loading experiments). The model provides insight into the structure and function of graded materials, as both the geometry (cross-sectional area) and the mechanical properties of the thread vary from the distal thread section to the proximal thread section.

The model developed and outlined herein provides a straightforward method for the modeling of mechanically-induced protein unfolding, and can be applied to the unfolding of any long-chain macromolecule. The 3-D finite element model provides insight into materials and structures with graded properties, and demonstrates how the 'smoothness' of the transitions (i.e. the smoothness of the transitions in geometry and the smoothness of transitions in mechanical properties) of a graded structure affects the loading behavior of the structure. Further, the 3-D model elucidates the role of microstructural evolution in load-sharing between connected materials, and demonstrates how two materials can interact

to maximize the amount of dissipation in a structure, without sacrificing resiliency. Finally, the 3-D model provides insight into the underlying mechanisms for connecting soft tissues to hard substrates, especially with regards to the role of the distal section's stress-plateau in limiting the maximum level of stress transmitted to the connection.

Although this thesis discusses several interesting properties and behaviors of mussel byssal threads, there are many aspects of these threads that remain to be investigated. First, the properties of the transition region should be investigated (most likely via nano-indentation). With this information, a better 3-D finite element model can be constructed. In its current state, the model uses a smooth but discretized and linear transition of mechanical properties. The actual transition in material properties would be continuously smooth and may not be linear. Second, different thread models should be built, varying the lengths of the proximal, distal and transition sections. Such models (both models with different section lengths and models that use different mechanical properties for the transition section) can help to elucidate novel and optimal methods of designing and building graded structures. Finally, the interaction between the thread and the stem and also between the thread, plaque, and rock should be investigated, and simulated. Such simulations could provide a better understanding of the slipping/locking (depending on the direction of pulling) interaction between the thread and the stem and of the soft-to-hard connection interaction between the thread, plaque, and rock, which are themselves interesting engineering applications.

6 Appendix I: Determination of Material Parameters

Table 12 gives the final values of the mechanical properties used in the proximal and distal thread models. Several of these parameters are taken from previous literature (e.g. the length and cross-sectional area of the fiber bundles is taken from Hassenkam et. al. [11]), while others (like the Young's Modulus of the filament bundles and the shear and bulk moduli of the matrix) must be determined experimentally.

6.1 Determination of the fiber Young's Modulus

The fiber bundles' Young's Modulus can be determined by looking at stress-stretch curves (see Figure 129). For the distal thread section, the initial stiffness of the curves is the same at all strain rates, and unfolding of folded protein domains does not occur until a true strain of approximately 0.2. Further, the bundles are more aligned (relative to the proximal thread section) with the thread axis. Thus, we infer that the initial stiffness seen in the stress-strain curves corresponds to the derivative of the fiber network stress with respect to stretch.

Noting the value of the slope shown in the figure (approximately $316MPa$), the derivative of the network stress with respect to stretch is calculated. For this derivative, the angle of orientation is ignored, the stretch in the middle section is approximated as the overall fiber stretch, and the determinant of the deformation gradient is taken to be one. These approximations introduce a slight error into the calculated value of E, but make the calculation of the derivative trivial. The derivative becomes:

$$\frac{\partial \mathbf{T}}{\partial \lambda_f} = \nu E A r_0 \left(\frac{1}{\lambda_f^2} \right) \tag{77}$$

Evaluating this function at a stretch of 1 i.e. taking the initial slope of the curve, yields a Young's Modulus of approximately $80GPa$. In the final model, $23GPa$ is found to best match the experimental results. Thus, this method provides an estimate of the Young's

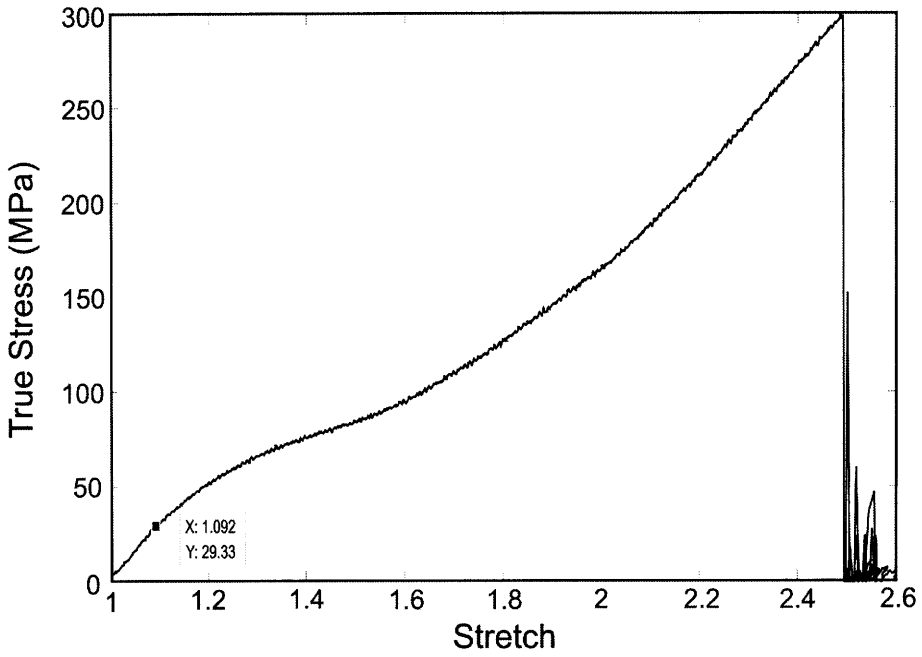

Figure 129: Stress vs. stretch for the distal thread section. A point on the curve in the initial linear elastic regime (stretch = 1.07, stress = $29.33MPa$) is highlighted to show the initial slope of the stress-stretch curve).

Modulus, not an exact value.

Estimating the Young's Modulus for the proximal thread section is more difficult. In this case, the fibers are not aligned with the thread axis, so the initial slope of the stress-stretch curve will be more compliant as the fibers rotate and align with the axis. Further, unfolding begins right away in the proximal section, causing the stress-stretch behavior to be even more compliant. However, the initial unloading curve can give an estimate of the Young's Modulus, if we assume that the inner rod-like domain is much stiffer than the folded end domains. This is because for unloading two springs in parallel, the stiffer spring will unload first, followed by the more compliant spring. In this case, this means that the rod-like domain will unstretch first, followed by the end domains.

Thus, looking at the experimental results (Figure 130), the slope of the initial unloading curve can be determined to be approximately $500MPa$. Taking the same derivative, and using the same approximations gives a value of the Young's Modulus of approximately

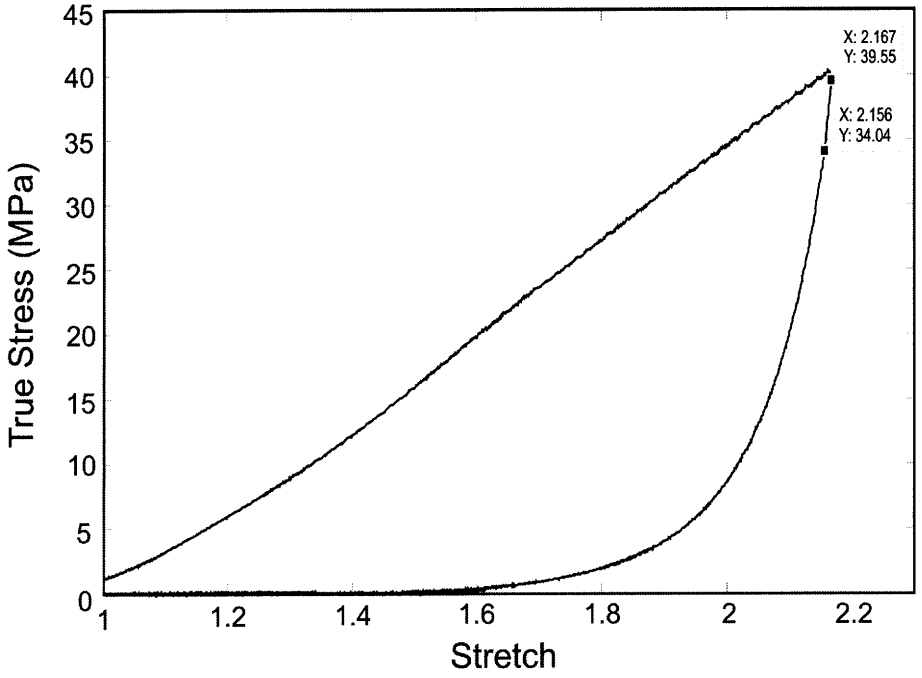

Figure 130: Stress vs. stretch for the proximal thread section. Two points at the beginning of the unloading curve are shown to highlight the initial slope of the unloading curve.

$2625GPa$. Again, this is very close to the final value of $3000GPa$, which was used in the constitutive model.

6.2 Determination of the Unfolding Constants

As discussed in the constitutive modeling section of this thesis, initially a linear locking stretch evolution equation was used. This equation:

$$\dot{\lambda}_L = \alpha_u \left(\lambda_{LMax} - \lambda_L\right) \exp\left[\frac{f_f X_u}{K_B \Theta}\right] \tag{78}$$

can be rearranged to form an equation for force as a logarithmic function of the rate of locking stretch evolution:

$$f_f X_u = K_B \Theta \ln\left(\dot{\lambda}_L\right) - K_B \Theta \ln\left[\alpha_u \left(\lambda_{LMax} - \lambda_L\right)\right] \tag{79}$$

Thus, plotting force vs. the logarithm of the rate of locking stretch evolution yields a straight line. The equation of this line can be fit to the above equation, yielding values for X_u and α_u.

Again, as in the case of the Young's Modulus derivation above, several approximations must be made, and the values acquired for X_u and α_u will be approximate values only. For example, since no single protein experiments were conducted, there are no experimental load-displacement curves for single protein bundles. Further, because the equation is phenomenological, the locking stretch is not a physical (measurable) parameter. As an approximation, we say that the rate of evolution of the locking stretch is the same as the rate of evolution of the overall stretch on the protein bundle, and that this rate of evolution of stretch is:

$$\dot{\lambda_L} = \dot{\lambda} = \dot{\epsilon} \tag{80}$$

where $\dot{\epsilon}$ is the nominal strain rate applied to the specimen. Next, the load on an individual bundle can be related to the nominal stress during testing:

$$f_f = \sigma A_0 \left(\frac{1}{\nu_A}\right) \tag{81}$$

where σ is the nominal stress, A_0 is the original cross-sectional area, and ν_A is the number density of fibers per unit area, which can be calculated by multiplying the number density per unit volume by some characteristic length. For this case, with a number density of fibers per unit volume of approximately $1\,(10^{20})$, and a fiber contour length of $300\,(10^{-9})$, the areal number density of fibers becomes approximately $3\,(10^{13})$. Figure 131 shows the force on a fiber bundle vs. the logarithm of the rate of evolution of the locking stretch (calculated using the above methods). From these equations, the values of the parameters in the distal section were found to be $X_u = 6\,(10^{-7})$ and $\alpha_u = 1\,(10^{-1})$. These values are approximately three orders of magnitude different from the final values used in the model. Aside from the

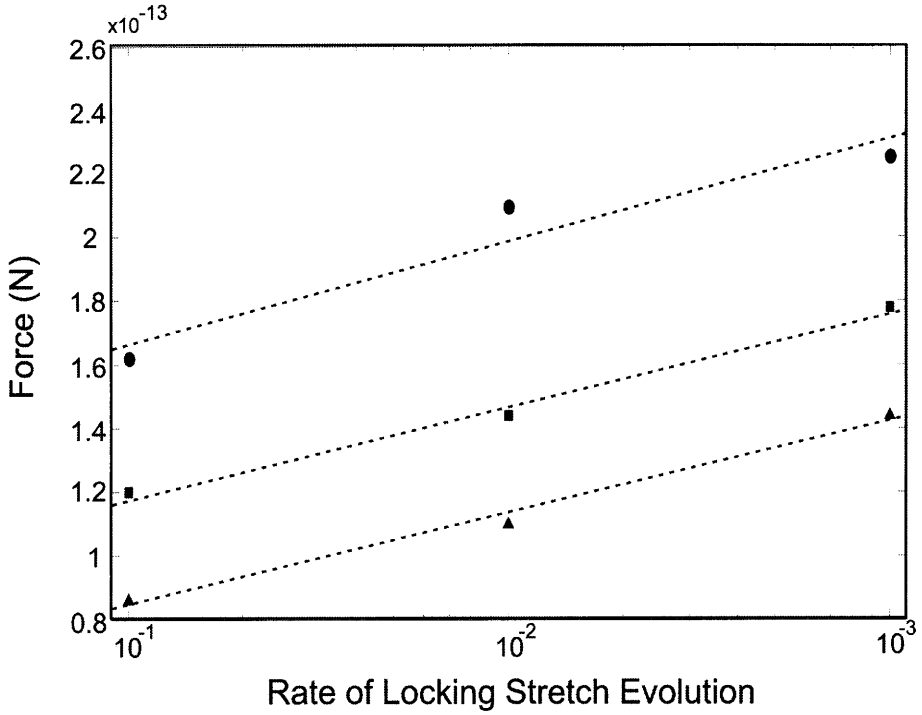

Figure 131: Force on an individual protein bundle (extrapolated from the above equations) vs. the rate of locking stretch evolution for the three locking stretch values (1.1 - lowest curve; 1.5 - middle curve; 2.1 - highest curve). Dotted lines show the linear fit to the curve.

error introduced by the approximations made, this difference also arises from the fact that the linear equation was solved to find these values, while the final model is nonlinear. The values for these parameters that provided a reasonable fit in the linear model were only an order of magnitude different from the calculated. Similar methods were used to determine the values of the constants in the proximal section.

Notice that the reverse process was neglected in the above discussion. This is because in loading the reverse process does not play a significant role in the evolution of the locking stretch. In unloading, for low enough forces, the opposite is true, namely that the reverse process dominates while the forward process does not significantly affect the evolution of the locking stretch. A similar analysis can be carried out for the reverse process, and α_r and X_r can be determined.

6.3 Determination of the Matrix Properties

The matrix, as discussed above, is modeled as a nearly incompressible Neo-Hookean material. This implies that the bulk modulus is much greater than the shear modulus i.e. $K \gg \mu$. Further, the matrix is taken to play only a small role in the overall stress-strain behavior of the material, so that the shear modulus of the matrix should be much less than the Young's modulus of the fibers i.e. $E \gg \mu$. Thus, an arbitrary 'small' value is assigned to the shear modulus in the proximal thread section. Assuming that the matrix should be roughly homogeneous throughout the material, the shear modulus of the matrix in the distal section should be roughly equal to the shear modulus of the matrix in the proximal section. In this case the shear modulus of the matrix in the distal section was increased slightly to correspond with the increased overall stiffness of the distal thread section.

The viscoelasticity of the matrix was determined by looking at the residual stresses in the material. Initially the viscoelastic element was modeled as linear, with a shear strain rate given by $\dot{\gamma} = \frac{\tau}{\eta}$, where τ is the magnitude of the shear stress, and η is the material viscosity. However, such a model predicted too much rate-dependence (see Figure 132) i.e. the linear model predicted that for a slower strain rate, the amount of residual strain in the material would increase dramatically.

Thus, a non-linear viscoelastic element (characterized by the constitutive model highlighted in the constitutive modeling section of this thesis) was chosen. The non-linear viscoelastic element was able to capture the rate-dependence of the residual strain more accurately. The material parameters (Ω and α_{ve}) were chosen so that the 'yield' point in the viscoelastic matrix corresponded to the 'yield' point in the fiber network. For any other values of Ω and α_{ve} 'bumps' appeared in the overall stress-strain curve corresponding to the 'yield' points in the matrix.

It should be noted that the non-linear viscoelasticity is not the best possible representation of what is physically happening in the matrix, as such a non-linear response implies some

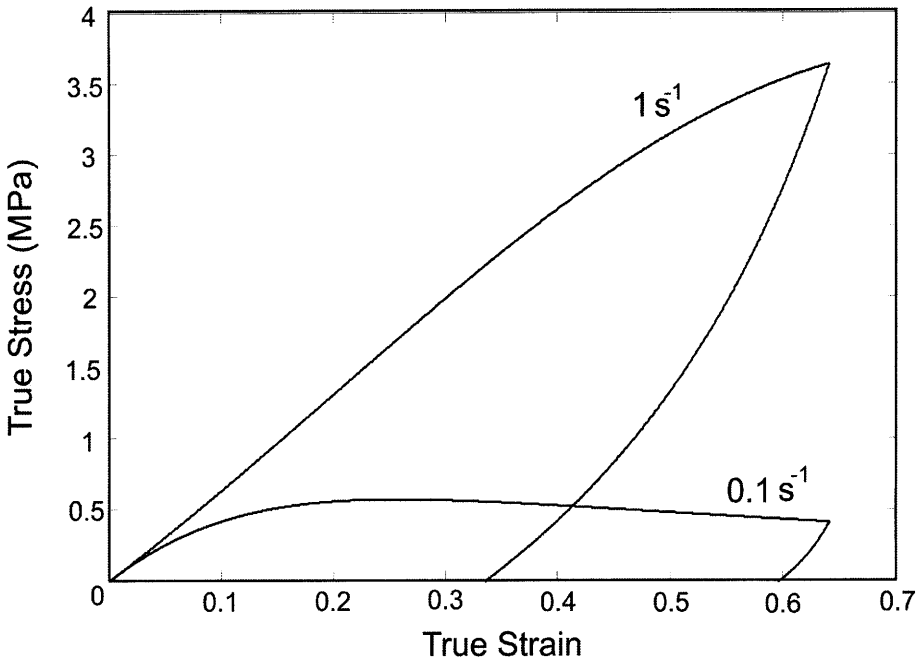

Figure 132: Stress-strain curves for a linear viscoelastic Neo-Hookean matrix. In this case, the model predicts extremely different residual strains for two similar strain rates.

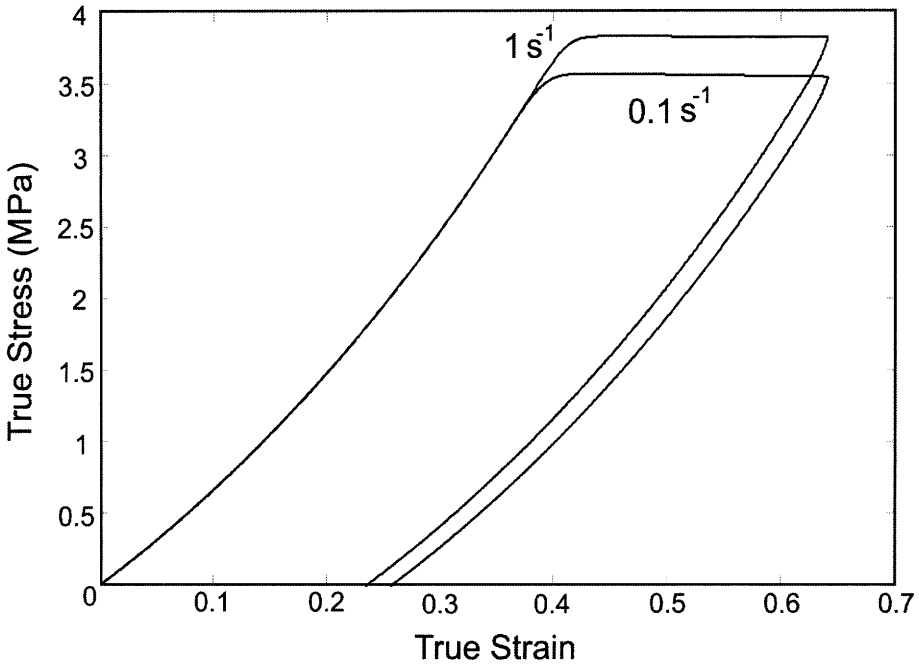

Figure 133: Stress-strain curves for a non-linear viscoelastic Neo-Hookean matrix. In this case, the model predicts similar residual strains for similar strain rates.

type of microstructural breakdown at the 'yield' strain (here a strain of approximately 0.37), similar to a plasticity event. However, in this case, because the stress contribution from

the matrix is so small and is only needed to account for the residual strain, the non-linear element was used to simplify the constitutive relationship. A linear viscoelastic behavior, characterized by a more complex system of springs and dashpots would provide a more 'physically realistic' characterization of the matrix behavior.

7 Appendix II: Determination of the fourth order Jacobian Tensors

The material Jacobian, which is required for the implementation of the constitutive model into ABAQUS, was calculated following the developments of Wilson (2005) and Bertoldi (2008). In ABAQUS, a material Jacobian is defined through the variation in Kirchhoff stress:

$$\delta\left(J\boldsymbol{\sigma}\right) = J\mathbb{C} : \mathbf{D} \tag{82}$$

where J is the determinant of the deformation gradient $\mathbf{F}$, $\boldsymbol{\sigma}$ is the Cauchy stress, and $\mathbf{D}$ is the virtual rate of deformation i.e. the symmetric part of the velocity gradient, $\mathbf{L}$. In terms of Cauchy stress $\boldsymbol{\sigma}$, and the deformation gradient $\mathbf{F}$, the Jacobian is given by:

$$\mathbb{C} = \frac{1}{J}\left(\boldsymbol{\sigma} \otimes \frac{\delta J}{\delta \mathbf{F}} + J\frac{\delta \boldsymbol{\sigma}}{\delta \mathbf{F}}\right)^{RT} \mathbf{F}^T \tag{83}$$

The derivative of J with respect to the deformation gradient $\mathbf{F}$, $\frac{\delta J}{\delta \mathbf{F}}$, is given by:

$$\frac{\delta J}{\delta \mathbf{F}} = \frac{\delta\left(det\mathbf{F}\right)}{\delta \mathbf{F}} = J\mathbf{F}^T \tag{84}$$

which leaves $\boldsymbol{\sigma}$ and $\frac{\delta \boldsymbol{\sigma}}{\delta \mathbf{F}}$ to be determined. Thus, the Jacobian for each constitutive model is different, since the Cauchy stress is a different function of the deformation gradient in each model. With regards to the phenomenological model of mussel byssal threads, the Jacobian of the matrix and the Jacobian of the fiber network must be calculated separately and summed in order to determine the overall material Jacobian.

7.1 The Jacobian for the extra-fibrillar Neo-Hookean matrix

As shown in the constitutive modeling section of this thesis, the Cauchy stress for an isotropic compressible Neo-Hookean material is given by

$$\boldsymbol{\sigma} = \frac{\mu}{J}(\mathbf{B} - \mathbf{I}) + K(J-1)\mathbf{I} \tag{85}$$

Thus, to calculate the Jacobian, only the derivative of this stress with respect to the deformation gradient $\frac{\delta \boldsymbol{\sigma}}{\delta \mathbf{F}}$ needs to be determined.

Using the chain rule, the derivative of Equation 85 with respect to the deformation gradient is:

$$\frac{\delta \boldsymbol{\sigma}}{\delta \mathbf{F}} = \mu \frac{\delta(1/J)}{\delta \mathbf{F}}(\mathbf{B} - \mathbf{I}) + \frac{\mu}{J}\frac{\delta \mathbf{B}}{\delta \mathbf{F}} + K\frac{\delta J}{\delta \mathbf{F}}\mathbf{I} = \frac{\delta J}{\delta \mathbf{F}}\left[K\mathbf{I} - \frac{\mu}{J^2}(\mathbf{B} - \mathbf{I})\right] + \frac{\mu}{J}\frac{\delta \mathbf{B}}{\delta \mathbf{F}} \tag{86}$$

where $\frac{\delta J}{\delta \mathbf{F}}$ is given by quation 84.

Noting that $\mathbf{B} = \mathbf{F}\mathbf{F}^T$, is is straightforward to calculate the derivative of the left Cauchy-Green tensor with respect to the deformation gradient.

$$\delta \mathbf{B} = \delta\left(\mathbf{F}\mathbf{F}^T\right) = \delta \mathbf{F}\mathbf{F}^T + \mathbf{F}\delta \mathbf{F}^T = 2\mathbb{I}\mathbf{F} : \delta \mathbf{F}^T = 2\left(\mathbb{I}\mathbf{F}\right)^{RT} : \delta \mathbf{F} \tag{87}$$

where $\mathbb{I}$ is the fourth order identity tensor.

Thus, the final equation for the derivative of the Cauchy stress with respect to the deformation gradient in the Neo-Hookean matrix is:

$$\frac{\delta \boldsymbol{\sigma}}{\delta \mathbf{F}} = \frac{\delta J}{\delta \mathbf{F}}\left[K\mathbf{I} - \frac{\mu}{J^2}(\mathbf{B} - \mathbf{I})\right] + 2\frac{\mu}{J}\left(\mathbb{I}\mathbf{F}\right)^{RT} \tag{88}$$

and, similarly, the final equation for the Jacobian of the Neo-Hookean matrix is:

$$\mathbb{C} = \frac{1}{J}\left[\boldsymbol{\sigma} \otimes \frac{\delta J}{\delta \mathbf{F}} + J\left(\frac{\delta J}{\delta \mathbf{F}}\left[K\mathbf{I} - \frac{\mu}{J^2}(\mathbf{B} - \mathbf{I})\right] + 2\frac{\mu}{J}(\mathbb{I}\mathbf{F})^{RT}\right)\right]^{RT} \mathbf{F}^T \tag{89}$$

In the following discussion, the Jacobian of the Neo-Hookean matrix will be referred to as $\mathbb{C}_{is}$.

7.2 The Jacobian for the eight-chain orthotropic unit cell of non-linear elastic fibers

Again, the stress in the fiber network is known (the derivation is outlined in the constitutive modeling section of this thesis). The equation for the Cauchy stress in the fiber network is:

$$\boldsymbol{\sigma} = \frac{\nu}{4J}\sum_{i=1}^{4}\frac{1}{\lambda_f^{(i)}}\left[\frac{EA}{L}r_0^2\left(\lambda_f^{(i)} - 1\right)\right]\mathbf{v}^{(i)} \otimes \mathbf{v}^{(i)} \tag{90}$$

and again, only the derivative of the Cauchy stress with respect to the deformation gradient needs to be calculated. Using the chain rule, this derivative becomes:

$$\begin{aligned}\frac{\delta \boldsymbol{\sigma}}{\delta \mathbf{F}} = -\frac{\nu}{4J^2}\sum_{i=1}^{4}\frac{1}{\lambda_f^{(i)}}\frac{\partial w_f}{\partial \lambda_f^{(i)}}\mathbf{V}^{(i)} \otimes \frac{\delta J}{\delta \mathbf{F}} \;&+\; \frac{\nu}{4J}\sum_{i=1}^{4}\left[\frac{1}{\lambda_f^{(i)}}\frac{\partial^2 w_f}{\partial \lambda_f^{(i)2}} - \frac{1}{\lambda_f^{(i)2}}\frac{\partial w_f}{\partial \lambda_f^{(i)}}\right]\mathbf{V}^{(i)} \otimes \frac{\delta \lambda_f^{(i)}}{\delta \mathbf{F}} \\ &+\; \frac{\nu}{4J}\sum_{i=1}^{4}\frac{1}{\lambda_f^{(i)}}\frac{\partial w_f}{\partial \lambda_f^{(i)}}\frac{\delta \mathbf{V}^{(i)}}{\delta \mathbf{F}}\end{aligned} \tag{91}$$

where $\mathbf{V}^{(i)}$ is the tensor product of the vectors $\mathbf{v}^{(i)}$.

With the derivative of J with respect to the deformation gradient known from Equation 84, and the derivative of the work with respect to fiber stretch known ($\frac{\partial w_f}{\partial \lambda_f^{(i)}} = f_f r_0$ and $\frac{\partial^2 w_f}{\partial \lambda_f^{(i)2}} = EAr_0$), it remains only to calculate $\frac{\delta \lambda_f^{(i)}}{\delta \mathbf{F}}$ and $\frac{\delta \mathbf{V}^{(i)}}{\delta \mathbf{F}}$. In the development of the

constitutive model, the overall fiber stretch was shown to be:

$$\lambda_f^{(i)} = \sqrt{\mathbf{v}_0^{(i)} \cdot \mathbf{C}\mathbf{v}_0^{(i)}} \tag{92}$$

Since $\mathbf{C}$ is a function of $\mathbf{F}$, the derivative of the fiber stretch with respect to the deformation gradient becomes:

$$\delta\lambda_f^{(i)} = \frac{1}{2\lambda_f^{(i)}} \left[\mathbf{v}_0^{(i)} \cdot \delta\mathbf{F}^T\mathbf{F}\mathbf{v}_0 + \mathbf{v}_0^{(i)} \cdot \mathbf{F}^T\delta\mathbf{F}\mathbf{v}_0\right] \tag{93}$$

which gives the final equation for the derivative of the fiber stretch with respect to the deformation gradient:

$$\frac{\delta\lambda_f^{(i)}}{\delta\mathbf{F}} = \frac{1}{\lambda_f^{(i)}} \left[\mathbf{v}_0^{(i)} \cdot \left(\mathbf{F}^T \otimes \mathbf{v}_0\right)\right]^T \tag{94}$$

To determine the derivative of the dyadic product of the vector orientations with respect to the deformation gradient, the dyadic product must first be written in terms of $\mathbf{F}$:

$$\mathbf{V}^{(i)} = \mathbf{v}^{(i)} \otimes \mathbf{v}^{(i)} = \mathbf{F}\mathbf{v}_0^{(i)} \otimes \mathbf{v}_0^{(i)}\mathbf{F}^T \tag{95}$$

Taking the derivative of each side yields:

$$\delta\mathbf{V}^{(i)} = \left(\delta\mathbf{F}\mathbf{v}_0^{(i)}\right) \otimes \left(\mathbf{v}_0^{(i)}\mathbf{F}^T\right) + \left(\mathbf{F}\mathbf{v}_0^{(i)}\right) \otimes \left(\mathbf{v}_0^{(i)}\delta\mathbf{F}^T\right) \tag{96}$$

which reduces to:

$$\delta\mathbf{V}^{(i)} = 2\left[\mathbb{I}\mathbf{F}\left(\mathbf{v}_0^{(i)} \otimes \mathbf{v}_0^{(i)}\right)\right]^{RT} : \delta\mathbf{F} \tag{97}$$

Thus, the derivative of $\mathbf{V}^{(i)}$ with respect to the deformation gradient is:

$$\frac{\delta\mathbf{V}^{(i)}}{\delta\mathbf{F}} = 2\left[\mathbb{I}\mathbf{F}\left(\mathbf{v}_0^{(i)} \otimes \mathbf{v}_0^{(i)}\right)\right]^{RT} \tag{98}$$

Thus, the derivative of the Cauchy stress with respect to the deformation gradient in the

eight-chain orthotropic unit cell is given by:

$$\frac{\delta\boldsymbol{\sigma}}{\delta\mathbf{F}} = \frac{-\nu}{4J^2}\sum_{i=1}^{4}\frac{1}{\lambda_f^{(i)}}\frac{\partial w_f}{\partial\lambda_f^{(i)}}\mathbf{V}^{(i)}\otimes\frac{\delta J}{\delta\mathbf{F}} + \frac{\nu}{4J}\sum_{i=1}^{4}\left[\frac{1}{\lambda_f^{(i)}}\frac{\partial^2 w_f}{\partial\lambda_f^{(i)2}} - \frac{1}{\lambda_f^{(i)2}}\frac{\partial w_f}{\partial\lambda_f^{(i)}}\right]\mathbf{V}^{(i)}\otimes\frac{\delta\lambda_f^{(i)}}{\delta\mathbf{F}} + \frac{\nu}{4J}\sum_{i=1}^{4}\frac{1}{\lambda_f^{(i)}}\frac{\partial w_f}{\partial\lambda_f^{(i)}}\frac{\delta\mathbf{V}^{(i)}}{\delta\mathbf{F}} \tag{99}$$

which can be inserted directly into the equation for the Jacobian in the fiber network. Once the Jacobian of the fiber network, $\mathbb{C}_{ani}$, is calculated, it must be summed with the Jacobian of the Neo-Hookean matrix, $\mathbb{C}_{iso}$, to give the final material Jacobian:

$$\mathbb{C} = \mathbb{C}_{iso} + \mathbb{C}_{ani} \tag{100}$$

8 Appendix III: Constitutive model using the FJC model

The Freely-jointed chain (FJC) model was also used to model the force-extension relationship of the protein bundles. Like the WLC model, the FJC is an entropic model, which is used more often in polymer mechanics, but has been shown to model the force-extension behavior of some bio-macromolecules quite well. For the FJC model, the strain energy function is given by:

$$u_c = K_B \Theta N \left(\frac{r}{L}\beta + \ln\left(\frac{\beta}{\sinh\beta}\right)\right) \tag{101}$$

where K_B is the Boltzmann constant, Θ is the temperature, N is the number of rigid links in the molecule, r is the chain end-to-end distance, L is the chain contour length, and β is the inverse Langevin function of the ratio of r to L i.e. $\beta = \mathcal{L}^{-1}\left(\frac{r}{L}\right)$. The inverse Langevin function is used to characterize the alignment of Kuhn segments towards the stretch direction and the corresponding reduction in entropy as the chain extends towards its contour length. However, because of the form of the Langevin function:

$$\mathcal{L}(\beta)) = \coth\beta - \frac{1}{\beta} \tag{102}$$

a closed form of the inverse Langevin function does not exist. Several approximations for the inverse Langevin have been developed and implemented with varying degrees of success. Here, the Pade approximant is used:

$$\beta\left(\frac{r}{L}\right) = \frac{r}{L}\left(\frac{3-\left(\frac{r}{L}\right)^2}{1-\left(\frac{r}{L}\right)^2}\right) \tag{103}$$

The force-extension relationship is obtained by differentiating the strain energy with respect to the chain end-to-end distance, and is given by:

$$f_c = \frac{NK_B\Theta}{L}\beta \tag{104}$$

In the case of the proteins in mussel byssal threads, as in the WLC development discussed in the constitutive modeling section of the thesis, the end (folded) domains are modeled using the FJC, while the central region is modeled as a stretching straight rod. Here too, the decomposition of the fiber stretch is additive.

$$L_f = L_m + L_e \tag{105}$$

$$\lambda_f = \frac{L_f}{L_{f0}} = \frac{(L_m + L_e)}{(L_m + L_e)_0} \tag{106}$$

and the force in the middle section is given by:

$$f_m = EA\,(\lambda_m - 1) \tag{107}$$

Similarly, the protein length evolution is captured by evolving the overall contour length of the end domains, with an unfolding equation of the same form as discussed with regards to the WLC model.

These equations were implemented into the fiber network stress-strain model, and monotonic and cyclic loading simulations were conducted. The results are shown in Figures 134 and 135 respectively. As can be seen, the Langevin chain model provides a good fit in monotonic loading. The model also demonstrates a fairly large amount of hysteresis (a comparable amount to the WLC model, and only slightly less than the actual material), and captures the non-linearity of the unloading much better than the WLC. However, the model predicts a residual (non-zero) stress after the material has been fully unloaded. Decreasing N (the number of rigid links in the polymer chain) decreases this residual stress, but cannot remove it completely - for N-values lower than the ones shown in this plot, the model becomes unstable, and force equilibrium cannot be achieved. Thus, the FJC model provides

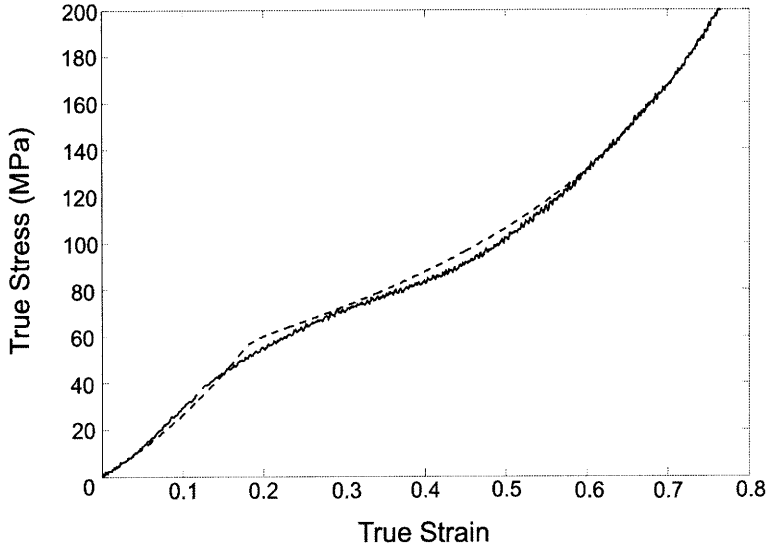

Figure 134: Stress-strain curve for monotonic loading of the distal thread section at a nominal strain rate of $1s^{-1}$. Experimental results are shown with a solid line, model results are shown with a dashed line.

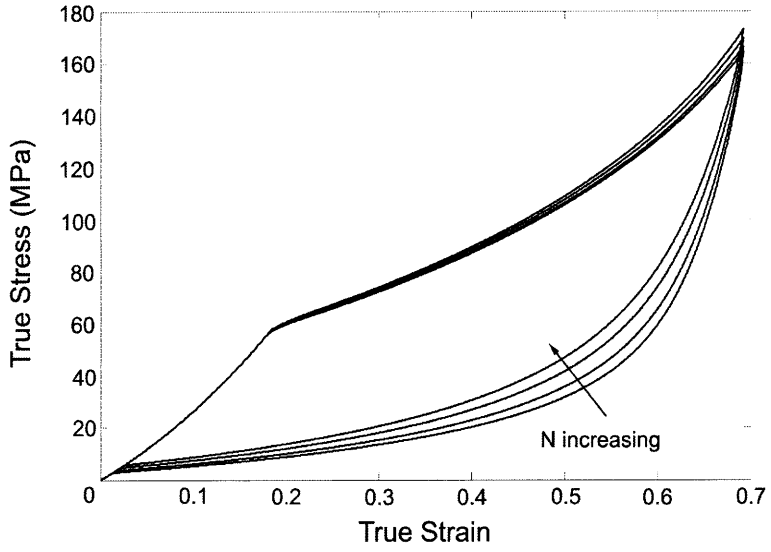

Figure 135: Stress-strain curve for cyclic loading of Langevin chain model at different N-values. Cyclic loading captures large hysteresis, and smoothness of unloading curve, but predicts a non-zero residual stress after loading. For N-values

a better fit than either the WLC or the Bertoldi model, but still demonstrates some serious short-comings with regard to capturing the material behavior.

References

[1] Bertoldi, K., and Boyce, M.C., 2007. Mechanics of the Hysteretic Large Strain Behavior of Mussel Byssus Threads. Journal of Materials Science 42, 8943-8956.

[2] Bell, E.C., and Gosline, J.M., 1996. Mechanical Design of Mussel Byssus: Material Yield Enhances Attachment Strength. Journal of Experimental Biology 199, 1005-1017.

[3] Bischoff, J.E., Arruda, E.M., and Grosh, K. 2002. A Microstructurally Based Orthotropic Hyperelastic Constitutive Law. Journal of Applied Mechanics - Transactions of the ASME 69, 570-579.

[4] Bischoff, J.E., Arruda, E.M., and Grosh, K. 2002. Orthotropic Hyperelasticity in Terms of an Arbitrary Molecular Chain Model. Journal of Applied Mechanics - Transactions of the ASME. 69, 198-201.

[5] Brazee, S.L., and Carrington, E., 2007. An Interspecific Comparison of the Mechanical Properties of Mussel Byssus. Biological Bulletin 211, 263-274.

[6] Carrington, E., 2008. Along the Silk Road, Spiders Make Way for Mussels. Trends in Biotechnology 26, 55-57.

[7] Carrington, E., and Gosline, J.M., 2004. Mechanical Design of Mussel Byssus: Load Cycle and Strain Rate Dependence. American Malacological Bulletin 18 135-142.

[8] Cha, H.J., Hwang, D.S., Lim, S., White, J.D., Matos-Perez, C.R., and Wilker, J.J., 2009. Bulk Adhesive Strength of Recombinant Mussel Adhesive Protein. Biofouling 25, 99-107.

[9] Eyring, H. 1936. Viscosity, Plasticity, and Diffusion as Examples of Absolute Reaction Rates. Journal of Chemical Physics 4, 283-291.

[10] Harrington, M.J., and Waite, J.H., 2007. Holdfast Heroics: Comparing the Molecular and Mechanical Properties of Mytilus Californianus Byssal Threads. Journal of Experimental Biology 210, 4307-4318.

[11] Hassenkam, T., Gutsmann, T., Hansma, P., Sagert, J., and Waite, J.H., 2004. Giant Bent-core Mesogens in the Thread Forming Process of Marine Mussels. Biomacromolecules 5, 1351-1355.

[12] Holten-Andersen, N., Zhao, H., Waite, J.H., 2009. Stiff Coatings on Compliant Biofibers: The Cuticle of Mytilus Californianus Byssal Threads. Biochemistry, 48, 2752-2759.

[13] Holten-Andersen, N., Mates, T.E., Toprak, M.S., Stucky, G.D., Zok, F.W., Waite, J.H., 2009. Metals and the Integrity of a Biological Coating: The Cuticle of Mussel Byssus. Langmuir, 25, 3323-3326.

[14] Holten-Andersen, N. Fantner, G.E., Hohlbauch, S., Waite, J.H., and Zok, F.W., 2007. Protective Coatings on Extensible Biofibers. Nature Materials 6, 669-672.

[15] Kroner, E. 1960. Allgemeine Kontinuumstheorie der Versetzungen und Eigenspannungen. Archive for Rational Mechanics and Analysis. 4, 273-334.

[16] Lee, E.H., 1969. Elastic-plastic Deformation at Finite Strains. Journal of Applied Mechanics 36, 1-6.

[17] MacKintosh, F.C., Kas, J., and Janmey, P.A., 1995. Elasticity of Semiflexible Biopolymer Networks. Physical Review Letters 75, 4425-4428.

[18] Marko, J.F., and Siggia, E.D., 1995. Stretching DNA. Macromolecules 28, 209-212.

[19] Marszalek, P.E., Lu, H., Li, H.B., Carrion-Vazquez M., Oberhauser, A.F., Schulten, K., and Fernandez, J.M., Mechanical Unfolding Intermediates in Titin Modules. Nature 402, 100-103.

[20] Moeser, G.M., and Carrington, E., 2006. Seasonal Variation in Mussel Byssal Thread Mechanics. Journal of Experimental Biology 209, 1996-2003.

[21] Mullins, L., 1969. Softening of Rubber by Deformation. Rubber Chemical Technology 42, 339-362.

[22] Palmer, J.S., 2008. Microstructurally-based Constitutive Models of Cytoskeletal Networks for Simulation of the Biomechanical Response of Biological Cells. MIT PhD Thesis.

[23] Qi, H.J., Ortiz, C., and Boyce, M.C., 2006. Mechanics of Biomacromolecular Networks Containing Folded Domains. Journal of Engineering Materials and Technology - Transactions of the ASME 128, 509-518.

[24] Rief, M., Gautel, M., Oesterhelt, F., Fernandez, J.M., and Gaub, H.E., 1996. Reversible Unfolding of Individual Titin Immunoglobulin Domains by AFM. Science 276, 5315.

[25] Silverman, H.G., Roberto, F.F., 2007. Understanding Marine Mussel Adhesion. Marine Biotechnology Review 9, 661-681.

[26] Smeathers, J.E., and Vincent, J.F.V., 1979. Mechanical Properties of Mussel Byssus Threads. Journal of Molluscan Studies 45, 219-230.

[27] Staple, D.B., Payne, S.H., Reddin, A.L.C., and K, H.J., 2008. Model for Stretching and Unfolding the Giant Multidomain Muscle Protein Using Single-Molecule Force Spectroscopy. Physical Review Letters 101, 248301.

[28] Vaccaro, E., and Waite, J.H., 2001. Yield and Post-Yield Behavior of Mussel Byssal Thread: A Self-Healing Biomolecular Material. Biomacromolecules 2 (3), 906-911.

[29] Waite, J.H., Zin, X., and Coyne, K.J., 2002. The Peculiar Collagens of Mussel Byssus. Matrix Biology 17, 93-106.

[30] Waite, J.H., Vaccaro, E., Sun, C., and Lucas, J.M., 2002. Elastomeric Gradients: A Hedge against Stress Concentration in Marine Holdfasts? Philosophical Transactions: Biological Sciences 357, 143-153.